London Centre for Nanotechnology
University College London
University of London

High Resolution Atomic Force Microscopy of Functional Biological Molecules

Alice Leonora Bedford Pyne

Submitted in partial fulfilment of the requirements
for the degree of Doctor of Engineering
at University College London

August 2, 2015

I declare that the work presented in this thesis is my own. Where information has been obtained from other sources, I declare this has been clearly indicated in the thesis.

Abstract

Nanoscale dynamic biological processes are central to the regulation of cellular processes within the body. The direct visualisation of these processes represents a challenge because of the intrinsic difficulties of imaging at the nanoscale, well below the diffraction limit of light. Here we use the Atomic Force Microscope to 'feel' the structure of single biomolecules adsorbed to a flat substrate at sub-nanometre resolution.

We have enhanced the performance and resolution of Atomic Force Microscopy (AFM) for imaging DNA plasmids in solution, resolving its secondary structure in the form of the double helix. We are able to observe local deviations from the average structure, and in particular variations in the depth of the grooves in the double-stranded DNA which may be attributed to supercoiling of the DNA. Such local variations of the DNA double helix structure are important in mediating protein-DNA binding specificity and thus in regulating gene expression. We show preliminary data on DNA minicircles, which can be used as a synthetic system to study how supercoiling affects DNA structure and influences DNA-protein binding interactions with implications for many genetic processes.

Going from fundamental science to a biomedical application, we have used AFM to study the functional mechanisms of antimicrobial peptides, which are developed in response to the growing problem of antimicrobial resistance. Antimicrobial peptides disrupt microbial phospholipid membranes but direct observation of the mode of action for the disruption is lacking. Here we visualise the mode of action of synthetic antimicrobial cationic alpha-helical peptides. Two of these peptides attack membrane via previously unknown mechanism: Amhelin forms pores which are not limited in size but expand from the nano to micrometre scale; amhelit also forms pores but only penetrating a single layer of the lipid bilayer that forms the membrane.

We present the first nanoscale visualisation of membrane disruption by the naturally occurring antimicrobial peptide cecropin B. This is complemented by the visualisation of peptides similar in sequence to cecropin B, but with structural modifications which are used to elucidate the structural origins of cecropin B's mechanism of action. Improvements in imaging capabilities of the AFM, as tested on DNA, were shown to benefit imaging of the mode of action for antimicrobial peptides, including time-lapse imaging of a novel expanding monolayer state.

We have thus used AFM to elucidate mechanisms of action for antimicrobial peptides. Relating these mechanisms to the peptide sequences, we can gain insight into how peptide sequence affects structure and function for these antimicrobial agents. This may aid in the development and improvement of novel peptide antibiotics.

Acknowledgements

Firstly I would like to thank my supervisor Dr. Bart Hoogenboom from the London Centre for Nanotechnology for his continued support and advice throughout my PhD, through all of its ups and downs, without whom I could not have accomplished all that I have in four years. Special thanks also goes to my second supervisor Rachel McKendry, whose unfailing enthusiasm and support of all my endeavours has helped me to achieve my goals.

I am also extremely grateful to the NPL as a co-supervising institution, including Dr Deb Roy, for their support of my project. I am grateful to Dr Max Ryadnov and all of his team at the NPL for the synthesis of antimicrobial peptides for this project, and for interesting and informative discussion on the effect of antimicrobial peptides on model membranes. I would also like to acknowledge the EPSRC funding I have received from the UCL Molecular Modelling and Materials Science Doctorate Training Centre.

I would like to thank all those at Bruker Santa Barbara for their support of my experiments and for having had me to visit their lab on multiple occasions, resulting in brilliant data. I would like to especially thank Andrea Slade for her help, support and guidance, and Bede Pittinger, Chanmin Su, Shuiqing Hu, and Steve Minne.

I would like to thank Tony Maxwell and his group at the John Innes Centre, Fiore and Michael, and all of the minicircles team, Andy Bates, Sarah Harris, Agnes Noy, for such stimulating meetings, and for the opportunity to collaborate on a new project, which has already yielded exciting results.

To all those at Bristol University, who I encountered on my path into AFM and those who I have collaborated with through my PhD, especially Merv, Loren and Ollie, thank you.

To my group past and present, Aizhan, Adrian, Alex, Ben, Carl, Dino, George, Hasan, Nitya, Richard, Rosie, Ruth, Sofya, and Zermina, thank you for all your help with experiments, papers and this thesis.

Finally to all of those people who have helped me through this PhD, my family, Grace, Mummy and Daddy, and all my wonderful friends, you know how much I appreciate you and your understanding, especially Ben, Lewis, Marianne and Tash.

Publications

Antimicrobial monolayer poration. **A. Pyne** et al., *in preparation.*

Atomic force microscopy with single-spot optical actuation/detection for imaging a mobile DNA double helix. **A. Pyne**, C. Leung, J. Stinson, D. Roy and B. W. Hoogenboom, *in preparation.*

High-speed AFM imaging of expanding pores in model membranes. O. Payton, L.Picco, **A. Pyne**, M. Miles, *in preparation.*

DNA minicircles as probes of topology. M. Piperakis, F. Cugliandolo, **A. Pyne**, A. Noy, A. Bates, S. A. Harris, B. W. Hoogenboom, A. Maxwell, *in preparation.*

Atomistic simulations of DNA topology A. Noy, **A. Pyne**, M. Piperakis, F. Cugliandolo, A. Bates, B. W. Hoogenboom, A. Maxwell, S. A. Harris, *in preparation.*

Single-Molecule Reconstruction of Oligonucleotide Secondary Structure by Atomic Force Microscopy. **A. Pyne,** R. Thompson, C. Leung, D. Roy and B. W. Hoogenboom, *Small* **10**(16), p.p.3257-3261 (2014). Highlighted by two front covers in Microscopy & Analysis, *Jan 2013, Jun 2014*

Nanoscale imaging reveals laterally expanding antimicrobial pores in lipid bilayers. P. Rakowska, H. Jiang, S. Ray, **A. Pyne, ,** B. Lamarre, M. Carr, P. Judge, J. Ravi, U. Gerling, B. Koksch, G. Martyna, B. W. Hoogenboom, A. Watts, J. Crain, C. Grovenor and M. Ryadnov, *Proc. Natl. Acad. Sci. USA* **110**(22), p.p.8918-8923 (2013).

Atomic Force Microscopy with Nanoscale Cantilevers Resolves Different Structural Conformations of the DNA Double Helix. C. Leung, A. Bestembayeva, R. Thorogate, J. Stinson, **A. Pyne,** C. Marcovich, J. Yang, U. Drechsler, M. Despont, T. Jankowsji, M. Tschöpe and B. W. Hoogenboom, *Nano Lett.* **12**(7), p.p.3846-3850 (2012). Highlighted in; D. Evanko, Biophysics: Upgrades for the AFM. *Nat. Methods* **9**, 778-779 (2012).

Presentations

Invited Talks

Imaging the secondary structure of DNA minicircles using Atomic Force Microscopy, UCL Institute of Physics of Living Systems Talk. *Dec 2014*

PeakForce Tapping Mode: Enabling High-Resolution Imaging of The DNA Double Helix, Bruker webinar invited guest speaker. *Mar 2013*

Conference Presentations

Single-molecule reconstruction of DNA secondary structure by atomic force microscopy, AFM Biomed, San Diego, CA, USA. *Dec 2014*
Journal of Molecular Recognition Oral Presentation Award

Single-molecule reconstruction of DNA secondary structure by Atomic Force Microscopy, Nanomeasure Conference, Beijing, China. *Sept 2014*

Single-molecule reconstruction of DNA secondary structure by Atomic Force Microscopy, British Biophysical Society Meeting, Warwick, UK. *Sept 2014*

Single-molecule reconstruction of DNA secondary structure by Atomic Force Microscopy, XVI. Linz Winter Workshop, Linz, Austria. *Jan 2014*

Contents

List of Figures

List of Tables

Chapter 1

Introduction

This chapter provides a background on different methods to elucidate the structure and function of biomolecules on the nanoscale. It highlights the importance of Atomic Force Microscopy (AFM) as a tool to study biomolecules at high spatial resolution in aqueous environment, and illustrates this importance with selected applications of AFM in biology. It briefly introduces some of the complications of AFM for imaging biomolecules, using DNA as an example. To set the stage for the AFM applications that are central in this thesis, it also provides a background on DNA biophysics and antimicrobial peptides, and concludes by defining the scope of this thesis.

1.1 Background

Living cells are fundamental units of life, but are not uniform building blocks, varying widely in their structure and function. The similarities between cells are shown when we look deeper, at their chemistry, and see that the building blocks for cells are essentially the same, coming from the single molecules such as amino acids, sugars, nucleic acids and lipids [1].

Since at the single-molecule level structure and function are inextricably linked [2], it is thus important to determine the structure of proteins and other biomolecules. Ideally, this is done for single molecules under physiological conditions, to elucidate the function of biological molecules within the cell, and to determine the behaviour of groups of biomolecules from the bottom up.

To understand how cells function, i.e., replicate, grow and die, we must look at the biological processes within the cell, again ideally from the single-molecule level upwards. The function of single biological molecules on the nanoscale is determined by their

structure and by their dynamics. This dynamics is hard to access with traditional techniques for structure determination, which require molecules to be crystallised, and/or imaged in vacuum. In this thesis, I will show how AFM can be used and optimised to image single molecules under near-physiological conditions (in aqueous salt solution) to determine their structure and function on the nanoscale, focussing on submolecular-resolution imaging of DNA and on time-lapse imaging of membrane perforation by antimicrobial peptides.

1.2 Dynamic Biomolecular Processes

Cells gain their specific attributes and functionality through a combination of many dynamic processes carried out by its constituent molecules. Molecules use both chemical energy and thermal fluctuations to perform essential tasks within the cell ,which have large effects on the organism as a whole. Dynamic processes within the cell at the nanoscale thus determine cellular characteristics and function [3]. The function of each biomolecule can be established either at the single-molecule level, as part of a larger working assembly of molecules such as the cell membrane, or on the larger scale of cells and cell assemblies [4]. Some examples of dynamic biomolecular processes relevant to the work in this thesis are discussed here.

The genetic material of the cell is contained within its DNA. Gene expression is the process by which this genetic material is first transcribed to RNA and next translated into proteins to form essential building blocks and machinery in the cell. The seminal example of regulation of gene expression is the *lac* operon, which allows modulation of gene transcription at the single molecule level. In the *lac* operon, gene expression can by suppressed due to a binding between DNA and the transcription factor protein. This system shows how changes at the molecular, nanoscale level determine which genes are expressed into a cell, and therefore determine properties of the cell.

The DNA within a cell must be protected, maintained and correctly packaged to allow it to be correctly replicated and transferred to daughter cells. DNA in an eukaryotic cell is packed into chromosomes which contain the genetic material in a form where it can be replicated. The packing of DNA into this form is non-trivial, given that the DNA in an eukaryotic chromosome can have a length at the scale of centimetres, and yet must be compressed into a the nucleus of less than a micron across. Local changes in DNA packing can lead to changes in the expression of proteins and peptides from the cells, e.g., by facilitating or preventing the binding of gene transcription machinery to the DNA. It is therefore important to understand how deviations in the local DNA structure can lead to changes in protein binding and therefore gene expression.

Many other fundamental biomolecular processes take place at, on, and in the 3∼5 nm

thick membrane that separated and protects the cell from its surroundings. This cell membrane is an essential part of the cell not only as the boundary to the cell, maintaining its integrity and function, but also as an activity hub for the cell with highly complex structure on the nano- and microscale. The cell membrane is a phospholipid bilayer into which many proteins of the cell are incorporated[1]. These proteins perform a range of essential functions including molecular transport, fuel generation, cell motility and response. Not only is the cell membrane of great interest for its intrinsic properties, but also as a target for toxins, which porate or disrupt the membrane, compromising cellular function [5]. Similarly, bacteria can be attacked by damaging and/or perforating their protective membrane, which can be achieved, e.g., with the antimicrobial peptides that will be described below.

1.3 Techniques to Study Biomolecules

A single biomolecule can be 5 orders of magnitude smaller than the objects we see with he naked eye. To observe objects at this scale we need to use techniques that improve our imaging power. The simplest of these is conventional optical microscopy, the resolution of which is defined by the wavelength of light: An optical microscope cannot resolve two separate and simultaneous light sources if they are separated by less than about half the wavelength of visible light. For visible light this several hundred nanometres, i.e., 2 orders of magnitude larger than the size of a typical biomolecule.

There are several powerful methods to visualise single molecules, probe their intrinsic properties, manipulate them and examine their behaviour and dynamics. Each technique provides insight into single-molecule biophysics, and each has its own advantages and disadvantages/limitations.

1.3.1 Techniques to Visualise Biomolecular Structure and Dynamics

Some of the most widely used techniques to image biomolecules are discussed here, including examples of their capabilities that are relevant to the studies carried out in this thesis. In addition, there are techniques which can measure the relative dynamics of intramolecular domains, such as FRET, which will also be discussed below.

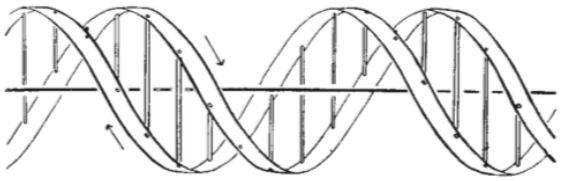

Figure 1.1: The original diagrammatic sketch of the DNA double helix, the two ribbons represent the phosphate backbones and the vertical rods the base bairs. Reproduced from [6]

1.3.1.1 X-ray Crystallography

Arguably the best-known discovery made using X-ray crystallography is that of the double helix structure of DNA, the original diagrammatic sketch is shown in figure 1.1, reproduced from [6].

The DNA double helix structure was elucidated using X-ray crystallography data obtained by Wilkins and Franklin [7], [8]. Franklin's data are shown in figure 1.2 The DNA structure provides an explanation of how genetic material is replicated and stored, which underpins most of our current molecular-scale understanding of the cell.

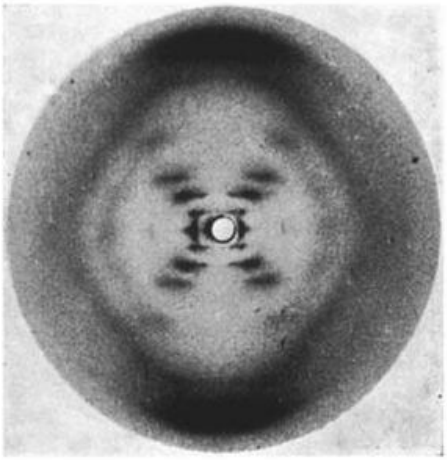

Figure 1.2: One of Rosalind Franklin's X-ray diffraction patterns, showing the diffraction pattern of B-form DNA. Reproduced from [8]

X-ray crystallography requires a molecule to be arranged in a periodic crystal, the preparation of which is non-trivial, requiring biomolecule purification and formation of a highly ordered crystal from the purified molecule. X-ray crystallography exploits the short (1-10 Ångström) wavelength of X-rays, which is of a similar size as interatomic spacings. The X-rays diffract and interfere with each other as they are scattered by

the periodic layers of the crystal. The obtained diffraction patterns can be analysed to reconstruct an atomic representation of the biomolecule. Crystallographic methods have determined the vast majority of the ∼100,000 structures in the Protein Data Bank [9].

The resolution of X-ray crystallography has improved substantially, with structures routinely being determined at Ångström resolution. Figure 1.3 shows a high resolution image of the Watson-Crick form of DNA (B-DNA). B-DNA exhibits a right-handed helix with a helical repeat (pitch) of ∼3.6 nm, showing major and minor grooves of widths 2.2 nm and 1.2 nm respectively.

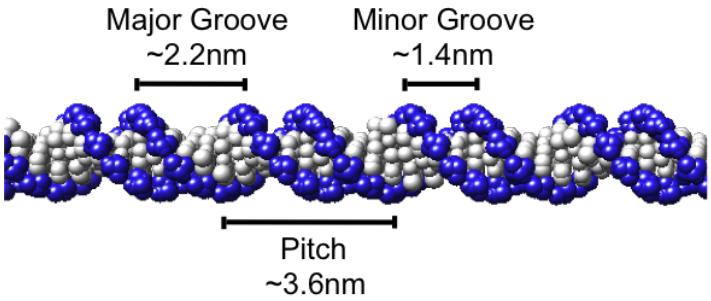

Figure 1.3: A space filling representation of B-DNA, annotated with the major and minor groove values. The image was rendered using Chimera [10] from the PDB file 1BNA [11].

X-ray crystallography requires samples to be in a highly ordered state in vacuum, and cannot probe biomolecular structure in solution, thus failing to capture the dynamics of the molecule, which could give further insight into its function.

X-ray crystallography has recently been enhanced by the development of X-ray free-electron laser (XFEL) techniques and their application to bimolecular structure determination. Structural information is obtained using short and intense pulse of X-rays, which can determine the structure to high resolution before radiation damage occurs. This higher intensity facilitates the use of smaller crystals than conventional X-ray crystallography, on the order of hundreds of nanometres [12]–[15].

1.3.1.2 Electron Cryo-Microscopy

Cryo-electron Microscopy (cryo-EM) uses the diffraction of electrons to map the charge density of a sample, which can be used to achieve high resolution images of biological samples such as membrane proteins [16]. As in X-ray crystallography, the sample must be kept under vacuum conditions. Electron microscopy has a simpler sample preparation process than X-ray crystallography, since the samples do not need to be crystallised. In addition, cryo-EM uses a cryogen to rapidly cool the biomolecule,

trapped in its physiological conformation. 3D structure is obtained by mapping images of identical biomolecules in different orientations. In cryo-EM, molecular structures are typically determined by fitting atomic models into density maps that result from averaging images of thousands of molecules, which can also provide snapshots of different biomolecular conformations [17]. Recent advances in electron cryo-EM, most notably in detector technology and processing, have led to greatly increased resolution in structure determination [18]. Cryo-EM performance can be illustrated by the ribo-

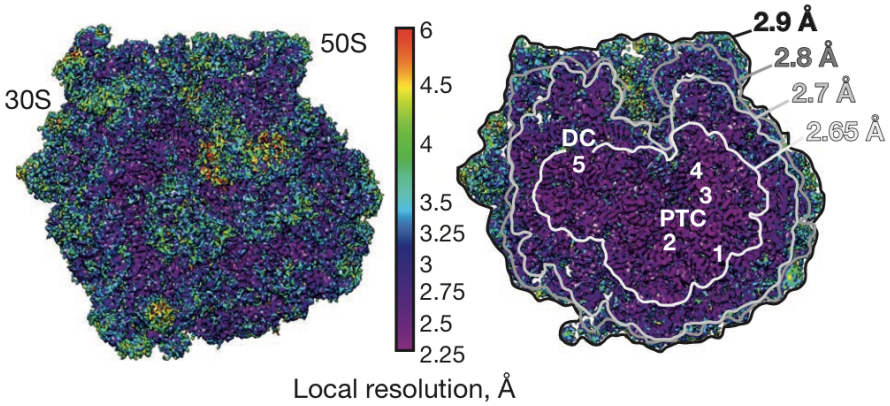

Figure 1.4: A cryo-EM map of 70S ribomose structure from textitE-coli, coloured according to local resolution. Reproduced from [19].

some, a large protein-RNA complex that translates RNA into proteins. The ribosome undergoes conformational changes during the binding of tRNA and protein factors, the dynamics of which are central to its ability to form proteins [20]. Cryo-EM has recently determined ribosomal structure at a resolution comparable to the best-resolved X-ray structures (figure 1.4) [19], providing essential information on how the ribosome performs its function.

1.3.1.3 Nuclear Magnetic Resonance (NMR)

Nuclear magnetic resonance (NMR) can obtain structural models of biomolecules to atomic resolution by measuring the distance between various proton spins on a molecule. The resolution of NMR is similar to crystallography, with the advantage that it does not require the molecules to be arranged in a crystalline lattice. NMR can also be carried out in liquid, and so visualise thermodynamics, kinetics and dynamics of biomolecules under physiological conditions [21]. NMR has traditionally been carried out on small molecules, of around 100 kDa, as increasing the molecule size results in broadening of the resonance peaks and complicate the analysis, increasing the uncertainty and therefore reducing the resolution. Under some circumstances and with recently developed techniques, it is to visualise proteins of sizes up to 1 MDa [22].

Membrane proteins present a challenge for structure determination, with only a few hundred structures determined to date [23], [24]. Many of the challenges associated with structural determination of membrane proteins are due to crystallisation. NMR provides means to circumvent these problems, and has been used to determine structures of membrane proteins reconstituted in lipid bilayers [25], [26] and characterise their function [27].

1.3.1.4 Super-resolution

For single-molecule studies on a larger scale, super-resolution optical microscopy allows the localisation of fluorescently labelled probes at a resolution of tens of nanometres used under physiological conditions [28]. This allows for fast and direct imaging of biomolecules in liquid.

Super-resolution optical microscopy uses techniques in fluorescent labelling to increase the resolution of optical microscopy beyond the diffraction limit. There are a number of techniques which have been developed to overcome the diffraction limit, including: stimulated emission depletion (STED) [29]; photoactivated localization microscopy (PALM) [30]; stochastic optical reconstruction microscopy (STORM) [31]; saturated structured-illumination microscopy (SSIM) [32].

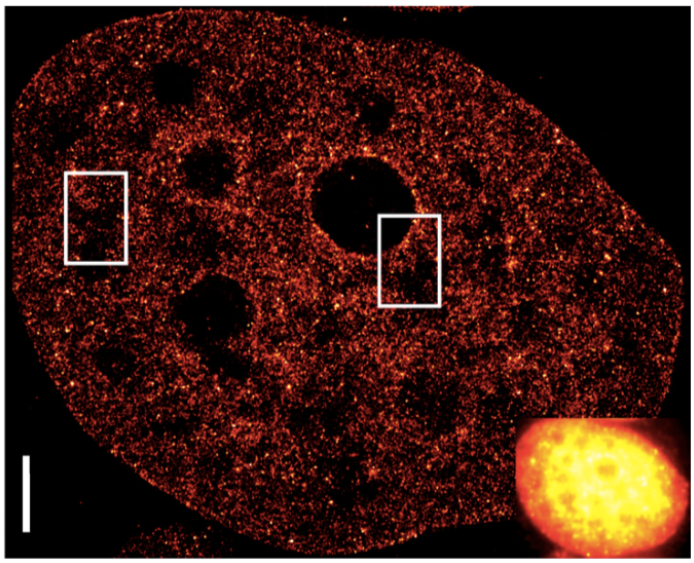

Figure 1.5: Super-resolution image of a HeLa cell nuclei showing nuclear chromatin imaged using dSTORM, inset; a diffraction limited image. Scale bar: 2 μm. Reproduced from [33].

Super-resolution microscopy is now being used to image DNA within the cell to examine its nanoscale organisation [34]. The manner in which DNA is organised in the cell

directly relates to its function for the essential cellular processes of transcription replication and repair [35]. Resolution better than 10 nm has been achieved on chromatin mapping in entire nucleus using dSTORM [33], as shown in figure 1.5. This technique has been used more recently to visualize replication and segregation processes in E. coli [36].

Though the resolution achievable by these techniques is an order of magnitude improved on optical microscopy, it is still one or two orders of magnitude worse than that achievable by AFM. In addition there are limitation due to the labelling required, which in itself can change the properties of the biomolecule, and due to bleaching of the fluorophores.

1.3.1.5 Fluorescence Resonance Energy Transfer (FRET)

FRET allows the measurement of motion at the nanoscale by measuring the separation of two different fluorophores attached to a biomolecule of interest and separated by 1-10 nm. The first of the two fluorophores (donor) is excited by an external source and emits light which excites the second fluorophore (acceptor) through non-radiative energy transfer [1]. The separation of these molecules is related to the intensity of emission of the second molecule. The intensity can then be interpreted as a the separation of the two fluorophores, giving rise to information on biomolecular dynamics [37]. FRET can be used for single molecule analysis, monitoring conformational changes as rotations and distance changes at the nanometer scale [38].

FRET has been shown to provide dynamics for a range of biomolecular dynamic processes including, DNA-protein interactions [39], protein folding [40] nucleosome unwinding [41] and ion channel mechanisms [42] amongst many others [43].

A main disadvantage of FRET is the requirement of a minimum of two fluorescent labels, which must have overlapping emission spectra and yet do not overlap too significantly in order that the acceptor is not excited by incident light [3]. In addition, the quantitative interpretation of FRET data is complicated by effects of the environment and molecular orientation on the energy transfer by the dyes [43].

1.3.2 Techniques to Manipulate Biomolecules

Force plays a fundamental role in biological processes. All biological motion, from cellular motility to the replication and segregation of DNA, is driven by molecular-scale forces. These forces are typically at the scale of picoNewtons, which can now be measured by several techniques that are described below[44].

By measuring single molecules, one avoids the implicit averaging required in ensemble measurements. Rare or transient conformations that might be obscured by an averaging technique can be resolved provided that the measurement technique can achieve the required resolution [45].

Single-molecule force measurements span approximately six orders of magnitude in length (0.1 nm - 0.1 mm) from the measurement of RNA polymerase advancing a single base pair (0.34 nm) along DNA [46] to the manipulation of cells (tenths of a mm), and in force (0.01 pN - 10 nN), from nucleic acid folding kinetics (∼0.1 pN) [47] to the mechanical disruption of covalent bonds (several nN) [44], [48].

Optical [45], [49] and magnetic tweezers [45], [50], [51] are commonly used for force measurements in the low-picoNewton force regime with AFM-based single-molecule force spectroscopy (SMFS) used for measurements of tens to hundreds of picoNewtons [37]. AFM force spectroscopy has become a widespread and powerful tool to investigate the mechanical properties of proteins and force-induced processes [44], [45].

1.3.2.1 Optical Tweezers

Optical tweezers are a versatile single-molecule manipulation technique. They can exert picoNewton forces on particles whilst measuring the three-dimensional displacement of the trapped particle with Ångström resolution. Figure 1.6 shows schematics of optical trap setups commonly used to measure biomolecule movements and interactions.

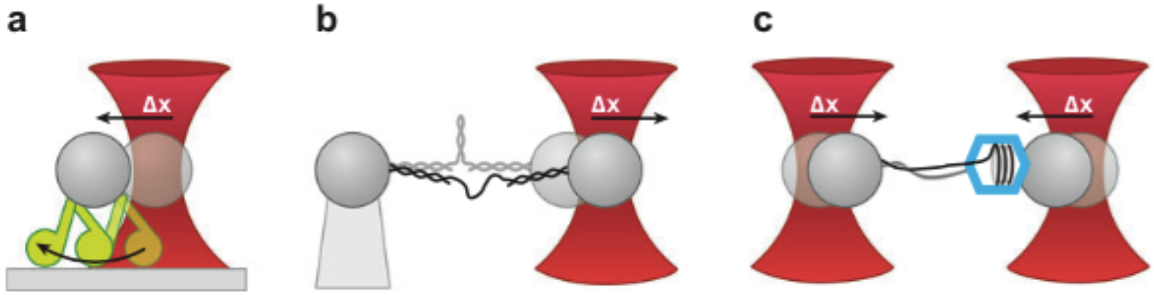

Figure 1.6: Experimental setups for optical tweezers. (a) A biomolecular motor e.g. kinesin is attached directly to a polystyrene bead held in an optical trap and its motion are revealed by movement of the trapped bead. (b) One end of the biological system is attached to a second polystyrene bead stabilised by suctioning onto the end of a micropipette. The motion of the biological system, e.g RNA unfolding, is revealed in the motion of the trapped bead. (c) A dual trap optical setup where the two beads give information on biomolecule motion, which used together can reduce noise. Figure reproduced from [49].

Optical tweezers have been used to show RNA polymerase performing single base pair

steps (0.34 nm) along a single strand of DNA. In those experiment, using a dual-trap setup, RNA polymerase was immobilised by tethering to a stable optical trap, reeled in a bead attached to the end of the transcribed DNA, with movement measured by the resulting motion of the bead in the second optical trap [46]. To achieve sufficient spatial and force resolution, many improvements in optical trapping were required, resulting in a resolution that is limited by Brownian motion [52].

Optical tweezer measurements of RNA polymerase on DNA have also revealed details of transcription including accurate measurements of the stall force (∼30 pN) [53], visualisation of backtracking of polymerase along a DNA template [52], [54], and elucidation of mechanisms of translocation[46].

In optical-tweezer experiments, limitations arise from from sample heating and photodamage issues. Distance measurements with optical tweezers are usually limited to applied forces in the range of 0.1-100 pN.

1.3.2.2 Magnetic Tweezers

In magnetic tweezers, single molecules are attached to small, magnetic particles and manipulated by alteration of the magnetic force. In addition the position of these particles can be measured to ∼10 nm accuracy by tracking scattered light from the magnetic particles [37].

This method has applications in monitoring DNA tertiary structure, or topology, whereby DNA forms complex higher order structures such as knots, coils or plectonemes, under torsional stress or supercoiling [45]. Plectonemes (interwound DNA structures) have been visualised as static conformations by EM [55] and other techniques. Monitoring how plectonemes form has implications for DNA structure in terms of long range DNA interactions mediated by the higher order structure, and also in DNA structural changes such as protein binding triggered by local structure changes. Figure 1.7 shows a typical experimental setup for monitoring the formation of plectonemes using magnetic tweezers [56].

This method has been used to study the topological changes in DNA during nucleosome formation [57] and combined with fluorescence techniques to explore the dynamics of diffusion and hopping of plectonemes in DNA [58].

Magnetic tweezers allow for effective manipulation of DNA. However, their time resolution is lower than that of optical tweezers by some orders of magnitude, in part since they require relatively large particles to exert the required magnetic torque [37], though unlike optical tweezers there is no thermal degradation. Experiments which combine visualisation with manipulation are currently only possible on homebuilt equipment

[3].

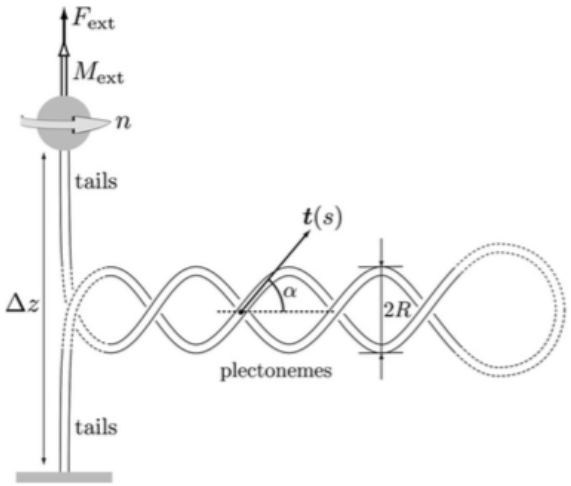

Figure 1.7: A sketch of a typical DNA supercoiling experiment using magnetic tweezers. A DNA strand is attached at one end to a glass slide and at the other to a magnetic particle which can be rotated in the magnetic field to introduce extra twist into the DNA and moved up and down in the field to exert a pulling force. The plectonemic section is clearly visible as the twisted part of the DNA. Figure reproduced from [56].

1.4 Atomic Force Microscopy (AFM)

Section 1.3 has illustrated the vast array of methods which can be used to probe biomolecular structure and function at the nanoscale. The majority of these techniques have important limitations for studying how biomolecular structure changes with time, either because they do not provide sufficient spatial resolution or because they rely on ensemble-averaging and measurement in vacuum, such that rare or transient conformations of biomolecules are averaged out [3], [45].

AFM is a label-free technique which can be operated under physiological conditions, i.e., in aqueous solution. The high signal-to-noise ratio of the AFM enables single-molecule imaging to ∼1 nanometre lateral resolution without ensemble averaging [59]. However, a fundamental limitation of AFM is that it is a surface technique, only producing topographic information on the surface-structure of a biomolecule as it is immobilised on a flat surface. AFM can also damage or influence the conformation of the biomolecule being imaged, because of the force that it applies to the sample. Time resolution is typically low: Images taken with the AFM are usually taken over the order of a few minutes for an image of 100s of nanometres scan size at nanometre resolution, though important progress has been made in enhancing AFM imaging speed to sub

second frame times [60].

1.4.1 Principles of AFM Operation

The AFM operates by the same principle as originally proposed for Binning, Quate and Gerber, similar to that of the scanning tunnelling microscope (STM) [61]. Compared to STM, it has the additional and important ability to image non-conducting materials. The AFM allows visualisation of how single biomolecules and biomolecular assemblies function in their native environment [62].

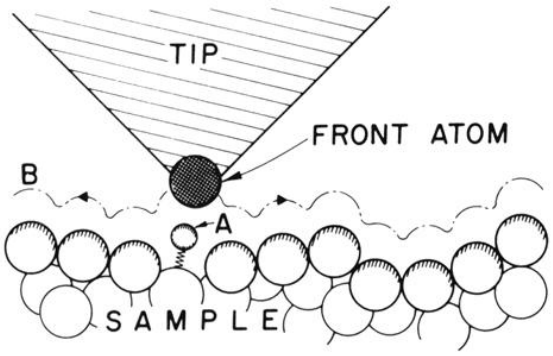

Figure 1.8: A schematic showing the principle of operation for an AFM or STM, where B is the path followed by the probe over the sample surface. A represents an atom adsorbed to the sample surface. Reproduced from [61].

The principle of AFM is simple to understand, as it is analogous to a blind person feeling the sample with a sharp stick: A sharp tip on a long flexible arm, known as the cantilever, is raster-scanned across a surface to determine its topography line by line [61]. The AFM monitors the bending of the cantilever through the deflection of a laser spot shining on the back of the cantilever, which is coated in gold or aluminium to enhance its reflectivity,. This is known as the optical-lever method [63]. In the simplest mode of AFM operation (contact mode), a piezo actuator moves the cantilever vertically from/to the sample to keep the cantilever bending, and therefore the applied force, constant. The topography of the surface is calculated from this piezo movement [64]. There are many modes of operating the AFM, several of which are discussed further in chapter 2.

1.4.2 Illustration of Atomic Force Microscopy Applied to Biomolecular Processes

AFM is a tool to visualise and probe the nanoscale [64]. It has two major functions as a visualisation tool, first to determine the structure of biomolecules in their native state, i.e., in aqueous solution and unlabelled; and second to determine how biomolecules move and interact under physiologically relevant conditions [65]. AFM has become a well-established technique for imaging individual macromolecules at nanometre resolution [66], in particular for densely packed and stabilised molecules [67]. AFM has the ability to image a range of biomolecules and biomolecular assemblies from single molecules, such as nucleic acids [68]–[73] and proteins [5], [74]–[78], to whole cells [79]–[81]. AFM has contributed a great deal to biology over the last few decades, with increasing numbers of studies exploiting the AFM to elucidate biomolecular processes at the nanoscale, examining structure-function relationships [82]. This section provides a non-exhaustive list of applications as an illustration of AFM contributions to biology.

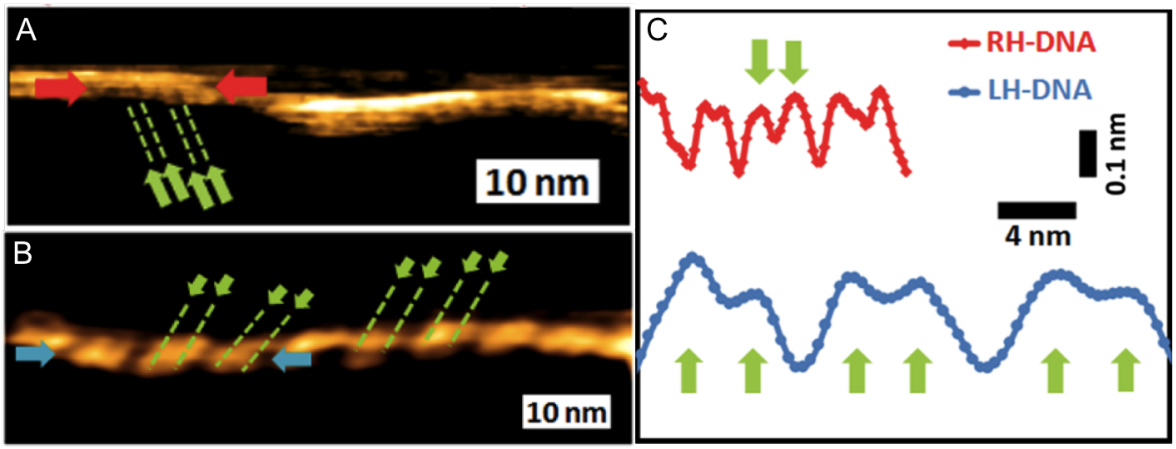

Figure 1.9: AFM images of DNA plasmids showing two different DNA conformations for the same plasmid. A) Right handed B-DNA, B) Left handed DNA. C) Line profiles taken along each of these images between the marked arrows showing variations in DNA structure. Adapted from [70].

DNA molecules for many years were imaged as long featureless polymer strands by AFM with little improvement in resolution [71], [83]. Over the past few years, substantial improvements in the AFM have yielded increased sensitivity and resolution, allowing the apparatus to image secondary structure on single DNA molecules physisorbed to mica in solution [70]. Figure 1.9 shows variation in DNA confirmation as observed by AFM. Figure 1.9A shows the Watson-Crick right-handed B-DNA, with 1.9B showing a stretched and left-handed form that is probably induced or stabilised by interaction with the sample substrate. Figure 1.9C shows line profiles taken along each

of these images between the marked arrows showing variations in the helical repeat of the DNA.

AFM has been used to visualise the process of transcription by visualising the movement of RNA polymerase (RNAP) along a strand of DNA to gain mechanistic understanding of transcription dynamics [84]. Nucleosome integrity and position after transcription was visualised. This is also relevant to other processes involving molecular motors on DNA wrapped in nucleosomes, including DNA replication and chromatin remodeling.

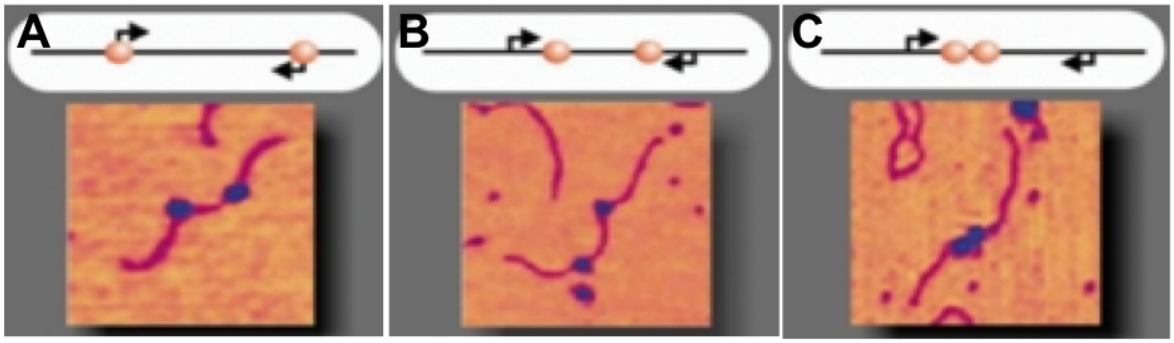

Figure 1.10: Images of RNAP DNA complexes situated asymmetrically on a DNA template imaged by time lapse AFM. Collided complexes were formed by two different methods. In the one-step method collisions were caused immediately by the addition of nucleotide triphosphates (A and C). In the two-step approach a stalled intermediate (B) was formed by nucleotide omission before the missing NTP was added allowing transcription elongation to proceed causing a collision between the two RNAPs (C). Reproduced from [85].

Figure 1.10 shows how AFM has been used to obtain snapshots of of RNA polymerase (RNAP) and nucleosome collisions, including stalling and backtracking [86]. Collided complexes were formed by two different methods. In a one-step method, collisions were caused directly by the addition of nucleotide triphosphates (NTPs). Figure 1.10A shows RNAP bound to DNA prior to the addition of NTPs, and 1.10C the collided state after the addition of four NTPs. In a two-step method, a stalled intermediary step is formed by the omission of one of the key NTPs. Figure 1.10B shows the stalled intermediary NTP omission, and 1.10C the collided state where both RNAPs collide after the addition of the required final NTP. This resulted in the unexpected conclusion that collided RNAPs remain bound to the DNA strand.

Membrane proteins occur in the cell membrane and play key roles in cell-cell communication, transportation, and energy conversion [87]. Ion channels are membrane proteins that regulate the flow of ions across the cell membrane, and play a central role in cell regulation. Ion channels are often targeted for drug development [88]. The opening and closing of ion channels is regulated by ligands which react to the presence

of molecular species, e.g., ATP or calcium, in their local environment [89]. Information on these structures can aid in drug development, and provide valuable insight into how these channels function for signalling transduction. Ion channels, as is the case for all membrane proteins, are non-trivial to examine by other methods.

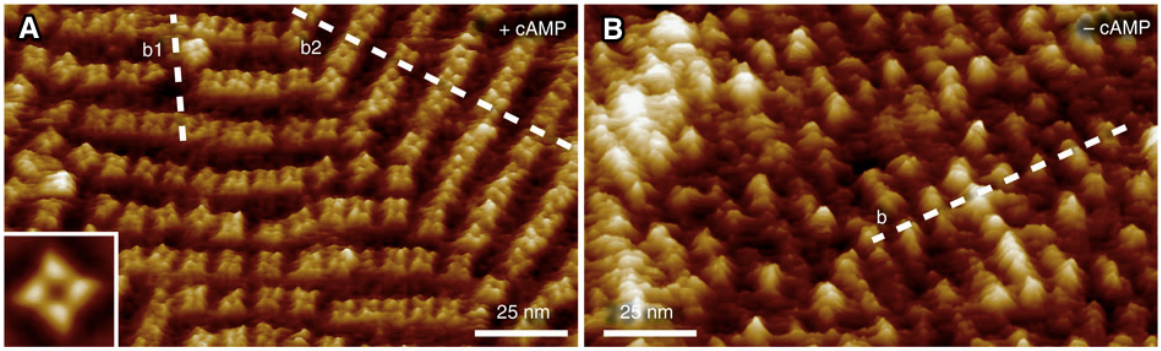

Figure 1.11: High-resolution AFM images of the ion channel MloK1. A) MloK1 imaged in the presence of cAMP, whereby each subunit of the tetrameric channels is well resolved on each single molecule. MloK1 imaged without cAMP no submolecular structure is visible, corresponding to a closed channel. Inset (both): Averaged images of the channels. Scale bar 10 nm. Reproduced from [90].

Many ion channels have been studied extensively by AFM. Such studies include the nucleotide-modulated potassium channe MloK1 which opens in the presence of the nucleotide cAMP as shown in figure 1.11; the conformation changes of the outer membrane protein F (OmpF) and changes in electrostatic surface potential generated by the pore opening [91]; the opening of the ATP-gated P2X4 receptor by ATP [92]; the arrangement of rhodopsin in membranes extracted from bovine eye [93]; the organisation of voltage dependant ion channels in tetramers and hexamers, in native membranes [94]; and the closing of the KirBac3.1 channel in the presence of magnesium ions [89].

More recently high-speed AFM has been utilised to show the association and dissociation of bacteriorhodopsin trimers, shown in figure 1.12, suggesting that these form trimers before assembling into the lattice [95], [96]. AFM has also been used to show conformational changes in bacteriorhodopsin upon illumination with green light. This generates long range effects across the membrane whereby a cytoplasmic portion of each bacteriorhodopsin monomer undergoes a conformational change to alter its position and come into contact with adjacent trimers [60], [97].

Myosin V, a processive motor which acts as a cargo transporter in cells, has been extensively studied by a number of techniques [98]. Most recently Myosin V has been visualised at high resolution by AFM stepping along actin filaments as shown in figure 1.13 [99]. This study was carried out at improved resolution over previous studies [100]. It was shown that both the generation of tension in the stepping leg and the

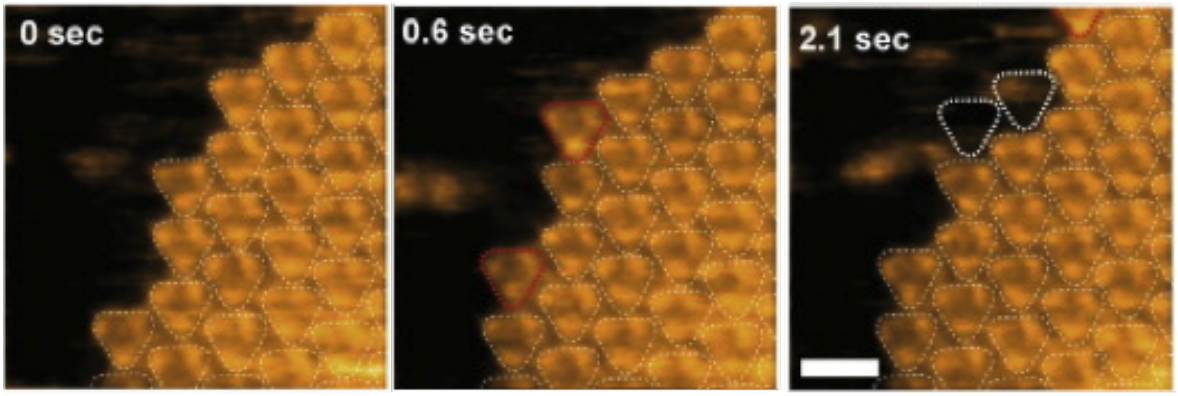

Figure 1.12: HS-AFM images of the bacteriorhodopsin cytoplasmic surface showing association and dissociation of a bR trimer as highlighted by the red and white triangles respectively. Adapted from [95].

powerstroke can be generated without ATP, a mechanism which had not previously been postulated or observed.

Force spectroscopy, or force pulling, is a much used AFM technique for determining the structure of proteins, based on measurement of mechanical properties rather than of surface topography. E.g., unfolding experiments on the large muscle protein titin by force spectroscopy have contributed to wour understanding of single-biomolecule mechanics [102]. In force-spectroscopy experiments, a protein is attached stably to the substrate, at one end, and to the AFM tip at the other. As the AFM probe moves up the protein is stretched. The force is monitored as the extension is increased, and as each domain of the protein is unfolded, the force versus extension shows a characteristic sawtooth pattern where each sawtooth corresponds to the unfolding of a different domain [103]. This method enables the determination of intra-molecular forces.

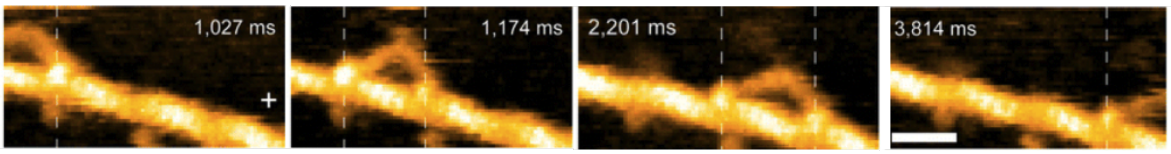

Figure 1.13: Successive HS-AFM images showing the movement of Myosin V along an actin filament in 1 μM ATP, scale bar 30 nm. The vertical dashed lines show the centres of mass of the motor domains, and the plus sign indicates the plus end of actin. Adapted from [101].

Force spectroscopy has also been extensively used to study the mechanical properties of DNA, which are relevant for DNA transcription, gene expression and regulation. It has been shown via force spectroscopy that the covalently closed back-bone of a single

DNA strand withstands forces of at least 800 pN and that this depends on applied force, ionic strength, temperature, and base pair sequence [104].

1.4.3 Limitations of AFM for Imaging Biomolecules at High Resolution

Under ideal circumstances, AFM has achieved atomic resolution in liquid, typically on extremely flat surfaces such as calcite and muscovite mica. Mica can be cleaved to reveal atomically flat planes with regular well defined lattices. These planes can be imaged with the AFM, revealing individual atom locations [105]–[108]. Figure 1.14 shows an atomic-resolution AFM image of muscovite mica, with a honeycomb lattice repeating every 0.52 nm. Height variations between different unit cells are also visible, which indicate the presence of atomic-scale defects.

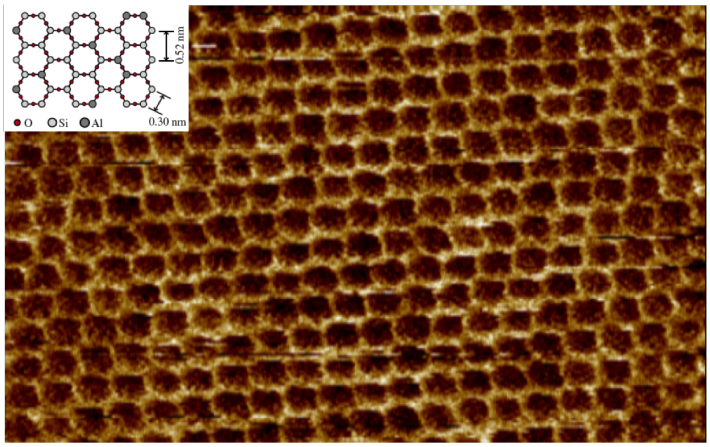

Figure 1.14: A single cleavage plane of the mica lattice, imaged using AFM [107]. Inset: mica structure, reproduced from [109].

There are a number of complications that currently prevent AFM from achieving atomic resolutions on biomolecules. These include: The binding of the biomolecule to an appropriate substrate, mobility of the molecule, the presence of contamination, the effect of forces exerted by the tip on the sample, and the difficulties in following the contours of a more complex and highly corrugated molecule using a feedback system, whilst accurately controlling the tip sample interaction and therefore the imaging force. The tip itself obviously has a large influence [110], with the sharp tips needing to probe corrugated surfaces, and with the risk of tip contamination during the imaging process.

1.4.4 Imaging Biomolecules at High Resolution: The Example of DNA

DNA was one of the first biological molecules visualised by AFM, and continues to be imaged by AFM for a wide range of studies [111]–[113]. As it is a widely available and easily prepared, it is a valuable sample for the evaluation of AFM performance. Moreover, by visualising the secondary structure of DNA in addition to the long range conformation of the molecules, we may infer how super- and supramolecular stuctures are related. However, this requires a spatial resolution that is not trivial to achieve, and several of the above-mentioned complications need to be addressed.

As mentioned previously, the simplest mode of AFM operation is contact mode, in which the AFM probe is held in constant contact with a sample as it scans across the sample surface. Contact mode has been used to obtain Å-resolution AFM images. However since it implies relatively high lateral or drag forces, contact mode is less effective for achieving high resolution if samples are not laterally stabilised, e.g., by there incorporation in a 2D lattice[114]. In tapping mode (also known as intermittent contact AFM, AC mode AFM or amplitude modulation AFM), the probe is oscillated above the surface, tapping the sample at the bottom of each oscillation cycle. It has been widely used for DNA studies, since it reduces the lateral forces on the sample (compared to contact mode) and thus avoids dragging the DNA across the sample substrate[73], [115]. However, the use of tapping mode often results in compression of the DNA molecule, with many studies showing the DNA height compressed by almost 50%, due to the applied vertical force on the sample.

Already in the early days of AFM, the helical pitch of DNA was resolved as a periodic modulation of 3.4±0.4 nm along the molecule [116]. To achieve this, cationic lipids were used to mediate the adsorption of DNA on a mica substrate, and dense packing of the DNA provided lateral stabilisation. This illustrates the key role of sample preparation for high resolution imaging using AFM. Divalent cations provide an alternative way to adsorb DNA to mica, where the adhesion can to some extent be tuned by the cationic concentration in the solution [117]. The cations are used to bridge the negative charge of the mica and and of the phosphate backbone of the DNA [118]. However, one of the most effective divalent ions (Ni^{2+}) also increases the surface contamination by aggregated salt, which can reduce resolution on the sample, for example because of tip contamination. Following this method, using a 1-5mM concentration of Ni^{2+} ions to adsorb the DNA onto a mica surface, the major and minor grooves of DNA were imaged in solution for single molecules [70]. Higher Ni^{2+} concentrations were also used to further immobilise the DNA, showing excellent resolution [69]. In both these experiments, the gain in resolution was attributed to improved force sensitivity, here achieved by use of a homebuilt AFMs and by tracking the resonance frequency of the cantilever above the surface [69], [70]. Similar techniques have also been applied to

more complex samples such as assemblies of IgG antibodies in solution [119].

1.4.5 Outlook

High-resolution AFM can be applied to DNA to study changes and variations in secondary and tertiary structure. In addition, with DNA as a test sample, AFM techniques can be optimised and next applied to other biomolecular systems, to allow high-resolution and minimally invasive imaging. This thesis describes development of AFM methodology, tested and demonstrated on DNA, and next applied to study the disruption of model membranes by antimicrobial peptides in real time. The next two sections provide further background on DNA biophysics and antimicrobial peptides.

1.5 DNA Biophysics

DNA molecules are long strands of repeating nucleotide units which contain: a phosphate - forming the backbone of the DNA chain; a sugar (2'-deoxyribose); and a base - adenine, thymine, guanine and cytosine (A, T, G and C); a sugar. The bases bind to each other in order to bind the two chains of the double helix together, this is done in purine (A and G) and pyrimidine (T and C) pairs, so that A always binds with T and G with C by hydrogen bonding. The resulting form is a helical form of DNA with the bases stacked upon each other in the hydrophobic centre and the hydrophilic sugar phosphate backbone on the outside. This results in a stable DNA structure [120]. Mismatches are possible and so are seemingly 'wrong' pairings which lead to configurations such as the Hoogsteen pairing of a DNA triplex (a triple-stranded DNA form).

DNA structure has been resolved to Ångström resolution using X-ray diffraction of crystals of short and linear segments of DNA. Double stranded DNA can adopt a variety of conformations, three of which (A-DNA, B-DNA and Z-DNA) are depicted in figure 1.15. These conformations are derived from x-ray diffraction studies, with A-DNA obtained under low humidity conditions, B-DNA under high ($\sim$92 %) humidity conditions, and Z-DNA under high ionic strength conditions. B-DNA is the most common form of DNA, though it is predicted that Z-DNA may occur transiently in the cell [121].

These structures have been determined by averaging short and straight segments of DNA molecules arranged in crystalline forms. The DNA double helix in the cell, however, is not static or straight but possesses dynamic flexibility and variability with curved, straight and flexible regions resulting from variations in base stacking and twist angles inherent in different DNA sequences. The resulting DNA supercoiling

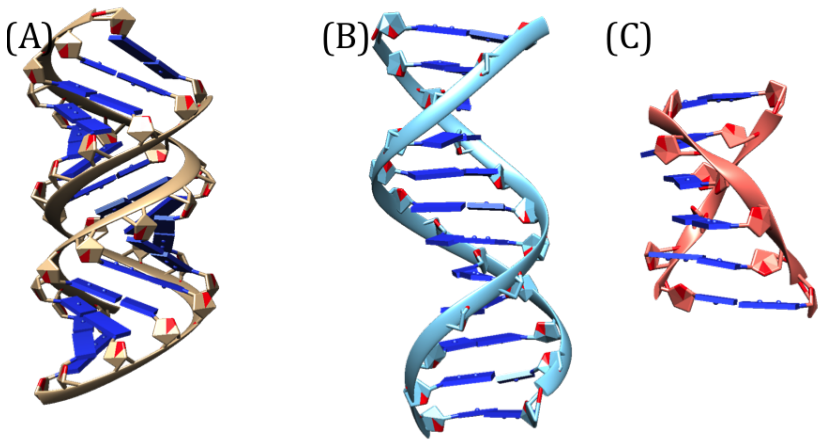

Figure 1.15: Three forms of the double helix derived from X-ray diffraction studies. (A) A-DNA, a right handed double helix which is wider and shallower than B-DNA form (B) B-DNA, the characteristic right-handed Watson-Crick double helix (C) Z-DNA a longer left handed double helix. Models were rendered as ribbon structures using Chimera [10] using PDB files 1ANA, 1BNA and 1ZNA respectively.

(see below) plays a major part in the dynamic flexibility and topological contortions of the DNA double helix [122]. High-resolution AFM has been used to show different conformations of the DNA double helix in plasmids [70] and can thus contribute to the study of the dynamic properties and structure of DNA .

1.5.1 DNA Supercoiling

DNA in the cell is long (many 1000s of base pairs) and is twisted, knotted and looped into various topological structures. This so-called supercoiling arises largely because of torsional stress around the DNA axis. The higher-order, supercoiled DNA structure varies during the life cycle of the cell. For example, bacteria dramatically alter their levels of DNA supercoiling in response to stress [123]. DNA supercoiling is known to influence DNA replication and transcription because it changes the energy required to separate the two DNA strands [124], and affects the gross and the fine structure of the helix and thus recognition by DNA-binding proteins, while it can also bring together two distant sites and hence facilitate target site location [125]. These processes are complex, and the interplay between DNA supercoiling, structure, and protein binding is still far from understood [58].

In all living systems, from bacteria to humans, DNA is globally underwound (negatively supercoiled) by ∼6 %, which slightly increases the single-stranded character of the double helix in the genome [120]. As a result, binding sites are more easily opened, facilitating DNA replication and transcription [126]. DNA supercoiling domains can

be induced and maintained, e.g., by the activity of RNA transcription, which induces positive supercoiling or overtwisting in front of it and negative supercoiling or undertwisting behind it. On the other hand, topoisomerase enzymes relieve supercoiling though nicking (topoisomerase I) or breaking (topoisomerase II) DNA strands [120].

1.5.1.1 Linking Number

DNA topology can de described by the linking number, Lk. This parameter is relevant for closed circular DNA as its closed nature can maintain torsional stress and/or supercoiling. If both ends are free the torsional stress can be dissipated by the unwinding of both ends. Lk is always an integer and cannot be changed by deformation of the DNA strands. To change the Lk the two strands must be separated and twisted or untwisted before being reattached, thus changing Lk, as is done by topoisomerases.

The linking number Lk is the sum of the two parameters: the twist, Tw, and writhe, Wr of the DNA. For B-DNA with a right-handed helix comprising 10.5 base pairs (bp) per turn, Tw is a large positive number. If the twist is changed, this must be compensated for by a change writhe, which is large scale twisting of the entire DNA double helix. This is analogous of the writhing of an old-fashioned telephone cord that emerges when it is twisted. The relation between Lk, Tw and Wr is shown in equation 1.1, where Lk is constant for closed circular DNA, but Tw and Wr can change with variations in temperature, ionic strength, pH and other environmental conditions.

$$Lk = Tw + Wr \tag{1.1}$$

The linking number can also be defined as the sum of the number of intersections of one DNA strand with the other, where each strand is given a directionality as shown in figure 1.17. By this convention by a crossing in one direction is positive and the other negative as shown in figure 1.16 [127].

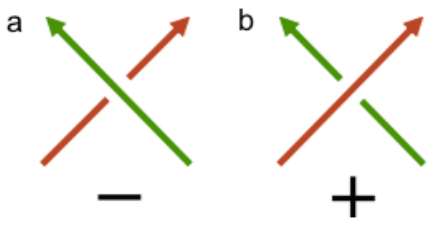

Figure 1.16: Sign convention for linking number calculation by crossings: a) left-handed 1 b) right-handed +1. Reproduced from [128]

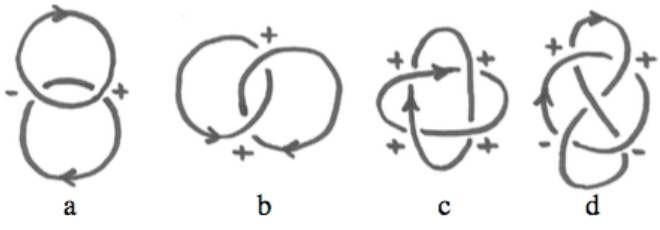

Figure 1.17: Simple links of oriented loops. Lk for each pair is computed by adding up the signs of the crossings and dividing the sum by 2. (a) Lk = 0. (b) Lk = +1 (c) Lk = +2 (d) Lk = 0 Reproduced from [128]

If we reduce the twist of closed circular DNA by -1, we must introduce a writhe of +1, or one positive supercoil, to offset the twist and ensure that the linking number remains constant [129]. Figure 1.18 shows the interplay between twist and writhe for a negatively supercoiled DNA closed circle, whereby twist may be exchanged for writhe and vice versa.

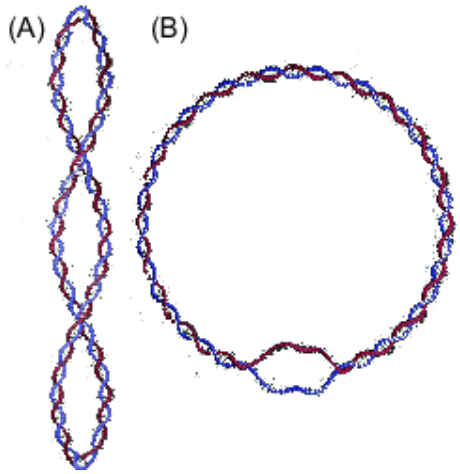

Figure 1.18: (A) Negatively supercoiled circular DNA plasmid showing a writhe of two. The writhe may reduced by unwinding part of the double helix, i.e., reducing the twist as shown in (B). Adapted from [130].

Supercoiling has traditionally been studied by gel electrophoresis. In an agarose gel, DNA strands of the same length and molecular weight travel though the gel at different speeds during electrophoresis, depending on their superstructure. Supercoiled molecules are more compact, moving easily through the gel. The molecules with no supercoiling, termed relaxed, move more slowly, resulting in separated bands in the gel. The cut or linear molecules can run very close to the relaxed molecules. Each supercoiled species will thus appear as a different band on the gel [131]. The exact distance between bands is influenced by percentage of agarose, time of electrophoresis, concentration of Ethidium bromide, degree of supercoiling and the size and complexity of the DNA.

Studies of DNA topology have also been carried out using magnetic and optical tweezers as described earlier [51], [132], [133]. Fluorescent microscopy of DNA supercoiling has also led to insights on prokaryotic and eukaryotic supercoiling, via the visualisation of transcription-coupled negative supercoils of DNA and their effect on higher order chromatin structure [134], [135].

AFM is a less well-established tool for the study of supercoiling, although there are a number of studies which have contributed to the understanding of DNA supercoiling and structure. The section of DNA containing separated strands in 1.18B is known as

a denaturation bubble. These bubbles are induced by supercoiling and are intrinsic to transcription and replication. AFM has been used to image denaturation bubbles in plasmid DNA, stabilised by negative supercoiling of the plasmids shown in figure 1.19 [130].

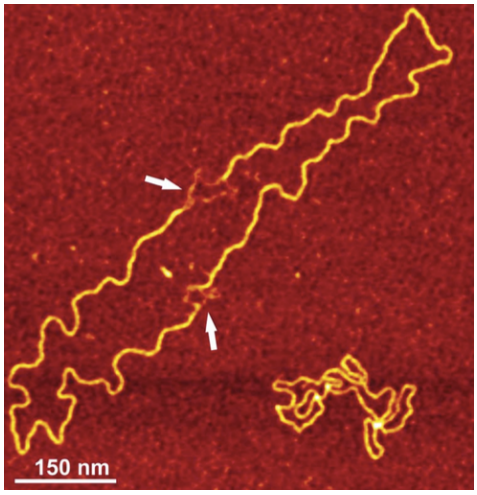

Figure 1.19: An AFM image of a DNA plasmid showing two denaturation bubbles marked by white arrows. Reproduced from [130]

1.5.2 DNA-Targeting Pharmaceuticals

Improvement in our understanding of the regulation of replication and transcription by supercoiling will aid in our understanding of genetically-based diseases and may ultimately lead to new treatments [136]. In addition, gene expression is strongly connected to the proliferation of cancer cells, with the example gene *c-myc* frequently deregulated and overexpressed in cancer cells [137]. Novel treatments to combat this disease include the formation of triplex strands of DNA at the gene expression site to prevent further expression, showing that specific target sequences can be designed with antigene and antiproliferative effects [138]. This is an example how the deliberate targeting of DNA structural variability may contribute to novel therapies.

DNA topoisomerases which catalyse changes in the topology of DNA are also key drug targets both for antibacterial and anti-cancer chemotherapy [136]. Human topoisomerase I is the target for multiple new anticancer drugs many of which stem from camptothecin, a chinese tree bark extract [139] with work ongoing in developing the anti-tumour activity and reducing side effects of these drugs [140]. These drugs are extremely active and show promise against malignancies that respond poorly to existing therapy, such as non-small cell lung, metastatic ovarian, and colorectal cancers [126]. However further investigation of the molecular determinants of drug activity in model

systems are required to determine the effective pathways of these drugs such that they may attain maximum potency [140].

1.5.3 How AFM Can Contribute to DNA Studies

As outlined above, DNA structure goes far beyond the relatively simple, short and straight DNA segments as characterised by X-ray crystallography. AFM offers a route to determine DNA structure for much larger molecular in more physiological, complex configurations, albeit limited to the surface structure. Future AFM studies could help elucidate how structural changes in torsionally strained DNA contribute to protein binding, an effect that has been inferred from other techniques discussed earlier such as optical and magnetic tweezers. In this thesis I will show how high-resolution AFM can be used for the study of DNA structure, including preliminary data showing how it can be applied to DNA supercoiling studies. I will also show how techniques that I developed to study DNA at low imaging force and high resolution can be applied to imaging the effects of antimicrobial cells as they attack model membranes, elucidating their nanoscale mechanism of attack.

1.6 Antimicrobial Peptides

Antimicrobial peptides (AMPs) are short chains of 20-40 amino acids that exhibit antimicrobial activity. AMPs are common to multi-cellular organisms including plants, animals, yeasts and algae functioning as part of their host-defence mechanism. AMPs can be found and made with varied amino acid sequence, mass, charge, properties and structure, resulting in wide ranging biological characteristics [141]. A large number of AMPs have been isolated and studied, including defensins, cecropins, magainins and cathelicidins. At the time of writing, the Antimicrobial Peptide Database (APD) contained 2541 antimicrobial peptides 317 of which are from plants, and 1912 from animals [142].

AMPs can broadly be divided into four categories based on their predominant secondary structure: alpha-helical, beta-sheet, extended and loop, as shown in figure 1.20 [143], [144]. The peptides discussed in this thesis are alpha-helical in form. An example of a naturally occurring alpha-helical AMP is cecropin B - a peptide produced by the silk moth *Hyalophora cecropia* [145], [146].

In solution, alpha-helical AMPs are monomeric in form and have a random coil structure. They assume their amphipathic alpha-helical form on contact with the membrane, as shown in figure 1.21 [147]. Their interaction with the membrane is electrostatically

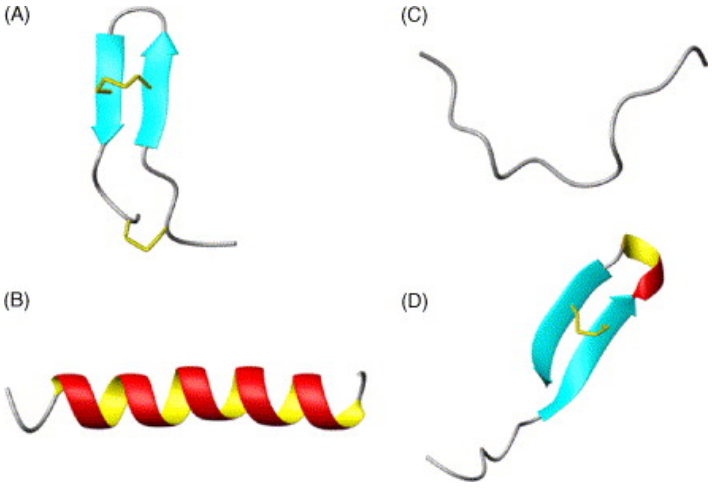

Figure 1.20: Schematic representations of the structural classes of antimicrobial peptides: (A) beta-sheet, (tachyplesin I); (B) alpha-helical, (magainin 2); (C) extended, (indolicidin); (D) loop, (thanatin). Reproduced from [143].

driven: the majority of AMPs are cationic and have a net positive charge in solution, whereas the surfaces of both Gram-negative and Gram-positive bacteria are negatively charged, due to lipopolysaccarides and polysaccharides (teichoic acids) in the case of Gram-negative bacteria and Gram-positive bacteria respectively [148]. The positive charge of AMPs also reduces the toxicity of AMPs to eukaryotic cells, as these do not show as negatively charged surfaces as bacteria. AMPs are generally amphipathic, with the charged and hydrophobic residues designed to sit on opposite sides of the molecule in its active form, allowing the peptide to embed into and disrupt the membrane, thus attacking the bacteria. Compared to other antibiotics, this rather generic attack mechanism is difficult for bacteria to develop resistance to [149].

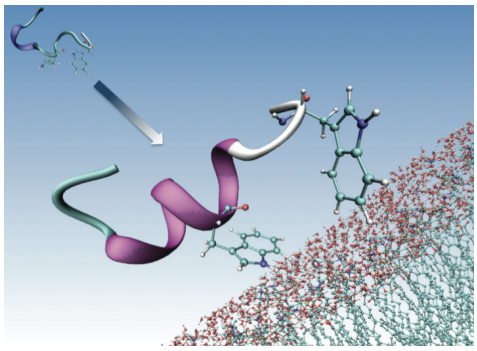

Figure 1.21: Representation of the monomeric unstructured form of an antimicrobial peptide in solution, showing its transition to its alpha-helical structure on binding to a lipid bilayer. Image courtesy of M. Ryadnov

The terms Gram-positive and Gram-negative refer to whether bacteria retain dye in

the Gram staining protocol where Gram-positive retain dye and Gram-negative do not. Whether or not dye is retained is due to structural differences in the cell wall. Cell membranes of Gram-negative bacteria are traditionally more difficult to disturb due to the presence of an outer membrane and periplasmic spaces, which provide additional barriers for bactericidal agents to cross before reaching the cell membrane. AMPs interact with the surface of Gram-negative bacteria and are taken up by self-promoted uptake to reach the cytoplasmic membrane [150]. The ability of a cationic alpha-helical peptide such as a cecropin to disrupt the cell membrane is depicted in figure 1.22, whereby the predicted model is that the peptide first binds to the outer membrane before translocating across the periplasmic space to disrupt the cell membrane [151].

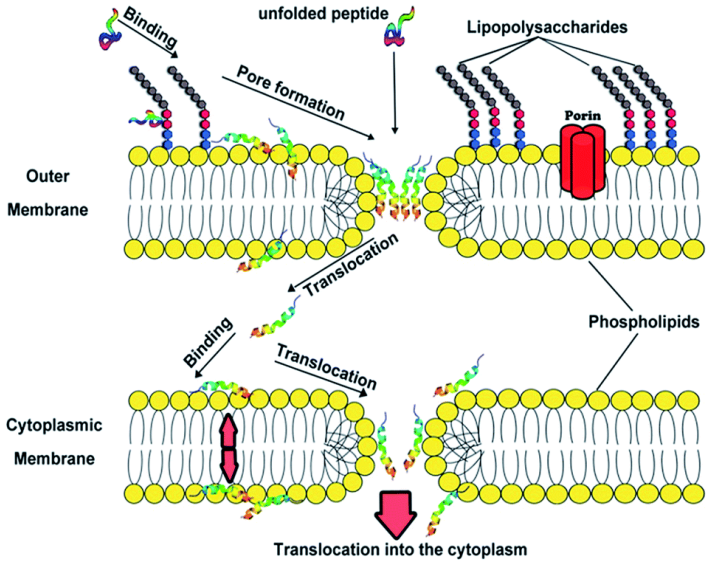

Figure 1.22: Schematic representation of the disruption of the cell membrane of a Gram-negative bacterial cell by a cationic antimicrobial peptide. Reproduced from [151].

Figure 1.23 shows the structure of an alpha-helical peptide displayed on a helical wheel, which assumes the same propensity to form an alpha helix for all amino acids. The distance between two adjacent amino acids is around 0.15 nm, and the angle between them is around 100 deg when the helix is observed along its longitudinal axis [152]. A cationic amphipathic AMP would have one side of its helix structure formed by hydrophobic amino acids, and the other side by positively charged amino acids.

Amphipathic alpha-helical AMPs initially to the cell membrane or lipid bilayer surface in a parallel orientation, in a surface bound S-state until enough peptide accumulates to achieve a critical membrane-bound concentration [154]. Once this condition has been reached the peptide can insert into the bilayer in an I-state causing a local destabilisation or collapse of the bilayer. This mechanism is still highly debated, however. Three commonly proposed models are the toroidal pore [155], the barrel-stave pore [156],

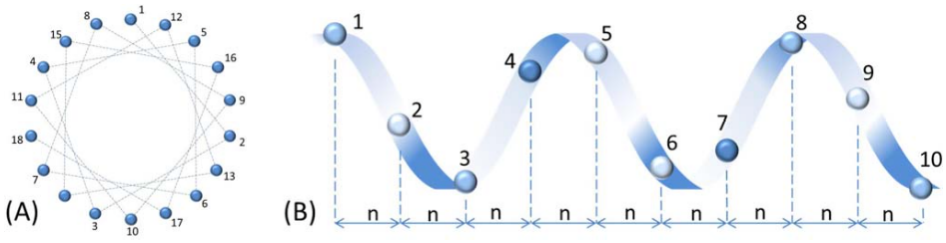

Figure 1.23: Schematic representations of an alpha-helical AMP after its secondary structure is formed; (A) a helical wheel projection (top view),(B) the side view of the peptide. Reproduced from [153].

[157] and the carpet mechanism [158]. Figure 1.24 shows schematics of AMP binding to the membrane as well as these three models for membrane degradation [152].

Because of their rapid and broad-spectrum antimicrobial properties, AMPs are pursued as potential antibiotic pharmaceuticals, especially against infections caused by antibiotic-resistant bacteria. Currently, there are at least 10 AMP-derived compounds in varying stages of clinical development [159]. However, to date AMPs have had limited success in clinical trials [150]. This is due to issues with in-vivo activity and toxicity, as well as due to the high costs of peptide production, which can run into 100s of pounds per gram. This was the case for Plectasin, a defensin isolated from the fungus Pseudoplectania nigrella [160], [161], which was hailed as a potent new antibiotic, and subsequently licensed to Sanofi Aventis (Paris, France): Despite its potent activity in-vitro and in animal models, despite low risk for unwanted toxicities, extended serum stability and in-vivo half-life, it was shelved because it was considered commercially unviable.

Two approaches have traditionally been taken towards developing AMPs as novel therapeutic agents [150], [159]. First, the isolation of naturally occurring AMPs such as cecropin [145], [162]; and second, the design of *de-novo* peptide sequences targeted to have specific effects against bacteria [163].

The first approach has led to most of the peptides currently in clinical trials mentioned above. Given their limited success, significant effort is being put into designing *de-novo* peptide sequences with engineered mechanisms of action. Bacterial assays can be performed to determine minimum inhibitory concentrations and minimum bactericidal concentrations. However, to optimise the AMP design, it is important to understand the specific mode of action, how it relates to peptide design, and how this relates to the bactericidal effect [159].

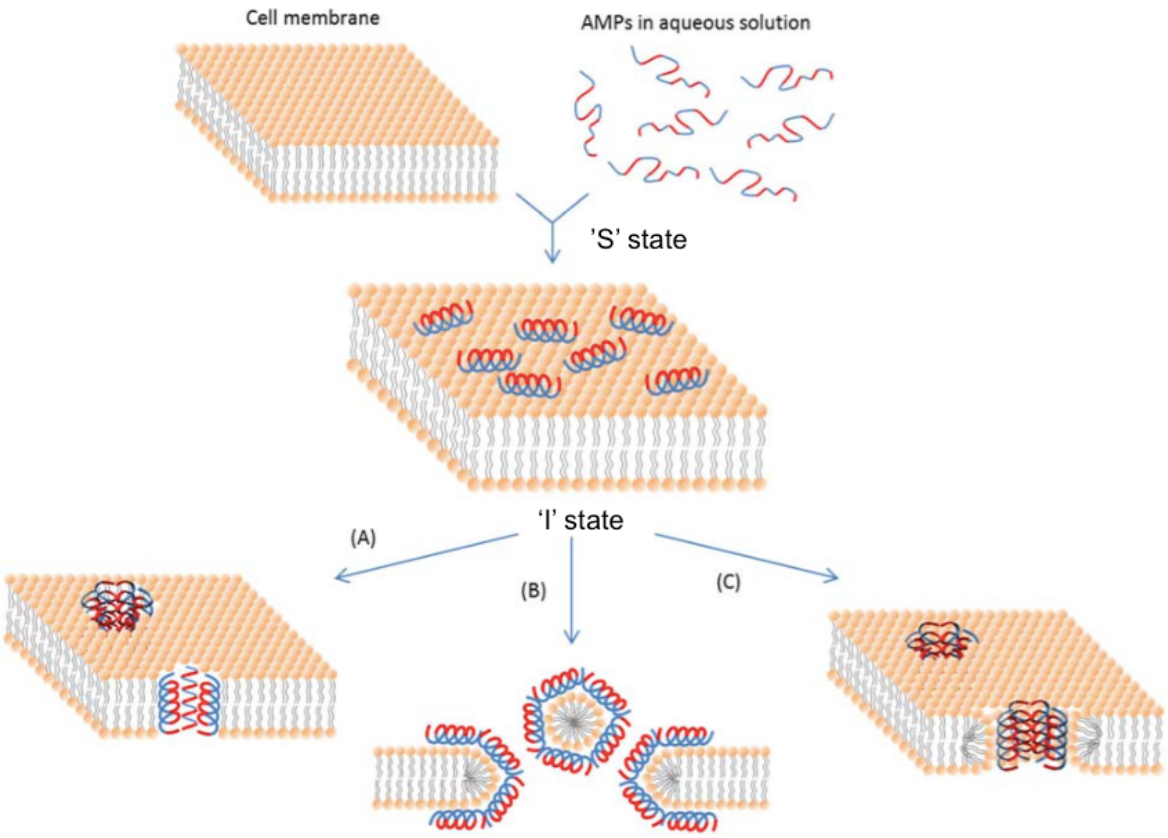

Figure 1.24: Schematic representations of mechanism of action for amphipathic cationic alpha-helical AMPs on a negatively charged lipid bilayer showing the AMPs binding to the lipid bilayer in the surface bound or S-state, assuming their secondary alpha-helical structure followed by insertion into the lipid bilayer in the 'I' state via the: (A) Barrel-Stave pore mechanism, (B) carpet mechanism, (C) toroidal pore mechanism. Adapted from [152].

1.6.1 Cecropin B - A Naturally Occurring Peptide

Cecropins are antibacterial peptides containing 35-37 amino acids that have been obtained from the silk moth *Hyalophora cecropia* [145]. All cecropins are active against both Gram-negative and Gram-positive bacteria, with Cecropin B the most active variant, with sequence KWKVFKKIEKMGRNIRNGIVKAGPAIAVLGEAKAL [162] (see Table 1.1 for the letter code for the difference amino acids). Cecropin B is an amphipatic, cationic peptide formed of two alpha helices, one at the C-terminus and the other at the N-terminus, separated by a short sequence which creates a hinge in the structure. This hinge is known as the GP bend motif, after the glycine and proline amino acids at positions 23 and 24 [164]. Glycines are the smallest amino acid, fitting into both hydrophobic and hydrophilic sequences and allowing them to form flexible regions.

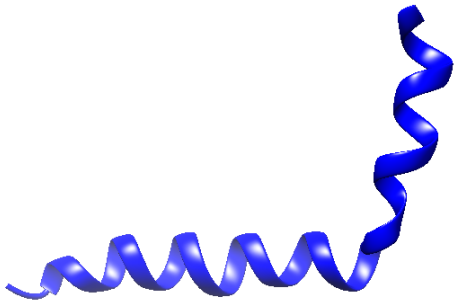

Figure 1.25: A ribbon representation of the structure of cecropin B based on a cecropin analogue CB1a rendered using Chimera [10] from PDB file 2IGR [165].

Figure 1.25 shows a representation of cecropin B based on a cecropin analogue CB1a, the structure of which was determined by NMR [165]. This peptide, like cecropin B, is formed of two alpha helices separated by a GP bend motif which acts as a hinge. We can therefore use this representation to visualise the form of cecropin B once it has adopted its membrane bound configuration.

Although the secondary structure and the functional properties of Cecropins have been characterised [150], [166]–[168], the detailed mechanism of antibiotic action is still unknown, though it is believed to interact with lipid bilayers via the carpet model [154], [169]. The carpet model is defined by electrostatically-driven peptide interaction with the phospholipid head groups only. The lipid bilayer is destablised as the number of peptides on the surface reaches a critical concentration [148], [170]. AMP mechanisms of action have been inferred from permeability measurements [158], solid state NMR [171], X-ray diffraction [172], electron microscopy [156] and computational modelling [146]. The direct visualisation of Cecropin on lipid bilayers (by AFM) could bring new insights into the Cecropin mechanism of action. It may also contribute to our understanding of how and if sequence modifications can increase the activity of cecropins as a potential therapeutic agent [173].

1.6.2 *De-novo* Construction of AMPs

Short sequence alpha helical AMPs are seen as a potential cost effective new class of peptides. However, many of the currently known naturally occurring AMPs do not exhibit sufficient antimicrobial activity. As a result new peptide sequences are being designed, and modified from existing sequences, resulting in highly active antimicrobials, exhibiting broad-spectrum activity with apparently low toxicity [146]. In addition to antimicrobial activity, other aspects need to be considered when developing these peptides as novel therapeutic agents, including in-vivo stability, side effects and production costs [174].

Amino Acid	Letter Code	Polarity	Charge	Hydropathy
Alanine	A	non-polar	neutral	1.8
Arginine	R	polar	positive	-4.5
Glutamine	Q	polar	neutral	-3.5
Glycine	G	non-polar	neutral	-0.4
Isoleucine	I	non-polar	neutral	4.5
Leucine	L	non-polar	neutral	3.8
Lysine	K	polar	positive	-3.9
Tryptophan	W	non-polar	neutral	-0.9

Table 1.1: A table showing the properties of selected amino acids used in the formation of antimicrobial peptides.

de-novo AMP sequences are generally designed by forming congeners - amino acid residue analogues of natural peptides that differ by one or more amino acids, by forming shortened analogues or analogues containing deletions, or by forming hybrid AMPs composed of fragments of two different natural peptides [163]. Alpha-helical AMPs are designed to span the thickness of the membrane bilayers. Changes in the size of the hydrophobic portion of amphipathic helix strongly influence the AMP orientation in the bilayer [174]. The AMPs studied in this thesis were congeners formed both by systematically altering specific amino acid residues within the parent AMP sequence, by systematically truncating the N-terminus and/or the C-terminus ends or by a combination of the two [175]. These modifications change the charge and/or amphipathic characteristics of the molecule, resulting in new mechanisms of action. By examining how each modification affects the overall function of the AMP, conclusions can be drawn as to how to design new therapeutic agents with high-broad spectrum activity and low toxicity.

Table 1.1 lists the polarity, charge and a measure of the hydrophobicity for a selection of the amino acids used to form the AMP sequences in this thesis. These amino acid properties are used to predict the effect of each sequence modification on the mode of action.

To guide *de-novo* peptide design, however, it is essential that we experimentally verify the effect off these changes, not only on the bactericidal effect but also on the mechanism of action for each modification. By developing a more rigorous understanding of the effect of sequence modification on the mechanism of action for AMPs, we can increase the likelihood of forming novel therapeutics for commercial use. We can AFM to visualise the mechanism of action of AMPs on negatively charged supported lipid bilayers as analogues to the bactericidal cell membrane, and relate the changes in observed mechanism to specific amino acid changes. Supported lipid bilayers are used in place of live cell membranes as a model membranes which can be prepared on an atomically

flat substrate (mica). The use of model membranes is well documented throughout the literature in the study of new molecular processes including the study of proteins, peptides and other membrane active drugs [92], [176]–[179]. The preparation of the peptides used in this thesis is described in chapter 3.1.3.

1.7 Scope of this Thesis

AFM is a particularly powerful tool to study biomolecules and biomolecular processes in action, because of its high spatial resolution and its ability to operate in aqueous solution. As with most experimental methods, it also has important limitations, including that ultimate or atomic resolution has only been achieved on ideal, atomically flat and solid surfaces. As mentioned in the context of DNA above, softer samples such as biomolecules may be imaged at higher spatial resolution than currently possible, if the AFM sensitivity to (forces and force gradients at) the sample surface can be improved.

The following chapters describe:

- A background on different methods to enhance AFM resolution and sensitivity, and some instrument development carried out within the context of this thesis (chapter 2).
- Further methodology used in experiments carried out for this thesis, including the optimisation of AFM imaging conditions (chapter 3).
- A validation of high-resolution AFM methods by visualising the DNA double helix and variations in the double helix structure (chapter 4).
- Preliminary data to show how these may be used to determine secondary structure for DNA minicircles, molecules of well-defined supercoiling, to study the interplay between DNA supercoiling, secondary structure, and protein binding (chapter 5).
- The application of high-resolution AFM methods to verify how rational *de-novo* antimicrobial peptide design can be tuned to yield the anticipated mechanism(s) of membrane degradation including novel, expanding-pore and monolayer-pore mechanisms of membrane perforation (chapter 6).
- The application of high-resolution AFM methods to verify how rational modifications of a natural antimicrobial peptide affect its mechanism(s) of membrane degradation (chapter 7).

Chapter 2

AFM Methods for Single-Molecule Imaging in Liquid

Compared to other experimental techniques, the main advantage of AFM is that it can image single biomolecules at ∼1 nm resolution in aqueous environment. This chapter provides a more detailed description of AFM in liquid, of various modes of operation that have been developed to facilitate high-resolution imaging, and of various determining factors for achieving high resolution. These include noise sources such as thermal noise and deflection detector noise, as well as ways of actuating the cantilever.

2.1 AFM Operation Principles

The AFM visualises by tracing a sharp tip attached to the underside of a flexible lever over the surface of interest, which may be a biological membrane, or a biomolecule attached to the surface. As the tip is raster scanned over the surface, the sample surface topography is reconstructed from these traces. In a typical AFM experiment, the traces represent profiles along which the tip-sample interaction (e.g., the tip-sample force or force gradient) is constant. AFM can be operated in various modes, which differ in their ways to control, manipulate and monitor the tip-sample interaction. AFM can be carried out in a vacuum, air or fluid, with fluid being the most relevant environment for imaging biomolecules.

The tip-sample interactions follows from the bending of the cantilever, e.g., via a static bending or by changes in a cantilever oscillation. In the majority of AFM setups, bending of the cantilever is monitored by a laser focused on the back side of the cantilever, which after reflection from the cantilever is detected on a position-sensitive detector (PSD), usually a quadrant photodiode. The quadrant photodiode measures

the bending of the cantilever through the displacement of the laser signal; this is known as the optical lever method, pioneered by Alexander in 1989 [63].

The optical lever method reads the deflection of the cantilever on the quadrant photodiode by converting the incident light on each quadrant into a voltage. The vertical displacement or deflection of the cantilever can therefore be measured by the difference between the upper and lower quadrants of the photodiode. In the same manner the voltage differences between the left and right quadrants can be used to determine the torsional motion of the cantilever, such as can be induced by frictional forces. The optical lever method amplifies the movement of the cantilever purely by path length, as the measured displacement on the photodiode (D) is proportional to the cantilever movement (z) multiplied by the path length from the cantilever to the photodiode (S) over the cantilever length (l) as shown in equation 2.1 [64].

$$D = \frac{3}{2}\frac{S}{l}z \tag{2.1}$$

The applied force in an experiment (F) can be recovered from the deflection of the cantilever, which gives the cantilever displacement (x) by Hooke's law via the stiffness of the cantilever (k) as shown in equation 2.2.

$$F = -kx \tag{2.2}$$

The applied force is therefore strongly influenced by the stiffness of the cantilever as discussed in section 2.3.3 and to the detectable movement which is one of the other main sources of noise. Alternatively or complementarily, force gradients and dissipation can be derived from changes in the oscillation of the cantilever when it modulated vertically during the (lateral) scanning over the sample surface, as described in section 2.2.2.

2.1.1 Tip-Sample Interaction Forces

Since the surface topography is determined from contours of constant tip-sample interaction, it is worthwhile to understand the forces acting on the tip. The dominant forces are long range attractive van der Waals interactions, electrostatics interactions, short-range repulsive interactions, and in air, capillary forces and the resultant adhesive forces. The long range van der Waals forces and electrostatic forces can act over tens of nanometres and are caused by dipole interactions between atoms, and by Coulomb interaction between surface charges, respectively. At the Ångström range the strong repulsive force originating from the overlap of atomic orbitals begins to dominate. At this point the tip is considered to be in contact with the sample. In air, the water meniscus formed between the tip and the sample causes an attractive capillary force

between the tip and the sample. In aqueous salt solutions, van der Waals forces and electrostatic forces are usually screened for tip-sample distances larger than a few Å, and there are no capillary forces.

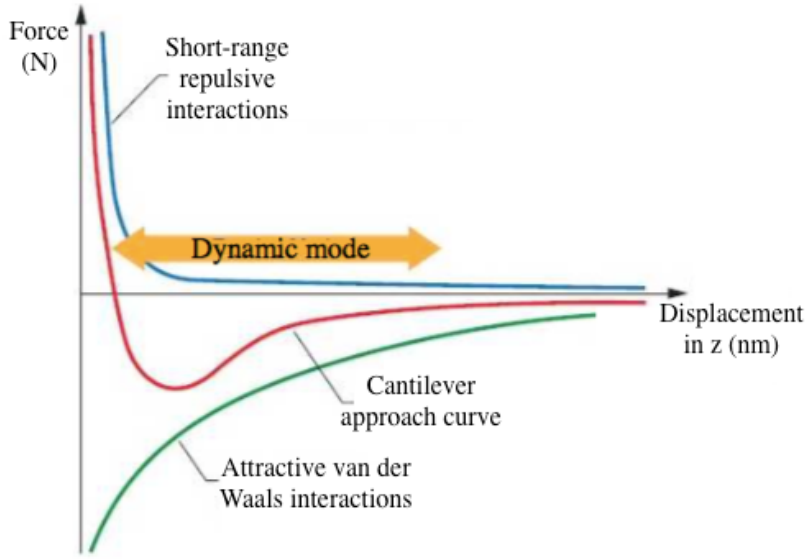

Figure 2.1: A representation of forces that can act on the AFM tip at various tip-sample separations, ignoring electrostatic interactions here. At high separations the attractive van der Waals dominate, with the repulsive short-range repulsive forces dominating at lower separations.

2.1.2 AFM Imaging in Liquid

One of the main advantages of using the AFM for imaging and manipulating biomolecules is the ability to work in fluid and thereby visualise and probe biomolecules in their natural hydrated state. Additional advantages gained by operating the AFM in liquid are the avoidance of the tip-sample capillary forces experienced in air, whereby the water layers on the tip and the sample, generated by the humidity of the environment generate a large force pulling the cantilever toward the sample, thereby increasing the contact area between the tip and the sample and thus reducing the spatial resolution [180].

The use of buffer solutions also permits tuning of the long range electrostatic forces between the tip and the sample, which can help to increase force control and therefore resolution [181].

$$\kappa^{-1} = \sqrt{\frac{\epsilon_0 \epsilon_b k_b T}{2e^2 I}} \tag{2.3}$$

The distance over which the long range electrostatic force decays is defined as the Debye screening length (κ^{-1}), which is dependant on the permittivity of a vacuum and

of the bulk solution or medium (ϵ_0 and ϵ_b), the absolute temperature (T), the ionic strength of the solution (I) and the electron charge (e) by equation 2.3 where k_B is Boltzmann's constant. Under typical conditions for AFM imaging of biomolecules, κ^{-1} is a few Å.

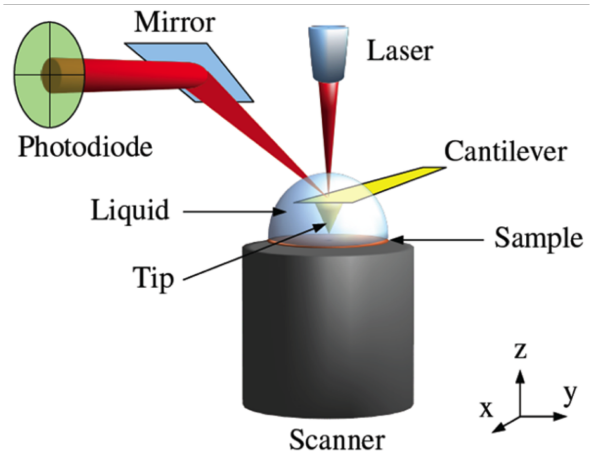

Figure 2.2: A schematic showing the operation of the AFM in fluid. Image courtesy of Dr Bart Hoogenboom

Figure 2.2 shows the standard setup of an AFM in liquid. The principle is the same as in air, but the sample and cantilever are immersed in fluid. For imaging in fluid, a fluid cell is used to hold the cantilever (not shown), such that the laser passes through a stable glass-liquid interface (and not through an air-liquid interface).

There are some disadvantages to AFM imaging in fluid related viscous damping, which are more pronounced for imaging in dynamic modes, since the damping force exerted by the viscous liquid causes the resonant frequency f_0 and the quality factor, Q, of the cantilever to decrease. These will be discussed more fully below.

All AFM experiments in this investigation were carried out in fluid under buffer conditions with near-physiological pH and salt concentrations. Protocols for the preparation of buffer solutions are outlined in Appendix C.

2.2 AFM Imaging Modes

As mentioned previously, AFM can function in a number of imaging modes, the most common of which are contact and tapping mode. Contact mode (section 2.2.1) is the simpler and faster mode, but its use for imaging biomolecules is limited because of the relatively high lateral forces exerted by this mode. Tapping mode (section 2.2.2) operates by oscillating the tip above the sample, with the tip continuously coming into and out of contact with the sample in a 'tapping' motion. This vertical modulation

reduces the lateral forces that the tip exerts on the sample. Tapping mode is therefore widely used for imaging biomolecules in liquid, reducing the lateral force on the sample compared to contact mode, and thus reducing the risk of distortion or destruction of the molecules under study. Other popular modes are frequency-modulation AFM (section 2.2.3) and multi-frequency AFM (section 2.2.4). Peak force tapping (section 2.2.5) is a relatively recent mode for high resolution imaging of biomolecules and has been used extensively throughout this thesis for high-resolution imaging of biomolecules at low force.

2.2.1 Contact Mode Imaging

In contact mode, the tip of the cantilever is kept in constant contact with the surface. In most commercially available AFMs, the bending of the cantilever is measured via the deflection of a laser, which reflects off the back of the cantilever onto a split quadrant photodiode as shown in figure 2.2.

Typically, the deflection signal is measured and used as input for a feedback loop that adjusts the height of the cantilever with respect to the sample (or vice versa) to keep the deflection signal at a predefined value known as the setpoint, thus maintaining a constant interaction force between the tip and the sample.[64]. The major drawback of contact mode even in constant force mode is the large lateral forces applied to the sample. In addition, the deflection of the cantilever will drift over time, even without contact with the sample, which results in a change in the applied imaging force as the setpoint is maintained. This can result in much larger forces than intended being applied to the sample. Typical applied forces are 100∼500 pN, at scan rates of around a frame per minute, when using cantilevers with spring constants of <0.1 Nm^1.

Contact mode has been used to image biomolecules at high resolution, however the sample must be prepared in a way that mitigates the large lateral forces, for example in a molecular array or as a flat surface. Studies on molecules such as such as purple membrane have used contact mode in this way [96].

Dynamic imaging modes were subsequently developed and introduced to reduce the lateral force applied to a biomolecule, which proved especially useful for single molecule studies [180], [182].

2.2.2 Tapping Mode Imaging

Tapping mode AFM, also known as amplitude modulation (AM-AFM) or intermittent-contact mode AFM is the most commonly used dynamic mode of AFM imaging. Dy-

namic modes of imaging are used to minimise the lateral forces applied to the sample, by moving the cantilever into and out of contact with the sample. This technique is particularly useful for imaging biological molecules loosely bound to a substrate where the use of contact mode AFM would result in sample damage or movement. The movement of a molecule during imaging will result in a loss of resolution and can also irreversibly blunt the tip, thus reducing the resolution.

In tapping mode, the tip is driven to oscillate sinusoidally above the sample at a frequency f close to the natural resonance of the cantilever, f_0, while the cantilever raster scans the surface. The resonance frequency is the frequency at which the driven cantilever amplitude response is largest. A cantilever with an effective mass m (which may include displaced liquid) and a stiffness k has a resonant frequency given by equation 2.4,

$$f_0 = \frac{1}{2\pi}\sqrt{\frac{k}{m}} \tag{2.4}$$

The cantilever is usually driven mechanically by a piezoactuator in the fluid cell. The amplitude of oscillation is monitored as the RMS value of the deflection readout on the detector. On sensing repulsive tip-sample forces, the effective stiffness of the cantilever increases, resulting in a change in resonance frequency, and energy is dissipated. With an actuation frequency f close to but below the resonance frequency, both effects result in a reduction of the detected oscillation amplitude. Figure 2.3 shows how the resonance curve of a cantilever will change as the tip-sample interaction increases, with the resonance frequency and amplitude both decreasing.

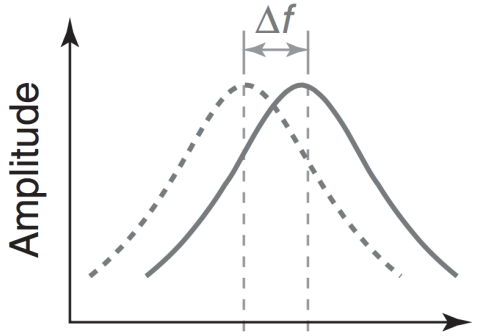

Figure 2.3: Amplitude versus frequency curves for a cantilever driven near resonance away from the sample (dotted line) and interacting with the sample (solid line).

The tip-sample interaction thus induces a reduction δA in the amplitude of oscillation. A feedback loop is used to maintain the amplitude of oscillation A of the cantilever by adjusting the position of the cantilever with respect to the sample (or vice versa), thus (approximately) yielding traces of constant tip-sample distance. The predefined value for the amplitude of oscillation in intermittent contact with the sample is defined by the setpoint A_{sp}, which in liquid is usually around 70-80% of the free amplitude of oscillation, as measured away from the sample. This mode of operation reduces the

lateral force applied to the sample, allowing softer biomolecules to be imaged. The topography of the sample follows from the movement of the tip or the sample as a function of lateral position on the sample.

In tapping mode, additional information can be inferred about the sample composition, from the change in the phase of the oscillation. Phase imaging monitors the phase lag between the signal that drives the cantilever to oscillate and the measured cantilever oscillation. Variations in a number of surface properties including elasticity, adhesion and friction can cause change in the phase of the oscillation and therefore affect the phase lag. Additional characteristics of a biomolecular surface can therefore be probed simultaneously to the topographic features. This can be used for example, to distinguish variations in the lipid composition of a bilayer which appears perfectly flat in topography but contains two phases of lipids.

The major drawbacks for tapping mode imaging in fluid are: (i) The reduction of the quality factor of the cantilever Q by viscous damping fluid itself. This reduces the sensitivity of the method to changes in amplitude, as a small shift in f_0 produces a much smaller δA than in air. (ii) Related to this, the convolution of the broad, low-quality factor cantilever resonance with the mechanical resonances of the fluid cell as shown in figure 2.4 in red. The cantilever is usually driven by a piezo actuator. This actuator drives the entire fluid cell, or cantilever holder, exciting mechanical resonances in the fluid cell, in addition to the cantilever. This results in an excitation spectrum that is commonly denoted as a 'forest of peaks'.

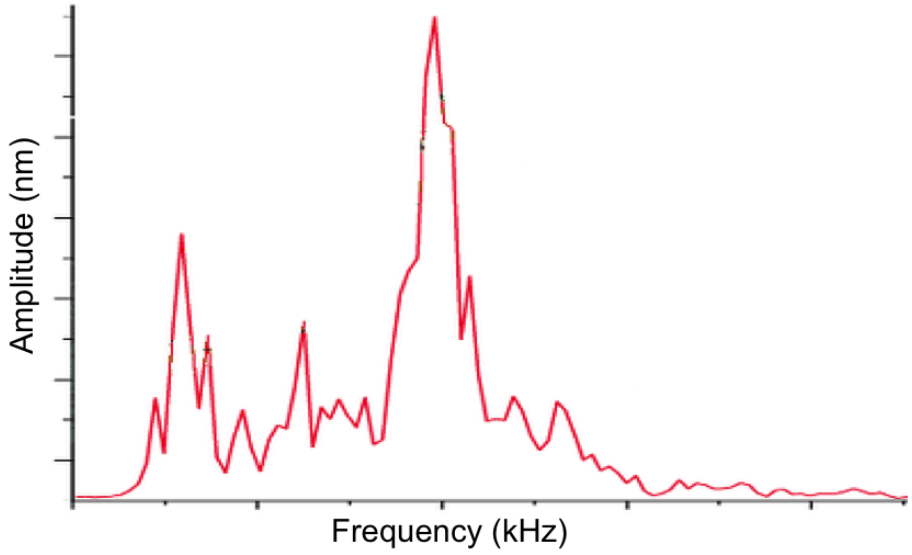

Figure 2.4: A plot of actuation amplitude versus frequency for a cantilever with $f_0 \sim$ 550 kHz showing the forest of peaks introduced by the actuation of other mechanical resonances

This forest of peaks varies as the fluid changes within the fluid cell. This can result in

large changes to the amplitude of the cantilever resonance peak as the forest of peaks moves [183]. Changes to the free amplitude of oscillation of the cantilever will result in changes in the load force. This is a major drawback for the imaging of biomolecules in fluid using tapping mode, as although the lateral forces are reduced, the applied force is ill-defined and can vary. The large changes in applied force can result in a loss of resolution, or damage to the sample or to the tip, which is another key for high resolution imaging using the AFM.

2.2.3 Frequency-Modulation AFM

In frequency-modulation AFM (FM-AFM), a cantilever is oscillated at its resonance frequency as in tapping mode. However, the actuation frequency is continuously adjusted to track the resonance frequency of the cantilever. The tip-sample interaction is monitored directly via a shift in the resonance frequency of the cantilever, instead of via a change in amplitude as is the case in tapping mode. This frequency shift is then used as the input signal for the feedback loop that adjusts the tip-sample distance. The shift in resonance frequency can be interpreted in terms of an elastic tip-sample interaction, whereas dissipative interactions can be probed via a simultaneously measured change in amplitude or in actuation signal that is required to maintain — using a separate feedback loop — the amplitude constant. In fluid, FM-AFM is performed in the repulsive force range, such that the frequency of the cantilever increases as a result of the repulsive tip-sample interaction as shown in figure 2.3. This allows precise control of the tip-sample distance and therefore the interaction force as the resonance frequency of the cantilever changes by a large amount near the surface. This allows small changes in tip-sample variation to be monitored as a comparatively large shift in the resonant frequency which allows for greater force control and therefore measurements with sub molecular resolution [105].

FM-AFM is typically operated with stiffer cantilevers than tapping mode in liquid, of 10's of N/m, as such cantilevers generally show a higher quality factor (up to $\sim$10) in liquid, such that the resonance frequency is easier to track and the resonance is more stable than for softer cantilevers. It has been shown to provide excellent results for imaging flat surfaces at atomic resolution in fluid [105], [107], in particular when operating at small (Å-sized) amplitudes. However, because of its resonance-tracking mechanism (involving an additional feedback loop), it is less robust than tapping mode, and the use of stiff cantilevers makes FM-AFM less tolerant to errors in the feedback for the tip-sample distance, with increased risk of sample damage and tip contamination, in particular for more corrugated samples. Nevertheless, FM-AFM has been used to achieve some of the high-resolution AFM images on some biomolecular samples in the literature [69], [119].

2.2.4 Multifrequency AFM

When imaging in dynamic modes in liquid, the dynamics of cantilever oscillation become increasingly complex [184]. Higher harmonic oscillations of the cantilever contain additional information on the tip-sample interaction and contribute to the cantilever thermal noise [185]. This information is often lost or ignored in standard imaging. The aim in multifrequency AFM is to measure this information and extract the physical properties of the sample from these. This is most effectively achieved in liquid as in air, with quality factors that can be several 100's, the contributions from higher harmonics components are often negligible [186].

The simplest method to accomplish this is to simply record the higher harmonic components. This has allowed for bacteria to be measured with a lateral precision of at 0.5 nm [187]. This technique also allows for the measurements of the mechanical properties of a cell [188]. Other multifrequency AFM methods include bimodal AFM where two driving forces are used and a large range of frequencies are excited and measured. Using these techniques, it is possible to measure in the low force regime allowing for protein flexibility to be mapped at forces as low as 50 pN [189].

2.2.5 Peak Force Tapping Mode

New techniques in AFM are being developed to simultaneously assess surface properties whilst imaging topography [190]. peak force tapping, an imaging mode developed by Bruker (Bruker LTD, Santa Barbara) performs a series of force curves at a frequency significantly lower than the resonance frequency of the cantilever. For imaging in fluid, the tip is 'tapped' on the surface in a sinusoidal motion at amplitudes that are typically less than 10 nm, at frequencies of 1-8 kHz. When the AFM probe interacts with the sample surface, the tip-sample interaction is controlled by maintaining the maximum force, or 'peak force', between the tip and the sample constant, see figure 2.5i for a schematic of the tip motion in peak force tapping.

If one considers the motion of the probe in terms of Z position, a force curve is performed at every pixel position on the sample surface, as shown in figure 2.5iii. This is similar to force volume imaging, a traditional AFM mode in which the surface below the tip is probed by force-vs-distance curves to gain elastic information [192], [193] with some differences. The main difference is that the sample (or tip) position is oscillated sinusoidally, instead of the linear approach-and-retract movement in force volume. This reduces the presence of higher-harmonic components in the deflection signal, which would otherwise results in undesired ringing of cantilever and/or scanner. In addition, force volume records a single force curve (force spectroscopy) for each pixel in the image, whereas peak force tapping continuously records force curves, at a rate that

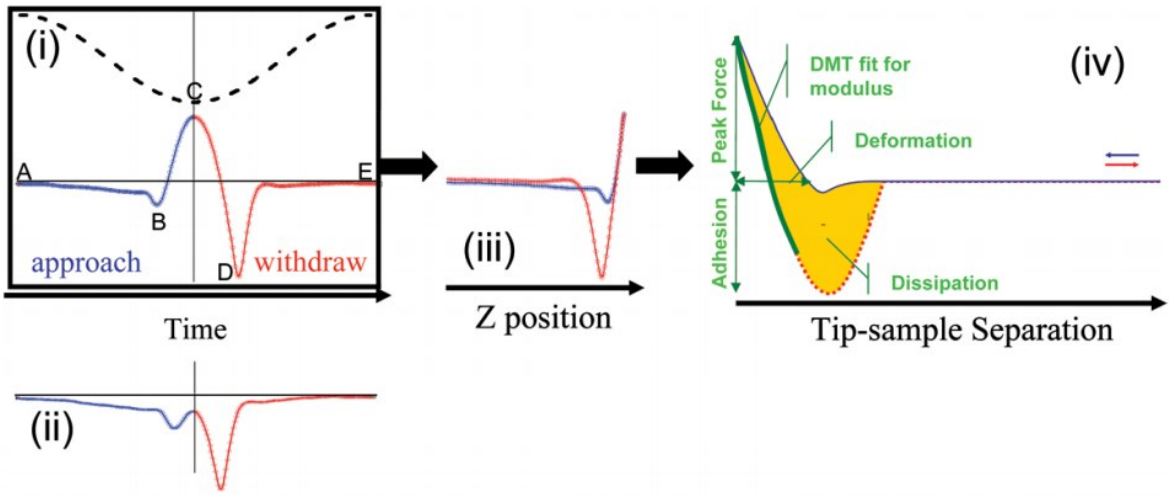

Figure 2.5: A schematic showing the data collected from an instantaneous peak force tapping force curve, reproduced from reference [191]. (i) Force (blue-approach and red-retract) and z-piezo (dotted) position as a function of time, where B is the jump to contact, C is the peak force, D is the adhesion force. (ii) A force versus time plot with small peak force. (iii) A force versus z position plot. (iv) Force versus tip-sample separation plot showing the different parameters calculated in peak force QNM.

can be much faster than the pixel rate, and peak force tapping contains algorithms to correct for hydrodynamic effects on the cantilever motion. Compared to other modes of operation, a key advantage of peak force tapping is that it continuously refers the measured peak deflection (and thus force) to the cantilever deflect away from the surface, and thus compensates for drift, allowing for imaging of the sample over extended time periods with minimal tip damage.

As mentioned above, peak force tapping uses sinusoidal sample (or tip) motion rather than the linear motion used in Force Volume which has the additional advantage of reducing the tip velocity as the tip approaches the surface. The force curves taken at each point on the surface allow precise control of the tip-sample interaction force, enabling imaging at peak forces of less than 200 pN, and as low as 30 pN in fluid environments. This helps protect both the AFM probe and the sample from potential damage and is a key factor in enabling high-resolution imaging. Additionally, imaging in peak force tapping is considerably quicker than Force Volume, since peak force tapping mode operates at higher frequencies (1-8 kHz) than Force Volume (1-10 Hz). This allows peak force tapping images to be acquired at scan rates that are comparable to other imaging modes, while still recording nanomechanical information.

The sample properties that can be obtained in addition to topographical information include adhesion, dissipation, deformation and elastic modulus [191]. Figure 2.5iv shows a typical peak force curve, and how these mechanical properties are calculated. These

are not used in high resolution imaging but can have been shown to give important structural information on biomolecules [194]–[196].

2.3 Optimising AFM Operation for Higher Spatial Resolution

There are many variables which must be optimised to achieve high-resolution imaging. These variables include sample preparation, cantilever characteristics and AFM performance. The vertical resolution limit of an AFM is limited by both noise from the detection system and thermal fluctuations of the cantilever. In general, the thermal noise of the cantilever is the largest source of noise in AFM for soft cantilevers like those used in tapping mode [184], but it is generally not the only factor that determines the spatial resolution. This section described various factors that are worthwhile taking into account when aiming to achieve high spatial resolution on biomolecules.

2.3.1 Force Sensitivity

The force sensitivity of the measurement is a critical factor in determining the spatial resolution and the degree of invasiveness of the measurement [197]. Imaging at too high a force can cause critical and irreversible damage to the tip or the sample, causing a loss of resolution [68]. Obviously, this also depends on the properties of the sample. More mobile or soft biomolecules are more easily deformed and/or lack contrast due to their motion. This illustrates that it is virtually impossible to provide one general theory for AFM resolution: It varies from sample to sample. In general though, by increasing the force sensitivity of the imaging technique, it is possible to resolve smaller changes in the tip-sample interaction, thus enabling the AFM feedback to react more accurately and thus yield a higher resolution.

To examine the force control of an AFM, we can examine the maximum apparent height of a soft biomolecule such as an antibody or DNA molecule when imaging with the minimum force. The extent to which the molecule is compressed gives insight into the applied force. Forces of less than 50 pN are required to image IgM antibodies and DNA molecules with minimal compression [68], [189]. The force exerted should be on the order of the interaction, i.e. 1-100's of pN for biomolecules [45].

FM-AFM has been shown to achieve high force control [70] with force gradients as low as 1-20 pN/nm being resolved using small cantilevers [105]. Low force imaging is also attainable in tapping mode with soft cantilevers ($k<0.1$ N/m) and small amplitudes of oscillation ($\sim$2 nm or less) [197].

Besides by a reduction of noise, the force sensitivity of the cantilever can also be improved by making it more responsive to small changes in the sample topography, which can be done, e.g., by reducing the amplitude of the cantilever oscillation in dynamic modes of operation.

2.3.1.1 Small Amplitudes

Improvements in imaging resolution have been achieved by reducing the amplitude of oscillation for imaging in tapping and frequency-modulation mode. For the oscillation amplitude, it has been experimentally and theoretically shown that the optimal value roughly corresponds to the interaction length of over which the force is constant [197]. This makes intuitive sense, as with an oscillation amplitude at the scale of the tip-sample interaction length, the cantilever spends most of its time in the interaction range that yields the contrast on the sample.

The force gradient varies considerably during an oscillation. This introduces non-linear features in the dynamics of the tip motion. Furthermore, dissipative processes such as surface adhesion hysteresis, viscoelasticity or electronic dissipation may also be involved in the tip-surface interaction [184].

2.3.2 Noise Sources

2.3.2.1 Mechanical and acoustic noise

Mechanical noise from the environment of the AFM can affect the stability and resolution of the AFM. Usually this mechanical noise can be sufficiently suppressed using air tables or active damping systems. Acoustic perturbations to the cantilever oscillation are more pronounced and care should be taken to operate the AFM in a quiet environment or in an acoustic enclosure. If given time to stabilise, an acoustic enclosure can also provide a more stable environment to operate the cantilever in, reducing drift and other instabilities.

2.3.2.2 Thermal Noise

When considering the noise generated in the AFM system itself, we can distinguish at least four sources of noise: Thermal vibrations of the cantilever, noise in the detector of the cantilever deflection, noise in the actuator that drives the cantilever oscillation, and noise generated during electronic signal-processing noise, e.g., in the electronic amplification, filtering, and analog-to-digital/digital-to-analog conversion. Thermal

noise and detector noise usually dominate other sources of noise. The minimum value of the thermal noise contribution of the cantilever follows from the equipartition theorem, see equation 2.5 with $\langle z^2 \rangle$ the averaged square noise amplitude (deflection) of the cantilever, k the spring constant in N/m, k_B the Boltzmann constant, and $T = 295K$ for measurements at room temperature [185].

$$\sqrt{\langle z^2 \rangle} = \sqrt{\frac{k_B T}{k}} = \frac{0.064nm}{\sqrt{k}} \tag{2.5}$$

For the soft ($k \sim 0.08N/m$ AC40 (Olympus, Japan) cantilevers used in this thesis, the thermal noise $\sqrt{\langle z^2 \rangle} \sim 0.25$ nm.

2.3.2.3 Detector Noise

Noise in the deflection detection can follow from unwanted interferences between different surfaces in the optical detection system. To some extent, this can be suppressed by using a superluminescent photodiode as a light source (instead of a laser), or by reducing the coherence length of the laser — and thus reduce interference — by modulating the laser power at a high frequency (300-400 MHz) [198].

Other types of noise are the Johnson noise from the transimpedance resistor in the electronic amplifier that converts currents from the detector photodiode(s) into a voltage, and the shot noise from the photodiodes itself, related to the finite photon and thus electron budget at the photodiode. These two dominate in state-of-the-art commercial AFM systems, resulting in a detector noise below 100 fm/$\sqrt{\text{Hz}}$, and below 10fm/$\sqrt{\text{Hz}}$ in more specialised systems [198], [199], which is particularly beneficial in measurements with stiff (>10 N/m) cantilevers.

2.3.2.4 Cantilever Drift

Drift or $1/f$ noise is another crucial factor in AFM experiments. In the example of contact mode, it causes the cantilever to show a variable bending even in absence of the sample surface, which makes it hard to define a clear non-contact deflection to which sample-induced cantilever defections should be referenced. Similar considerations apply to the amplitude in tapping mode and to the resonance frequency in FM-AFM. This leads to one of the main advantages of the peak force tapping mode that has been extensively used in the experiments for this thesis: By continuously recording force curves, it can determine a cantilever deflection (and thus force) at the closest point of approach, while using the deflection away from the surface (i.e., at the largest distance from the surface during the vertical modulation) as a continuously updated reference.

2.3.2.5 Piezoelectric Creep and Hysteresis

Piezoelectric crystals (or briefly piezos) are crystals in which charge accumulates when a mechanical stress is placed on the crystal. Conversely by placing a potential difference across the crystal, the crystal expands or contracts. This effect is used to used to generate the atomic-scale motion of the tip (or of the sample) in scanning probe techniques such as AFM. For each line scan of the AFM cantilever, the lateral motion is generated by applying an (approximately) triangular waveform voltage to one of the axes of the piezo scanner.

When operated in traditional 'open loop' scanning, the major drawback of piezo scanners is that they are subject to creep and hysteresis. Creep manifests itself by a change in the piezo position over time even when the applied voltage is constant. For AFM imaging this results in image distortion and a loss of resolution [200]. Further image distortions can arise from hysteresis and the generally non-linear piezo response to the applied voltage.

To reduce or eliminate these effects, the piezo scanner can also be operated in 'closed loop', where the position of the scanner is tracked by a position sensor (e.g., a capacitive sensor), and where a feedback loop corrects any deviation from the target position. Although this reduces the measurement error due to piezo effects, the position sensor itself is an additional source of noise, which can affect the spatial resolution. For the measurements in this thesis, the benefits of state-of-the-art closed-loop scanners were found to outweigh the disadvantage of additional sensor noise, and for DNA, the highest-quality data were obtained with closed-loop scanners [68].

2.3.3 Cantilevers/Probes

To enhance the force sensitivity, one can reduce the stiffness of the cantilever. The cantilever is the sensor for the AFM, and can vary substantially in its design and characteristics for different functions. For imaging biomolecules, these characteristics are exploited to increase the force sensitivity a characteristic highlighted as key to high resolution imaging [68]–[70] minimising the load force applied to a molecule, thereby improving the spatial resolution. The cantilever tip also has a large effect on image resolution as the point of interaction between the AFM and the surface. Each image by definition is a convolution of the tip shape and the sample topography, and tip sharpness has been identified as a key component in increasing resolution, and for larger biomolecules both the tip apex and its aspect ratio are relevant [70].

2.3.3.1 Mechanical Properties of the Cantilever

For imaging of biomolecules in fluid in contact mode, tapping mode and peak force tapping mode, soft cantilevers are used to obtain high force sensitivity, minimising the load force on the sample. In FM-AFM stiffer levers are used to increase the quality factor, to generate a more stable oscillation and to thus allow stabler imaging above the surface of a biomolecule. In fluid the damping effects of the fluid cause the quality factor to reduce to ~ 1 for soft levers.

2.3.3.2 Small Levers

Work has been carried out in miniaturising cantilevers for high resolution imaging of biomolecules to achieve higher resonance frequencies for use in liquid whilst maintaining the low stiffness required for good force sensitivity. Small cantilevers have been predicted to yield improvement in image stability, imaging speed and thermal noise, however they have been traditionally difficult to manufacture, and much work on these has been focussed on high-speed AFM using tapping mode [201]. Small cantilevers with high resonance frequencies are now commercially available due to the work achieved by a small number of groups and AFM manufacturers [199], [202], [203]. Figure 2.6 shows the size difference between a conventional cantilever (100's of μm) and a small cantilever ($\sim$20 μm).

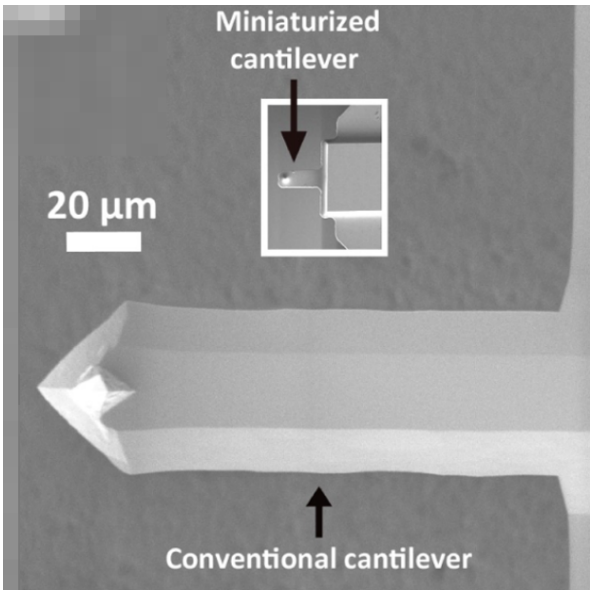

Figure 2.6: Scanning electron microscopy image of a small cantilever compared to a conventional NCH cantilever. Reproduced from [70]

Small cantilevers show improvements in time-response and force sensitivity, having

been shown to yield improvements in force sensitivity of 5 times [204]. There are however a number of drawbacks that can limit their use. Caused by the interaction between the beam of a cantilever and the sample surface, hydrodynamic damping of the cantilever varies more rapidly near the sample surface for smaller levers, as this variation scales with the cantilever width, leading to a less clearly defined force baseline above the sample [70]. More generally, it is difficult to fabricate a sharp tip at the end of a small cantilever and the mass of the tip contributes more heavily, reducing the f_0 [64]. Carbon tips are therefore often grown on the end of these cantilevers, which increases the cost of manufacturing by a large amount, and have also been shown to reduce resolution by changing the interaction strength in some cases [105]. This effect is less pronounced for biological samples where electron-beam deposited tips have been used to probe the double helix of DNA [70], however the aspect ratio and tip apex may still not be ideal for high resolution imaging on most conventional systems.

2.3.3.3 Tip

The use of sharp probes is generally acknowledged as a necessary condition to achieve high-resolution images [205]. The convolution with the tip apex is responsible for the broadening effects that are observed in most AFM images, and that lead to an over-estimation of the lateral dimensions of measured objects [184]. For atomic-resolution imaging of a flat surface such as mica or calcite, an increase of the tip radius hardly affects the image quality as the short-range interaction between the tip front atom and the surface topmost atom predominantly contributes to the frequency shift [206]. However, for a surface with larger protrusions and corrugations the effect of increasing the tip apex is exacerbated.

Tip manufacture is an area of interest both to research groups and companies [207]. Ideally the tip would be a sharp needle with a radius of less than a nanometre, for example a carbon nanotube mounted on a flexible cantilever. The development of carbon nanotube tips, however, has considerable manufacturing obstacles, and is not cost efficient [208]. The most commonly used cantilevers are silicon with silicon tips and silicon nitride with silicon tips. There has been large progress in the manufacturing process of these over the years, yet most cantilever manufacturers still define their cantilever tip radius as ∼2-10 nm. Table 2.1 shows the specifications of the cantilevers mainly used in this study, and the mode they were used for. These cantilevers are commercially available silicon, or silicon nitride cantilevers with silicon tips.

It has been postulated that to obtain molecular resolution on biological samples, small cantilevers with carbon tips, formed by electron beam deposition (EBD) are required. EBD probes are formed by the deposition of high density carbon onto silicon nitride levers, this high density carbon is extremely durable and can give images over a long

Type	k (N/m)	f_0 (kHz)	R (nm)	Mode Used
MSNL-C	0.01	1.5	2	Contact
MSNL-D	0.03	4	2	Contact
MSNL-E	0.1	6	2	Contact/PFT
MSNL-F	0.6	40	2	Tapping/PFT
Biolever Mini (AC40)	0.1	25	10	Tapping/PFT
Fastscan DX	0.25	110	8	Tapping/PFT

Table 2.1: Nominal specifications for spring constant k, resonance frequency in fluid f_0, tip radius R and mode of imaging employed, for the cantilevers used in this investigation.

imaging period. The process of manufacturing EBD probes is more complex than that of manufacturing silicon probes, and results in increased costs. It has also been shown that EBD tips may result in lower resolution on some samples, due to the lessening of the interaction of the carbon tip with the sample [105] although many high resolution AFM studies of biological samples have been achieved using EBD probes [70], [73], [209]–[212].

The aspect ratio of the tip must also be considered, especially for biomolecules or biomolecular complexes/assemblies with large narrow variations in sample topography. A high aspect ratio tip minimises the interaction of the surface with the sides of the tip, thus allowing smaller topographic features on the surface to be observed.

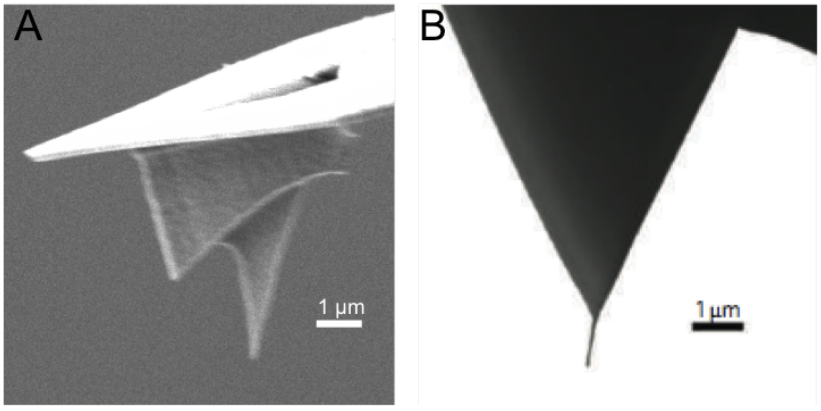

Figure 2.7: Electron microscopy images of two small cantilevers one with standard silicon tip and one with a carbon nanotube tip. A) SEM image of the AC40 or biolever mini probe (Olympus, Tokyo, Japan) - a silicon high resolution probe for biological imaging and B) TEM image of a carbon nanotube high aspect ratio probe [213]

Figure 2.7 shows images of two cantilevers, A) SEM image of the AC40 or biolever mini probe (Olympus, Tokyo, Japan) - a silicon high resolution probe for biological imaging and B) TEM image of a carbon nanotube high aspect ratio probe [213].

2.3.4 Cantilever Actuation

In order to obtain a clean, reproducible cantilever signal for measuring the tip sample interaction, it follows that the cantilever must be actuated in a way that facilitates this. Typically the cantilever is actuated by a piezoactuator, however this has drawbacks in liquid where the cantilever resonance is convoluted with the other mechanical resonances of the fluid cell causing a 'forest of peaks' as discussed in section 2.2.2 [183]. This affects tapping mode in that the force exerted by the cantilever on the surface cannot be easily monitored during experiments, and this is exacerbated by the drifting of the 'forest of peaks'. It is for this reason that many groups and AFM manufacturers are investing in directly driving the cantilever using a range of methods. Some of these require specialised cantilevers, but as the field grows the availability of these will increase with decreasing cost.

2.3.4.1 Alternative Methods of Cantilever Actuation

To date, several alternative actuation methods have been developed to improve over the standard piezo-acoustic actuation, such as magnetic actuation [214], [215], electrostatic actuation [216], and improved, composite fluid cells to suppress spurious mechanical resonances in piezo-acoustic actuation [217].

For high-resolution imaging it is preferable to use commercially available standard cantilevers, as the correct choice of cantilever mechanical properties with a well-defined small tip radius are essential. It is for this reason that photothermal or optical actuation is being adopted in severl groups, as it can be implemented using standard cantilever holders and cantilevers.

2.3.4.2 Tapping Mode with Optical Cantilever Actuation

Due to their bimetallic nature, AFM cantilevers can be actuated by local laser heating [218], [219] exploiting their propensity to bend [220]. By focusing a modulated actuation laser on the cantilever surface, it can be brought to resonance without exciting the support chip or other spurious resonances in the fluid cell. In addition, optical actuation does not require any electrical connections or corrosive coatings, making it an ideal technique for use in fluid, with laser modulation allowing the use of both small cantilevers with ∼MHz resonance frequencies, and standard cantilevers. Photothermal actuation becomes increasingly important on further miniaturization of cantilevers and on the corresponding increase in resonance frequencies [70], [105], [202], [212], [221], since problems related to spurious resonances are aggravated when the cantilever resonance covers a broader frequency spectrum.

Unfortunately, the amplitudes achieved by photothermal actuation are usually rather small [218], [222], [223]. To extend the amplitude range that is accessible by photothermal actuation, previous authors blackened their cantilevers by a sputtered gold-palladium coating to enhance light adsorption [218], or exploited the trapezoidal form of the cantilever cross-section [224].

For tapping mode in liquid, FastScan D and AC40 cantilevers were used, these are soft cantilevers, ideal for tapping mode imaging of biomolecules, with spring constants of 0.25 and 1 N/m respectively. These cantilevers were actuated using the setup shown in figure 2.8 to achieve free amplitudes of up to 2 nm in fluid. For imaging DNA in liquid the amplitude of oscillation required at the sample is on the order of 1 nm allowing these to be used without further coating.

The work presented here uses optical actuation on a home built system using an interferometer to detect the cantilever movement. This is achieved by focussing two lasers at the same point on the cantilever, one of which is used to detect the cantilever movement, and one which actuates the cantilever. Figure 2.8 shows a schematic of the setup used here.

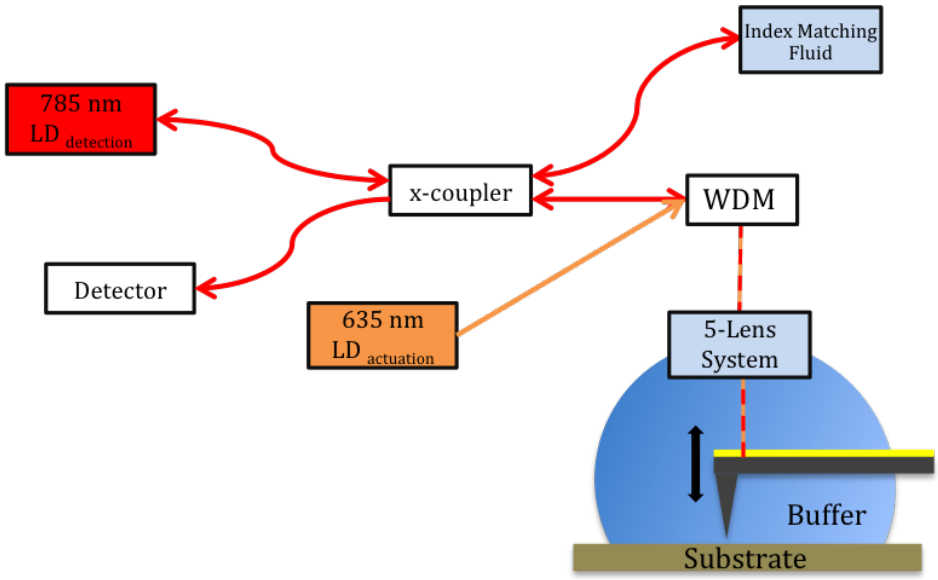

Figure 2.8: A schematic of the setup used here for optical actuation of cantilevers.

A 785 nm laser is used to detect the motion of the cantilever and a 635 nm laser is used to actuate the cantilever with a power of 1 mW (peak to peak). Both lasers are coupled into the interferometer fibre using a wavelength-division multiplexer (WDM) (FONT, Surrey, British Columbia, Canada) in a similar manner to [225] whereby the light form the detection laser travels though a 99/1 x-coupler before reaching the WDM as shown in 2.8. A photodiode is coupled to another arm of the fibre coupler to give a position readout based on the reflected power of the detection laser. The two laser

spots are focused to the same 3 μm point on the cantilever using a five lens system. The small spot size achieved here allows the entire spot to be reflected by the cantilever, maximising efficiency.

For efficient actuation, the laser spot was moved through the length of the cantilever to determine the point of largest amplitude. This measured amplitude (z_{max}) was converted into the amplitude of oscillation at the end of the cantilever (z_{end}), by a factor that followed from the ratio of the measured thermal noise power at the end of the cantilever and at the point of maximum actuation:

$$\sqrt{\frac{\langle z_{end}^2 \rangle}{\langle z_{max}^2 \rangle}} \tag{2.6}$$

2.4 High-Resolution Imaging of Biomolecules

Given the large differences between the different modes of operation, it may seem surprising that these modes have resulted in rather similar resolution on standard biological samples such as bacteriorhodopsin and DNA (though there may be variation in the ease at which this resolution was obtained)). Bacteriorhodopsin has been imaged to molecular resolution using contact mode [96], [226], tapping mode [97], [227] and FM-AFM [70] and DNA with contact mode [116], tapping mode [68], peak force tapping mode [68] and FM-AFM [69], [70] with the best images in the literature appearing highly similar. This illustrates that there is more than one route to highest-resolution imaging. Common factors for all modes are sample preparation, tip size and aspect ratio, and noise sources such as thermal noise and deflection detector noise, as well as the mobility and softness of the sample itself.

In general, all these factors need to be optimised, as well as the exact imaging parameters in each individual mode of operation. The next chapter describes the Materials and Methods for this thesis, including details on sample preparation and parameter optimisation for peak force tapping mode.

Chapter 3

Materials and Methods

To achieve high resolution by AFM on single biomolecules it is necessary to optimise both the imaging technique and the sample. In this chapter the methods used for preparing the samples for imaging with AFM are described. This includes the adsorption of DNA to an atomically flat substrate, and the formation of model membranes. Additionally, methods to optimise imaging resolution in peak force tapping and advanced image analysis techniques to evaluate DNA structure are described.

3.1 Sample Preparation

For high-resolution AFM imaging in fluid, the sample must be adsorbed onto an atomically flat substrate, such that observed topographic features can be attributed to the biological sample and not to the substrate. Here we describe the methods used in this investigation for adsorption of biomolecules to a substrate for studies of DNA structure and antimicrobial peptide modes of action.

3.1.1 Use of Appropriate Substrate

Muscovite mica is often used as a substrate for AFM imaging. It has a structure which consists of planes which only weakly interact with one another. These planes can be cleaved using sticky tape, resulting in an atomically flat surface [228]. A layer of (hydrophobic) Teflon is placed below the mica to confine the liquid solution to the mica disk and avoid contamination and spillage when imaging in fluid.

3.1.2 Immobilising DNA on a Mica Substrate

Divalent cations are used to overcome the repulsion between the negative surface charge of mica and the negatively charged DNA in aqueous solution (at neutral pH). The DNA adhesion to mica can be tuned via the cationic concentration of the solution. Nickel Chloride, $NiCl_2$, was the divalent cation chosen for use in this study, as the corresponding protocol is relatively simple and produces sufficiently strong binding of DNA to the substrate for imaging in solution. Ni^{2+} cations have been widely used in AFM studies of DNA and protein-DNA complexes. The correlation between the DNA-binding activity of the cation and its hydrated radii suggests that divalent cations bridge the negatively charged DNA backbone at the mica surface [117], [229]. Typically, higher Ni^{2+} concentrations lead to a stronger binding of adsorbed DNA molecules to the mica, but also result in an increased surface contamination by aggregated salt.

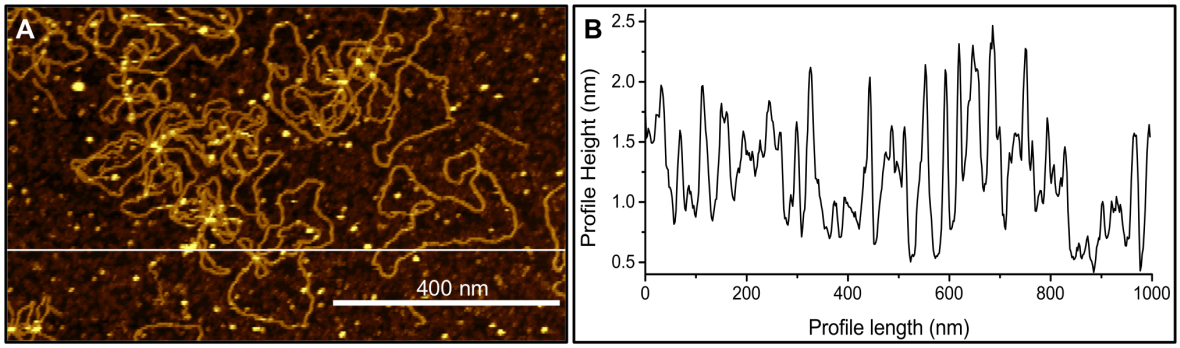

Figure 3.1: Adsorbing DNA plasmids on a mica substrate aided by Ni^{2+} ions. (A) AFM topography of plasmids adsorbed for 3 hours in a solution with high (20 mM) Ni^{2+} concentration. (B) A height profile taken along the white line in A.

Figure 3.1 shows such a sample, where a high $NiCl_2$ concentration has resulted in precipitated salt obscuring the substrate. This can result in poor height measurements (by lack of a clear reference) and increases the risk of tip contamination. At 5 mM or lower concentrations of Ni^{2+} as used in this study, the plasmids are sufficiently immobilized on the mica substrate to facilitate high-resolution imaging, while not yet suffering from excessive salt precipitation over the time scales of our experiments ($\sim$hour).

For the experiments carried out here, freshly cleaved mica (Agar Scientific, UK) was covered with 25 μL of 20 mM $NiCl_2$ (Sigma-Aldrich, UK) solution, followed by addition of 25 μL of 10 mM HEPES pH 7.0 (Sigma-Aldrich) buffer, and of 7 μL of 3 μg/mL 3486 base-pair plasmid DNA solution (pmaxGFP nucleofector kit, Lonza, Basel, Switzerland). All solutions were allowed to equilibrate at room temperature before the sample preparation, to reduce subsequent drift in the microscope. After 30 minutes, the solution was diluted by addition of 50 μL of 10 mM HEPES pH 7.3. This reduced the $NiCl_2$ concentration to 5 mM $NiCl_2$, which implies a Debye screening length of $\sim$ 2.5

nm. All AFM measurements were performed in liquid under buffer conditions. The DNA adsorption protocol is also detailed in appendix A.

We note that Magnesium cations (Mg^{2+}) can also be used, but the attachment is much weaker, resulting in DNA molecules bound unstably on the surface, which limits the spatial resolution that can be obtained [117]. There are several alternative methods for DNA adsorption, e.g., via chemical modification of the mica surface charge to facilitate the adsorption of DNA, using aminopropyltriethoxy silane (APTES) and aminopropyl silatrane (APS), termed AP and APS mica respectively. APS-mica has beeen reported to improve upon AP mica, creating a smoother surface [230] however both of these have been reported to provide variable surfaces leading to non-uniform distributions of adsorbed DNA across the sample indicating they may not be appropriate for high resolution imaging [231]. Monovalent cations have also been shown to facilitate adsorption of DNA to mica, but this process leads to less stable adsorption and requires increased preparation time [232]. None of these other methods were pursued in this thesis.

3.1.3 Use of Supported Lipid Bilayers as Model Membranes

Antimicrobial peptides attack the negatively charged outer membrane of a bacterial cell. The cell is a large, fluctuating object, with a large number of distinct components, many of which are not yet characterised. This greatly compromises the resolution and interpretation of AFM at the nanoscale. Additional complications arise because of the hydrodynamic interaction between the cantilever beam and the surface of the cell [233]. To circumvent these problems, supported model membranes are usually preferred for AFM experiments on the mechanisms of membrane degradation by proteins and peptides [77], [177]–[179], [234].

Model membranes have been shown to be a key tool in the study of lipid bilayer interactions with proteins, peptides and other membrane active drugs [77], [144], [235]. They are prepared using a range of phospholipids and substrates, with the most commonly used technique of vesicle fusion requiring the formation of small unilamellar vesicles, which can subsequently be adsorbed onto a cleaved mica substrate [176], as will be described here. The full protocol for lipid preparation for the fused vesicle method is shown in appendix B. Other methods for the formation of supported lipid bilayers include the use of a Langmuir-Blodgett trough to form monolayers or bilayers. Lipids are spread at the air-water interface in chloroform/methanol mixtures and then compressed after letting the solvent to evaporate for 15 min. The surface pressure at the interface is recorded, which can give information on the packing and organisation of the lipid molecules. The mica substrate is raised and lowered through the interface keeping the pressure constant to create monolayers and bilayers. This method was also tested in preliminary experiments, but in the context of this thesis did not yield improvement

over the much simpler vesicle fusion method, and therefore was not further used.

3.1.3.1 Formation of Small Unilamellar Vesicles

DLPC (1,2-dilauroyl-sn-glycero-3-phosphocholine) and DLPG (1,2-dilauroyl-sn-gly-cero-3-phospho-(1-rac-glycerol)) were used in a weight ratio of 75% DLPC / 25% DLPG for liposome construction (Avanti Polar Lipids, Alabaster, AL, USA). These lipids were chosen to be fluid phase at room temperature. In addition, the choice of lipid was made to match that used in complementary techniques for further analysis of the peptides, including molecular dynamics simulations and solid-state NMR [236] and for comparison with previous studies [237].

The preparation of mixed lipid species requires the lipids to be dissolved and mixed in a non-polar organic solvent solution to obtain a homogeneous mixture. The organic solvent is then removed by evaporation under a steady nitrogen stream to form a dry film. To hydrate the lipid films, buffer solution or deionised water is added to the dried film. The lipid suspension is vortexed for 30 minutes at room temperature to agitate the mixture. At this point the lipids will form large multilamellar vesicles (LMVs) in solution, these must be dispersed and reduced to single unilamellar vesicles (SUVs) before the vesicle fusion process through sonication and extrusion.

The cloudy suspension of multilamellar vesicles is sonicated above the transition temperature the lipids for sixty minutes in a bath sonicator. The use of the 80 kHz frequency during sonication allows the small vesicles to be ruptured and broken down into SUVs. To ensure a uniform size distribution of vesicles in suspension, extrusion is performed [238]. Extrusion is the process by which the lipid suspension is forced through a polycarbonate membrane with pre-defined pore sizes. The lipid suspension is passed through a 50 nm pore membrane a minimum of twenty times using an Avanti mini-extruder to ensure a uniform size distribution.

3.1.3.2 Vesicle Fusion

The preparation of supported lipid bilayers is performed via the vesicle fusion method, described fully in [176]. The vesicle fusion method cannot be used to form asymmetric bilayers or closely regulate the packing density of the lipids in the bilayer as can be achieved via the Langmuir-Blodgett technique, but the vesicle fusion technique allows bilayers to be assembled quickly. In the vesicle fusion method, SUVs in suspension are allowed to adsorb onto mica over a period of 30-60 minutes. If the transition temperature of the lipids is above room temperature, the mica should be heated to at least the maximum lipid transition temperature before and during absorption [239].

As the lipids reach the surface the spherical vesicles deform onto the surface as they adsorb, becoming ellipsoidal in form, before rupturing to form a bilayer fused to the mica surface [240]. A schematic of the vesicle fusion process is shown in figure 3.2.

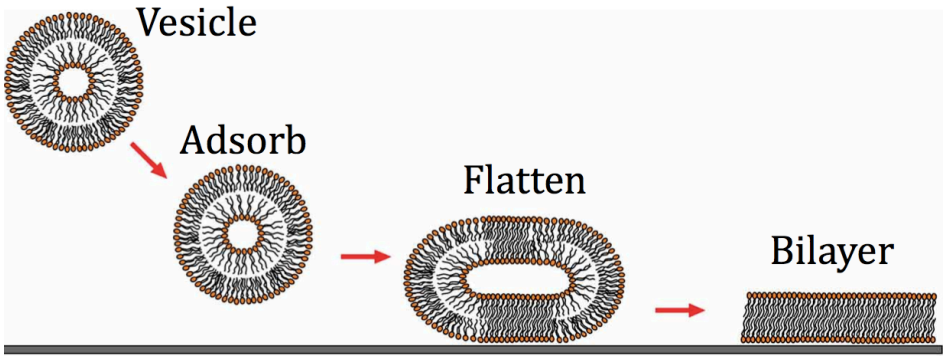

Figure 3.2: A schematic showing the deformation of a vesicle as it fuses to the mica substrate (adapted from [176]

This technique has been successfully used to form mixed phase separated bilayers, and continuous bilayers with both full and partial coverage on the mica. There are a number of parameters which can influence this process, including vesicle composition, temperature, and the composition of the buffer solution [241]. These parameters include the presence of cations in the buffer solution [242]: It has been found that when forming negatively charged lipid bilayers, calcium chloride ions must be present in solution, and when forming bilayers of neutral charge, magnesium chloride ions must be present in solution.

3.1.3.3 Absorption of Lipids to a Mica Surface

All lipid suspensions were prepared at 4 mg/ml in MilliQ water. 1 μl of lipid suspension and 99 μl of 20 mM HEPES, 150 mM potassium chloride, buffer solution were deposited on a freshly cleaved mica disk, with 10 mM divalent cation content to aid absorption and fusion to the mica. The suspension is left to adsorb at room temperature, which is well above the transition temperature of both lipids, for 45 minutes. The mica is then washed three times with the same buffer solution to remove any lipids remaining in the fluid which were not adsorbed to the substrate.

These bilayers are formed entirely covering the mica, with no topographic features as the lipids used are of equal chain length and are mixed with no phase separation. A flat model system to examine the effect of peptides on the cell membrane is thereby achieved.

3.1.4 Antimicrobial Peptides for AFM Imaging

Antimicrobial peptides are prepared in a form and at a concentration that allows their injection into the fluid cell during imaging of a supported lipid bilayer. The antimicrobial peptides used in this investigation were prepared at the National Physical Laboratory by collaborators as detailed in [236], [243].

Each *de-novo* designed peptide was synthesised in a form that folds upon contact with the membrane and forms a helical amphipathic structure. To ensure amphipathic characteristics, the peptide sequence followed the heptad repeat strategy which uses a CNCHNCH repeating pattern, where C is cationic and N is neutral polar, ensuring that on folding the cationic and hydrophobic amino acids were segregated on either side of the helix. The pattern also ensures that a 1:1.5 ratio of hydrophobic and cationic residues is maintained, which prevents the cytotoxic and hemolytic effects of venom peptides. The neutral residues are separated in the sequence at standard i, i+3 and i, i+4 helical spacings, i.e., in the hydrophobic face, and are alanines and glutamines to reduce aggregation by limiting the large hydrophobic interactions commonly experienced by having them all of one type.

Peptide sequences once designed were assembled on a Liberty-1 automated microwave peptide synthesizer (CEM Inc.) using standard solid phase Fmoc-based protocols using HBTU/DIPEA for amino-acid couplings and Rink amide MBHA resin. Carboxyfluorescein succinimidyl ester was used to label the N-terminus [236], [244].

3.1.4.1 Purification

The peptides were purified using high performance reverse liquid chromatography (HPLC) after de-protection with 95% TFA, 2.5 % TIS, and 2.5 % water on a JASCO HPLC system using Vydac C5 analytical at the NPL to 99% purity and their identity confirmed using MALDI-ToF mass spectrometry [236], [244].

3.1.4.2 Solution

The dried peptide was suspended in deionised water to form a high concentration stock solution for storage in a refrigerated environment. The stock solution was further diluted in buffer for use in phospholipid experiments [146]. The buffer used in this experiment contained 20 mM HEPES, 150 mM NaCl diluted in MilliQ water > 18.2 $M\Omega cm^{-1}$ at pH 7.2. The concentrations were calculated in μg/ml for AFM imaging, however the molar concentration was later determined using the Beer-Lambert Law, with pre-determined amino acid molar extinction coefficient values.

3.1.4.3 UV-Vis spectroscopy to Determine the Peptide Concentration

UV-Vis spectroscopy was used to determine the molar concentration of a peptide solution to ensure concentrations were consistent across experiments, as the weights used to make solutions here are too small to measure. This is here illustrated by the peptide Amhelin [236], designed and synthesised at the NPL and evaluated using fluid AFM in this thesis. The molar extinction coefficient ε of Amhelin was calculated using the peptide sequence. The numerical values of the ε for each free amino acid present in Amhelin including bonding contributions were summed to gain a value for the peptide as a whole [245]. Peptide molar extinction coefficient values calculated in this manner have been checked against experimentally measured values for a number of proteins and peptides and agree well. The calculations for the molar extinction coefficient of the peptide Amhelin are shown in table 3.3.

Peptide	Abbreviation	epsilon	number	Sum
Alanine	A	32	3	96
Glutamine	Q	142	3	426
Leucine	L	45	6	270
Lysine	K	41	9	369
Peptide Bond		923	20	18460
	$\varepsilon(M^{-1}cm^{-1})$			19621

Figure 3.3: Molar extinction coefficient calculations for the peptide Amhelin for $\lambda = 214$ as adapted from [245]

The molar extinction coefficient of a substance can be related to its absorbance, a measure of how well it absorbs light, and its concentration in Moles, for a given path length via the Beer-Lambert law, equation 3.1.

To calculate the concentration of a solution of Amhelin, a spectrophotometer was used to accurately determine the absorbance of the solution. The spectrophotometer was operated at the same wavelength used in the molar absorptivity calculations (214 nm). The absorbance was measured to be 0.515 for a solution of 100 $\mu g/ml$ over a 1 cm path length. From these known values, equation 3.1, The Beer-Lambert Law, was used to calculate the molar concentration of the peptide solution. The same procedure was carried out for each peptide used in this study.

$$A = \varepsilon lc \tag{3.1}$$

Where A is absorbance, l is path length, and c is concentration in Moles

The calculated value for the molar extinction coefficient and the value of the absorbance, measured at 214 nm are substituted into equation 3.1 to give the molar concentration of a peptide solution.

3.1.4.4 Addition of Peptides during AFM Experiments

Peptide suspensions are stored at -20 °C or -80 °C to minimise the risk of contamination due to bacterial growth in solution. By defrosting individual aliquots of peptide suspension on the day of experiment, the likelihood of aggregation is minimised, as aggregation can reduce and alter the antimicrobial action of the peptide. To minimise the aggregation, contamination, and denaturing risks, the peptide is kept on ice during the experiment. The peptide suspension will already be of a known molar concentration, as characterised in sectoin 3.1.4.3, it can be added to the imaging solution by volume to give the required concentration in the fluid cell.

AFM imaging is performed on the model membranes prior to the insertion of the peptides, to ensure a flat lipid bilayer substrate is present. The peptide can then be directly injected into the imaging buffer using a Gilson pipette.

3.2 Optimising Peak Force Tapping AFM for High Resolution Imaging

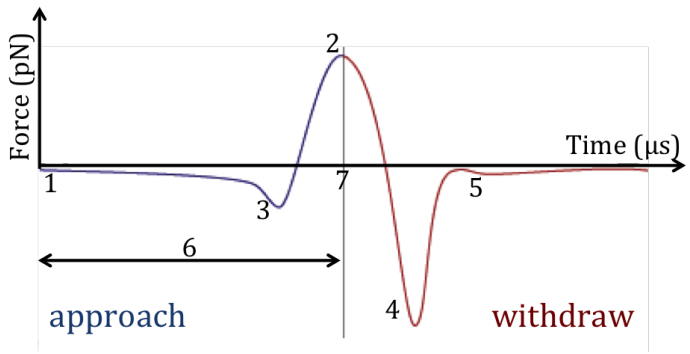

Figure 3.4: A peak force tapping force curve, taken at each pixel across the surface, showing: 1) the baseline, 2) the maximum applied force (peak force) during imaging, 3) an attractive tip-sample force, 4) adhesion between the tip and the sample, 5) the point at which the tip pulls off the sample, 6) the magnitude of the movement in z, or twice the peak force amplitude, 7) the time period after which the peak force is reached (the sync distance is half of this).

Figure 3.4 is a schematic of a peak force tapping curve, showing the different elements. (1), the baseline, is the background for the peak force. (2) is the maximum applied force (peak force) at each pixel. (3) represents an attractive tip sample interaction. (4) is the adhesion, i.e. how much the tip sticks to the sample on pull off. Higher levels of adhesion in liquid can indicate a blunt or damaged tip. (5), the point at which the tip pulls off the sample. There can be ringing on pull off caused by the simple harmonic oscillator response of the tip when being pulled off a surface at these speeds. (6) is twice the peak force amplitude, a measure of the z travel of the cantilever for each force curve (7) is twice the sync distance, which is the time from the start of the cycle to the time of peak force being applied measured in 2 μs time steps (with the odd units being related to the underlying computer code).

In this example, there is an attractive force (3) between the tip and sample. This can also be used as a peak force setpoint, which would then be negative. In practice, for imaging in liquids, this is usually not sufficiently stable for imaging.

3.2.1 Limiting Factors for High Resolution Imaging in Peak Force Tapping

Peak force tapping is typically performed at lower imaging speeds than tapping mode, as the standard modulation frequency for the tip-sample distance is 2 kHz, compared to 10 kHz to 1 MHz frequencies for the cantilever oscillation in tapping mode. Typically, this allows for an image to be obtained in two to three minutes. We can increase the modulation frequency to 4 kHz, if the cantilever resonance in liquid is high enough. This doubles the bandwidth, but has the downside that the signal-to-noise can be reduced by driving the cantilever at higher frequencies.

The force control is limited by the noise floor. Cantilevers with a spring constant of $\leq$ 0.1 N/m allow for sufficient force control for high resolution imaging, since a setpoint increase of 1 mV will elicit a smaller increase in force than a 1 mV increase when using a stiffer lever. The same preference for softer levels applies if the measurement noise is dominated by the thermal fluctuations of the cantilever, as the equivalent force noise scales with $\sqrt{\text{spring constant}}$ (i.e., a smaller spring constant yields smaller force noise) [215]. On the other hand, softer cantilevers generally have lower resonance frequencies than stiffer cantilevers, which limits the response speed of the cantilever, and they show show larger amplitude noise due to thermal fluctuations (though lower force noise, as stated above), which translates to noise in the tip-sample distance. Olympus AC40 and Bruker FastScan D cantilever were found to represent a good compromise for the measurements in this thesis.

To perform high resolution imaging we require a sharp tip to probe the surface, such

that tip-convolution does not dominate small corrugations of the sample surface. As will be shown in chapter 4, a tip radius of ∼1 nm can yield images of the secondary structure of DNA, while with tip radii larger than 2 nm, secondary structure is harder to resolve. It would follow that the smaller the tip radius, the higher resolution can be achieved, but this does not generally follow. For smaller tip radii the same tip-sample force is exerted on a smaller area of the sample, implying a larger pressure, and correspondingly a larger risk of sample distortion.

3.2.2 Optimising Imaging Parameters

The parameters given in table 3.1, must be optimised for each sample, this is discussed here.

Parameter	Value
Approach Setpoint	0.03 V
Approach Gain	8
Scan Size	120 nm
Aspect Ratio	2
Lines/Samples	512
Line rate	3 Hz
Peak Force Amplitude	5 nm
Peak Force Frequency	4 kHz
Z range	1 μm
Deflection Limit	12.24 V
Sync Distance	70
Gain	15
Setpoint	0.025-0.045 V

Table 3.1: A table showing the parameters used for high resolution imaging of DNA in peak force tapping using a Multimode 8 and AC40 cantilever. *(f=32 kHz, k=0.08 N/m, deflection sensitivity = 15 nm/V)*

The approach setpoint is set to slightly higher than the imaging setpoint to ensure that, during the approach of the tip to the sample, fluctuations in the soft cantilever do not trigger the threshold algorithm to conclude that the cantilever has reached the sample surface (a so-called 'false engage'). This setpoint can be set as low as 0.03 V (approximately 40 pN for a typical AC40 cantilever, depending on the deflection sensitivity and the spring constant), but may need to be higher if using a softer cantilever. The use of a low setpoint implies a careful approach to the sample, reducing the risk of tip damage at the first contact. This results in a slow approach, since the approach algorithm takes into account the difference between measured and setpoint deflection in the speed of its approach. It may be necessary to increase the setpoint if far from the

sample. To increase the speed of approach the gain may also be increased, although this can also lead to tip damage due on the approach.

Once the tip has approached the sample, the 'sync distance' must be set. The sync distance is the distance (in 2 μs time steps) between the start point of an extend-retract cycle and the point of peak force marked as (2) in figure 3.4. It can therefore be calculated and input as half of the peak force distance in time or half of (7) in μs. If this parameter is not immediately input after the approach, the peak force may not be calculated correctly, which could result in a tip crash or contamination. The sync distance can be calculated by using the autoconfig option in the software, however for small peak forces a user estimate may be required, as the peak force will be barely discernible above the noise.

The peak force frequency can be set to 0.25, 0.5, 1 or 2 kHz in standard configurations, and increased to 4 kHz on some systems. The use of a high peak force frequency facilitates faster imaging and higher bandwidth. This improves the resolution, but can result in higher noise as the cantilever is driven faster. For high-resolution imaging of DNA, 4 kHz is used to facilitate larger scan rates and thus reduce drift effects on the Multimode system.

For high-resolution imaging, the peak force amplitude is kept small, or the order of nm, such that a relative large fraction of the peak force cycle occurs in contact with the sample, where the topography contrast is obtained. Too small an amplitude, however, compromises the estimate for the baseline force.

Another key parameter is the lift height, which corresponds to the height above the surface at which the sample no longer interacts with the cantilever. This can be seen on the force curve monitor as the part of the curve where the force curve is flat and unchanging in y. The lift height is therefore set to the value in z where the force curve becomes flat and non-interacting if z is taken to be 0 at the point of maximum interaction or peak force. The lift height can also be calculated by the software using the auto config function.

For high-resolution imaging, the scan size is kept small to ensure sufficient pixel resolution to visualise topographic variations at the scale of 1 nm. For an image of 120 nm at 512 pixels, each pixel will be 0.23 nm in size, such that $\sim$4 pixels will span a nm length.

The speed of imaging is determined by the rate at which each line is scanned. Here we use a line rate of 2 Hz or more. By scanning faster we can reduce the effect of x, y drift on the image. The scan rate can be increased further to 5 or 8 Hz if the peak force frequency is increased, when using a FastScan Bio or Icon system, rather than a Multimode.

The setpoint must be minimised to allow for low force imaging. A setpoint of 0.02-0.04 V is used, however it must be noted that the applied force is a function of the setpoint and the cantilever sensitivity and stiffness, and therefore a 0.02 V setpoint can correspond to a high force if using a cantilever which is too stiff. For cantilevers used in our DNA experiments on the Multimode system, this setpoint roughly corresponds to 40 pN. The setpoint may need to be increased in this case to ensure the tip is tracking the sample, however imaging should be begun with the minimum force to minimise the likelihood of damage to the tip.

For high-resolution experiments, the gain is maximised to just below the ringing point. To reduce the ringing on pull off, which can affect the baseline measurement, the lowpass filter can be used. The lowpass filter should be set at ∼20 times the peak force frequency, up to a maximum of 65 kHz.

Once imaging is begun it is important to reduce the approach setpoint to equal or lower than the imaging setpoint, in this case 0.01 V is used. This is because changes to the peak force amplitude, lift height, sync distance, or pressing autoconfig, will trigger a tip engage. The higher engage setpoint is no longer required (while implying increased risk of tip damage) as the tip is already very near the surface, such that the probability of a false engage is reduced.

3.3 Image Processing

3.3.1 Digital Straightening of DNA

DNA plasmids, appear as long curved strands on the mica substrate, when imaged by AFM. The secondary structure will therefore vary in its orientation, along the x and y axes of the AFM image. To enable structural analysis to be carried out on the secondary structure, in one direction, a dedicated Matlab code (MathWorks, Natick, Massachusetts) was written to load the AFM images as ASCII files, trace the DNA, and carry out a transformation from the xyz coordinates of the surface topography to sqz coordinates [246][1]. In the sqz coordinates, the unit vector $\hat{s}$ refers to the direction along the contour of the DNA, and $\hat{q}$ to the direction perpendicular to $\hat{s}$ at all points. Figure 3.5 shows a schematic representation of this transformation. For any particular position s along the DNA, the q coordinate of a nearby pixel was determined from the vector product $\vec{p} \times \hat{s}$, where $\vec{p}$ was the vector from the position defined by s to the position of the nearby pixel. The surface height z was not affected by this transformation.

The DNA was traced, starting from a user-defined point on the DNA, by defining (q,z)

[1] All Matlab code described here was developed by Ruth Thompson.

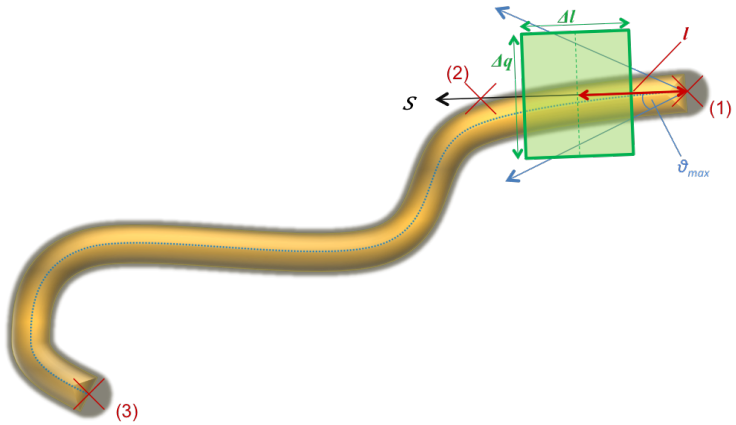

Figure 3.5: Digitally straightening the DNA topography by a transformation from (x,y,z) to (s,q,z) coordinates. The s coordinates measure the distance along a smooth spline following the DNA backbone. For each point s_i (with $i = 1, 2, 3, \ldots$), the perpendicular bisectors between (s_{i-1},s_i) and (s_i,s_{i+1}) are calculated. The data points in the area between these bisectors (green) are assigned the s coordinate s_i. The q coordinate of a point p in this area is calculated using the cross product between $\vec{p}$ and $\hat{s}$, the tangential unit vector at s_i. Image courtesy of Ruth Thompson

points with respect to a segment of set length Δs typically about 2 nm along a trial direction $\hat{s}$; fitting of these nearby (q,z) points with a Gaussian superposed to a linear background; defining the peak position of this Gaussian as a new point on the DNA contour; defining a new trial direction from the line connecting the previous two points; and repeating this procedure until a user-defined end-point was reached. The DNA contour was then traced by a smooth spline along thus defined positions.

In the next step, this DNA trace was divided into s values at a resolution corresponding to the pixel size in the original image, and all (x,y) points in the images attributed to the nearest s position on the DNA contour. Finally, the resulting (s,q,z) coordinates were interpolated to yield an image with equally spaced (s,q) pixels.

3.3.2 Deconvoluting the effect of the Tip

In scanning probe microscopy techniques the image obtained is by definition a convolution of the tip and the sample topography. This can lead to an artefactual representation of the sample topography. This can partly be corrected for, for example to obtain the correct chiral angles in the structure of carbon nanotubes by STM [247]. A similar process can be applied to AFM images of DNA.

Figure 3.6 is a schematic of the tip passing over a DNA molecule, viewed along the s-axis. This illustrates that the measured tip position q_{tip} yields an overestimate of

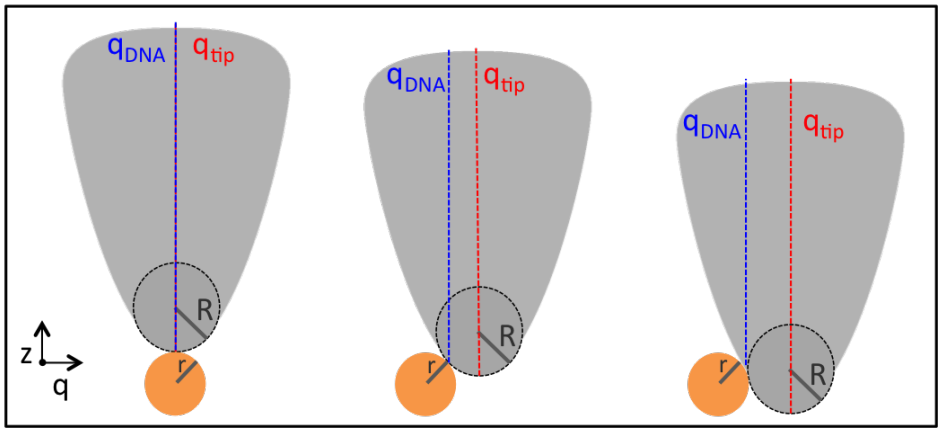

Figure 3.6: A schematic showing the AFM tip of radius R at different positions with respect to a cylindrical molecule of radius r (viewed as cross section).

the q-coordinate q_{DNA} of the DNA surface, except when the tip is directly above the DNA. The AFM measurement thus yields an overestimate of the DNA width, which also results in an overestimation of the chiral angle of DNA. This obviously depends on the tip radius, as has also been shown in simulations of DNA imaging by AFM [69].

We can deconvolute the tip effect from the data in this case using a geometric transformation. To do this, we first estimate the molecular radius from the DNA height in the AFM topography, and estimate the tip radius based on the full-width half maximum width of the (averaged) height profile across the DNA. With these two radii, the AFM images can be corrected for the finite size of the tip via the following procedure.

For our calculations we assume a cylindrical molecule and a spherical AFM tip (with radii defined as r and R, respectively; as shown in figure 3.6. The lateral position of the point of contact between a sample and tip (q_{DNA}) relates to the lateral position of the tip (q_{tip}, *i.e.*, the measured position in an AFM experiment) via equation 3.2.

$$q_{\mathrm{DNA}} = \frac{q_{\mathrm{tip}}}{1 + R/r}\,, \tag{3.2}$$

In our experiments, r was estimated from accurate, low-force measurements of the maximum height of the molecule ($= 2r$), and R from its measured full-width half maximum ($\equiv 2q_{\mathrm{tip},1/2}$):

$$R = \frac{(q_{\mathrm{tip},1/2})^2 - r^2}{2r}\,. \tag{3.3}$$

Here, $q_{\mathrm{tip},1/2}$ was determined from a fit with a Gaussian peak function (since more complicated and accurate descriptions of the cross-sectional profile did not lead to significantly different results). Using Equation 3.2, straightened nucleic acid AFM

images in *sqz* coordinates were thus corrected for the effects of tip convolution.

Coordinates with $q^*_{\mathrm{tip}} > 2\sqrt{rR}$ were excluded from the analysis, as these correspond to positions where the tip is expected to be in contact with the substrate, and not with the DNA any more. Consequently, the DNA surface is only probed over a width of $2q^*_{\mathrm{DNA}} = 4\sqrt{rR}/(1 + R/r) \leq 2r$. In other words, though tips with larger sizes yield a wider appearance of the plasmid, they will probe a narrower part of the molecular surface. Using similar geometrical arguments, one may calculate a corrected height $z_{\mathrm{DNA}} \geq z_{\mathrm{tip}}$, where z_{tip} refers to the very end of the tip. However, unlike the correction of the lateral dimension q, this height correction in our experiments was not significant compared to the noise, and therefore was not pursued any further.

As outlined above, this procedure includes an estimate of the tip radius from the DNA width, which can also be verified by comparing the corrected chiral angle of the DNA to the DNA crystal structure, and which can be useful for calibration purposes in general. For the higher-quality images of DNA secondary structure, tip radii are found to be close to 1 nm. This is below nominal manufacturers' specifications, as shown in table 2.1.

Chapter 4

Visualisation of DNA Secondary Structure

Atomic Force Microscopy (AFM) allows imaging of single molecules at high resolution under near-physiological conditions. Recently it has been shown that by finely tuning imaging techniques and sample preparation, it is possible to visualise the double helix structure of DNA in solution. Here a method is presented to image DNA at ∼1 nm resolution. This allows for the visualisation of the double helix secondary structure of DNA and variations therein by precise control of the applied force during imaging. In addition the convolution of the tip and the sample in the topographic image is analysed and accounted for, resulting in accurate structural parameters for DNA at the single molecule level.

4.1 Introduction

DNA is one of the extensively studied biological molecules, due in part to its significance, and in part to its iconic structure. The double helix secondary structure of the DNA polymer is a key element for the storage of our genetic information, and for our understanding of how our cells, grow, replicate and die. DNA is a long linear polymer whose structural properties and interactions with proteins have been traditionally elucidated by Electron Microscope (EM) and X-ray diffraction techniques. The disadvantage of these techniques is that they rely on ensemble averaging or ordered molecules. AFM allows the imaging of single molecules under physiological conditions, and can monitor these over time, providing information on conformational dynamics in addition to structure at nanometre resolution.

DNA was one of the first biological molecules visualised by AFM and its structure,

topology, dynamics, and interactions continue to be examined. B-DNA, the Watson-Crick form of DNA, is the most commonly occurring form of DNA under physiological conditions. The structure of B-DNA has been elucidated by X-ray crystallography, as described in chapter 1. B-DNA exhibits a right-handed helix with a helical repeat (pitch) of ∼3.6 nm, with major and minor grooves of widths ∼2.2 nm and ∼1.2 nm respectively. A space-filling representation of the structure of B-DNA was generated from PDB file 1BNA [11] and rendered using Chimera [10] and is shown in figure 4.1.

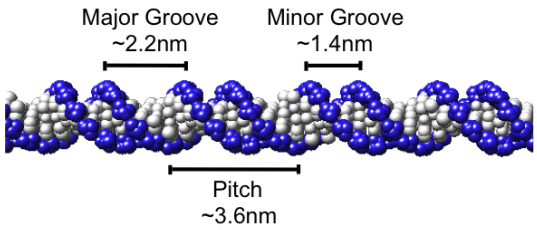

Figure 4.1: A space filling representation of B-DNA, annotated with the pitch, major and minor groove values, rendered using Chimera [10] from the PDB file 1BNA [11].

AFM is exquisitely suited to study DNA structure under conditions that are hard to study in methods that rely on ensemble-averaging: In the presence of supercoiling and in aqueous solutions. This may thus allow to elucidate the interplay between supercoiling, protein binding, and secondary structure. An important step to such studies would be the development of robust methods for visualising the DNA double helix structure and its variations, in particular since the vast majority of DNA images in the AFM literature so far show DNA molecules as featureless strands [230], [248].

There are some early exceptions where the secondary structure of DNA was imaged by DNA through manipulation of the sample preparation. In 1995, Mou et al. resolved the pitch of B-DNA as a periodic modulation of 3.4 ± 0.4 nm [116]. In their study, DNA was adsorbed onto the surface of a cationic supported lipid bilayer, deposited on a mica substrate. The pitch of the DNA was only observed when the DNA strands were densely and uniformly packed on the bilayer surface, and not where bilayers were populated by individual isolated DNA strands. The researchers concluded that close packing limited the movement of the molecules. The resolution obtained on DNA thus depends on the degree of adhesion and immobilisation of the DNA molecules on the substrate.

Only recently have developments in AFM technology resulted in the visualisation of both strands of the DNA double helix [69], [70], showing a tilted, double-banded structure repeating along the molecule. Here we show a method by which commercial instrumentation can be used to image the secondary structure of DNA plasmids, adsorbed on a mica surface, to obtain relevant structural information, allowing us to visualise structural variations in the secondary structure of DNA, at the single molecule level.

4.2 Results and Discussion

DNA was prepared and immobilised on the mica substrate via the divalent cation method as described in chapter 3.1.2 using a $NiCl_2$ solution. 20 ng DNA (3486 base-pair plasmid DNA solution, pmaxGFP nucleofector kit, Lonza, Basel, Switzerland) was suspended in a 10 mM HEPES buffer solution, containing 150 mM NaCl at pH 7.4. The solution also contained 10 mM $NiCl_2$ for the 15 minute absorption, but this was diluted to 5 mM for imaging. The sample was allowed to equilibrate at room temperature, to minimise subsequent drift in the microscope, as that affects imaging at this length scale. The $NiCl_2$ concentration chosen was high enough to adsorb the DNA to the mica in a static or semi-static configuration, whilst retaining some elements of its twisted structure as a 2D projection. At higher $NiCl_2$ concentrations, it is difficult to discern the DNA from the background $NiCl_2$ precipitates. This has been further detailed and illustrated in section 3.1.2.

Imaging was performed on FastScan Bio and Multimode 8 systems (Bruker, CA, USA) in peak force tapping with parameters: peak force frequency 2-16 kHz, peak force amplitude 5-10 nm, and setpoint 30-100 pN. Imaging was performed using commercially available cantilevers, AC40, MSNL-E, MSNL-F, and FastScan D, the characteristics of which are described in described in table 2.1. Tapping mode was also performed using the AC40 cantilever and a Cypher system (Asylum Research, UK), with a typical oscillation amplitude of $\sim$2 nm, a typical line rate 6 Hz, and with the force continuously being minimised to the point of lifting the cantilever off the surface.

4.2.1 Imaging DNA Secondary Structure by AFM

Figure 4.2 shows a plasmid adsorbed on a mica surface using divalent cations as described above. The contrast has been reduced to the point of saturation (3 nm black to white), showing the variations in height along the molecule as colour changes, with white being higher than red. The variations in height of the molecule imply that it is not adsorbed in a completely flat 2D configuration on the surface. This can be attributed to the local bending of the molecule, which does not allow the molecule to lie totally flat. This method shows that we are able to adsorb a DNA plasmid to the mica surface using divalent cations, while observing local height variations.

To visualise further detail on the DNA, i.e., to resolve the 1.2 nm wide minor groove and 2.2 nm wide major groove shown in 1.3, we must zoom in to smaller image sizes than used in figure 4.2. For an image size of 120 nm, with 512 by 512 pixels (the standard pixel value for high resolution imaging) each pixel will be $\sim$0.25 nm. This pixel resolution is sufficient to visualise the major and minor grooves of the DNA.

Figure 4.2: An AFM topographic image of plasmid DNA captured in peak force tapping Mode on a FastScan Bio in buffer solution using a FastScan DX cantilever ($k \sim 0.3N/m$). Local height variations are visible along the molecule as changes in colour.

Figure 4.3 shows a 120 nm wide image of a DNA plasmid, with corrugation corresponding to small height changes along it. This corrugation corresponds to the major and minor grooves of DNA. Imaging was performed on a Multimode 8 (Bruker, CA, USA) in peak force tapping at a peak force frequency of 4 kHz, peak force amplitude of 5 nm, and setpoint 50 pN. The Multimode 8 is an open loop system, which is susceptible to effects from the piezoelectric scanner as described in chapter 2.3.2.5.

Figure 4.3: An AFM topographic image of plasmid DNA captured in open loop peak force Tapping Mode in buffer solution, small height changes along the molecule are clearly visible as corrugation. This corrugation corresponds to the major and minor grooves of the DNA structure. Colour scale: 3 nm.

4.2.2 Controlling the Imaging Force to Improve Resolution

To optimise our imaging conditions in 'peak force tapping' mode, we can control the load force applied to the sample as described in 2.2.5. Peak force tapping mode essentially performs a force curve at every pixel position on the sample surface. It then uses a continuous feedback loop to detect the sample position and apply a pre-determined force defined by the user, referenced with respect to the force baseline that is determined at every force curve as well. The resulting precise control of the load force is an advantage over the traditional tapping mode, in which the drift in resonance peaks within the fluid cell, caused by the mechanical resonances within the cell in addition to the cantilever, leads to uncertainties in the applied force. Figure 4.4 shows the effect of increasing the force on the imaging of DNA, both in the larger topographic features and in the resolution.

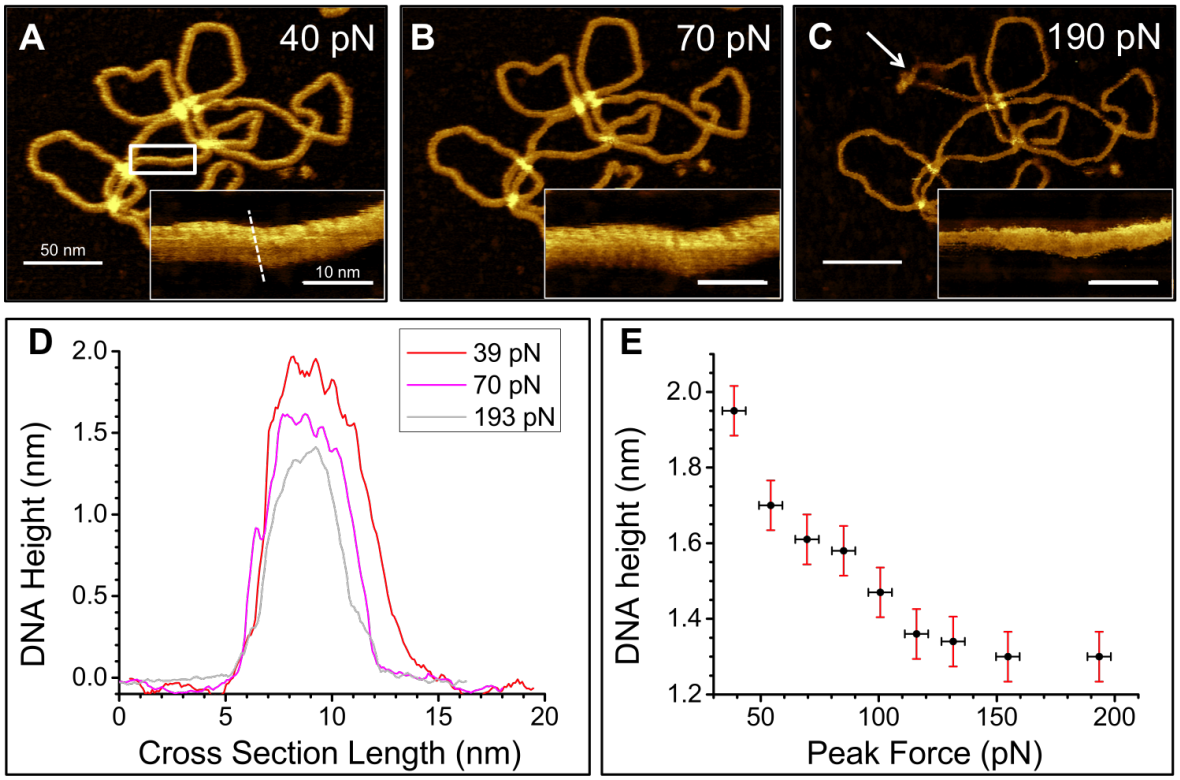

Figure 4.4: A DNA plasmid imaged at peak load forces of (A) 40, (B) 70, and (C) 190 pN, respectively, with the major and minor grooves of the DNA double helix visualized at higher magnification (insets). Colour scales (see figure 4.3 for scale bar): 3 nm (for low magnification); 2 nm (for the insets). (D) Height profiles measured across the DNA, as marked on the inset of A by a dashed line, for different peak forces. (E) Measured height along the same section across the molecule (as D), as a function of peak force.

Figures 4.4A-C show how the molecule is compressed under increasing force. The colour scale is the same for each image (3 nm). However, the DNA appears darker

(lower) as the force is increased. This increase of force also disrupts the structure, as shown by the arrow in figure 4.4C, showing a movement in the plasmid for imaging at a peak force of 200 pN. In addition to the overall compression, we can also examine the effect that increased force has on imaging the secondary structure of the molecule. The insets in 4.4A-C show smaller scans of the molecule, in the area highlighted by a white rectangle in figure 4.4A. These smaller scans show the secondary structure of the molecule as clear lines perpendicular to the direction of imaging.

Figure 4.4A is taken at a setpoint of 40 pN, a setpoint close to the minimum possible force which can be applied in peak force tapping to stay above the noise threshold. At this force, corrugation corresponding to the double helix is visible in the inset, and the height is calculated accurately at ∼2 nm (see figure 4.4D for a line profile showing this). However when we look at the image we see some 'parachuting', where the tip does not follow the contours of the sample well when scanning strands perpendicular to the fast scan direction. This occurs when the setpoint is too low for the feedback to accurately track the sample. At 70 pN, as in figure 4.4B, we record around 20% compression of the structure, and the feedback accurately traces the sample surface, as verified, e.g., by comparing the left-to-right ('trace') and right-to-left ('retrace') scan lines. In addition, the corrugation is more visible across the entirety of the plasmid in the large image. In the inset, the corrugation seems to be better resolved than in the large image. At higher forces of 190 pN, we see little evidence of corrugation, in either the main or inset images in figure 4.4C. There is significant compression, and areas where the plasmid appears very thin as it is moved by the force exerted by the tip.

The compression visible in figures 4.4A-C is shown in figure 4.4D. The heights were measured for each inset along the line marked in figure 4.4A, with a 0.5 nm width on the line profile to reduce any errors. At 40 pN, the minimum peak force, the measured height of the DNA (1.9 ± 0.2 nm) agrees with the diameter of B-DNA. At about 70 pN there is 20% compression of the molecule, this is when the corrugation is most pronounced. At up to 200 pN, the corrugation is less clear and the measured heights reduce to <1.5 nm, similar to most earlier tapping mode AFM experiments in liquid.

In figure 4.4E we plot the measured heights for a number of plasmids, measured in the same manner as for figure 4.4D. This gives rise to a clear trend in compression as a function of the applied force. This trend could be used in traditional tapping mode experiments in fluid, with the DNA molecule acting as a 'force gauge' to estimate the applied force during imaging.

Figure 4.5 shows that this effect is reversible for forces of up to 200 pN. The imaging was performed by increasing the force to 200 pN and subsequently reducing this back to the minimum force of ∼30 pN. The experiments were stopped at a maximum force of 200 pN as tip damage occurs at forces higher than this. The evidence of corrugation after imaging at 200 pN implies that at this force we can retain the sharpness of the tip.

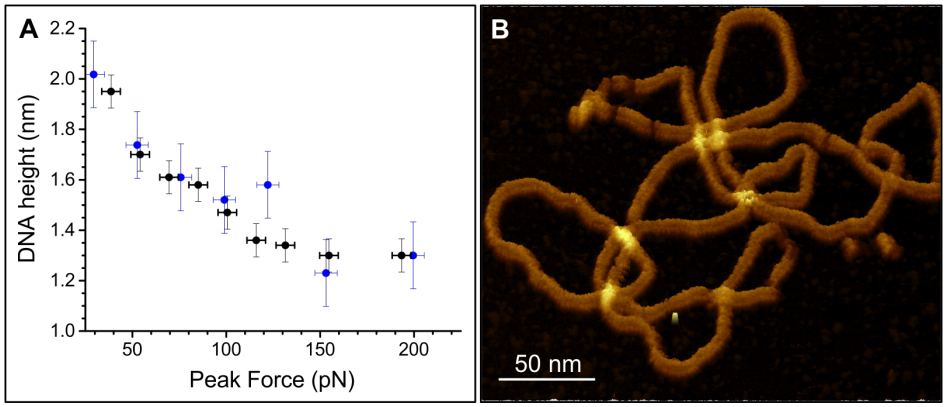

Figure 4.5: Repeatability of DNA height measurements in the AFM topography. (A) Measured height of the DNA plasmid on repeated ramps of the peak force. (B) AFM topography recorded at a peak force of 65 pN, after the two force ramps of (A), showing that the plasmid is still intact. Colour scale (see figure 4.3 for scale bar): 3.7 nm.

The data sets taken match well as expected, following the same trend as figure 4.4D. The black data points here are determined from high-magnification images for peak forces increasing from 40 to 190 pN, the blue data points were collected from lower magnification images and thus have larger error bars. This shows the repeatability of these measurements as a technique for verifying applied force in AFM experiments conducted in fluid.

4.2.3 Secondary Structure

We have established a protocol by which we can image the secondary structure of DNA using the AFM. The resolution limit of these measurements can now be probed. Figure 4.6 shows a large scale image of a DNA plasmid with corrugation. By reducing the scan size to around 80 nm, we can see the major and minor grooves of the DNA double helix structure, as in the inset.

Here we process the data further to extract structural parameters from the AFM images. Figure 4.7A shows the image shown in the inset of figure 4.6 as a complete image. A deep major groove in the structure is marked by a green asterisk, and a very shallow one by the green triangle. It is useful to have all the features aligned in one direction, i.e. to examine the variation along the backbone of the DNA. We digitally straightened the DNA plasmid in figure 4.7A, using a coordinate transformation system of (s,q,z) coordinates, where (s) represents the position along the longitudinal axis of the molecule, (q) the distance from this central axis. This method is described in chapter 3.3.1. The straightened trace (top) and retrace (bottom) images of the plasmid are shown in figure 4.7B with the same markings as A. Also shown in B, is a space filling representation of B-DNA crystal structure, generated from the PDB structure 1BNA

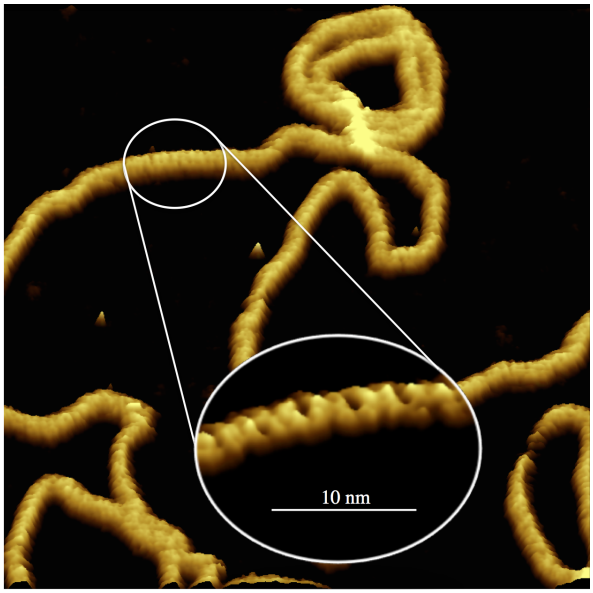

Figure 4.6: AFM topographic image of a DNA plasmid adsorbed on mica, in peak force Tapping mode showing corrugation along the plasmid which corresponds to the major and minor grooves. Inset: a higher resolution image showing the major and minor grooves of the DNA plasmid more clearly. Colour scale (see figure 4.3 for scale bar): 2 nm (main), 1.1 nm (inset).

using Chimera, which was analysed in the same way for comparison [10], [11].

To calculate the helical repeat of the DNA structure, 1D Fourier transforms were taken along each image in 4.7B, and compared in figure 4.7C using gwyddion [249]. The trace and retrace match well in their wavenumber, k, to that of the crystal structure for B-DNA, with a peak at 1.8 nm^{-1}, which corresponds to a period of 3.6 ± 0.2 nm by equation 4.1, where N is an integer value.

$$k = N(2\pi/\lambda) \tag{4.1}$$

Higher order multiple wavevectors are also visible, with the 3rd and smallest visible peak in the experimental power spectrum corresponding to the third order wave vector, indicating we have 1.2 ± 0.2 nm resolution. This level of resolution is comparable to the nanometre resolution achieved on densely packed arrays of biological samples.

The similarities in structure between the trace and retrace are visible in figure 4.7B and C. To confirm the structure is as it appears in the images, line profiles along the trace, retrace, and spacefilling representations, as marked by the dotted white lines were taken. Each line profile had a 0.5 nm width. The line profiles are shown in figure 4.7D, where trace is marked in black, retrace in blue, and the crystal structure in red, and the crystal structure has been offset by 0.8 nm for clarity. The line profiles taken

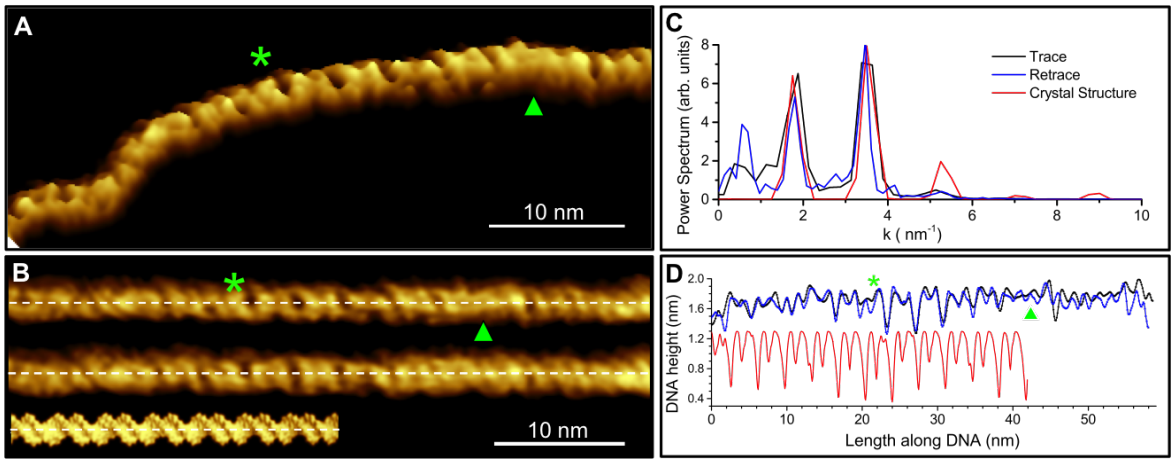

Figure 4.7: Analysis of DNA secondary structure by AFM. Green asterisks in each image mark the location of a deep major groove, and green triangles a shallow one. (A) AFM topography of plasmid DNA, displayed at a (saturated) color scale of 1.1 nm. (B) Digitally straightened trace (top) and retrace (bottom) image of A, compared with a space-filling representation of the B-DNA crystal structure. (C) Power spectra for the images in B, obtained by a Fourier transform in the horizontal direction. The black and blue lines refer to the trace and retrace AFM images, respectively; the red trace refers to a similarly processed image of the crystal structure. (D) Height profiles taken along the dashed lines in B averaged over a 5 pixel (∼0.5 nm) width. The profile of the crystal structure has been offset by ∼0.8 nm for clarity.

along the AFM images correlate to the crystal structure. In addition the deep and shallow grooves marked on the image are particularly prominent.

To further probe this apparent variation in the groove depth of the DNA, we here examine multiple images of the same area. Figure 4.8A shows the same plasmid as in figure 4.6, with the rectangle showing the location of the higher resolution scans shown in B. Figure 4.8B shows the trace and retrace for a number of consecutive scans. The direction of scan for each image is marked with an arrow, with the forwards scan being the trace, and backwards the retrace. The shallow and deep grooves appear throughout. To examine this, line profiles were taken as before for figure 4.7 along the dotted lines for each image. The line profiles are shown in figure 4.8C, with the time stamp relating directly to that on the image. The trace for each time is shown in a thick line, the retrace in a dashed line, heights have been offset for clarity. By verifying that any variations in the double helix structure of a single DNA molecule are present in both scan directions and in multiple scans over time, we can conclude that this effect is real and not a scanning related artefact.

We can accurately determine the helical repeat of the DNA, the height and therefore diameter of the DNA, and examine variations in the major and minor groove depth using AFM, however the chiral angle of the DNA is not correctly represented due to

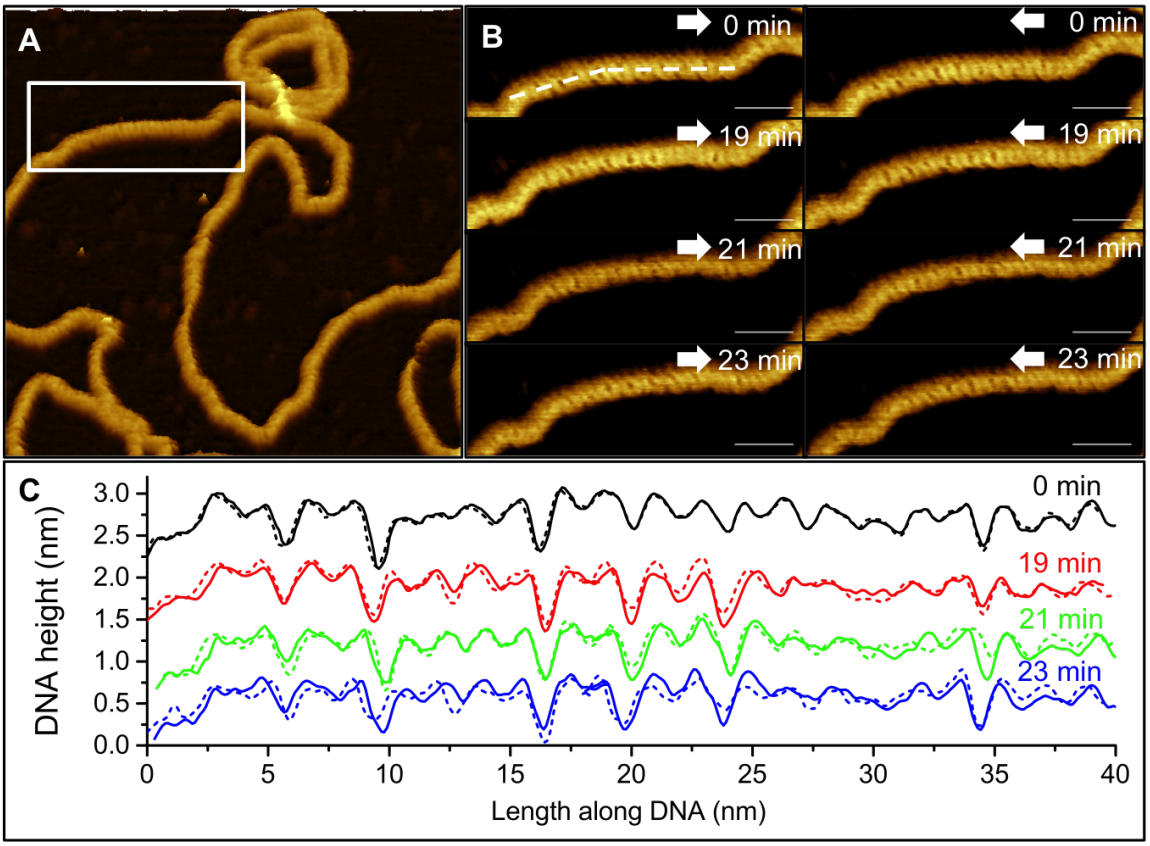

Figure 4.8: Reproducibility of groove depth variations in the AFM topography. (a) Low-magnification AFM topography of a plasmid. The white rectangle marks the area displayed in Figure 2 of the main text. (b) Higher-magnification trace (white arrow to right) and retrace (white arrow to left) images of this area, for AFM data recorded at different times. (c) Trace (solid) and retrace (dashed) height profiles taken along straight lines as indicated in b, closely following the backbone of the 4 plasmid scans and averaged over a 5 pixel (∼0.5 nm) width. The height profiles have been offset by multiples of 0.6 nm for clarity.

tip-sample convolution. The chiral angle represents the way in which the base pairs are stacked, which results in the twisting of the DNA helices. As discussed before, every AFM image is a convolution of the tip and the molecule being imaged, and this is especially apparent for the chiral angle of the DNA. Tip effects on chiral angle have been deconvoluted for carbon nanotubes [247] imaged using STM. Recently simulations of DNA have shown how the chiral angle of DNA can vary as a result of the tip shape [69]. Here we estimate the tip radius from the measured width of the DNA and deconvolute the AFM images following procedures described in section 3.3.2, and use the results to obtain an accurate value for the chiral angle of the DNA structure.

High-quality images typically yielded estimates of the tip radius of ∼1 nm. E.g., in figure 4.9, the tip radii were estimated as 1.3 ± 0.2 nm and 1.7 ± 0.2 nm in A and B,

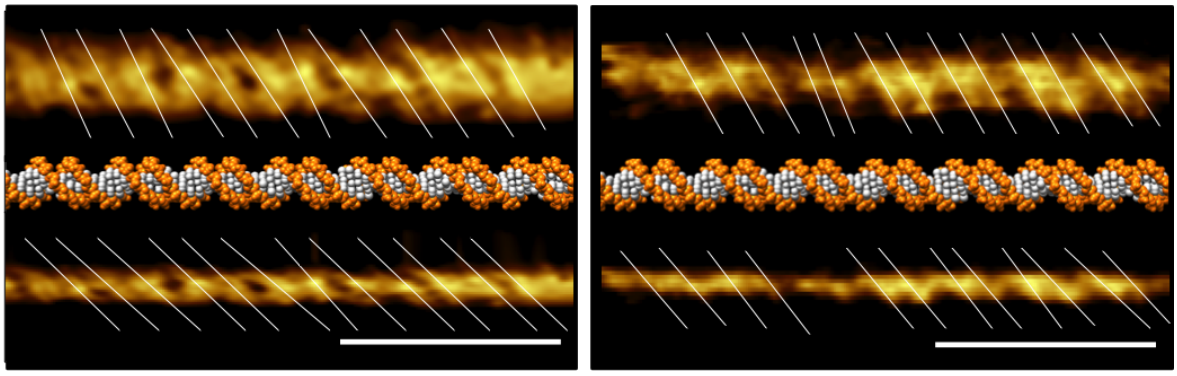

Figure 4.9: AFM topography of digitally straightened DNA segments before (top) and after (bottom) correction for the finite tip size, compared with the B-DNA crystal structure, in two different experiments. A) AFM image obtained in peak force tapping on a FastScan Bio (Bruker, CA) using FastScan DX cantilevers (Bruker CA). B) AFM image obtained in tapping mode on a Cypher (Asylum Research, UK) using AC40 cantilevers (Olympus, Japan). Colour scales: 1.1 nm. Straight lines in the AFM images mark the strands of the double helix that were used to determine the average chiral angle with respect to the longitudinal axis of the molecule.

respectively. This figure shows two AFM images before and after tip deconvolution. The top image in A, was taken on a Bruker FastScan Bio in peak force tapping mode, using Bruker FastScan-D cantilevers, with a small lever and standard silicon tip. The top image in B was taken on an Asylum Cypher in tapping mode, using AC40 cantilevers from Olympus, with standard cantilevers and silicon tips. Both of these images suffer from overestimation of the chiral angle, with A and B estimating the chiral angle at 67 ± 4° and 69 ± 3° respectively. The chiral angles calculated for the corrected images in A and B are 36 ± 4°and 37 ± 5°respectively. These values are in excellent agreement with the 36 ± 1°predicted from the B-DNA crystal structure showing that we have a method for calibrating the tip shape and deconvoluting this from the AFM measurements.

Importantly, the two images in figure 4.9 were recorded using two different imaging modes and cantilevers. This shows the spatial resolution is therefore not limited to a specific imaging mode, and more likely to be limited by common factors such as the smallest available tip radii (high-quality images typically yielded tip estimates that were considerably better than the nominal specifications), the mobility of the DNA, and the force noise in the measurements as set by thermal fluctuations.

Table 4.1 shows the dimensions measured for the molecule shown in figure 4.7, as compared with the crystal structure of B-DNA. It demonstrates that AFM can resolve the secondary structure of DNA, obtaining values for the helical repeat, molecule diameter and chiral angle in excellent agreement with the crystal structure. The major and minor groove depth tend to be underestimated, due to the tip diameter, and show

	Crystal structure	AFM
Height / diameter	2.0 ± 0.1 nm	1.9 ± 0.2 nm
Helical repeat	3.6 ± 0.1 nm	3.6 ± 0.2 nm
Major groove depth	0.8 ± 0.2 nm	0.1-0.7 nm
Minor groove depth	0.4 ± 0.2 nm	0.1 ± 0.1 nm
Chiral angle	36 ± 1 deg	37 ± 3 deg

Table 4.1: Comparison of double-helix dimensions as determined from the B-DNA crystal structure (RCSB protein data bank data file 1BNA [11] and from the AFM measurements.

variations that are reproducible between subsequent scans (figure 4.8). We also observe reproducible variations in the groove depth. Our present data do not allow us to be conclusive about the origin of these variations. They may be caused by supercoiling of the molecule. Supercoiling causes over- or undertwisting of the double helix (positive and negative supercoiling respectively), which may open up the groove sites in the case of negative supercoiling, making the major groove appear larger as seen here. Areas where the double helix is no longer visible could be explained by local negative supercoiling of the molecule. Another possible explanation lies in an uneven binding of the Ni^{2+} ions to the DNA, causing apparent variations in its helical surface structure.

4.3 Conclusion and Outlook

Here we have shown that we can use AFM to evaluate the secondary structure of a single DNA plasmid. Through accurate force control and optimisation of imaging parameters, we can visualise the secondary structure of DNA using commercial AFM systems and cantilevers.

The lateral resolution for DNA molecules adsorbed to a mica substrate using the divalent cation method is shown to be $\sim$1 nm via Fourier image analysis. While similar resolution has before been shown using the AFM in fluid, this has been on densely packed substrates such as protein arrays, where force control is less significant due to their lateral stabilisation. This resolution was achieved both in peak force tapping mode and in tapping mode on two commercial instruments. Closed loop scanning was used to achieve the highest resolution images, as at this length scale, drift effects are pronounced and have a detrimental effect on the imaging. The double helix was also resolved with open loop scanners, but the image quality was typically somewhat lower. This implies that by careful tuning of the imaging parameters in both tapping and peak force tapping modes we can minimise the applied force during imaging. This allows us to achieve high resolution imaging on DNA molecules in both of these dynamic modes. These results show tapping mode and peak force tapping to yield similar if not

improved resolution to that achioeved in the literature using FM-AFM [69], [70].

By a characterisation of image quality and biomolecule deformation by AFM over a range of forces in the 30-250 pN regime, it has been shown that there is a narrow force window at which high resolution imaging can best be achieved on DNA with the cantilevers used here. At the lowest applied imaging forces achievable using the AFM (30-40 pN), it is possible to resolve the true 2 nm height (i.e., diameter) of a DNA molecule, implying that the DNA is barely compressed at this force. By increasing the applied force to 70-80 pN, it is possible to clearly resolve the secondary structure of the DNA double helix whilst only compressing the molecule by $\sim$20%. At even higher forces of $<$100 pN the sample deformation becomes significant at up $\sim$50% and the DNA secondary structure is no longer visible. This effect is reversible, i.e., if the force is reduced, the secondary structure again becomes visible, implying that the effect is on the image resolution, and not the sample or the tip at this force, although tip contamination is more likely at higher forces.

The here found structural parameters for the secondary structure of DNA agree well with those from the crystal structure of DNA, in particular after correction of the AFM images for the finite size of the AFM tip. The here presented correction procedure includes an estimate of the tip radius from the DNA images, based on the apparent width of the DNA. In addition, these measurements allow for an examination of variations in the major and minor groove depths along longer stretches of supercoiled DNA. This intramolecular variability is inaccessible to other commonly used methods, which rely on ensemble averaging. This may be exploited for imaging higher order DNA structures such as DNA origami to provide greater information on their secondary and tertiary structure in solution during and after self-assembly.

DNA interactions with proteins are key to a number of critical biomolecular processes including replication and transcription. Many of these processes are triggered and regulated by proteins binding preferentially to either the minor or major grooves of DNA. The ability to study the secondary structure of DNA for these interactions may provide insight into the structure of DNA-protein complexes and into the role of variations in DNA structure in DNA-DNA and DNA-protein binding events for molecular recognition at the single molecule level.

Our results also indicate that DNA can be used as a 'nanometre ruler' for AFM imaging in fluid, for example to characterise the AFM tip radius during imaging and at a scale where this is hard to achieve by other methods, and as a force monitor when imaging in tapping mode, where the applied force can be less easily regulated. This method could therefore give rise to an increased accuracy for AFM imaging in fluid.

One of the most intriguing results in this chapter is the variation in groove depth along a single molecule of DNA. A possible cause of these variations is supercoiling of the

DNA. The plasmids used in this investigation are long, ∼3500 base pairs, and the supercoiling can only be determined for the entire molecule by traditional methods such as gel electrophoresis. Though most DNA in vivo is negatively supercoiled, i.e., overtwisted, the supercoiling may vary along the molecule with areas of both positive and negative supercoiling contributing to a net negative supercoiling. In addition this effect may be exacerbated by the binding of DNA to a substrate which could stabilise any variation in both supercoiling and structure. For this reason smaller lengths of DNA could be used to study supercoiling. These shorter lengths should exhibit similar supercoiling along the entirety of the molecule as shorter lengths are more highly constrained [250]. The next chapter (Chap. 5.1) shows preliminary data taken on small circles of DNA to determine whether the same level of resolution is achievable on these molecules, and therefore whether they can be used as a tool to study the interplay between supercoiling and DNA interactions by AFM.

Chapter 5

Simultaneous Imaging of DNA Secondary Structure and Supercoiling

In chapter 4 we showed that AFM can be used to visualise variations in the secondary structure of plasmid DNA. For these long DNA plasmids physisorbed onto a mica substrate, we suggested that these variations may be attributed to supercoiling. DNA supercoiling is important in a number of biological processes and is known to influence DNA replication and transcription, but the mechanism through which this occurs remains unclear. Here we present preliminary data on synthetic DNA minicircles, short circles of DNA that - because of their short and curved geometry - show well defined supercoiling. We show that we can visualise these circles in different conformations of well-defined supercoiling, and also that we can apply the high resolution imaging methods developed in chapter 4 to visualise the secondary structure of the minicircles.

5.1 Introduction

As discussed in chapter 1.5, the Watson-Crick DNA double helix has been instrumental in understanding how our genetic information is stored. Most of our structural information on DNA is based on X-ray diffraction of short and straight fragments. In the living cell, however, DNA is seldom short and straight, typically forming higher-order structures. These include supercoiled states, which arise from physical principles similar to those that cause an old-fashioned telephone cord to curl up when it is twisted . This supercoiling is key to many genetic processes, in particular through modulating how proteins bind to DNA, but the biophysical mechanisms of this modulation are largely

unknown [251]. We must therefore examine the conformation and structural variations in DNA of DNA, and the implications that this has for protein-DNA, DNA-DNA and drug-DNA interactions [120].

To examine the effect of supercoiling on DNA structure and interactions, closed loops of DNA must be used to allow for supercoiled states to be formed. Small circles of less than 500 bp (minicircles) are used as they are very tractable, containing specific binding and formation sites without the complications of large amounts of non-specific DNA [252]. An additional benefit of using small circles is the ability to isolate and examine a single supercoiled species or topoisomer, with well defined Linking number Lk. A final benefit is that at this length scale atomistic simulations of DNA structure and interactions can be performed which have aided in the interpretation of DNA experiments on flexibility, distortion and molecular recognition [253].

One of the main issues with the study of DNA minicircles in biological experiments is the difficulty of forming these short sequences, as for circles of a few hundred base pairs or less, the rigidity of the helix prevents it being easily bent into a circle [254]. Using λ-integrase recombination, minicircles of 339 bp were formed. These minicircles were shown to contain multiple topoisomers of varying degrees of supercoiling which exhibited different electrophoretic mobilities. The variation in electrophoretic mobility implies differences in the writhe of the minicircles - supercoiling is mitigated at least in part by writhing of the molecule [254].

Here these synthetic DNA minicircles are used to study the effects of supercoiling on DNA structure. As atomistic simulations would be performed on the DNA minicircles used in this study, minicircles of lengths 260 and 339 bp were chosen to minimise computational cost [253] whilst remaining above the 250 bp cutoff for the λ-integrase recombination procedure used to form the minicircles [254]. Figure 5.1 shows snapshots from atomistic simulations of 260 bp minicircles with various degrees of supercoiling [250]. The intrinsic rigidity of the minicircles due to their length results in the supercoiling being manifested in part as large scale changes in the writhe of the molecule. The degree of supercoiling in the molecule can be characterised by the number and orientation of crossings in the projected view on the minicircle [120], [255].

The minicircle structures show in figure 5.1 have Linking difference, δLk, of -2, -1, 0, $+1$ from left to right, i.e. 2 negative supercoils to one positive supercoil. This manifests as writhed changes in structure, a double crossed circle results for negatively supercoiled molecule with Lk -2, a figure of eight for negative of positively supercoiled molecules with ΔLk $+1$ and -1, and an open circle corresponding to the relaxed or non-supercoiled state with ΔLk 0.

AFM can be used to visualise supercoiling in DNA (minicircles) in a similar way as in electron microscopy experiments [256], but it is unique in its ability to image DNA

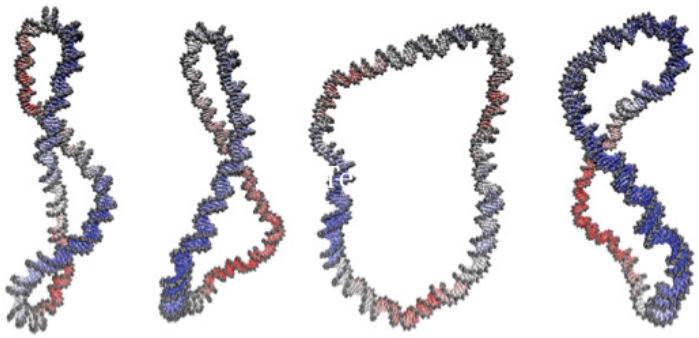

Figure 5.1: Molecular conformations sampled from atomistic simulations of 260 bp circles showing the global shape for the DNA minicircles with supercoiling increasing from -2 to +1 (left to right). Figure is reproduced from [250] with permission.

molecules at Ångström resolution in aqueous solution [68], allowing the DNA - weakly bound to a substrate - to keep changing its conformation. AFM has already been used for the real-time visualisation of polymerase moving along DNA, albeit at lower resolution [257]. Traditional methods to study supercoiling include gel electrophoresis, which allows accurate determination of the supercoiled state, but no information on the 3D conformation and cryo-electron microscopy, which provides averaged 3D structural information for conformations that cannot change.

This chapter shows preliminary data obtained on 339 bp DNA minicircles showing that we can visualise supercoiling in DNA minicircles as higher order structural conformations. We confirm this by removing any supercoiling from the molecules, and visualising the resulting conformations. In addition we show that by using high resolution AFM with accurate force control, we can image the secondary structure of DNA minicircles, even for a loosely bound molecule.

5.2 Results and Discussion

339 bp minicircles were prepared by our collaborators at the John Innes Centre using λ-Int recombination in E. coli [254]. The minicircles as prepared are known as the native species, and these contain a number of supercoiled species when prepared.

Figure 5.2 shows an acrylamide gel analysis of the native minicircles, showing the presence of multiple topoisomers of Lk -3, -2, -1, and 0 in lane 1. The gel used was 5 % acrylamide gel (29:1 acrylamide:bis) containing 10 mM $CaCl_2$ and was performed by our collaborator Michael Piperakis at the JIC. The divalent cations ($CaCl_2$ are used to screen the negative charges between the DNA phosphate backbones at crossing sites to allow the helices to cross more closely, aiding in the formation of more heavily writhed

structures which separate better on the gel.

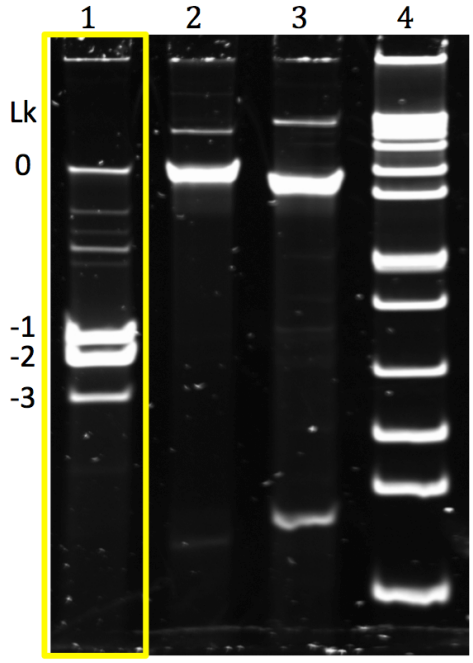

Figure 5.2: An Acrylamide gel showing the supercoiled states of the 339 bp minicircles. Lane 1 is the 339 bp in native state showing supercoiled states of *Lk* -3, -2, -1 and 0. Lane 2 contains relaxed 339 bp minicircles. Lane 3 contains nicked minicircles, with a small amount of linearised minicircles in the band at the bottom. Lane 4 is a 1 kbp ladder.

Lanes 2 and 3 show relaxed and nicked minicircles respectively. The relaxed circles are treated with type IB topisomerase which removes any supercoiling by cutting the 3' strand, which uncoils due to the torque created by the supecoiled state. When the strand no is on longer supercoiled, this is then religated by the topoisomerase, creating a topoisomer species with both strands intact and supercoiling of 0. There may be a very small amount of writhe or supercoiling in the molecule as it is re-ligated and therefore a closed circle, but this will be minimal. The nicked circles have also had their supercoiling removed using BbvCI, a nicking endonuclease that cuts one strand of the double stranded DNA, leaving the second strand free to uncoil around it removing any supercoiling creating a species containing topoisomers with supercoiling of 0. Linear DNA species were also created using NDeI, an endonuclease which cuts both strands of the DNA creating two ends which are not easily re-ligated. Linearised DNA minicircles by nature contain no supercoiling and run much faster on a gel as they are not circular, these can be seen at the bottom of lane 3 in figure 5.2.

AFM imaging was carried out in peak force tapping mode on a Multimode 8 (Bruker AXS, CA, USA) at a peak force amplitude of 5 nm,peak force frequency of 4 kHz, and force of 50 pN under buffer conditions: 10 mM HEPES, 150 mM NaCl, 5 mM $NiCl_2$;

pH 8.0, unless otherwise stated and optimised as detailed in chapter 3.2. Cantilevers used were AC40 (Olympus, Japan), MSNL-E, and MSNL-F, detailed in table 2.1.

5.2.1 Visualising Supercoiling

Figure 5.3 shows the effects of nicking, relaxing, and linearising minicircles on their conformations, as compared to the native distribution which contains a mixture of -3, -2, -1 and 0 topoisomers as shown in figure 5.2.

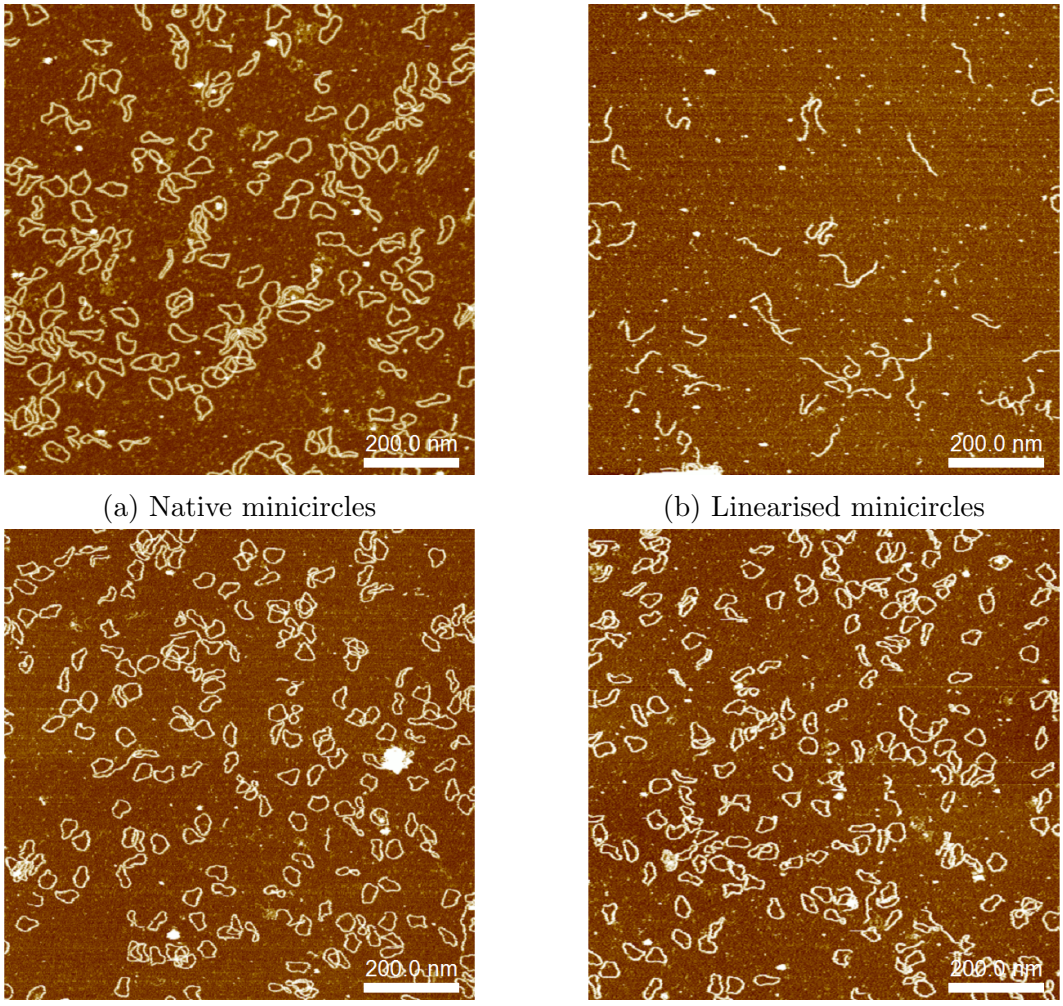

(a) Native minicircles

(b) Linearised minicircles

(c) Relaxed minicircles

(d) Nicked minicircles

Figure 5.3: AFM topographic images showing: (a) native, (b) linearised, (c) relaxed and (d) nicked, 339 bp DNA minicircles immobilised on a mica substrate using Ni^{2+} divalent cations. Colour scale (see inset in figure 5.4) 6 nm.

Figure 5.3a, shows that the native sample contains a mixture of negatively supercoiled topoisomers which adopt a large distribution of shapes. It should be noted that the

minicircles are imaged as 2D projections of their shapes by the nature of surface adsorption for AFM imaging. As 2D projections, many of these shapes may be the same configuration in solution, but adsorb as different projections.

We must first confirm that our method of substrate immobilisation and AFM imaging is appropriate to visualise the global conformation of DNA minicircles, i.e., if we are introducing extra structural configurations into the minicircles by adsorbing them to the mica. To do this, we can compare the native species with those which have been linearised, relaxed and nicked. These modified minicircles should contain only one topoisomer, and should appear as a near uniform distribution of open circles for the relaxed and nicked species.

The linearised minicircles have had both strands of the double helix cut at the same point. This should result in a linear structure with no torsional stress. As a result we would expect this strand to appear as a 339 bp long structure on the surface. Since there is no stress on the molecule, we would expect the secondary structure to exhibit the same properties as B-form DNA, with length ∼122 nm. Figure 5.3b shows the linearised DNA appearing as strands of length 120 ± 10 nm.

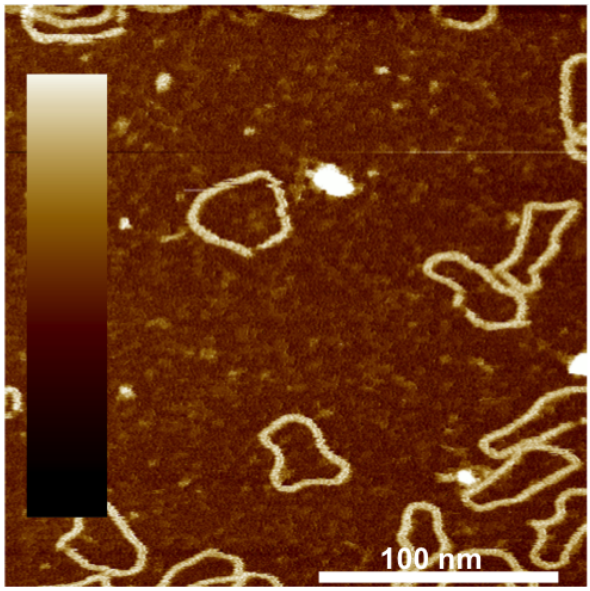

Figure 5.4: An AFM image showing possible defects in the minicircles, caused by the nicking of one strand. Colour scale: 6 nm.

The relaxed strand is cut and religated. As such it should resemble an open circle since it has no torsional stress to perturb the molecule The nicked sample has one of the strands of the double helix cut, and therefore can dissipate its torsional stress and appear as an open circle. Figures 5.3c and 5.3d show these DNA minicircles to appear mostly as open circles, with only a few in the supercoiled configuration as expected. These samples differ only by a very small torsional stress component which is too small

to visualise when imaging the molecules as a 2D projection on the mica surface. The few minicircles visible in supercoiled configurations in figure 5.3d can be attributed to non-nicked or unrelaxed DNA being present in solution, or to increased crossing of the minicircle strands mediated by the cations in solution which screen the negative charge of the strand. This is an intrinsic problem with the adsorption of DNA to mica using divalent cations.

On further imaging of the nicked species at higher resolution as shown in figure 5.3d, there appear to be defects within the nicked samples, which are not present within the relaxed species. Figure 5.4 shows images of the nicked minicircles at higher magnification. At this length scale there are discontinuities in the minicircle structure. It is possible that we are seeing the manifestation of any remaining torsion through the nicked minicircle. As one strand of the double helix is nicked, the helix is allowed to relax, the other strand rids itself of its torsional strain by unwinding the second strand. We may therefore be able to visualise the nick in the single strand of the DNA.

5.2.2 Observing Secondary Structure of Minicircle DNA

In chapter 4 we observed the helical structure of plasmid DNA under physiological conditions, visualising variations in the double helix at the single molecule level. Here we show preliminary data showing that this resolution can also be btained on the smaller minicircle structures.

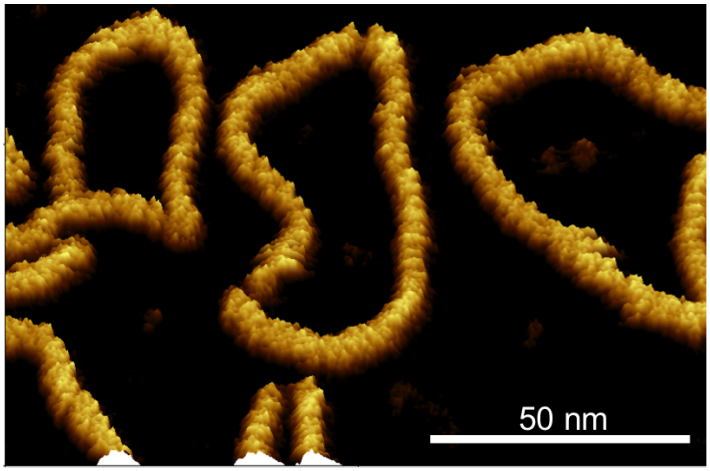

Figure 5.5: An AFM topographic image showing native DNA minicircles with corrugation corresponding to secondary structure. Colour scale (see inset in figure 5.4) 2 nm

Figure 5.5 shows three minicircles with corrugation corresponding to their secondary structure, imaged using a low (40 pN) force, in peak force tapping, optimised for

imaging as in the case of DNA plasmids in chapter 4. This allows us to look at the secondary structure by AFM in addition to the larger scale conformations of minicircles which have been visualised previously by AFM [254].

The ability to visualise secondary structure is of particular interest in monitoring DNA interactions, however, peak force tapping is limited to images in a matter of minutes, which may be too slow to monitor the process. Tapping mode AFM is faster than peak force tapping, with images obtainable in less than a minute on standard AFM's. In addition, we showed in chapter 4 that tapping mode also enables imaging of the double helix of DNA if the imaging force is precisely controlled and minimised.

To test the possibility of imaging mobile DNA minicircles, we use a homebuilt AFM [70] which actuates the cantilevers photothermally as described in section 2.3.4.2. Optical or photothermal actuation also allows for the applied imaging force in tapping mode to be better regulated, as the fluctuations in the amplitude of oscillation of the cantilever are reduced by the avoiding yje piezo-acoustic excitation. Here we also used small cantilevers which increase the time resolution of imaging whilst also reducing the thermal noise contributions, again improving stability. The cantilevers used were AC40 (Olympus, Japan) which have a resonant frequency of ∼30 kHz in liquid and a spring constant of ∼0.08 N/m as described in table 2.1. The homebuilt system has an additional advantage of being a closed loop system, the benefits of which are described in chapter 2.3.2.5, which allows us to easily mitigate the effects of drift which can contribute to reduced resolution.

Here we image loosely bound 339 bp DNA minicircles with the aim of visualising real time structural changes to the molecule whilst imaging at sub-nanometre resolution. To this end time-lapse images were taken of a 339 bp minicircle from the native species immobilised on a mica substrate using a low, 1 mM $NiCl_2$, concentration to allow for increased DNA mobility on the substrate.

Figure 5.6 shows time-lapse images of a native 339 bp minicircle as described above. The secondary structure of the molecule is clearly visible in each image as corrugation. To further examine the secondary structure across the entire molecule, and to reduce the effect of imaging artefacts, the fast scan direction was rotated in the images taken at 10 and 44 minutes. The fast scan direction is marked by a grey arrow in the bottom left of each image. The AFM tends to image more clearly when features are aligned along the fast scan direction than the slow direction, due to inconsistencies between scan lines. It is possible to visualise the secondary structure of this mobile minicircle over time.

Whilst visualising the secondary structure throughout imaging, it can be seen that there is a change in the conformation of the molecule over time. The crossing point of the two strands moving up and down the molecule. This implies that the molecule can

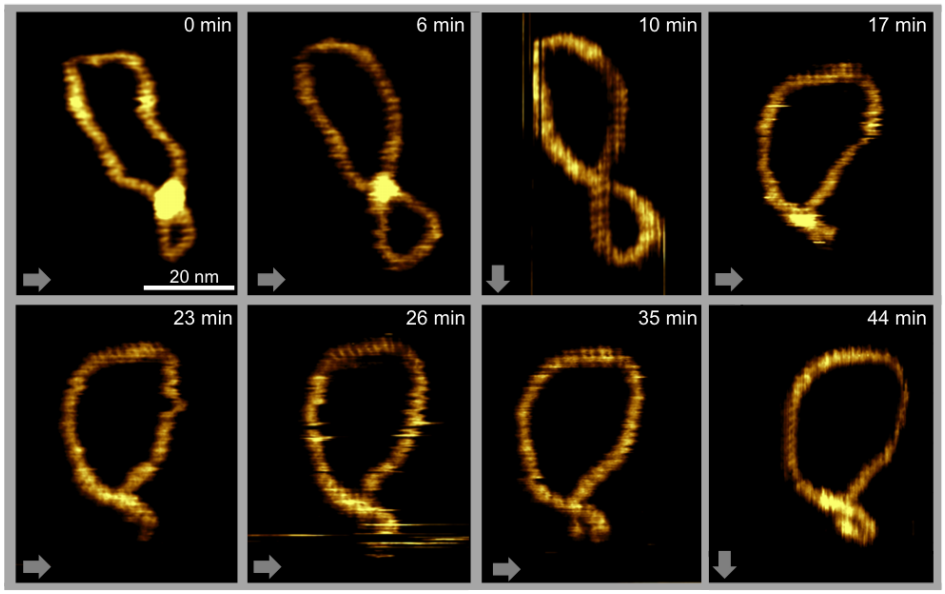

Figure 5.6: Time-lapse AFM images showing the movement of a DNA minicircle whilst resolving its secondary structure. Grey arrows in each image mark the direction of the fast scan axis. Colour scale (see inset in figure 5.4): 1.5 nm

change its conformation whilst weakly adsorbed to a substrate, which may allow for conformational changes in topology due to DNA-DNA or DNA-protein interactions to be visualised in future studies.

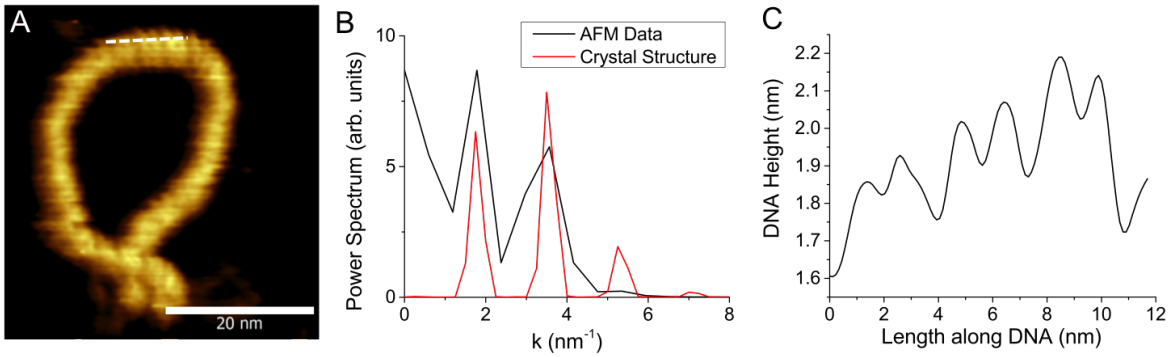

Figure 5.7: Analysis of the '35 min' image from figure 5.6. A) A high resolution image with corrugation corresponding to the double helix. B) The power spectrum of the section marked by the dotted line in A (black) as compared to that of the crystal structure for B-DNA (red). C) A line profile taken along the white dotted line clearly shows the major and minor grooves. Colour scale (see inset in figure 5.4): 1.5 nm

We can use the same methods as shown in chapter 4 to analyse the secondary structure of the DNA minicircles shown here, and gain insight into their form. The structural analysis of the '35 min' image in figure 5.6, carried out and displayed in figure 5.7

shows the double helix structure of the molecule. The corresponding line profile and Fourier transform show that the structure clearly matches that of B-DNA. This method can therefore be extrapolated for use in imaging DNA structural and conformational changes with AFM.

5.2.3 Visualising Single-Stranded DNA

Figure 5.8 shows a dimeric sample of the native 339 bp minicircles, immobilised on the DNA using $NiCl_2$ as before. Figure 5.8A shows the dimeric sample conformations, which show elements of corrugation, although they are at too low a resolution for a more detailed structural analysis.

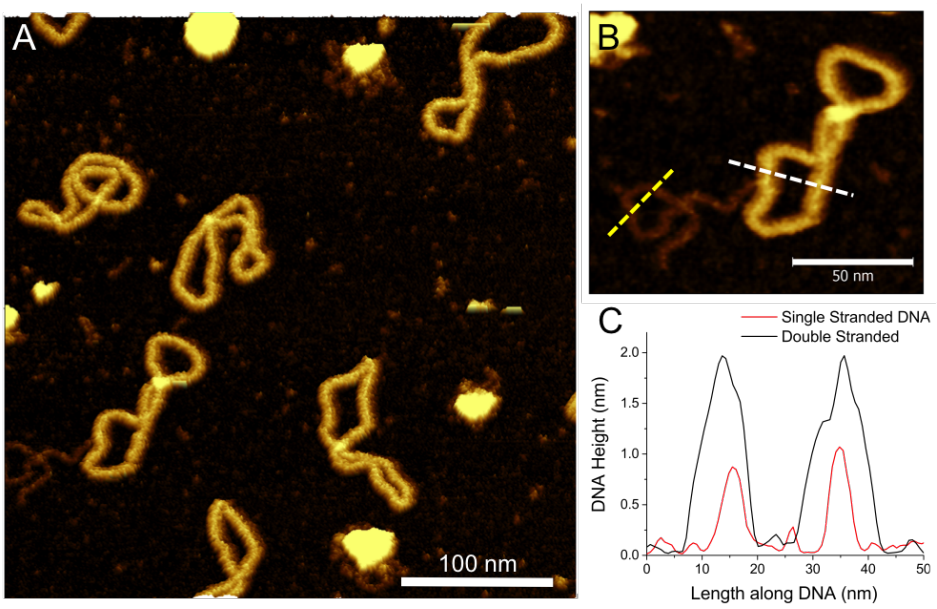

Figure 5.8: Dimeric species of the 339 bp native DNA minicircles immobilised using 5 mM $NiCl_2$. A) A topographic image of the dimeric species showing single stranded DNA attached to the double stranded dimer. B) a higher resolution image of the molecule in question showing single and double stranded DNA. C) Line profiles taken along the yellow and white dotted lines in B showing a single stranded height (red) and double stranded height (black) respectively. Colour scale (see inset in figure 5.4) 2 nm.

Figure 5.8B shows a cropped image of the dimer with single-stranded DNA attached. This remained attached throughout the imaging process, implying that it was bound to the DNA. Height profiles were taken across the double and single stranded DNA sections and are shown in figure 5.8C. These show the heights to be 2 nm and 0.6 nm for double and single stranded DNA respectively.

This demonstrates that we can clearly distinguish between single- and double-stranded DNA, and indicates that it is possible to discern height changes due to binding of single-stranded DNA to double-stranded DNA.This could be of use in monitoring DNA-DNA interactions e.g., the formation of a triplex where a single stranded oligonucleotide binds to a double stranded DNA creating a short triple stranded region.

5.3 Conclusion

Here we have shown that the high resolution imaging techniques developed to image the secondary structure of DNA plasmids adsorbed to a mica substrate by AFM [68]–[70] are applicable to smaller DNA structures in the form of minicircles. Minicircles are used as a synthetic DNA system which can be used to examine the effects of supercoiling on DNA structure [256], [258]–[260]. Previous work has shown that AFM can be used as a method to examine the writhe of a minicircle to determine its supercoiled structure [254].

These are preliminary data on DNA minicircles, visualising supercoiled topological states of the minicircle in a 2D conformation as it lies immobilised on a mica substrate. The different topological states can be identified as crossings of the DNA strands as figure eights (supercoiling of -1) or higher order twisted structures. These conformations agree with preliminary atomistic simulation data for the 339 bp minicircles, similar to those shown in figure 5.1 for 260 bp minicircles [250] and in the literature [258]. Both show open circular configurations for the relaxed minicircles, and a range of crossed and open configurations for the native species [254]. This also agrees well with gel electrophoresis which showed that there were minicircles of supercoiling 0, -1, -2 and -3 in the native species.

To extend these studies, it would be useful to examine the contour lengths of these molecules, to determine whether they deviate from the expected 122 nm length for B-DNA, and to examine any variation in length between the relaxed and supercoiled species. In addition it would be useful to examine the variations in conformation as 2D projections and calculate the number of configurations corresponding to each supercoiled configuration by crossing, and to examine how this agrees with electrophoresis and atomic simulation data.

It would also be beneficial to examine the effect of surface adsorption on the visualised DNA conformations. The divalent cations used here to mediate adsorption to the mica could give rise to additional crossings in the DNA minicircles, by screening the negative charge of the phosphate backbone, which causes electrostatic repulsion between the two strands [253]. Experiments adsorbing DNA to the substrate using a non-cation containing buffer solution would be appropriate for this study. These methods could

include: the use of cationic lipid bilayers as a secondary substrate on top of the mica surface for absorption of DNA [261]; the use of Poly-l-lysine, poly-l-ornithine, and poly-l-histidine [262]; or APS mica [111]. These adsorption methods could be used in the same way as the divalent cation adsorption method used here, and the resultant minicircle conformations compared to monitor their variation as a function of surface preparation which has been shown to heavily influence DNA conformation [130].

In addition to examining the supercoiled conformation of the molecule, we have shown that we can also probe the secondary structure of the minicircles, even for a loosely bound minicircle which changes its conformation during imaging. It is clear from figure 5.7 that we can obtain resolution clear enough to analyse the secondary structure of DNA minicirles whilst visualising changes in the larger scale conformation of the molecule using AFM, even for mobile conformations of DNA. This has applications in examining how supercoiling affects DNA interaction, including DNA-DNA interactions such as single stranded (triplex forming) DNA and DNA-binding events such as protein binding [252].

High resolution AFM could be used to study the mechanisms by which DNA supercoiling affects its secondary structure and how this influences protein binding and triplex formation as the minicircles synthesised here contain a protein binding site and a triplex formation site [254]. This could be achieved using the following specific objectives: determining how deviations from the Watson-Crick structure of DNA can be induced by supercoiling; examining how supercoiling can inhibit or promote binding of proteins and single-stranded DNA to the double helix, leading to changes in the expression of genetic material; elucidation of the interplay between protein binding and triplex formation, as a function of secondary structure

This chapter thus shows preliminary AFM data, identifying DNA minicircles as a means of increasing our understanding of the structural and dynamic diversity of DNA structure and topology, and of how its properties modulate biological processes.

Chapter 6

From Antimicrobial Peptide Design to Mode of Action

Antimicrobial peptides (AMPs) could present a novel therapeutic approach to fighting bacterial infection, a problem exacerbated by a decline in the number of antibiotics being approved for medical usage. The molecular mechanisms for the antibacterial activity of AMPs are not yet fully understood, and a greater understanding will enable the development of more effective therapeutics. De-novo peptide design represents one route to developing AMPs with higher bactericidal effects. Here AFM is used to image the effects of de-novo designed AMPs on model membranes, verifying and confirming our ability to rationally design peptides for attacking membranes according to predefined mechanisms.

6.1 Introduction

Antimicrobial peptides (AMPs) are small cationic amino acid residue chains which have been shown to exhibit broad spectrum antimicrobial activity. As described in chapter 1, antimicrobial peptides are being postulated as a new class of antibiotic. Natural AMPs are found in all multi-cellular organisms, and were first discovered in insects [145]. To date, most naturally isolated AMPs originate from amphibians and insects, with 987 and 250 identified, respectively, at the time of writing [263]. One of the most well studied peptides is cecropin, a peptide isolated from the silk moth *Hyalophora cecropia* which has shown antimicrobial activity against bacteria and fungi [264] and is discussed further in chapter 1.6.1.

AMPs have great therapeutic potential since the probability of microbial resistance developing is lower than that observed with conventional antibiotics due to the membrane

targeting nature of the AMPs antimicrobial activity [153]. AMPs have demonstrated their ability to kill rapidly a broad spectrum of microorganisms including multidrug resistant bacteria, fungi and viruses however, for these to be considered as an antibiotic treatment, the toxicity must be reduced and the bactericidal effect increased. In particular, improvements need to be made to the activity of these peptides such that they are bactericidal at sufficiently low concentrations to be considered for clinical trials [150]. The activity of an AMP can be evaluated by monitoring: the minimum inhibitory concentration (MIC), the lowest concentration of an antimicrobial that will inhibit the visible growth of a microorganism after overnight incubation; the specificity, the range of bacteria which are targeted; and resultant minimum bactericidal concentration (MBC), the lowest concentration of an antibacterial agent required to kill a particular bacterium [236].

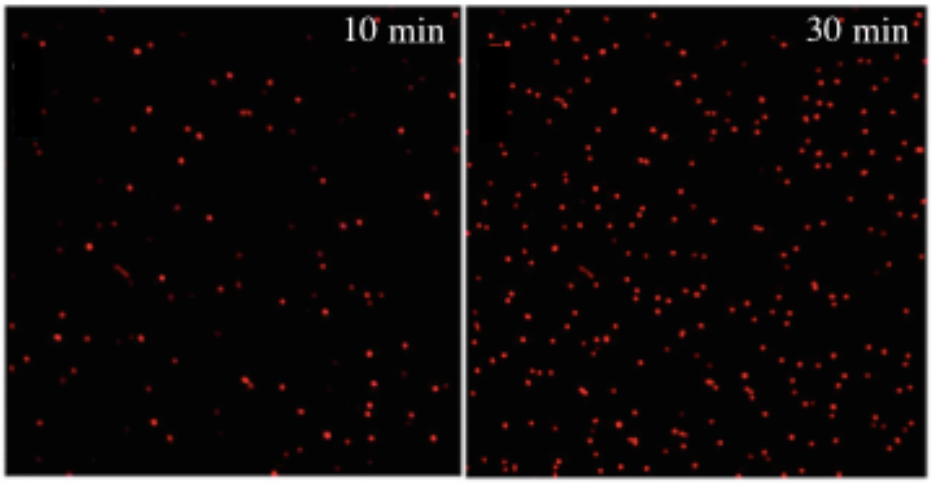

Figure 6.1: Fluorescence microscopy images of PI-stained *E. coli* cells. Incubation conditions: 10 μM Amhelin, adapted from [236].

Figure 6.1 illustrates the activity of a *de-novo* designed peptide (Amhelin) on *E-coli*. *E-coli* cells are incubated in a marker which fluoresces red on cell lysis. The increase in dead cells after 30 mins of incubation with Amhelin is clear. This clearly demonstrates the antibacterial properties of Amhelin. The cells were incubated in a (1/500) propidium iodide (PI) solution and monitored at 625 nm by fluorescence microscopy to observe any increased red fluorescence, indicating cell death [236].

To improve the antimicrobial activity of peptides we must look to the mode of action of the peptide, which is key to its antimicrobial mechanism and therefore its activity. There are a number of ways to alter the mechanism of activity: by designing *de-novo* AMP sequences which are predicted to have high antimicrobial activity or novel and targeted mechanisms of action [163]; by sequence modification, where targeted changes in the amino acid residue sequence are made to alter the mechanism of action or

increase antimicrobial activity [164], [265]; or by examining the mechanism of action for naturally occurring AMPs [153] and by examining the effect of sequence changes on their mechanism of action and antimicrobial activity [164], [265]. The *de-novo* designed AMPs used in this investigation were loosely based on a shortened version of the native peptide cecropin B which is a small antibacterial peptide from the giant silkmoth, *Hyalophora cecropia* [264].

The mechanism of action for AMPs is determined by the type, order and number amino acid residues in the peptide which form its structure [154]. Table 6.1 lists the polarity, charge and a measure of the hydrophobicity for the amino acids employed to synthesise the antimicrobial peptides. These features are used to determine what modifications should be made to each peptide sequence to alter the mode of action.

Amino Acid	Letter Code	Polarity	Charge	Hydropathy
Alanine	A	non-polar	neutral	1.8
Arginine	R	polar	positive	-4.5
Glutamine	Q	polar	neutral	-3.5
Glycine	G	non-polar	neutral	-0.4
Isoleucine	I	non-polar	neutral	4.5
Leucine	L	non-polar	neutral	3.8
Lysine	K	polar	positive	-3.9
Tryptophan	W	non-polar	neutral	-0.9
Tyrosine	Y	polar	positive	-1.3

Table 6.1: A table showing the properties of selected amino acids used in the formation of antimicrobial peptides [266].

The AMPs used in this investigation are designed using the - PPPHPPH - repeating template sequence of polar (P) and hydrophobic (H) amino acids [267]. The polar amino acids, lysines and arginines, are electrostatically attracted to the negatively charged lipid bilayer, allowing the peptide to adsorb on the surface in the S-state. It has been shown by NMR that alpha-helical peptides of this type fold from the central amino acid region to form their helical structure [236]. The PPPHPPH motif also encourages amphipathic alpha helix formation [268], placing the ith and (i+7)th residues together on the cylindrical alpha helix in an formation which separates the hydrophilic and polar residues [146], [269]. The segregated regions of each peptide are clearly visible in figure 6.2. This shows a helical representation of the peptide's alpha-helical structure as viewed from the top of the helix with one hydrophobic region, the hydrophobic core, in green, two charged regions in blue, and a neutral (or small) region in orange/red.

The insertion of the peptide in the membrane is driven by the assembly of the amphipathic helices into perpendicular stacks that close into pore-like structures which

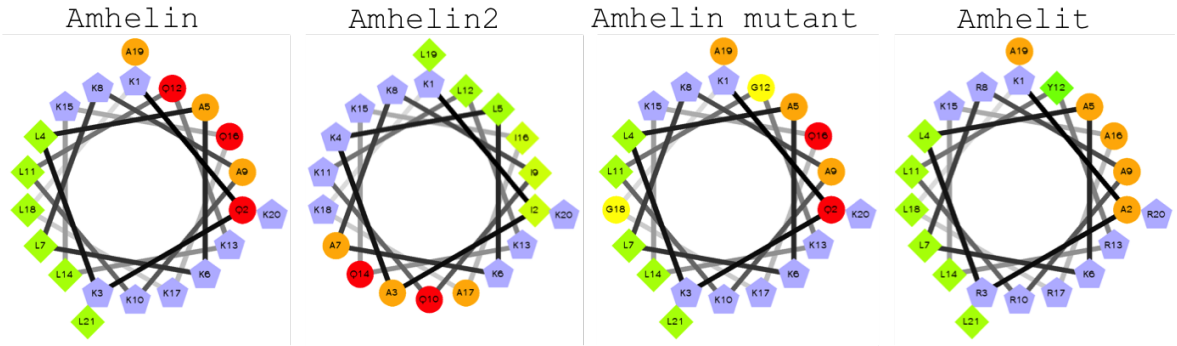

Figure 6.2: Helical representations of the synthetic antimicrobial peptides investigated here. Each amino acid residue is marked with a letter and a number describing the amino acid type and position in the sequence.

penetrate the membrane to minimise their hydrophobic interactions [270], [271]. This process is known as the insertion or I-state [272].

To investigate the effect of the primary sequence (and therefore the structure) on the mechanism of membrane disruption, we must understand how the proposed amino acid sequences determine the peptide's antimicrobial mechanism of action [268]. Figure 6.3 shows a table of the antimicrobial peptide sequences analysed in this investigation with the changes in sequence as compared to the initial peptide Amhelin highlighted.

KQKLAKLKAKLQKLKQKLAKL	Amhelin
KIAKLKAKIQKLKQKIAKLK	Amhelin2
KQKLAKLKAKLGKLKQKGAKL	Amhelin mutant
KARLAKLRARLYRLKARLARL	Amhelit

Figure 6.3: The amino acid sequences of the antimicrobial peptides investigated here with changes made as compared to the reference peptide Amhelin marked. The colours used refer to those in figure 6.2

Amhelin was designed by our collaborators at National Physical Laboratories (NPL) to porate the bilayer by a novel mechanism of action, the expanding pore state [236]. To achieve this the peptide was designed as shown in figure 6.2 and described below.

In solution Amhelin is polymorphic, containing positively charged lysines, which are electrostatically attracted to the negatively charged bacterial membrane, facilitating peptide binding on the surface in the S-state. At this point Amhelin will transform into its rigid alpha-helical amphipathic conformation. The Amhelin alpha helix as shown in figure 6.2 contains two charged lysine regions (blue), between which are a neutral region formed of small hydrophobic alanines (orange) and hydrophilic glutamines (red), and a hydrophobic leucine (green) containing region. The hydrophobicity index for leucines

as shown in table 6.1 is one of the highest. This results in Amhelin binding strongly and inserting into the hydrophobic core of the lipids to minimise any hydrophobic interactions in the I-state. In addition, the high hydropathy of the leucine region supports cooperative AMP oligomerisation whereby peptides are continually recruited into the lipid bilayer, leading to expansion of the pore due to the number of peptides recruited. This results in the proposed expanding pore state, or 'E-state'. The neutral region acts to stabilise this assembly by mediating the interaction of the peptides with the solution in the centre of the pore. This process is illustrated by the schematic in figure 6.4I.

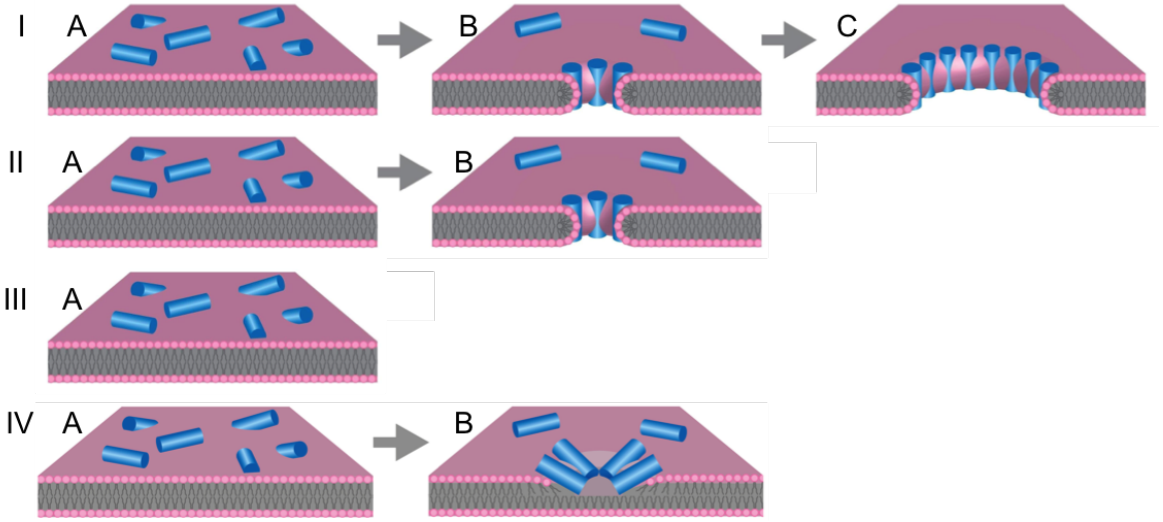

Figure 6.4: Proposed mechanisms of action for antimicrobial disruption of a lipid bilayer by Amhelin (I), Amhelin2 (I or II), Amhelin mutant (III) and Amhelit (IV) where; blue cylinders represent AMP alpha-helices and the lipid bilayer is represented by pink hydrophilic headgroups and grey hydrophobic tails. I) pore expansion mechanism: A) antimicrobial peptides bind to the surface of the membrane (S-state), B) peptides insert into lipid bilayers forming pores (I-state), C) pores expand indefinitely (E-state). II) static poration mechanism: A) antimicrobial peptides bind to the surface of the membrane (S-state), B) peptides insert into lipid bilayers forming pores (I-state). III) Non-porating mechanism: A) antimicrobial peptides bind to the surface of the membrane (S-state) and do not insert. IV) monolayer poration mechanism: A) antimicrobial peptides bind to the surface of the membrane (S-state), B peptides insert forming pores in the outer leaflet of the bilayer.

Amhelin2 is nearly identical in form to Amhelin, with a small sequence change made in the hydrophobic leucine region where three of the leucines have been substituted for isoleucines (see figure 6.3). Isoleucines have a lower hydropathic index and form lower order oligomers than leucines [266]. The formation of higher order structures is not considered key to the pore expansion process, and it is believed that Amhelin2 will disrupt the membrane via the expanding pore mechanism. This is illustrated in figure 6.4I. It is possible however that this substitution may lower the cooperativity of the

peptides resulting in the formation of static pores of fixed diameter as shown in figure 6.4II.

Amhelin mutant was created by modifying the Amhelin sequence by replacing the glutamine residue at position 12, and the leucine residue at position 18 with two glycines. The introduction of the glycines into the central part of the helix is important since the peptide forms its alpha-helical structure from this region on binding with the membrane surface. Amhelin mutant's formation of a regular helical structure is therefore interrupted by the introduction of small glycines, compromising the integrity and rigidity of the helix [268]. Amhelin mutant is predicted to not insert into the membrane as a result of this modification as shown in figure 6.4III.

Amhelit is a synthetic peptide designed to disturb the membrane by a different mechanism to Amhelin, only penetrating the outer leaflet of the membrane. This mechanism has been postulated in the literature [146]. The charged (blue) region has been modified to contain arginines in place of lysines. The introduction of more positively charged amino acids into the central region of the peptide, where it folds, results in a stronger binding between the peptide and the polar head groups of the lipid due to the increased electrostatic interaction. The neutral (orange) region has also been modified to contain only the hydrophobic alanines by replacing the glutamines with alanines. This creates a second hydrophobic region (orange) in addition to the leucine (green) hydrophobic region which will act to destabilise the peptide in the membrane. A tryptophan (green) has also been placed in the centre of the helix to encourage bending of the helix, accomodating Amhelit in the outer leaflet of the bilayer. The stronger binding of Amhelit to the membrane and the introduction of a second destabilising hydrophobic region should result in Amhelit inserting preferentially into the outer leaflet of the membrane as the inherent instabilities in its position limit full bilayer pore formation as shown in figure 6.4IV.

De-novo peptide design is a mechanism for designing novel therapeutics with predetermined antimicrobial mechanism of action and increased antimicrobial activity. In this chapter, we use Atomic Force Microscopy (AFM) to verify and confirm if *de-novo* peptide designs attack mimics of bacterial membranes according to the predefined mechanisms. To this end, we visualise *de-novo* designed peptide (Amhelin) disrupting the membrane via a predicted expanding pore state. Next, we examine how targeted changes in amino acid sequence for an AMP correlate to changes in the mechanism of membrane degradation by arresting the pore formation entirely (Amhelin mutant) or by restricting it to the outer monolayer (Amhelit). Through a better understanding of the sequence dependency of peptide effects, it is anticipated that peptides can be created as novel therapeutic agents with higher selective toxicity and increased bactericidal effects.

6.2 Results and Discussion

All peptides used here were synthesised and purified at the National Physical Laboratory (NPL) as described in chapter 3 and in [236].

All imaging is carried out using AFM under buffer conditions of 10 mM HEPES, 150 mM NaCl, 5 mM $MgCl_2$, 5 mM $CaCl_2$ pH 7.4 at 22°C unless otherwise stated. Various modes of AFM imaging were used, and as such will be stated for each investigation. The properties of all cantilevers used in this investigation are shown in figure 2.1.

6.2.1 Characterisation of a Supported Lipid Bilayer

As discussed in chapter 1.6, the mechanism of action for most antimicrobial peptides is electrostatically driven by their cationic nature [150]. Bacteria exhibit an overall anionic charge, since they contain an anionic cell membrane, cell wall, and for Gram-negative bacteria, lipopolysaccharide coat [273]. Bacterial cell membranes contain 20-25% of negatively charged lipids including phosphatidylglycerol and cardiolipin [274]. Bacterial membranes contain on average 30% PG, an anionic lipid, although this varies greatly between bacteria. The remaining lipid composition is formed mainly of uncharged lipids, principally phosphatidylethanolamine (PE) [275]. In contrast eukaryotic cells contain 20-50% phosphatidylcholine (PC).

Supported lipid bilayers (SLBs), also known as model membranes, are model systems used to study the structure and function of membrane bound and membrane active biomolecules at the nanoscale using AFM [5], [59], [144], [160], [179], [234], [276]–[278]. Here we form supported lipid bilayers to mimic bacterial cell membranes, as described in chapter 3.1.3. Model membranes are used to obtain the flat featureless surfaces required to observe membrane disruption by AMPs at the nanoscale, allowing for the observations of pores which may be only a few nanometres wide.

In these studies bilayers were formed of composition DLPC:DLPG in a 3:1 (w/w) ratio as described in chapter 3.1.3 to maintain a similar level of anionic charge to bacterial membranes. The vesicle fusion method was used as described in 3.1.3.2 to form a single bilayer on the mica [176]. The use of DLPC in place of the more commonly occurring PE in bacterial cells was chosen due to its fluid form at room temperature, the fact that it has the same chain length and therefore height as its DLPG counterpart and also to complement other studies. DLPG and DLPC lipids both form bilayers in the fluid phase at room temperature due to their gel to fluid transition temperatures which are significantly lower than room temperature at -1°C and -3°C respectively. As these lipids have equal chain length, they will form a flat bilayer of one continuous height for AFM studies. In addition other studies such as molecular dynamics simulations, NMR,

and nano-sims, were carried out on the same peptide using this lipid composition as described in [236].

AFM imaging is carried out in contact mode on a JPK Nanowizard 1 using MSNL-C and D cantilevers ($k = 0.03 - 0.05$) in buffer solution to determine the presence of a bilayer on the mica surface. The AFM image of the surface in figure 6.5D shows a flat featureless substrate, identical to a flat featureless mica surface, shown in figure 6.5B, and as such further experiments must be done to prove the presence of a bilayer on the surface prior to the addition of peptides.

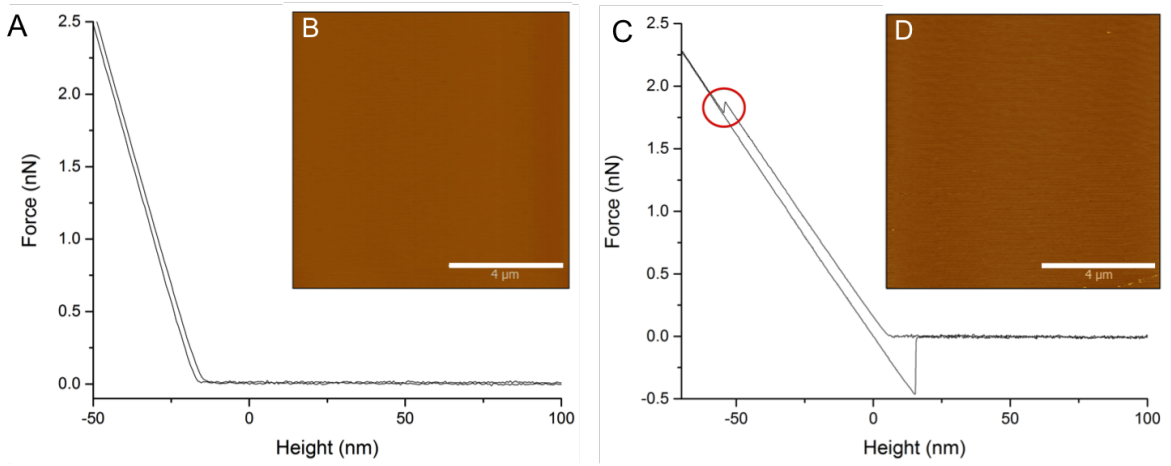

Figure 6.5: Verification of the presence of a DLPC:DLPG (3:1) lipid bilayer on a mica surface by AFM. A) A force curve taken on a mica surface. B) A contact mode AFM image of a mica surface. C) A force curve taken on the DLPC:DLPG (3:1) lipid bilayer surface with a breakthrough event (marked by the red circle) confirming the presence of the lipid bilayer. D) A contact mode AFM image of a supported lipid bilayer.

Force spectroscopy can be used to measure the mechanical properties of a surface by indenting or deforming the surface with the AFM tip. For force spectroscopy, the tip is approached to and retracted from the surface, and while measuring the force exerted by the sample surface. To measure this force, the deflection of the cantilever is monitored and converted into a force using the spring constant of the cantilever. Figure 6.5A shows a force curve taken on mica, versus the motion of the sample surface ('piezo height'), while the AFM topography images of the surface is shown in figure 6.5B. The region of zero force is where the tip is not interacting with the sample. The section of increasing force is where the tip is pushing on the mica substrate and the cantilever is bending as a result of the interaction. This can be directly compared to figure 6.5C, where after the zero force region, the tip pushes on the lipids, elastically deforming them before breaking through the bilayer as the force exerted by the tip ruptures the membrane and pushes on the mica substrate [234]. The presence of a breakthrough in the force curve allows us to confirm the presence of a bilayer on the mica surface,

while the topography appears similarly flat (figure 6.5D). This breakthrough occurs in the low nN regime as expected for a fluid phase bilayer of short chain length [278].

Having confirmed the presence of a bilayer on the surface, we must now confirm that we can image the surface under buffer conditions with no damage to the sample, to ensure that any effects observed on the membranes are a result of the membrane disruption by the antimicrobial peptides and not due to the tip-surface interaction. A DLPC:DLPG (3:1) bilayer was again prepared as outlined in section 3.1.3. The lipid bilayer was then imaged in contact mode on a JPK Nanowizard 1 using MSNL-C and D cantilevers ($k = 0.03 - 0.05$) in a buffer solution for an hour. Figure 6.6 shows no disruption to the bilayer occurring over a period of 50 minutes of imaging under these conditions. The use of calcium and magnesium cations in solution promotes the adsorption of the lipids to the mica in a more stable conformation with greater surface coverage by screening the electrostatic repulsion between the negatively charged mica and the negatively charged lipids [242]. The use of divalent and monovalent cations can also affect the antimicrobial peptides, reducing their efficacy. However, the action of antimicrobial peptides in the presence of salt is anyway important, as this represents more physiologically relevant conditions (e.g., 1-2 mM Ca^{2+}, 1-2 mM Mg^{2+} and 100-150 mM NaCl) [150].

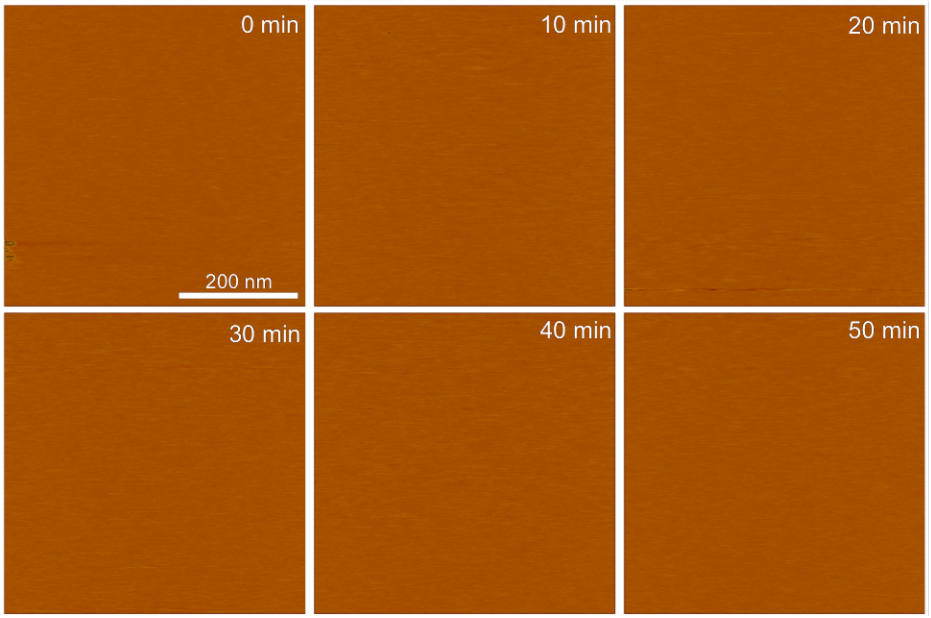

Figure 6.6: AFM images of a DLPC:DLPG (3:1) lipid bilayer surface imaged in buffer solution over the course of an hour.

This flat lipid substrate must be both reproducible and unaffected by the movement of the cantilever during AFM imaging. Having confirmed by control experiments that the bilayer is not disrupted by AFM imaging, we can inject antimicrobial peptides into the fluid cell to examine their effect on the lipid bilayer and evaluate the mechanism

of disruption by AFM.

6.2.2 Amhelin

Amhelin was designed to disrupt lipid bilayers by an expanding pore mechanism. To verify the mechanism of action for Amhelin, a supported lipid bilayer was formed on the mica substrate and imaged in contact mode on a JPK Nanowizard 1 using MSNL-C and D cantilevers ($k = 0.03 - 0.05$). The force was constantly adjusted by reducing the setpoint to compensate for drift. By ensuring the cantilever was on the point of lifting off the surface it is possible to minimise the applied force when imaging, however due to the raster scanning nature of contact mode imaging, the lateral forces remain high.

Amhelin was injected into the fluid cell at a final concentration of 0.5 μM. This is a lower concentration than those obtained in MIC studies, to reduce the speed of disruption to the membrane surface by Amhelin. This lower concentration should enable visualisation of the kinetics of the mechanism of poration. The formation of pores is clearly visible across the surface in figure 6.7A.

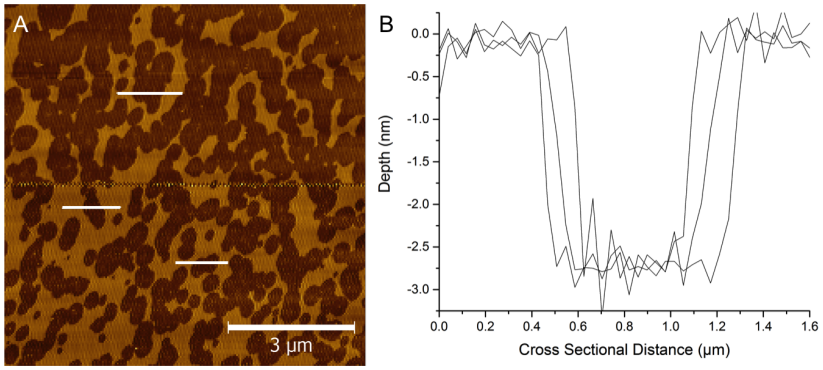

Figure 6.7: A) An AFM image of a negatively charged DLPC:DLPG (3:1) lipid bilayer surface imaged in buffer solution showing poration by 0.5 μM Amhelin B) Line profiles taken along the lines marked in figure 6.7 showing the depth of poration of the lipid bilayer.

To investigate the depth of the pores, we can take a line profile across the image, showing the height of the surface at each point. To take an accurate depth measurement we must ensure the tip can fully penetrate the pore. A scan was therefore taken of an area which displayed large pores. This image, figure 6.7 was then analysed to calculate the poration depth. Line profiles are taken using Gwyddion [249] for a number of pores in figure 6.7 as marked by the white lines, these are shown in figure 6.7B.

The pore depth is measured to be 2.8 nm from the graph in figure 6.7B. This is ~85% of the expected bilayer height of 3.15 nm. This apparent lack of height could be explained in many ways; there could be salt deposits or other contaminants that could result in

this higher level of mica surface, or our tip could be compressing the soft bilayer in the fluid phase by ∼10%. It is difficult to distinguish which of these effects is responsible for this apparent height difference, but given the close agreement of the measured depth to the bilayer thickness, we can be certain that the bilayer is fully porated.

The pores observed in figure 6.7 show that Amhelin porates the bilayer, forming pores of various sizes. This indicates that the peptides may not only bind to the membrane and insert to form pores, but also continue to expand in the membrane. To visualise the dynamics of the pore expansion process in the lipid bilayer, the experiment was repeated multiple times. This is made more complex by the presence of local concentration gradients, leading to concentration variations across the sample. At nominally the same concentration, some areas of the surface may experience more degradation than others. This can result in areas with little effect being monitored, while there may be a large effect on the surface at other locations on the surface.

Figure 6.8 shows the effect of 0.5 μM Amhelin on a supported bilayer, with the concentration empirically defined to tune the kinetics of membrane degradation to rates that are accessible by conventional AFM. The progression from the flat lipid bilayer shown on the left, prior to treatment with Amhelin, to the complete removal of the bilayer on the far right via the pore expansion state can be seen as was described previously.

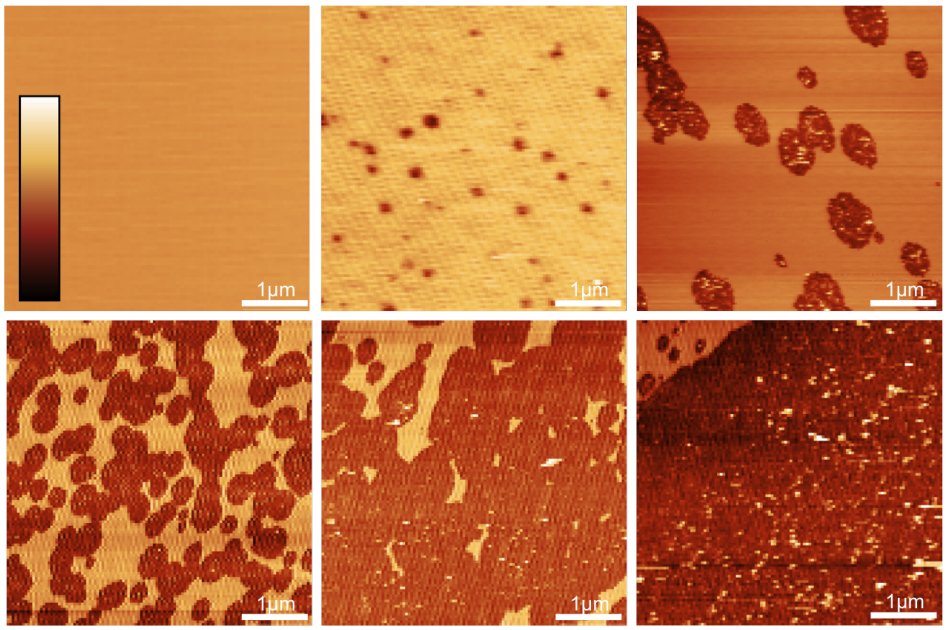

Figure 6.8: AFM imaging showing the expanding poration of a negatively charged DLPC:DLPG (3:1) lipid bilayer in buffer solution induced by Amhelin. The first image shows the bilayer prior to treatment with Amhelin. Subsequent images show the effect of 0.5 μM Amhelin on lipid bilayer surfaces, showing significant variation in pore size. Colour scale (see inset): 3 nm (1st two images); 9 nm (all others).

In summary, we have monitored effect of Amhelin on the lipid bilayer by AFM. We

have verified that Amhelin porates the bilayer via the expanding pore state as designed. We have also found a concentration range within which we can observe the kinetics of its antimicrobial action on lipid bilayers. We will now examine the effect of sequence changes on the mechanism of action of the peptide, using Amhelin as a control for comparison of the poration mechanisms.

6.2.3 Amhelin2

Amhelin2 is similar in sequence to Amhelin, with three isoleucines substituted in place of leucines. This change is small as both amino acids have similar properties (see table 6.1 for detailed properties). The main difference is that isoleucines form dimeric structures, whereas leucines form trimers and higher order structures. Isoleucines were introduced in place of leucines to examine whether the formation of higher order structures is key to the pore expansion process. The lower order structure formation could lower the cooperativity of the peptides for pore formation resulting in static pores of fixed diameter as shown in figure 6.4IIB.

Amhelin2 should form pores, if these pores expand we can see that the formation of trimers and higher order structures by leucines is not a requirement for the expanding pore state.

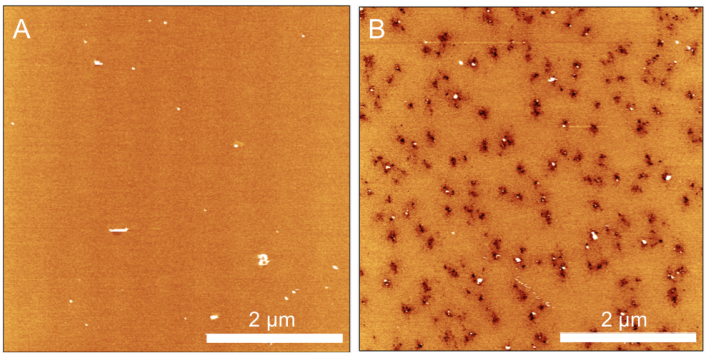

Figure 6.9: AFM images of the poration of negatively charged DLPC:DLPG (3:1) lipid bilayers by Amhelin2. A) The bilayer prior to the addition of Amhelin2, B) The bilayer after treatment with Amhelin2. Colour scales (see figure 6.8 for scale bar) from left to right: 3 nm, 6 nm, 8 nm. Amhelin2 concentration: 1.3 μM.

Figure 6.9 shows AFM measurements of the effect of Amhelin2 on supported lipid bilayers at a concentration of 1.3 μM. The left hand image shows the bilayer prior to treatment with Amhelin, showing a flat bilayer. These measurements were taken in tapping mode on a Cypher using AC40 cantilevers (Olympus, Japan) (k=0.08 N/m). Figure 6.9A shows the bilayer prior to treatment with Amhelin2, showing a flat featureless bilayer. Figure 6.9B shows the bilayer after treatment with Amhelin2, showing poration of the lipid bilayer with visible variation in pore diameter. This implies the

formation of expanding pores, where peptides are continually recruited to the pore as seen for Amhelin in figure 6.7.

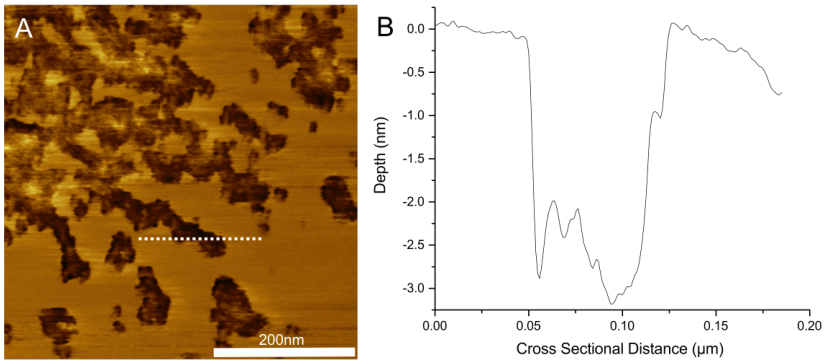

Figure 6.10: Poration of negatively charged DLPC:DLPG (3:1) lipid bilayers by Amhelin2. A) An AFM image of the lipid bilayer after treatment with Amhelin2. B) A depth profile taken across the marked line (A) showing poration depth of 3 nm, indicating bilayer poration. Colour scales (see figure 6.8 for scale bar): 6 nm. AMP2 concentration: 1 μM.

We can take a cross section across the pores to determine whether Amhelin2 fully porates the bilayer, as done for Amhelin. Figure 6.10A shows an AFM image of the effect of Amhelin2 on supported lipid bilayers, similar to figure 6.9. The image is taken at higher resolution to ensure there is sufficient pixel resolution for the cross section to probe the full depth of the pore. The graph in figure 6.10B is a line profile taken along the dotted line in the left hand AFM image. The line profile shows the depth of poration to be 3 ± 0.3 nm. This depth implies that Amhelin2 forms pores which span the bilayer in the same manner as Amhelin.

We can conclude from these results, which show Amhelin2 behaving in a very similar manner to Amhelin, that the formation of higher order structures by leucines is not central to the pore expansion process.

6.2.4 Amhelin Mutant

Amhelin mutant differs from Amhelin by the introduction of two small glycines in the central part of its sequence. This change reduces the rigidity of the helical structure for Amhelin mutant, which is predicted to inhibit the insertion of Amhelin mutant into the bilayer. We therefore predict that Amhelin mutant will not form pores.

Figure 6.11 shows an AFM image, taken on a Multimode 8 in peak force tapping mode using AC40 cantilevers (Olympus, Japan), showing the effect of 2.5 μM Amhelin mutant on a supported lipid bilayer. The concentration is at least double that used in other experiments to ensure that we are not below the critical concentration for

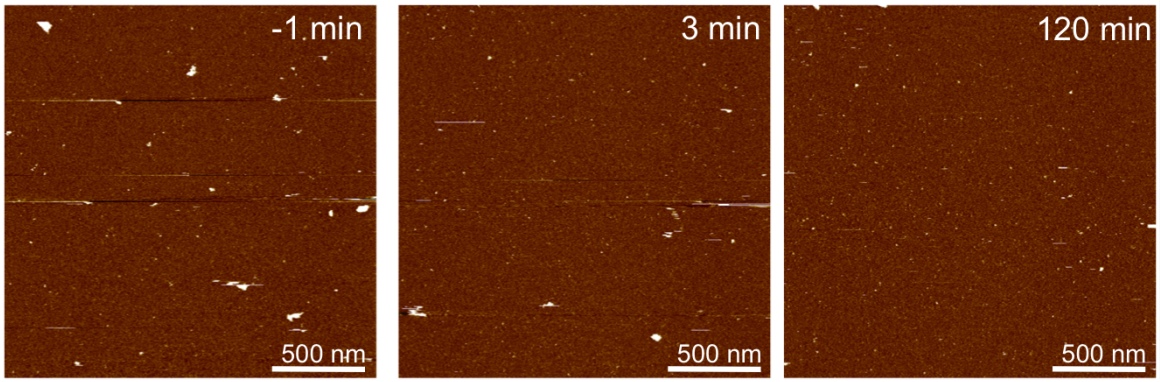

Figure 6.11: AFM images showing no change in the surface of a DLPC:DLPG (3:1) lipid bilayer over 2 hours of imaging in a solution containing Amhelin mutant. Colour scale (see figure 6.8 for scale bar): 6 nm. Amhelin mutant concentration: 2.5 μM.

membrane degradation. There appears to be no surface change during 120 minutes of imaging. Any surface deposits shown in the images were also present in the left hand image, taken before the addition of the Amhelin mutant.

Amhelin mutant exhibits no surface effect at a concentration of 2.5 μM, a concentration higher than that used for other experiments of this type. This is consistent with our prediction that the insertion of glycines in the central part of the peptide disrupts this helix. The disruption to the helix is significant enough to stop the peptide porating the bilayer. This implies that Amhelin mutant exhibits minimal antimicrobial activity.

6.2.5 Amhelit

Amhelit is designed to disturb the membrane by a different mechanism to Amhelin, only penetrating the outer leaflet. This mechanism has been postulated in the literature [146]. The Amhelin sequence has been modified to encourage this mechanism of action creating Amhelit via: a stronger electrostatic interaction with the lipids through the introduction of arginines in place of lysines; the introduction of a second destabilising hydrophobic region of alanines in place of a neutral alanine-glycine region; and the introduction of a bulky tyrosine in the centre to allow Amhelit to adopt a bent conformation in the membrane. These sequence modifications should combine to result in Amhelit inserting preferentially into the outer leaflet of the membrane, with inherent instabilities in its position which limit full bilayer pore formation.

The effect of Amhelin on the membrane was monitored using peak force tapping AFM on a Multimode 8 using AC40 cantilevers (Olympus, Japan) at an applied force of $\sim$50 pN. Figure 6.12 shows the effect of Amhelit on a lipid bilayer at a concentration of 1.8 μM. The left hand image shows the lipid bilayer as a flat substrate prior to the insertion

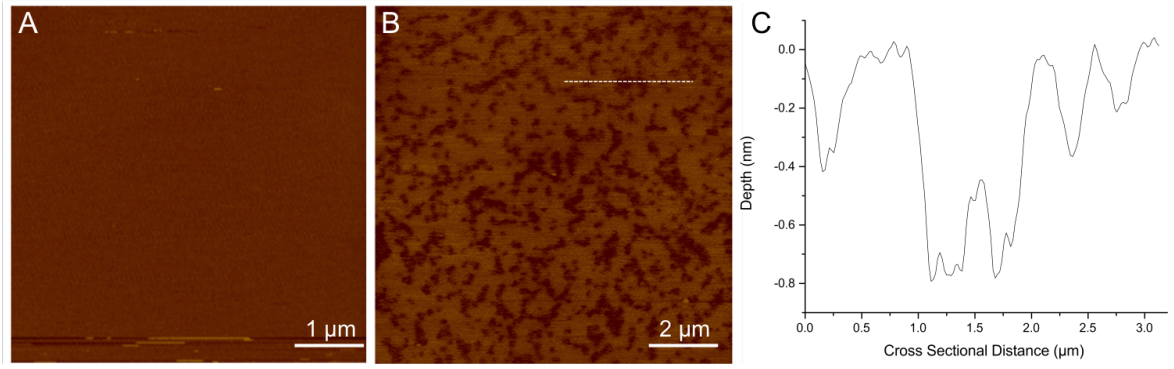

Figure 6.12: AFM images showing the effect of the peptide Amhelit on a negatively charged DLPC:DLPG (3:1) lipid bilayer. A) An AFM image of the lipid bilayer prior to the addition of Amhelit showing a flat surface. B) An AFM image taken after the addition of 1.8 μM Amhelit showing poration of the surface. C) A line profile taken along the dotted line in (B) showing the depth of poration to be 0.8 nm, corresponding to monolayer poration. Colour Scale (see figure 6.8 for scale bar): 6 nm. Amhelit concentration: 1.8 μM

of Amhelit. The central image shows pores of varied size across the lipid bilayer after treatment with Amhelit. The graph on the right shows a line profile taken across the dotted line in the central image. This line profile shows the depth of poration as 0.8 ± 0.3 nm (excluding the significantly lower depths that are found for smaller pores, where the tip size becomes a limitation). This is less than half the 3.2 nm depth of the bilayer.

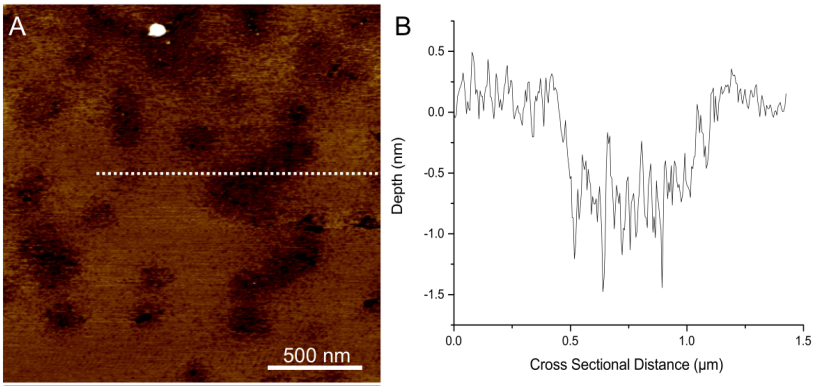

Figure 6.13: A) An AFM image showing poration of a negatively charged DLPC:DLPG (3:1) lipid bilayer by Amhelit. B) A line profile taken along the dotted line in A showing the depth of the pore formed by Amhelit. Amhelit concentration 1.8 μM. Colour Scale (see figure 6.8 for scale bar): 3 nm.

Figures 6.13 and 6.14 show AFM images of pores formed by Amhelit in the lipid bilayer at two concentrations. The image in figure 6.13 shows a large pore in the bilayer. The graph shows a line profile taken along the dotted line in the image. The pore depth is shown to be 1 ± 0.3 nm. There are small pores visible in the lipid membrane with

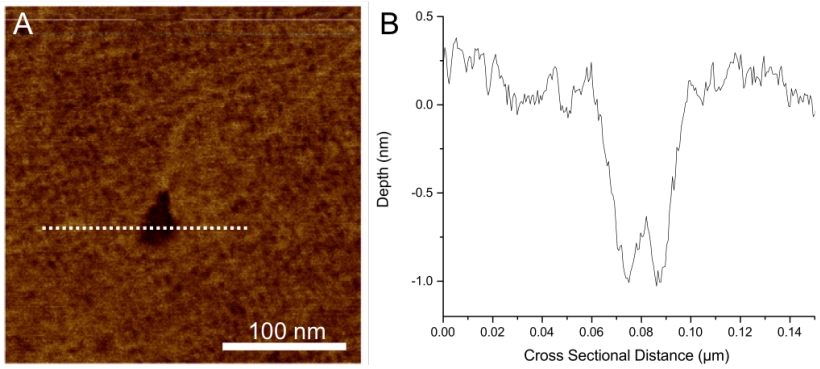

Figure 6.14: A) An AFM image showing poration of a negatively charged DLPC:DLPG (3:1) lipid bilayer by Amhelit at higher resolution than figure 6.13. B) A line profile taken along the dotted line in A showing the depth of the pore formed by Amhelit. Amhelit concentration 1.8 μM. Colour Scale (see figure 6.8 for scale bar): 3 nm.

greater numbers around the edges of the larger pores. Figure 6.14 shows an AFM image of these smaller pores. The small pores are too narrow to be probed to their full depth by the AFM tip due to its radius, which is too wide to fully insert into the pore. There is an area with a larger pore visible and the graph shows a line profile taken along the dotted white line in the image. The pore depth for this is measured as 1 ± 0.3 nm. Both measurements of pore depth agree with the measurements taken previously in figure 6.12 and are less than half the bilayer depth of 3.2 nm.

We have shown that Amhelit disrupts the bilayer forming pores of depth $\sim$1 nm. This indicates that Amhelit only disrupts the upper monolayer of the lipid bilayer as predicted.

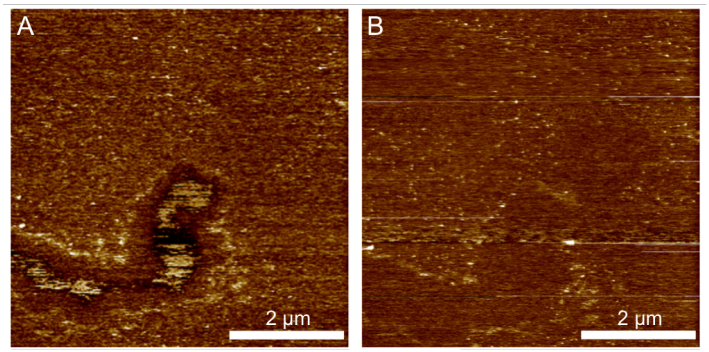

Figure 6.15: Two consecutive AFM images of negatively charged DLPC:DLPG (3:1) lipid bilayer after treatment with Amhelit. A) A pore created by Amhelit in the lipid bilayer, B) A subsequent image showing the pore visible in A has been filled in. Colour Scale (see figure 6.8 for scale bar): 3 nm. Amhelit concentration: 1.8 μM

Figure 6.15 shows two consecutive AFM images of a membrane porated by Amhelit. The left hand image shows a lipid bilayer with a pore formed by Amhelit. The right hand image was taken 3 minutes later showing the same area of the bilayer, with the

pore having been filled in. The edges of the pore are still visible however the bilayer is complete across the surface.

The pores created by Amhelit appear less stable than those created by Amhelin. This may be attributed either to the unstable position of Amhelit in the top monolayer of the membrane which allows the fluid lipids to flow into the pore, or to any removed lipids in solution re-adsorbing onto the exposed monolayer. This effect may be artificial and induced by the monolayer which would not be in a stable configuration if it were not bound to the mica support.

It should be mentioned that there are added difficulties with visualising the lipid monolayers when imaging in peak force tapping. The nature of the hydrophobic surface, and the interaction with the tip during each force curve can result in the tip pushing through the monolayer and imaging the surface underneath. This effect is more pronounced at small scan sizes where the tip is interacting for longer periods of time with a given area of the sample. This is shown in appendix D.

6.3 Conclusion

Here we have used AFM to verify that the synthetic peptide, Amhelin, which was designed to include the properties of cationic, helical antimicrobial peptides, forms expanding pores as proposed. Pores formed by Amhelin in supported lipid bilayers are not limited to a particular diameter, but exhibit a wide variation in size. This is visualised in AFM images of lipid bilayers treated with Amhelin, which show variation in pore diameter across the surface. These pores can expand laterally from nanometres to micrometres, resulting in removal of the entire membrane. The increase in pore size is shown by AFM images which show a map of the process, from the formation of nanometre sized pores, to the removal of the bilayer via the expanding pore state. These results are a basis for better understanding of membrane poration by antimicrobial peptides, and show a novel expanding pore state which can be understood as cooperative and continuous as peptides are recruited within the lipid bilayer.

Figure 6.16 summarises the different types of activity on the membrane by Amhelin, Amhelin2, Amhelin mutant and Amhelit.

Amhelin2 was designed to investigate the effect of oligomerisation on cooperativity. Leucines were substituted for isoleucines, which have lower hydrophobicity and oligomerise in dimers. By limiting the oligomerisation of the peptide from higher order structures to dimers, and therefore lowering the cooperativity we may have reduced Amhelin2's ability to form expanding pores. Here we show that Amhelin2 can also form membrane spanning pores which expand, as shown in figure 6.4I, which implies

Antimicrobial Peptide	Sequence	Mode of Action	Poration
Amhelin	KQKLAKLKAKLQKLKQKLAKL	Expanding Pore	Bilayer
Amhelin2:	KIAKLKAKIQKLKQKIAKLK	Expanding Pore	Bilayer
Amhelin mutant:	KQKLAKLKAKLGKLKQKGAKL	Non Porating	
Amhelit:	KARLAKLRARLYRLKARLARL	Poration	Monolayer

Figure 6.16: A table showing the mode of action for membrane degradation by the antimicrobial peptides discussed in this chapter

that higher order oligomerisation is not a pre-requisite for the expanding pore state.

Amhelin mutant was shown to exhibit no membrane disruption activity at concentrations close to those expected. The mechanism of action for Amhelin mutant was altered from that of Amhelin by inserting glycines into the central region of the peptide where the peptide folds into its helical conformation. This reduces the rigidity of the Amhelin helix, which prevents it inserting into the membrane in the I-state, therefore resulting in a non-porating mechanism where the peptides remain in the S-state. This is shown in figure 6.4III.

Amhelit was designed to porate in a similar manner to Amhelin, however to porate only the outer leaflet of the bilayer. This novel mechanism was postulated in the literature and is referred to as monolayer poration. The mechanism of action was altered both by introducing a second hydrophobic region formed entirely of alanines, and also by increasing the electrostatic interaction between the peptide and the membrane. Using the imaging techniques developed for imaging DNA at high resolution, pores as small as 10 nm were imaged in the membrane, and a second novel mechanism of action - monolayer poration was confirmed, a schematic of which is shown in figure 6.4IV.

There are a number of complications in imaging disrupted membrane surfaces, these include both local concentration variations, which can affect the surface activity of the peptides and the depletion of surface active peptides which can arrest the process. The use of imaging techniques developed on DNA, for imaging at low force and high resolution enabled the visualisation of more complex poration states, including the visualisation of the removal of the outer lipid monolayer. This was achieved by being able to continually monitor the same area of despite large fluctuations in the fluid cell.

These results aid in or understanding of the structure-function relationship between amino acid sequence and antimicrobial peptide mechanism of action. We have visualised multiple mechanisms of action for antimicrobial peptides, following *de-novo* peptide design and subsequent strategic substitutions. These results therefore verify the *de-novo* peptide design rationale whilst offering a mechanistic basis for designing

more effective antibiotics.

The following chapter builds on this understanding to explore how we can alter and improve the properties of naturally occurring antimicrobial peptides through sequence modifications as an alternative route to obtain novel antibiotics.

Chapter 7

Manipulating Native Peptide Sequences to Affect Their Mechanism of Membrane Degradation

Native antimicrobial peptides (AMPs) exist as a part of the host defence mechanism in multicellular organisms. To develop AMPs as novel therapeutics, one can modify these naturally occurring AMPs to increase their bactericidal effects, possibly also altering their mechanism of action. Here the mechanism of action for the natural AMP cecropin B is determined by visualising its effect on model membranes using Atomic Force Microscopy (AFM). The effect of rational sequence modification on its mechanism of action was examined by the same method to verify the changes made had the anticipated effect.

7.1 Introduction

There are a number of native antimicrobial peptides found in multicellular organisms including the well documented cecropin B [150], [166]–[168]. Cecropin B has been shown to be effective against a range of Gram-positive and Gram-negative bacteria [151]. Here we examine the mechanism of action for cecropin B by using AFM to directly visualise membrane degradation. We then investigate how strategic changes to the amino acid sequence of cecropin B can be made to elicit changes in the mechanism of action leading to an increased understanding of the structure-function relationship for cecropin B, with the aim of increasing the efficiency of cecropin B as a possible

therapeutic.

In general, cationic alpha-helical antimicrobial peptides such as cecropin are active in the low-medium micromolar range [279] and despite being active against a range of bacterial cells, the efficiency of their activity for killing different cell types varies [170]. Understanding the factors behind this variability may lead to the design of novel peptide antibiotics. One of the mechanisms for the development of antimicrobial peptides with stronger antimicrobial effects is the strategic alteration of amino acid residues in the peptide sequence to achieve increased antimicrobial activity through alteration of the mechanism of membrane degradation [141].

Cecropin B is a native peptide 35 amino acids long, corresponding to a helix length of ∼5 nm, meaning it cannot sit vertically in the lipid bilayer which is 3.2 nm deep. Cecropin B is polymorphic in solution, but forms alpha-helices on binding to lipids, as described in chapter 1.6. Cecropin B is known to disrupt the membrane via the carpet mechanism as stated in the literature [154]. In contrast to Amhelin (see chapter 6 for detailed analysis of Amhelin), cecropin B is believed to bind to the membrane as monomers, not requiring aggregation on the surface before disrupting the membrane [264]. Cecropin B has two alpha-helices, one at the C-terminus and the other at the N-terminus, separated by a short sequence which creates a hinge in the structure. This hinge is known as the GP bend motif after the glycine and proline amino acids at positions 23 and 24 [164]. It is the helix-bend-helix structure, which is believed to be key to its antimicrobial mechanism of action [173].

KWKVFKKIEKMGRNIRNGIVKAGPAIAVLGEAKAL	cecropin B
KWKVFKKIEKMGRNIRNGIVK	ChoC
KWKVFKKIEKMIRNIRNKIVK	ChoM
KWKVLKKKIKMLRNRINGLVKAGPALKVKLQALAL	cecropin mutant

Figure 7.1: The amino acid sequences of the antimicrobial peptides investigated here. The colours used refer to those in figure 7.2. Amino acid substitutions as compared to the cecropin B sequence are highlighted and the GP bend motif or hinge region is marked in yellow.

To investigate the structure-function dependence of cecropin B, different changes were made to the primary sequence of cecropin B including the removal of the bend-helix or hinge region [280] by creating the peptide sequences shown in figures 7.1 and 7.2. The GP bend motif is marked in figure 7.1 in yellow.

As cecropin B is cationic it is electrostatically attracted to the bilayer, and should bind to the membrane. As discussed previously cecropin B contains two alpha-helices separated by a hinge region. The N-terminal alpha helix is amphipathic and very

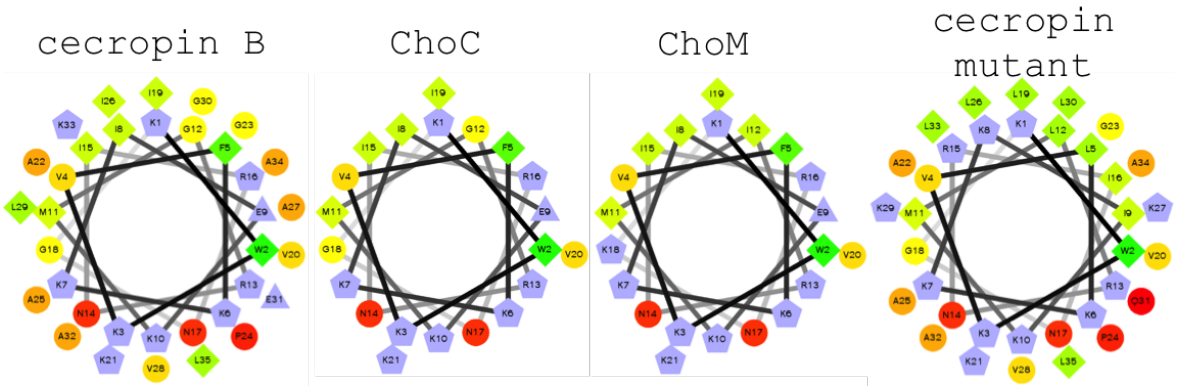

Figure 7.2: Helical representations of the amino acid sequence for cecropin B and the other antimicrobial peptides based on cecropin B's structure investigated here. Each amino acid residue is marked with a letter and a number describing the amino acid type and position in the sequence.

similar to the peptides discussed in the previous chapters, as a result it will most likely bind to the surface in the S-state. The C-terminus alpha helix after the GP bend motif is a non-polar structure which will most likely insert into the alkyl chains of the lipid bilayer. This can occur while the N-terminus alpha helix remains bound to the surface in a parallel orientation due to the flexibility of the hinge region. It is the C-terminus alpha helix which is predicted to cause surface bound disruption of the membrane as shown in figure 7.3I.

To investigate whether it is indeed the second alpha helix of cecropin B which causes cecropin B not to porate the membrane, a second peptide, ChoC, was created by removing the C-terminus alpha helix of cecropin B at the GP bend. The removal of the C-terminus to create ChoC shortens cecropin B. As ChoC has a cationic, amphipathic structure more similar to that of the synthetic peptide Amhelin, discussed earlier in this study, we would expect that it would porate the bilayer via a similar mechanism as shown in figure 7.3II.

ChoM is obtained by taking cecropin B and removing the C-terminus alpha helix, as was done for ChoC. In addition two glycines in the centre of the structure are replaced with an isoleucine and a lysine. This results in ChoM having a larger hydrophobic core affording a structure more similar to Amhelit than Amhelin. When ChoM porates the bilayer, part of the hydrophobic core will be exposed to the solution destabilising the position of ChoM in the bilayer. This should result in ChoM porating only the top monolayer of the membrane as seen in chapter 6 for Amhelit and shown in figure 7.3III.

Finally, cecropin B was converted into a template that could accept coiled-coil interactions, as described in the literature [243]. Coiled-coil interactions are key to oligomerisation through directing the manner of peptide interactions [281]. The ce-

cropin B template, here termed cecropin mutant, is able to oligomerise via a coiled-coil mechanism, which is predicted to lead to static pore formation as shown in figure 7.3IV.

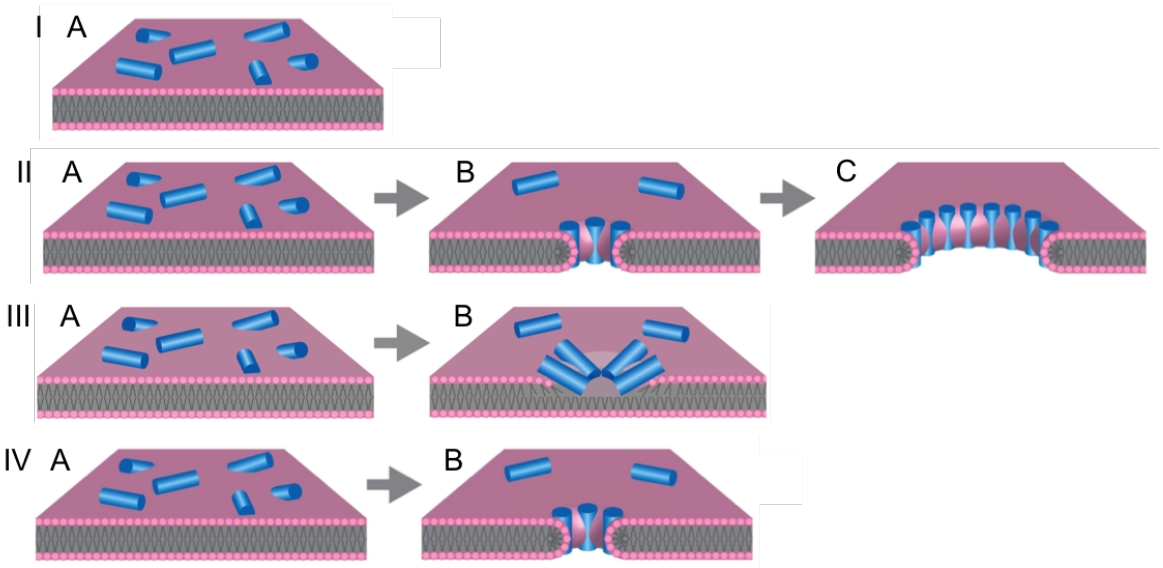

Figure 7.3: Proposed mechanisms of action for antimicrobial disruption of a lipid bilayer by cecropin B (I), ChoC (I or II), ChoM (III) and cecropin mutant (IV) where blue cylinders represent AMP alpha-helices and the lipid bilayer is represented by pink hydrophilic headgroups and grey hydrophobic tails. I) Carpet or surface disruption mechanism: A) antimicrobial peptides bind to the surface of the membrane (S-state) and disrupt the membrane surface. II) pore expansion mechanism: A) antimicrobial peptides bind to the surface of the membrane (S-state), B) peptides insert into lipid bilayers forming pores (I-state), C) pores expand indefinitely (E-state). III) monolayer poration mechanism: A) antimicrobial peptides bind to the surface of the membrane (S-state), B peptides insert forming pores in the outer leaflet of the bilayer. IV) static poration mechanism: A) antimicrobial peptides bind to the surface of the membrane (S-state), B) peptides insert into lipid bilayers forming pores (I-state).

7.2 Results and Discussion

All peptides used here were synthesised and purified at the National Physical Laboratory (NPL) as described in chapter 3 and in [236].

All imaging is carried out using AFM under buffer conditions of 10 mM HEPES, 150 mM NaCl, 5 mM $MgCl_2$, 5 mM $CaCl_2$ pH 7.4 at 22°C unless otherwise stated. The lipids used for this investigation were DLPC:DLPG (3:1) used for the study of *de-novo* designed peptide activity in chapter 6 and in [236], to allow comparison between the two and for continuity. Lipid bilayers were prepared as described in chapter 3.1.3. The divalent cations Mg^{2+} and Ca^{2+} were used to stabilise the bilayers for imaging and

also to promote fusion of the negatively charged vesicles with the negatively charged mica . The use of cations can reduce the efficacy of the peptides however here the concentrations used are of the same order of magnitude as physiological conditions, and as such the peptides should be able to exhibit sufficient antimicrobial activity under these conditions.

AFM imaging was carried out in peak force tapping with a peak force amplitude of 10 nm on a Multimode 8 using AC40 cantilevers (k=0.08 N/m) the properties of which are shown in table 2.1. The applied force was kept at approximately 50 pN for imaging.

7.2.1 Cecropin B

Cecropin B is predicted to effect its antimicrobial activity via surface bound disruption of the lipid bilayer. Cecropin B's sequence, as shown in figure 7.1, is formed of two alpha-helices separated by a hinge in the form of a GP (glycine, proline) motif. The N-terminus helix is a cationic alpha helix, which is polymorphic in solution, and adopts an amphipathic helical configuration on binding to the lipids. This helix is stablised on the surface by the C-terminus alpha helix, which is non-polar or hydrophobic and as such preferentially inserts into the lipid bilayer, destabilising it. This insertion is mediated by the GP bend motif which introduces a kink between the two structures.

Figure 7.4 shows AFM images taken before and after the addition of cecropin B to the fluid cell. Figure 7.4A shows the flat lipid substrate prior to the addition of cecropin B. Figure 7.4B shows the lipid bilayer after the treatment with 0.3 μM cecropin B. There is a distinct roughening of the surface visible in the right hand image with no poration to the membrane. These images remained the same over a period of one hour of imaging. Line profiles taken across the centre of each image to show the surface roughness are displayed underneath. For the untreated flat lipid bilayer the roughness is about 0.1 nm, which can be attributed to the system. This increases roughly eight-fold to 0.8 ± 0.2 nm after treatment with cecropin B.

It can also be noted that the concentration used for cecropin B in these studies is 0.3 μM, much lower than that used in any other peptide study in this investigation, which is an indication of its relatively high activity.

Cecropin B behaves as predicted; it disrupts the lipid bilayer in a surface bound state without porating the bilayer. This is in agreement with both our prediction of a surface bound disruption state as shown in figure 7.3I and the carpet mechanism proposed in the literature [154].

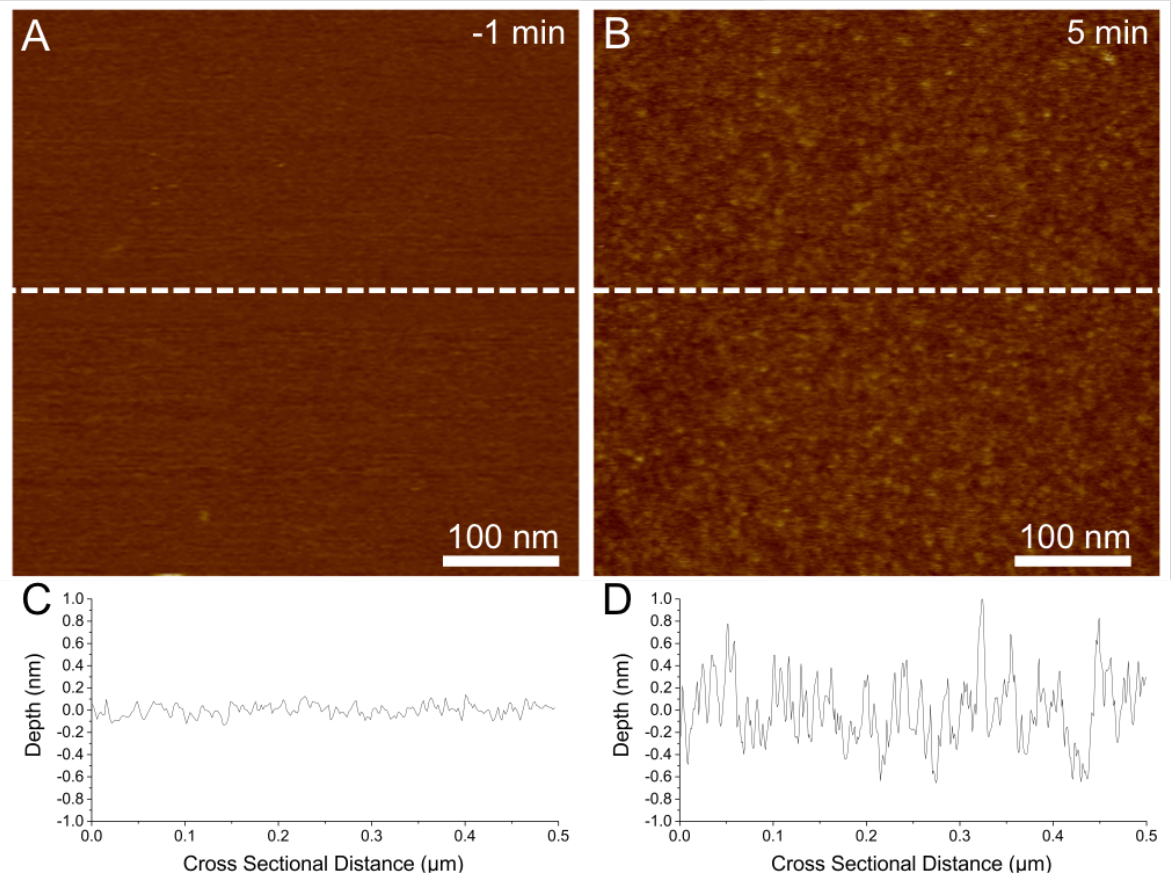

Figure 7.4: AFM images showing a negatively charged DLPC:DLPG (3:1) lipid bilayer before (A) and after (B) treatment with 0.3 μM cecropin B. C) and D) Line profiles taken along the dotted lines marked in (A) and (B) respectively. Colour Scale (see figure 6.8 for scale bar): 6 nm. Cecropin B concentration: 0.3 μM

7.2.2 ChoC

To confirm that the C-terminus of cecropin B inhibits the insertion of the peptide in the I-state and subsequent pore formation, the C-terminus alpha helix of cecropin B was removed, including the GP bend motif, to obtain ChoC, an amphipathic cationic alpha helix the sequence of which is shown in figures 7.1 and 7.2. Choc is also very similar in sequence to Amhelin, which forms pores via an expanding pore mechanism, as discussed in chapter 6. It is therefore believed that ChoC will form pores of varied diameter which fully porate the bilayer in the same manner as Amhelin.

Figure 7.5 shows the effect of ChoC on a lipid bilayer. Figure 7.5A shows the model membrane prior to treatment with ChoC as a flat substrate. Figure 7.5B was taken 20 minutes after treatment with 1.2 μM ChoC and shows that pores of varying diameter have formed in the bilayer. Figure 7.5C was taken 90 minutes after treatment with 1.2 μM ChoC, and shows an increased number of pores on the surface as compared to the

image taken at 20 minutes after treatment.

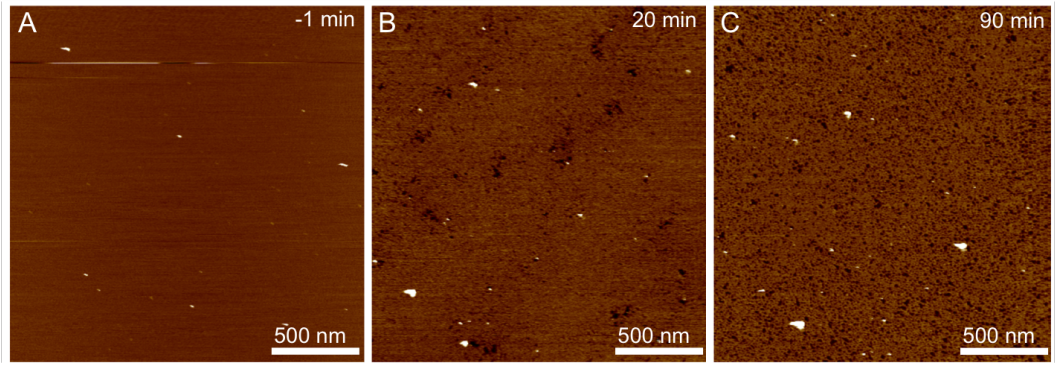

Figure 7.5: AFM images showing the effect of ChoC on a negatively charged DLPC:DLPG (3:1) lipid bilayer over time. A) A lipid bilayer imaged prior to treatment with ChoC, B) and C) AFM images taken 20 and 90 minutes respectively after the treatment with ChoC. Colour Scale (see figure 6.8 for scale bar): 5 nm. ChoC concentration: 1.2 μM

These pores are too narrow to be probed by the AFM tip at this resolution. Therefore higher resolution images were taken of the surface to probe the full depth of the pore.

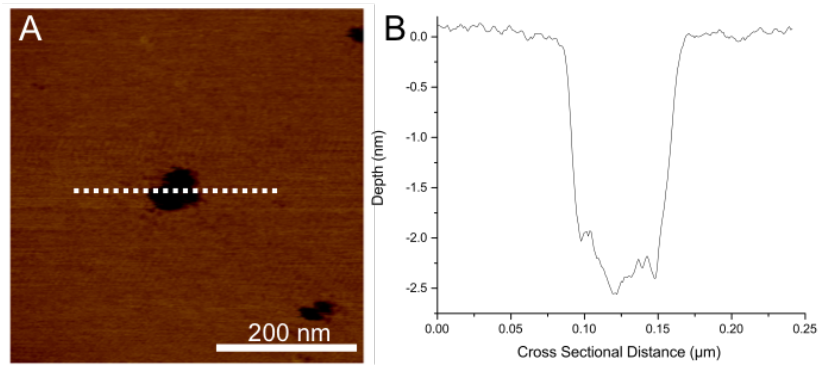

Figure 7.6: A) A higher resolution AFM image of a pore formed by ChoC in a negatively charged DLPC:DLPG (3:1) lipid bilayer. B) A line profile taken along the dotted line marked in (A) to show the depth of the pore. Colour Scale (see figure 6.8 for scale bar): 6 nm. ChoC concentration: 1 μM

Figure 7.6A shows a higher resolution AFM image of a pore created by ChoC. Figure 7.6B shows a line profiletaken along the dotted line in (A) displaying the depth of the pore. This shows the depth to be 2.7 ± 0.3 nm. The edges of the pore are also well defined with vertical edges similar to those observed for Amhelin in figure 6.7.

As expected, ChoC displays a mode of action very similar to that of Amhelin however ChoC has not been specifically designed to create expanding pores and as a consequence the pore expansion is much reduced. ChoC is amphipathic in nature, however the segregation of the amino acid residues by type is less pronounced. This can be

visualised by examining the sequences on helical wheels side by side as displayed in figure 7.7. We can see that in addition to the reduction in segregation, there is variation in hydrophobic amino acids (green) which may reduce the cooperativity. Also the lack of a stabilising neutral or small region as seen in orange/red may have a detrimental effect on the pore expansion process.

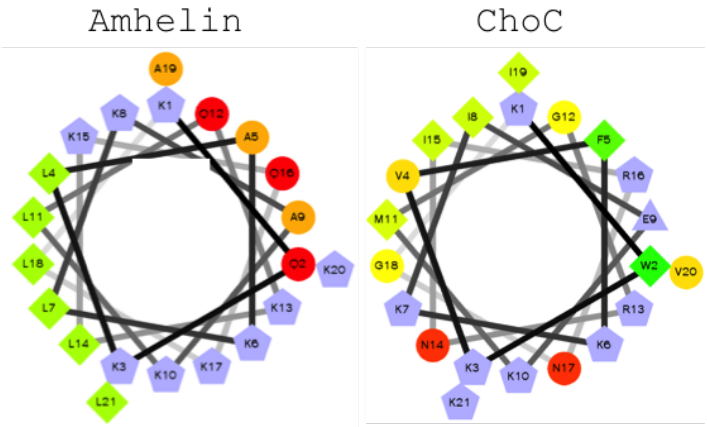

Figure 7.7: Helical representations of the sequences for Amhelin and ChoC, reproduced from figures 6.2 and 7.2 and placed side by side for direct comparison.

These effects have reduced the efficacy of the expanding pore mechanism however, ChoC maintains similarities with Amhelin, including its ability to porate a full bilayer. The fact that the pores are ∼0.5 nm less than the full bilayer was also seen for Amhelin in chapter 6.2.2 and could be explained by: salt deposits, peptides or other contaminants aggregating on the mica surface increasing its height; compression of the soft bilayer in the fluid phase by ∼10 %, or; charge interaction effects between the tip and the surface. It is difficult to distinguish which of these effects is responsible for this apparent height difference, however we can be certain that we are fully porating the bilayer. This implies that the removal of the non-polar C-terminus alpha helix of cecropin B alters the mechanism of the peptide from surface disruption to bilayer poration.

7.2.3 ChoM

ChoM is a modified version of ChoC which has a higher cationic charge and larger hydrophobic core due to the substitution of two small glycines for a lysine and isoleucine respectively. The increase in charge attraction to the lipid headgroups and hydrophobic core will act to destabilise ChoC in the membrane as was done to create Amhelit in chapter 6.2.5. We therefore hypothesise that this will result in ChoM porating the outer leaflet of the bilayer in an expanding pore state similar to that exxhibited by Amhelit.

Figure 7.8 shows consecutive images of the effect of ChoM on the bilayer. The top left image shows the lipid bilayer prior to the insertion of ChoM, while the top right image shows the surface three minutes after treatment with 1.2 μM ChoM with pores visible across the surface and small pores barely visible in the background. The bottom left image shows the surface six minutes after treatment where the pores have expanded to hundreds of nanometres. The bottom right image shows that nine minutes after treatment the pores have merged with one another and totally removed the surface.

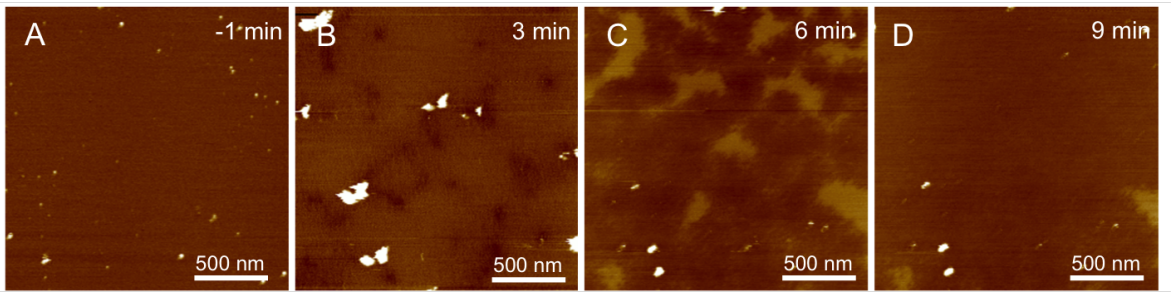

Figure 7.8: AFM time-lapse images of ChoM porating a negatively charged DLPC:DLPG (3:1) lipid bilayer. Each sequential image shows a larger area of the top monolayer removed. Colour Scale (see figure 6.8 for scale bar): 6 nm. ChoM concentration: 1.2 μM

It should be noted that in figure 7.8B the white deposits on the surface, which are most likely contamination of some sort, are shown as doubled across the image. This phenomena is known as a double tip image, where the tip contains two protrusions at its end, possibly due to contamination of the tip. The tip then images the surface feature with both of the protrusions, showing each feature as doubled. The pores are visible across the lipid surface and seem to be less affected by the double tip.

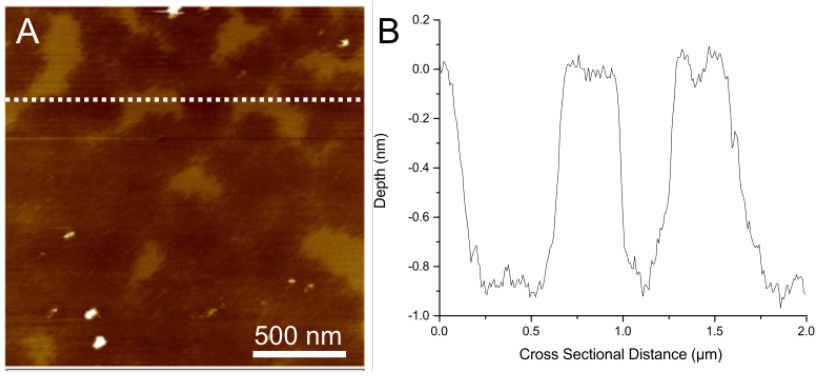

Figure 7.9: A) An image showing poration of a negatively charged DLPC:DLPG (3:1) lipid bilayer by ChoM reproduced from figure 7.8. B) A line profile taken along the dotted line in A showing a poration depth of s ~0.9 nm. Colour Scale (see figure 6.8 for scale bar): 6 nm. ChoM concentration: 1.2 μM

To examine the depth of poration figure 7.8C is reproduced as figure 7.9A and a line

profile is taken along the dotted line marked. The line profile is shown in figure 7.9B and shows a poration depth of 0.9 ± 0.1 nm, less than half the bilayer depth of 3.2 nm. We can conclude from this that ChoM porates the membrane in expanding pores which remove the top monolayer of the lipid bilayer by a similar mechanism to Amhelit

The alteration of two amino acids in the structure of the shortened cecropin B peptide to form ChoM has affected its mechanism of action as proposed. ChoM only porates the top monolayer of the lipid bilayer in expanding pores as shown in figure 7.3III. This is the same mechanism exhibited by Amhelit, which also porates the top monolayer of the membrane.

These time-lapse images were taken in peak force tapping using the low force imaging protocols optimised on DNA. The accurate control of the tip-sample interaction enabled by this method allows for continuous imaging of the degradation of the membrane despite the fluctuations in the fluid cell due to the active peptides and removal of lipids, resulting in time-lapse images of the mode of action for ChoM.

7.2.4 Cecropin Mutant

We predict that the formation of static pores in the membrane is caused by the oligomerisation of the peptide to a set structure. To investigate this, cecropin B was converted into a template that can oligomerise via coiled coil interactions termed cecropin mutant. As such it is predicted that it will form static pores in the membrane as shown in figure 7.3IV.

Figure 7.10 shows the formation of pores in the lipid bilayer by cecropin mutant. The pores formed are determined to be static (not expanding) due to their identical size. Since the pores are of the same size, we can measure the pore diameter by AFM. The pore diameter is measured by taking a line profile across the sample as shown in figure 7.10. The pore diameter is determined to be 10 ± 2 nm. The narrow width does not allow the tip to probe the full depth of the pore as it is of a similar size to the tip radius as stated by the manufacturer and summarised in table 2.1.

Figure 7.11 shows another AFM image taken at a larger scan size in a different area of the sample. This image shows the small pores displayed in figure 7.10 in the background, with areas where the high density of pores results in an instability for any remaining lipids such that the surface collapses. This is observed as a large area of disruption. The graph in figure 7.11 shows the depth of this disruption, as taken along the dotted line. The depth is measured as 0.8 ± 0.2 nm. This implies that cecropin mutant only disrupts the outer leaflet of the membrane, either due to the length of cecropin, which at almost twice the height of the bilayer, does not favour vertical insertion, or due to the mechanism of coiled-coil interactions, which may stabilise cecropin mutant

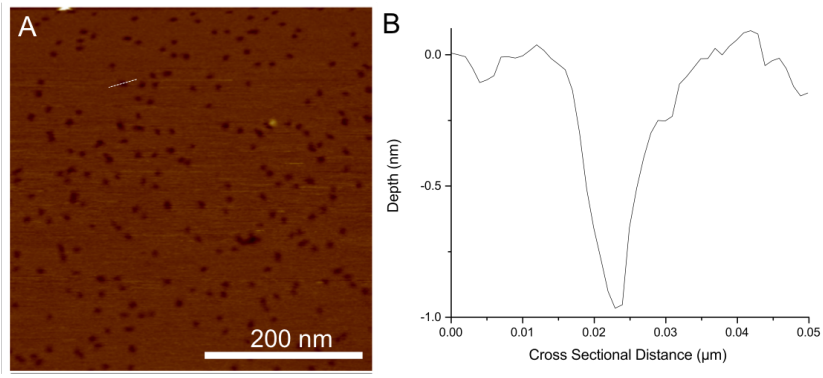

Figure 7.10: A) An AFM image showing the formation of small pores in a negatively charged DLPC:DLPG (3:1) lipid bilayer in the presence of low concentrations of cecropin mutant. B) A line profile taken along the dotted line in the image showing a pore width of 10 ± 2 nm. Colour Scale (see figure 6.8 for scale bar): 6 nm. Cecropin mutant concentration: 0.3 μM

in a monolayer spanning conformation or by a combination of both.

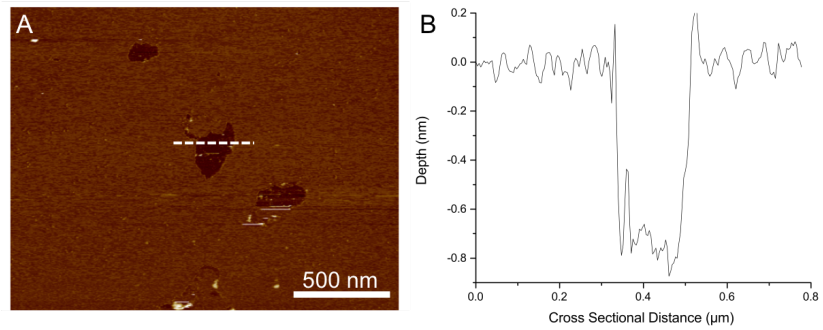

Figure 7.11: A) An AFM image taken in another area of the sample showing poration of a negatively charged DLPC:DLPG (3:1) lipid bilayer by cecropin mutant. B) A line profile along the dotted line in the image showing a 1 nm depth of poration confirming the removal of the outer leaflet of the lipid bilayer. Colour Scale (see figure 6.8 for scale bar): 6 nm. Cecropin mutant concentration: 0.3 μM

We have observed static pore formation in the membrane by cecropin mutant as predicted, which we attribute to its ability to oligomerise through coiled-coil interactions. The $\sim$1 nm depth of pores formed by cecropin mutant indicates that it disrupts the membrane by static monolayer pore formation as shown in figure 7.3IV.

7.3 Conclusion

Cecropin B is a naturally ocurring antimicrobial peptide isolated from the silk moth species *Hyalophora cecropia* [145], [282]. Cecropins have been shown to exhibit broad

spectrum antimicrobial activity [154], with Cecropin B the most active of the cecropin family [162]. Ceropins have been shown to have polymorphic structure in solution, adopting their alpha helical structure on binding to a lipid bilayer [264], where they are believed to disrupt the membrane killing bacterial cells [154], [164]. To date many studies have been carried out on cecropin B and similar peptides [145], [154], [170], [171], [282], [283]. However, the intricacies of its molecular mechanisms of action have been under debate for more than 30 years [145], [173].

Here we show direct visualisation of the mechanism of action for membrane degradation by cecropin B using low force AFM methods developed to visualise the secondary structure of DNA. Cecropin B degrades the membrane by surface bound disruption which we attribute the the C-terminus apha helix inserting in the lipid membrane. To investigate the effect of this alpha helix, subsequent studies which removed this were carried out, along with systematic changes to the amino acid sequence to alter the mechanism of disruption. Figure 7.12 summarises the effect of each modification to cecropin B in terms of its effect on the membrane.

Antimicrobial Peptide	Sequence	Mode of Action	Poration
cecropin B:	KWKVFKKIEKMGRNIRNGIVKAGPAIAVLGEAKAL	Surface disruption	
ChoC:	KWKVFKKIEKMGRNIRNGIVK	Poration	Bilayer
ChoM:	KWKVFKKIEKMIRNIRNKIVK	Expanding pore	Monolayer
cecropin mutant:	KWKVLKKKIKMLRNRINGLVKAGPALKVKLQALAL	Fixed pore	Monolayer

Figure 7.12: A table showing the mode of action for membrane degradation by the antimicrobial peptides discussed in this chapter

We have shown that cecropin B causes surface bound membrane disruption. On removal of the hydrophobic C-terminus after the GP bend, creating ChoC, the antimicrobial mechanism of action is altered, with poration of the bilayer occurring. This implies that the C-terminus of cecropin B may be a key component of the carpet mechanism.

Through increasing the size of the hydrophobic core by replacing two glycines with an isoleucine and a lysine to create ChoM, we can destabilise the binding of the peptide to the membrane. This results in ChoM porating only the top monolayer of the membrane. Time-lapse AFM images of the expanding monolayer poration mechanism exhibited by ChoM are shown. These were taken using the optimised methodology for peak force tapping established for imaging the model system of DNA which allowed the entire process to be monitored in one experiment.

By modifying cecropin B into a structure which can oligomerise through coiled-coil interactions, we have formed a porating version of cecropin B termed cecropin mutant. This shows oligomerisation to be key in the formation of the I-state where peptides

insert into the membrane.

Through modifications to the amino acid sequence of cecropin B, we have gained an increased understanding of the structure-function relationship of the amino acid sequence of the native antimicrobial peptide cecropin B. We have directly visualised the mechanism of action for cecropin B confirming this as the carpet mechanism, which we can attribute to the hydrophobic C-terminus alpha-helix. This study therefore provides new insight into the mechanism of action for the natural antimicrobial peptide cecropin B, and a rationale for sequence modification of natural antimicrobial peptides to create novel peptide antibiotics.

Chapter 8

Conclusion

This thesis presents results with the aim of improving our understanding of fundamental biomolecule structure and function by visualising biological molecules at the nanoscale. We showed the structure of DNA at sub-nm resolution, following the optimisation of Atomic Force Microscopy (AFM) methods. Variations in DNA groove depth were visualised and attributed to supercoiling effects on the conformation. Preliminary data on synthetic DNA minicircles was shown, indicating that these methods can be used to study DNA secondary structure and protein binding as a function of supercoiling. Similar AFM methods were then used to visualise the degradation of model membranes by both synthetic and naturally occurring antimicrobial peptides, a possible novel class of antibiotics, to validate predictions for their modes of action. Information gained on the mechanism of action for these peptides will aid in the understanding of how amino-acid sequence drives antimicrobial action, which is believed to be critical in the development of more potent novel antibiotics.

In chapter 4 we showed that by optimising imaging parameters, sample preparation and choice of AFM probe, we can enhance the spatial resolution of AFM in solution. This was demonstrated by the robust and reproducible visualisation of the DNA double helix in solution using for two modes of AFM imaging. As a result of this enhanced resolution, it was possible to see structural variability along a single DNA molecule as variations in the groove depth of the double helix. Key to this result was ensuring that the applied force was maintained in the 40-80 pN region whilst imaging, as a compromise between applying enough force to track the molecule and applying little enough to avoid that the molecule was not overly deformed and spatial resolution consequently reduced. In addition it was found that soft cantilevers with $k \sim 0.1$ N/m and radius 1-2 nm were found to give the best resolution for imaging the double helix. In addition, sample preparation using divalent cations in the concentration 1-5 mM was found to be an appropriate compromise between resolution and allowing the molecule to retain some of its inherent flexibility.

This method allows for the study of DNA secondary structure along a long and coiled molecule. Despite the resolution being lower than that achievable by other methods (e.g., X-ray diffraction and cryo-EM) [284]–[287], the use of high-resolution AFM as a tool to study DNA structure is unique in its ability to study a single molecule under near-physiological conditions without ensemble averaging [68]–[70]. The disadvantage of this technique remains however that the molecule must be adsorbed to a flat substrate for imaging.

DNA imaging at this resolution has the secondary use of being an extremely sensitive measurement and calibration tool for AFM imaging. We have shown that the height of DNA relates to the applied force and as such it can be used as a force monitor for in-liquid AFM imaging. In addition the imaged width of the molecule directly relates to the radius of an AFM probe's tip radius in the $\sim$1 nm range [68], [69]. We can therefore use low force DNA imaging, where we are not compressing the molecule, to quantify the tip radius whilst imaging. Current methods of tip calibration must be performed post imaging and can determine radii in the range 10-100 nm [288]. In addition, these methods are often destructive to the tip.

In chapter 5, we showed that the high-resolution AFM imaging techniques developed in chapter 4 can be applied to smaller DNA structures such as minicircles. Synthetic DNA minicircles can be used to experimentally monitor the effects of supercoiling on DNA structure [254] whilst remaining accessible to computational methods [253]. Supercoiling is key to the fundamental biological process of gene expression [120]. We used high-resolution AFM to monitor DNA structure and conformation as a function of supercoiling showing preliminary data visualising the supercoiled state of a molecule as a 2D conformation immobilised on a mica substrate. The minicircle structures followed the predicted dependence on supercoiling despite their immobilisation. Relaxed and nicked structures of zero supercoiling appeared mainly as open configurations, and supercoiled species appeared as crossed configurations such as figure of eights as was expected [254] whilst showing corrugation corresponding to the double helix.

Importantly, we also showed that we can monitor the secondary structure of a minicircle, even for a loosely bound molecule changing its confirmation during imaging. We believe this to be a model system for future studies of DNA binding events as a function of DNA supercoiling, conformation and structure [252]. We envisage future experiments which study real-time DNA interactions on a timescale influenced by the strength of the DNA binding to the substrate [117].

Moving from fundamental biology to a current biological question, we examine how we can contribute to the problem of antibiotic resistance, where antibiotics are becoming less effective in the fight against bacterial infection [150], [175]. To this end we examined the mechanism of action for antimicrobial peptides as a novel class of antibiotic [159]. Antimicrobial peptides disrupt negatively charged bilayers [154], [164], but

our understanding of their mechanisms of action is hampered by a lack of nanoscale visualisation of this disruption process [289].

In chapter 6, we used AFM to observe the effect of antimicrobial peptides on model membranes designed to mimic negatively charged bacterial cells [276]. These results were used to verify the *de-novo* peptide design methodology whereby novel antimicrobial peptides are created with specific modes of action. To this end, we showed that the synthetic peptide Amhelin forms pores as proposed via a novel expanding pore mechanism [236]. This can be understood as cooperative and continuous pore formation as peptides are recruited within the lipid bilayer.

In chapter 6, we also showed AFM as a method to verify how amino acid sequence substitutions affect the mode of action for antimicrobial peptides. To this end, sequence modifications were made to increase the electrostatic interaction between the peptide and the membrane and to add a destabilising second hydrophobic region. This change was shown by AFM to elicit a second novel poration mechanism which disrupts only the outer monolayer of the bilayer as predicted [146]. In addition it was shown that by the substitution of two amino acid residues, it was possible to lower the rigidity of the alpha helix, and prevent it from inserting into the bilayer.

We have shown that AFM can be used to verify design rationales by directly visualising the mechanism of membrane disruption for *de-novo* designed antimicrobial peptides, showing excellent correlation with predicted mechanisms of action in chapter 6. In chapter 7 we examined the mechanism of naturally occurring antimicrobial peptide cecropin B, isolated from from the silk moth *Hyalophora cecropia*. This peptide is believed to disrupt bacterial membranes via surface bound disruption termed the 'carpet mechanism' however the exact mechanism has been under debate for over thirty years [173], [264].

In chapter 7 we use low force AFM imaging to show that cecropin B perturbs a model membrane by creating surface bound disruption as predicted by the carpet mechanism [290]. To probe the origin of this surface disruption we created a novel peptide, ChoC, containing only the N-terminus alpha helix of cecropin B. ChoC was shown to porate the bilayer. This implies that that the C-terminus alpha helix stabilises cecropin B on the membrane surface and is a key component of the carpet mechanism.

We then carried out sequence modifications to increase the electrostatic and hydrophobic interactions for ChoC to create ChoM, as was done in chapter 6 to create Amhelit. ChoM was shown to act in a similar manner to Amhelit, implying that the origin of Amhelit's monolayer poration mechanism is the increase in hydrophobic and electrostatic attraction as predicted. In addition we were able to obtain time-lapse AFM images of the expanding monolayer poration mechanism exhibited by ChoM using the optimised methodology for Peak Force Tapping established in chapter 4.

It is anticipated that AFM can further contribute to an increased understanding of the mechanism of action for antimicrobial peptides, in particular by monitoring how targeted changes to their structure, charge and hydrophobicity can elicit large changes in their mechanism of action [291]. This work may therefore aid in the development of novel therapeutic antimicrobial therapeutics [150].

References

[1] M. C. Leake, *Single-Molecule Cellular Biophysics*. Cambridge: Cambridge University Press, 2013.

[2] C. Bustamante, "In singulo biochemistry: when less is more.", *Annual Review of Biochemistry*, vol. 77, pp. 45–50, 2008.

[3] M. C. Leake, "Introduction: The physics of life: one molecule at a time", *Philosophical Transactions: Biological Sciences*, vol. 368, no. 1611, pp. 1–9, Feb. 2013.

[4] B. Alberts, D. Bray, K. Hopkin, A. Johnson, J. Lewis, *et al.*, *Essential Cell Biology, Fourth Edition*. Taylor & Francis Group, 2013.

[5] C. Leung, N. V. Dudkina, N. Lukoyanova, A. W. Hodel, I. Farabella, *et al.*, "Stepwise visualization of membrane pore formation by suilysin, a bacterial cholesterol-dependent cytolysin", *eLife Sciences*, vol. 3, Dec. 2014.

[6] J. D. Watson and F. H. C. Crick, "Molecular Structure of Nucleic Acids: A Structure for Deoxyribose Nucleic Acid", *Nature*, vol. 171, no. 4356, pp. 737–738, Apr. 1953.

[7] M. H. F. Wilkins, A. R. Stokes, and H. R. Wilson, "Molecular Structure of Nucleic Acids: Molecular Structure of Deoxypentose Nucleic Acids", *Nature*, vol. 171, no. 4356, pp. 738–740, Apr. 1953.

[8] R. E. Franklin and R. G. Gosling, "Molecular Configuration in Sodium Thymonucleate", *Nature*, vol. 171, no. 4, pp. 740–741, Apr. 1953.

[9] A. Wlodawer, W. Minor, Z. Dauter, and M. Jaskolski, "Protein crystallography for aspiring crystallographers or how to avoid pitfalls and traps in macromolecular structure determination.", *The FEBS journal*, vol. 280, no. 22, pp. 5705–5736, Nov. 2013.

[10] E. F. Pettersen, T. D. Goddard, C. C. Huang, G. S. Couch, D. M. Greenblatt, *et al.*, "UCSF Chimera–a visualization system for exploratory research and analysis.", *Journal of computational chemistry*, vol. 25, no. 13, pp. 1605–1612, Oct. 2004.

[11] H. R. Drew, R. M. Wing, T. Takano, C. Broka, S. Tanaka, *et al.*, "Structure of a B-DNA dodecamer: conformation and dynamics.", *Proceedings of the National Academy of Sciences of the United States of America*, vol. 78, no. 4, pp. 2179–2183, Apr. 1981.

[12] E. F. Garman, "Developments in X-ray Crystallographic Structure Determination of Biological Macromolecules", *Science*, vol. 343, no. 6175, pp. 1102–1108, Mar. 2014.

[13] C. Kupitz, S. Basu, I. Grotjohann, R. Fromme, N. A. Zatsepin, *et al.*, "Serial time-resolved crystallography of photosystem II using a femtosecond X-ray laser", *Nature*, vol. 513, no. 7517, pp. 261–265, Sep. 2014.

[14] S. Boutet, L. Lomb, G. J. Williams, T. R. M. Barends, A. Aquila, *et al.*, "High-Resolution Protein Structure Determination by Serial Femtosecond Crystallography", *Science*, vol. 337, no. 6092, pp. 362–364, Jul. 2012.

[15] H. N. Chapman, A. Barty, M. J. Bogan, S. Boutet, M. Frank, *et al.*, "Femtosecond diffractive imaging with a soft-X-ray free-electron laser", *Nature Physics*, vol. 2, no. 12, pp. 839–843, Nov. 2006.

[16] J. Frank, "Cryo-electron microscopy as an investigative tool: the ribosome as an example", *Bioessays*, vol. 23, no. 8, pp. 725–732, Aug. 2001.

[17] H. R. Saibil, "Conformational changes studied by cryo-electron microscopy", *Nature Structural Biology*, vol. 7, no. 9, pp. 711–714, 2000.

[18] W. Kuhlbrandt, "The Resolution Revolution", *Science*, vol. 343, no. 6178, pp. 1443–1444, Mar. 2014.

[19] N. Fischer, P. Neumann, A. L. Konevega, L. V. Bock, R. Ficner, *et al.*, "Structure of the E. coli ribosome-EF-Tu complex at ¡3 A resolution by Cs-corrected cryo-EM", *Nature*, vol. 520, no. 7548, pp. 567–570, Feb. 2015.

[20] X.-c. Bai, I. S. Fernandez, G. McMullan, and S. H. W. Scheres, "Ribosome structures to near-atomic resolution from thirty thousand cryo-EM particles.", *eLife Sciences*, vol. 2, e00461, 2013.

[21] D. P. Frueh, A. C. Goodrich, S. H. Mishra, and S. R. Nichols, "NMR methods for structural studies of large monomeric and multimeric proteins", *Current Opinion in Structural Biology*, vol. 23, no. 5, pp. 734–739, Oct. 2013.

[22] A. G. Tzakos, C. R. R. Grace, P. J. Lukavsky, and R. Riek, "NMR Techniques for Very Large Proteins and RNAs in Solution", *Annual review of biophysics and biomolecular structure*, vol. 35, no. 1, pp. 319–342, May 2006.

[23] T. Gonen and G. Waksman, "Editorial overview: Membranes: Recent methods in the study of membrane protein structure", *Current Opinion in Structural Biology*, vol. 27, pp. IV–V, Aug. 2014.

[24] G. Bellot, M. A. McClintock, J. J. Chou, and W. M. Shih, "DNA nanotubes for NMR structure determination of membrane proteins", *Nature Protocols*, vol. 8, no. 4, pp. 755–770, Apr. 2013.

[25] S. Wang, R. A. Munro, L. Shi, I. Kawamura, T. Okitsu, *et al.*, "Solid-state NMR spectroscopy structure determination of a lipid-embedded heptahelical membrane protein", *Nature Publishing Group*, vol. 10, no. 10, pp. 1007–1012, Oct. 2013.

[26] T. Jacso, W. T. Franks, H. Rose, U. Fink, J. Broecker, *et al.*, "Characterization of Membrane Proteins in Isolated Native Cellular Membranes by Dynamic Nuclear Polarization Solid-State NMR Spectroscopy without Purification and Reconstitution", *Angewandte Chemie International Edition*, vol. 51, no. 2, pp. 432–435, Jan. 2012.

[27] L. A. Baker and M. Baldus, "Characterization of membrane protein function by solid-state NMR spectroscopy", *Current Opinion in Structural Biology*, vol. 27, pp. 48–55, Aug. 2014.

[28] B. Huang, M. Bates, and X. Zhuang, "Super-Resolution Fluorescence Microscopy", *Annual Review of Biochemistry*, vol. 78, no. 1, pp. 993–1016, Jun. 2009.

[29] B. Hein, K. I. Willig, and S. W. Hell, "Stimulated emission depletion (STED) nanoscopy of a fluorescent protein-labeled organelle inside a living cell", *Proceedings of the National Academy of Sciences of the United States of America*, vol. 105, no. 38, pp. 14 271–14 276, Sep. 2008.

[30] E. Betzig, G. H. Patterson, R. Sougrat, O. W. Lindwasser, S. Olenych, *et al.*, "Imaging Intracellular Fluorescent Proteins at Nanometer Resolution", *Science*, vol. 313, no. 5793, pp. 1642–1645, Sep. 2006.

[31] M. J. Rust, M. Bates, and X. Zhuang, "Sub-diffraction-limit imaging by stochastic optical reconstruction microscopy (STORM)", *Nature Publishing Group*, vol. 3, no. 10, pp. 793–796, Aug. 2006.

[32] M. G. L. Gustafsson, "Nonlinear structured-illumination microscopy: Wide-field fluorescence imaging with theoretically unlimited resolution", *Proceedings of the National Academy of Sciences of the United States of America*, vol. 102, no. 37, pp. 13 081–13 086, Sep. 2005.

[33] P. J. M. Zessin, K. Finan, and M. Heilemann, "Super-resolution fluorescence imaging of chromosomal DNA", *Journal of structural biology*, vol. 177, no. 2, pp. 344–348, Feb. 2012.

[34] C. Flors and W. C. Earnshaw, "Super-resolution fluorescence microscopy as a tool to study the nanoscale organization of chromosomes.", *Current Opinion in Chemical Biology*, vol. 15, no. 6, pp. 838–844, Dec. 2011.

[35] L. Chakalova, E. Debrand, J. A. Mitchell, C. S. Osborne, and P. Fraser, "Replication and transcription: Shaping the landscape of the genome", *Nature Reviews Genetics*, vol. 6, no. 9, pp. 669–677, Sep. 2005.

[36] C. Spahn, U. Endesfelder, and M. Heilemann, "Super-resolution imaging of Escherichia coli nucleoids reveals highly structured and asymmetric segregation during fast growth", *Journal of structural biology*, vol. 185, no. 3, pp. 243–249, Mar. 2014.

[37] W. J. Greenleaf, M. T. Woodside, and S. M. Block, "High-resolution, single-molecule measurements of biomolecular motion.", *Annual review of biophysics and biomolecular structure*, vol. 36, pp. 171–190, 2007.

[38] T. Ha, T. Enderle, D. F. Ogletree, D. S. Chemla, P. R. Selvin, *et al.*, "Probing the interaction between two single molecules: fluorescence resonance energy transfer between a single donor and a single acceptor.", *Proceedings of the National Academy of Sciences*, vol. 93, no. 13, pp. 6264–6268, Jun. 1996.

[39] T. Ha, I. Rasnik, W. Cheng, H. P. Babcock, G. H. Gauss, *et al.*, "Initiation and re-initiation of DNA unwinding by the Escherichia coli Rep helicase", *Nature*, vol. 419, no. 6907, pp. 638–641, Oct. 2002.

[40] B. Schuler and W. A. Eaton, "Protein folding studied by single-molecule FRET.", *Current Opinion in Structural Biology*, vol. 18, no. 1, pp. 16–26, Feb. 2008.

[41] A. Gansen, A. Valeri, F. Hauger, S. Felekyan, S. Kalinin, *et al.*, "Nucleosome disassembly intermediates characterized by single-molecule FRET.", *Proceedings of the National Academy of Sciences of the United States of America*, vol. 106, no. 36, pp. 15 308–15 313, Sep. 2009.

[42] Y. Wang, Y. Liu, H. A. Deberg, T. Nomura, M. T. Hoffman, *et al.*, "Single molecule FRET reveals pore size and opening mechanism of a mechano-sensitive ion channel.", *eLife Sciences*, vol. 3, e01834, 2014.

[43] R. Roy, S. Hohng, and T. Ha, "A practical guide to single-molecule FRET.", *Nature methods*, vol. 5, no. 6, pp. 507–516, Jun. 2008.

[44] E. M. Puchner and H. E. Gaub, "Force and function: probing proteins with AFM-based force spectroscopy.", *Current Opinion in Structural Biology*, vol. 19, no. 5, pp. 605–614, Oct. 2009.

[45] K. C. Neuman and A. Nagy, "Single-molecule force spectroscopy: optical tweezers, magnetic tweezers and atomic force microscopy.", *Nature methods*, vol. 5, no. 6, pp. 491–505, Jun. 2008.

[46] E. A. Abbondanzieri, W. J. Greenleaf, J. W. Shaevitz, R. Landick, and S. M. Block, "Direct observation of base-pair stepping by RNA polymerase.", *Nature*, vol. 438, no. 7067, pp. 460–465, Nov. 2005.

[47] S. Hohng, R. Zhou, M. K. Nahas, J. Yu, K. Schulten, *et al.*, "Fluorescence-Force Spectroscopy Maps Two-Dimensional Reaction Landscape of the Holliday Junction", *Science*, vol. 318, no. 5848, pp. 279–283, Oct. 2007.

[48] M. Grandbois, M. Beyer, M. Rief, H. Clausen-Schaumann, and H. E. Gaub, "How Strong Is a Covalent Bond?", *Science*, vol. 283, no. 5408, pp. 1727–1730, Mar. 1999.

[49] J. R. Moffitt, Y. R. Chemla, S. B. Smith, and C. Bustamante, "Recent advances in optical tweezers.", *Annual Review of Biochemistry*, vol. 77, no. 1, pp. 205–228, 2008.

[50] I. De Vlaminck and C. Dekker, "Recent advances in magnetic tweezers.", *Annual review of biophysics*, vol. 41, no. 1, pp. 453–472, 2012.

[51] A. Celedon, I. M. Nodelman, B. Wildt, R. Dewan, P. Searson, *et al.*, "Magnetic tweezers measurement of single molecule torque.", *Nano letters*, vol. 9, no. 4, pp. 1720–1725, Apr. 2009.

[52] J. R. Moffitt, Y. R. Chemla, D. Izhaky, and C. Bustamante, "Differential detection of dual traps improves the spatial resolution of optical tweezers.", *Proceedings of the National Academy of Sciences*, vol. 103, no. 24, pp. 9006–9011, Jun. 2006.

[53] M. D. Wang, "Force and Velocity Measured for Single Molecules of RNA Polymerase", *Science*, vol. 282, no. 5390, pp. 902–907, Oct. 1998.

[54] J. W. Shaevitz, E. A. Abbondanzieri, R. Landick, and S. M. Block, "Backtracking by single RNA polymerase molecules observed at near-base-pair resolution.", *Nature*, vol. 426, no. 6967, pp. 684–687, Dec. 2003.

[55] T. C. Boles, J. H. White, and N. R. Cozzarelli, "Structure of plectonemically supercoiled DNA.", *Journal of molecular biology*, vol. 213, no. 4, pp. 931–951, Jun. 1990.

[56] N. Clauvelin, B. Audoly, and S. Neukirch, "Elasticity and Electrostatics of Plectonemic DNA", *Biophysical Journal*, vol. 96, no. 9, pp. 3716–3723, May 2009.

[57] R. Vlijm, J. S. J. Smitshuijzen, A. Lusser, and C. Dekker, "NAP1-Assisted Nucleosome Assembly on DNA Measured in Real Time by Single-Molecule Magnetic Tweezers", *PloS one*, vol. 7, no. 9, e46306, 2012.

[58] M. T. J. van Loenhout, M. V. de Grunt, and C. Dekker, "Dynamics of DNA supercoils.", *Science*, vol. 338, no. 6103, pp. 94–97, Oct. 2012.

[59] D. J. Müller, "AFM: a nanotool in membrane biology.", *Biochemistry*, vol. 47, no. 31, pp. 7986–7998, Aug. 2008.

[60] M. Shibata, H. Yamashita, T. Uchihashi, H. Kandori, and T. Ando, "High-speed atomic force microscopy shows dynamic molecular processes in photoactivated bacteriorhodopsin", *Nature Nanotechnology*, vol. 5, no. 3, pp. 208–212, Feb. 2010.

[61] G. Binnig and C. F. Quate, "Atomic Force Microscope", *Physical Review Letters*, vol. 56, no. 9, pp. 930–933, Mar. 1986.

[62] M. Radmacher, R. W. Tillmann, M. Fritz, and H. E. Gaub, "From Molecules to Cells - Imaging Soft Samples with the Atomic Force Microscope", *Science*, vol. 257, no. 5078, pp. 1900–1905, 1992.

[63] S. Alexander, L. Hellemans, O. Marti, J. Schneir, V. Elings, *et al.*, "An atomic-resolution atomic-force microscope implemented using an optical lever", *Journal of Applied Physics*, vol. 65, no. 1, p. 164, 1989.

[64] F. Moreno-Herrero and J. Gomez-Herrero, *AFM: Basic Concepts*, ser. Biological Applications. Weinheim, Germany: Wiley-VCH Verlag GmbH & Co. KGaA, 2012.

[65] H. G. Hansma, "Atomic force microscopy of biomolecules", *Journal of Vacuum Science & Technology B: Microelectronics and Nanometer Structures*, vol. 14, no. 2, p. 1390, Mar. 1996.

[66] B. Drake, C. B. Prater, A. L. Weisenhorn, S. A. C. Gould, T. R. Albrecht, *et al.*, "Imaging crystals, polymers, and processes in water with the atomic force microscope.", *Science*, vol. 243, no. 4898, pp. 1586–1589, Mar. 1989.

[67] D. J. Müller and K. Anderson, "Biomolecular imaging using atomic force microscopy", *Trends in biotechnology*, vol. 20, no. 8, S45–S49, Aug. 2002.

[68] A. Pyne, R. Thompson, C. Leung, D. Roy, and B. W. Hoogenboom, "Single-Molecule Reconstruction of Oligonucleotide Secondary Structure by Atomic Force Microscopy", *Small*, vol. 10, no. 16, pp. 3257–3261, Apr. 2014.

[69] S. Ido, K. Kimura, N. Oyabu, K. Kobayashi, M. Tsukada, *et al.*, "Beyond the Helix Pitch: Direct Visualization of Native DNA in Aqueous Solution", *ACS Nano*, vol. 7, no. 2, pp. 1817–1822, Feb. 2013.

[70] C. Leung, A. Bestembayeva, R. Thorogate, J. Stinson, A. Pyne, *et al.*, "Atomic Force Microscopy with Nanoscale Cantilevers Resolves Different Structural Conformations of the DNA Double Helix", *Nano letters*, vol. 12, no. 7, pp. 3846–3850, 2012.

[71] Y. L. Lyubchenko, L. S. Shlyakhtenko, and T. Ando, "Imaging of nucleic acids with atomic force microscopy", *Methods*, vol. 54, no. 2, pp. 274–283, Jun. 2011.

[72] K. Umemura, F. Nagami, T. Okada, and R. Kuroda, "AFM characterization of single strand-specific endonuclease activity on linear DNA", *Nucleic Acids Research*, vol. 28, no. 9, e39–e39, May 2000.

[73] N. H. Thomson, S. Kasas, Smith, H. G. Hansma, and P. K. Hansma, "Reversible Binding of DNA to Mica for AFM Imaging", *Langmuir*, vol. 12, no. 24, pp. 5905–5908, Jan. 1996.

[74] M. Imamura, T. Uchihashi, T. Ando, A. Leifert, U. Simon, *et al.*, "Probing Structural Dynamics of an Artificial Protein Cage Using High-Speed Atomic Force Microscopy", *Nano letters*, vol. 15, no. 2, pp. 1331–1335, Jan. 2015.

[75] N. Kodera, K. Uchida, T. Ando, and S.-I. Aizawa, "Two-Ball Structure of the Flagellar Hook-Length Control Protein FliK as Revealed by High-Speed Atomic Force Microscopy", *Journal of molecular biology*, vol. 427, no. 2, pp. 406–414, Jan. 2015.

[76] S. A. Contera, K. Voitchovsky, and J. F. Ryan, "Controlled ionic condensation at the surface of a native extremophile membrane", *Nanoscale*, vol. 2, no. 2, p. 222, 2010.

[77] P.-E. Milhiet, F. Gubellini, A. Berquand, P. Dosset, J.-L. Rigaud, *et al.*, "High-resolution AFM of membrane proteins directly incorporated at high density in planar lipid bilayer.", *Biophysical Journal*, vol. 91, no. 9, pp. 3268–3275, Nov. 2006.

[78] A. Engel and D. J. Müller, "Observing single biomolecules at work with the atomic force microscope", *Nature Structural Biology*, vol. 7, no. 9, pp. 715–718, Sep. 2000.

[79] A. Colom, I. Casuso, F. Rico, and S. Scheuring, "A hybrid high-speed atomic force-optical microscope for visualizing single membrane proteins on eukaryotic cells.", *Nature Communications*, vol. 4, p. 2155, 2013.

[80] I. Casuso, J. Khao, M. Chami, P. Paul-Gilloteaux, M. Husain, *et al.*, "Characterization of the motion of membrane proteins using high-speed atomic force microscopy", *Nature Nanotechnology*, vol. 7, no. 8, pp. 525–529, Aug. 2012.

[81] H. Yamashita, A. Taoka, T. Uchihashi, T. Asano, T. Ando, *et al.*, "Single-Molecule Imaging on Living Bacterial Cell Surface by High-Speed AFM", *Journal of molecular biology*, vol. 422, no. 2, pp. 300–309, Sep. 2012.

[82] P. Parot, Y. F. Dufrêne, P. Hinterdorfer, C. Le Grimellec, D. Navajas, *et al.*, "Past, present and future of atomic force microscopy in life sciences and medicine.", *Journal of molecular recognition : JMR*, vol. 20, no. 6, pp. 418–431, Nov. 2007.

[83] H. G. Hansma, "Surface Biology of DNA by Atomic Force Microscopy", *Annual Review of Physical Chemistry*, vol. 52, no. 1, pp. 71–92, Oct. 2001.

[84] L. Bintu, M. Kopaczynska, C. Hodges, L. Lubkowska, M. Kashlev, *et al.*, "The elongation rate of RNA polymerase determines the fate of transcribed nucleosomes", *Nature Structural & Molecular Biology*, vol. 18, no. 12, pp. 1394–1399, Dec. 2011.

[85] D. J. Billingsley, W. A. Bonass, N. Crampton, J. Kirkham, and N. H. Thomson, "Single-molecule studies of DNA transcription using atomic force microscopy", *Physical Biology*, vol. 9, no. 2, p. 021 001, Apr. 2012.

[86] N. Crampton, W. A. Bonass, J. Kirkham, C. Rivetti, and N. H. Thomson, "Collision events between RNA polymerases in convergent transcription studied by atomic force microscopy.", *Nucleic Acids Research*, vol. 34, no. 19, pp. 5416–5425, 2006.

[87] A. Engel and H. E. Gaub, "Structure and Mechanics of Membrane Proteins", *Annual Review of Biochemistry*, vol. 77, no. 1, pp. 127–148, Jun. 2008.

[88] M. T. Young, "P2X receptors: dawn of the post-structure era", *Trends in Biochemical Sciences*, vol. 35, no. 2, pp. 83–90, Feb. 2010.

[89] S. Jarosławski, B. Zadek, F. Ashcroft, C. Vénien-Bryan, and S. Scheuring, "Direct Visualization of KirBac3.1 Potassium Channel Gating by Atomic Force Microscopy", *Journal of molecular biology*, vol. 374, no. 2, pp. 500–505, Nov. 2007.

[90] J. Kowal, M. Chami, P. Baumgartner, M. Arheit, P.-L. Chiu, *et al.*, "Ligand-induced structural changes in the cyclic nucleotide-modulated potassium channel MloK1", *Nature Communications*, vol. 5, Jan. 2014.

[91] M. Pfreundschuh, U. Hensen, and D. J. Müller, "Quantitative Imaging of the Electrostatic Field and Potential Generated by a Transmembrane Protein Pore at Subnanometer Resolution", *Nano letters*, vol. 13, no. 11, pp. 5585–5593, Nov. 2013.

[92] Y. Shinozaki, K. Sumitomo, M. Tsuda, S. Koizumi, K. Inoue, *et al.*, "Direct Observation of ATP-Induced Conformational Changes in Single P2X4 Receptors", *PLoS Biology*, vol. 7, no. 5, e103, 2009.

[93] D. Fotiadis, Y. Liang, S. Filipek, D. A. Saperstein, A. Engel, *et al.*, "Atomic-force microscopy: Rhodopsin dimers in native disc membranes.", *Nature*, vol. 421, no. 6919, pp. 127–128, Jan. 2003.

[94] B. W. Hoogenboom, K. Suda, A. Engel, and D. Fotiadis, "The Supramolecular Assemblies of Voltage-dependent Anion Channels in the Native Membrane", *Journal of molecular biology*, vol. 370, no. 2, pp. 246–255, Jul. 2007.

[95] H. Yamashita, K. Voitchovsky, T. Uchihashi, S. A. Contera, J. F. Ryan, *et al.*, "Dynamics of bacteriorhodopsin 2D crystal observed by high-speed atomic force microscopy", *Journal of structural biology*, vol. 167, no. 2, pp. 153–158, Aug. 2009.

[96] I. Casuso, N. Kodera, C. Le Grimellec, T. Ando, and S. Scheuring, "Contact-Mode High-Resolution High-Speed Atomic Force Microscopy Movies of the Purple Membrane", *Biophysical Journal*, vol. 97, no. 5, pp. 1354–1361, Sep. 2009.

[97] K. Voitchovsky, S. A. Contera, and J. F. Ryan, "Lateral coupling and cooperative dynamics in the function of the native membrane protein bacteriorhodopsin", *Soft Matter*, vol. 5, no. 24, p. 4899, 2009.

[98] J. R. Sellers, "Myosins: a diverse superfamily", *Biochimica et Biophysica Acta (BBA) - Molecular Cell Research*, vol. 1496, no. 1, pp. 3–22, Mar. 2000.

[99] N. Kodera, D. Yamamoto, R. Ishikawa, and T. Ando, "Video imaging of walking myosin V by high-speed atomic force microscopy", *Nature*, vol. 468, no. 7320, pp. 72–76, Oct. 2010.

[100] T. Sakamoto, I. Amitani, E. Yokota, and T. Ando, "Direct Observation of Processive Movement by Individual Myosin V Molecules", *Biochemical and Biophysical Research Communications*, vol. 272, no. 2, pp. 586–590, Jun. 2000.

[101] N. Kodera and T. Ando, "The path to visualization of walking myosin V by high-speed atomic force microscopy", *Biophysical Reviews*, vol. 6, no. 3-4, pp. 237–260, Jun. 2014.

[102] F. Rico, L. Gonzalez, I. Casuso, M. Puig-Vidal, and S. Scheuring, "High-speed force spectroscopy unfolds titin at the velocity of molecular dynamics simulations.", *Science*, vol. 342, no. 6159, pp. 741–743, Nov. 2013.

[103] M. Rief, M. Gautel, F. Oesterhelt, J. M. Fernandez, and H. E. Gaub, "Reversible unfolding of individual titin immunoglobulin domains by AFM", *Science*, vol. 276, no. 5315, pp. 1109–1112, 1997.

[104] H. Clausen-Schaumann, M. Rief, C. Tolksdorf, and H. E. Gaub, "Mechanical stability of single DNA molecules", *Biophysical Journal*, vol. 78, no. 4, pp. 1997–2007, Apr. 2000.

[105] T. Fukuma, K. Onishi, N. Kobayashi, A. Matsuki, and H. Asakawa, "Atomic-resolution imaging in liquid by frequency modulation atomic force microscopy using small cantilevers with megahertz-order resonance frequencies", *Nanotechnology*, vol. 23, no. 13, p. 135 706, Mar. 2012.

[106] K. Suzuki, S.-i. Kitamura, S. Tanaka, K. Kobayashi, and H. Yamada, "Development of High-Resolution Imaging of Solid–Liquid Interface by Frequency Modulation Atomic Force Microscopy", *Japanese Journal of Applied Physics*, vol. 49, no. 8, 08LB12, Aug. 2010.

[107] Z. Khan, C. Leung, B. A. Tahir, and B. W. Hoogenboom, "Digitally tunable, wide-band amplitude, phase, and frequency detection for atomic-resolution scanning force microscopy", *Review of Scientific Instruments*, vol. 81, no. 7, p. 073 704, 2010.

[108] K. Voitchovsky, J. J. Kuna, S. A. Contera, E. Tosatti, and F. Stellacci, "Direct mapping of the solid–liquid adhesion energy with subnanometre resolution", *Nature Nanotechnology*, vol. 5, no. 6, pp. 401–405, Apr. 2010.

[109] T. Fukuma, K. Kobayashi, K. Matsushige, and H. Yamada, "True atomic resolution in liquid by frequency-modulation atomic force microscopy", *Applied Physics Letters*, vol. 87, no. 3, p. 034 101, 2005.

[110] S. M. R. Akrami, H. Nakayachi, T. Watanabe-Nakayama, H. Asakawa, and T. Fukuma, "Significant improvements in stability and reproducibility of atomic-scale atomic force microscopy in liquid.", *Nanotechnology*, vol. 25, no. 45, p. 455 701, Nov. 2014.

[111] Y. L. Lyubchenko, "AFM Imaging in Liquid of DNA and Protein–DNA Complexes", in *Biological Applications*, Weinheim, Germany: Wiley-VCH Verlag GmbH & Co. KGaA, 2012, pp. 231–258.

[112] H. Sánchez, Y. Suzuki, M. Yokokawa, K. Takeyasu, and C. Wyman, "Protein-DNA interactions in high speed AFM: single molecule diffusion analysis of human RAD54.", *Integrative biology : quantitative biosciences from nano to macro*, vol. 3, no. 11, pp. 1127–1134, Nov. 2011.

[113] A. Miyagi, T. Ando, and Y. L. Lyubchenko, "Dynamics of Nucleosomes Assessed with Time-Lapse High-Speed Atomic Force Microscopy", *Biochemistry*, vol. 50, no. 37, pp. 7901–7908, Sep. 2011.

[114] I. Casuso, F. Rico, and S. Scheuring, "Biological AFM: where we come from - where we are - where we may go", *Journal of molecular recognition : JMR*, vol. 24, no. 3, pp. 406–413, Apr. 2011.

[115] Y. Li, Y. D. Tseng, S. Y. Kwon, L. d'Espaux, J. S. Bunch, *et al.*, "Controlled assembly of dendrimer-like DNA", *Nature materials*, vol. 3, no. 1, pp. 38–42, Dec. 2003.

[116] J. Mou, D. M. Czajkowsky, Y. Zhang, and Z. Shao, "High-resolution atomic-force microscopy of DNA: the pitch of the double helix", *FEBS letters*, vol. 371, no. 3, pp. 279–282, Sep. 1995.

[117] H. G. Hansma and D. E. Laney, "DNA binding to mica correlates with cationic radius: assay by atomic force microscopy", *Biophysical Journal*, vol. 70, no. 4, pp. 1933–1939, Apr. 1996.

[118] D. Pastré, L. Hamon, F. Landousy, I. Sorel, M.-O. David, *et al.*, "Anionic Polyelectrolyte Adsorption on Mica Mediated by Multivalent Cations: A Solution to DNA Imaging by Atomic Force Microscopy under High Ionic Strengths", *Langmuir*, vol. 22, no. 15, pp. 6651–6660, Jul. 2006.

[119] S. Ido, H. Kimiya, K. Kobayashi, H. Kominami, K. Matsushige, *et al.*, "Immunoactive two-dimensional self-assembly of monoclonal antibodies in aqueous solution revealed by atomic force microscopy", *Nature materials*, vol. 13, no. 3, pp. 264–270, Jan. 2014.

[120] A. D. Bates and A. Maxwell, *DNA Topology*, ser. Oxford bioscience. OUP Oxford, 2005, vol. 9.

[121] A. Rich and S. Zhang, "Z-DNA: the long road to biological function", *Nature Reviews Genetics*, vol. 4, no. 7, pp. 566–572, Jul. 2003.

[122] R. R. Sinden, "The helix turns at 60: writhing free in chromosomes", *Nature Structural & Molecular Biology*, vol. 20, no. 3, pp. 251–253, Mar. 2013.

[123] C. J. Dorman, "DNA supercoiling and bacterial gene expression", *Science Progress*, vol. 89, no. 3, pp. 151–166, Aug. 2006.

[124] G. M. Andrew Travers, "A common topology for bacterial and eukaryotic transcription initiation?", *EMBO reports*, vol. 8, no. 2, pp. 147–151, Feb. 2007.

[125] D. M. Gowers and S. E. Halford, "Protein motion from non-specific to specific DNA by three-dimensional routes aided by supercoiling", *The EMBO Journal*, vol. 22, no. 6, pp. 1410–1418, Mar. 2003.

[126] J. E. Deweese, M. A. Osheroff, and N. Osheroff, "DNA Topology and Topoisomerases: Teaching a "Knotty" Subject", *Biochemistry and molecular biology education : a bimonthly publication of the International Union of Biochemistry and Molecular Biology*, vol. 37, no. 1, pp. 2–10, 2008.

[127] S. M. Mirkin, *DNA Topology: Fundamentals*. Chichester, UK: John Wiley & Sons, Ltd, 2001.

[128] J. F. Marko, "Biophysics of protein-DNA interactions and chromosome organization", *Physica a-Statistical Mechanics and Its Applications*, vol. 418, pp. 126–153, 2015.

[129] S. A. Harris, "Modelling the biomechanical properties of DNA using computer simulation", *Philosophical Transactions of the Royal Society of London A: Mathematical, Physical and Engineering Sciences*, vol. 364, no. 1849, pp. 3319–3334, Dec. 2006.

[130] J. Adamcik, J.-H. Jeon, K. J. Karczewski, R. Metzler, and G. Dietler, "Quantifying supercoiling-induced denaturation bubbles in DNA", *Soft Matter*, vol. 8, no. 33, pp. 8651–8658, 2012.

[131] B. Akerman, "Effects of supercoiling in electrophoretic trapping of circular DNA in polyacrylamide gels.", *Biophysical Journal*, vol. 74, no. 6, pp. 3140–3151, Jun. 1998.

[132] J. Zlatanova and S. H. Leuba, "Magnetic tweezers: a sensitive tool to study DNA and chromatin at the single-molecule level", *Biochemistry and Cell Biology*, Jan. 2011.

[133] P. Gross, N. Laurens, L. B. Oddershede, U. Bockelmann, E. J. G. Peterman, *et al.*, "Quantifying how DNA stretches, melts and changes twist under tension", *Nature Physics*, vol. 7, no. 9, pp. 731–736, May 2011.

[134] C. Naughton, N. Avlonitis, S. Corless, J. G. Prendergast, I. K. Mati, *et al.*, "Transcription forms and remodels supercoiling domains unfolding large-scale chromatin structures.", *Nature Structural Biology*, vol. 20, no. 3, pp. 387–395, Mar. 2013.

[135] K. Matsumoto and S. Hirose, "Visualization of unconstrained negative supercoils of DNA on polytene chromosomes of Drosophila.", *Journal of cell science*, vol. 117, no. Pt 17, pp. 3797–3805, Aug. 2004.

[136] F. Collin, S. Karkare, and A. Maxwell, "Exploiting bacterial DNA gyrase as a drug target: current state and perspectives", *Applied Microbiology and Biotechnology*, vol. 92, no. 3, pp. 479–497, Sep. 2011.

[137] E. M. McGuffie, D. Pacheco, G. M. Carbone, and C. V. Catapano, "Antigene and antiproliferative effects of a c-myc-targeting phosphorothioate triple helix-forming oligonucleotide in human leukemia cells.", *Cancer research*, vol. 60, no. 14, pp. 3790–3799, Jul. 2000.

[138] P. W. Hewett, E. L. Daft, C. A. Laughton, S. Ahmad, A. Ahmed, *et al.*, "Selective inhibition of the human tie-1 promoter with triplex-forming oligonucleotides targeted to Ets binding sites", *Molecular Medicine*, vol. 12, no. 1-3, p. 8, 2006.

[139] A. Veloso, B. Biewen, M. T. Paulsen, N. Berg, L. C. de Andrade Lima, *et al.*, "Genome-Wide Transcriptional Effects of the Anti-Cancer Agent Camptothecin", *PloS one*, vol. 8, no. 10, e78190, Oct. 2013.

[140] Y. Pommier, "Drugging Topoisomerases: Lessons and Challenges", *ACS Chemical Biology*, vol. 8, no. 1, pp. 82–95, Jan. 2013.

[141] N. K. Brogden and K. A. Brogden, "Will new generations of modified antimicrobial peptides improve their potential as pharmaceuticals?", *International journal of antimicrobial agents*, Jul. 2011.

[142] G. Wang, X. Li, and Z. Wang, "APD2: the updated antimicrobial peptide database and its application in peptide design", *Nucleic Acids Research*, vol. 37, no. Database issue, pp. D933–D937, Jan. 2009.

[143] J.-P. S. Powers and R. E. Hancock, "The relationship between peptide structure and antibacterial activity.", *Peptides*, vol. 24, no. 11, pp. 1681–1691, Nov. 2003.

[144] L. Zhang, A. Rozek, and R. E. W. Hancock, "Interaction of Cationic Antimicrobial Peptides with Model Membranes", *The Journal of Biological Chemistry*, vol. 276, no. 38, pp. 35 714–35 722, Sep. 2001.

[145] H. Steiner, D. Hultmark, A. Engström, H. Bennich, and H. G. Boman, "Sequence and specificity of two antibacterial proteins involved in insect immunity.", *Nature*, vol. 292, no. 5820, pp. 246–248, Jul. 1981.

[146] C. D. Fjell, J. A. Hiss, R. E. Hancock, and G. Schneider, "Designing antimicrobial peptides: form follows function", *Nature Reviews Drug Discovery*, Dec. 2011.

[147] L. Yang, T. A. Harroun, T. M. Weiss, L. Ding, and H. W. Huang, "Barrel-Stave Model or Toroidal Model? A Case Study on Melittin Pores", *Biophysical Journal*, vol. 81, no. 3, pp. 1475–1485, Sep. 2001.

[148] Z. Oren and Y. Shai, "Mode of action of linear amphipathic alpha-helical antimicrobial peptides.", *Biopolymers*, vol. 47, no. 6, pp. 451–463, 1998.

[149] H. Jenssen, P. Hamill, and R. E. W. Hancock, "Peptide Antimicrobial Agents", *Clinical Microbiology Reviews*, vol. 19, no. 3, pp. 491–511, Jul. 2006.

[150] R. E. Hancock and H.-G. Sahl, "Antimicrobial and host-defense peptides as new anti-infective therapeutic strategies", vol. 24, no. 12, pp. 1551–1557, Dec. 2006.

[151] O. K. Abou-Zied, A. Barbour, N. A. Al-Sharji, and K. Philip, "Elucidating the mechanism of peptide interaction with membranes using the intrinsic fluorescence of tryptophan: perpendicular penetration of cecropin B-like peptides into Pseudomonas aeruginosa", *RSC Advances*, vol. 5, no. 19, pp. 14 214–14 220, 2015.

[152] A. Bahar and D. Ren, "Antimicrobial Peptides", *Pharmaceuticals*, vol. 6, no. 12, pp. 1543–1575, Nov. 2013.

[153] M. Zasloff, "Antimicrobial peptides of multicellular organisms", *Nature*, vol. 415, no. 6870, pp. 389–395, Jan. 2002.

[154] H. Sato and J. B. Feix, "Peptide-membrane interactions and mechanisms of membrane destruction by amphipathic alpha-helical antimicrobial peptides.", *Biochimica et biophysica acta*, vol. 1758, no. 9, pp. 1245–1256, Sep. 2006.

[155] S. Qian, W. Wang, L. Yang, and H. W. Huang, "Structure of transmembrane pore induced by Bax-derived peptide: Evidence for lipidic pores", *Proceedings of the National Academy of Sciences of the United States of America*, vol. 105, no. 45, pp. 17 379–17 383, Nov. 2008.

[156] K. Matsuzaki, S. Yoneyama, and K. Miyajima, "Pore formation and translocation of melittin", *Biophysical Journal*, vol. 73, no. 2, pp. 831–838, Aug. 1997.

[157] Y. Pouny, D. Rapaport, A. Mor, P. Nicolas, and Y. Shai, "Interaction of antimicrobial dermaseptin and its fluorescently labeled analogs with phospholipid membranes", *Biochemistry*, vol. 31, no. 49, pp. 12 416–12 423, Dec. 1992.

[158] H. W. Huang, "Action of Antimicrobial Peptides: Two-State Model", *Biochemistry*, vol. 39, no. 29, pp. 8347–8352, Jul. 2000.

[159] J. L. Fox, "Antimicrobial peptides stage a comeback", *Nature Biotechnology*, vol. 31, no. 5, pp. 379–382, May 2013.

[160] T. Schneider, T. Kruse, R. Wimmer, I. Wiedemann, V. Sass, *et al.*, "Plectasin, a fungal defensin, targets the bacterial cell wall precursor Lipid II.", *Science*, vol. 328, no. 5982, pp. 1168–1172, May 2010.

[161] P. H. Mygind, R. L. Fischer, K. M. Schnorr, M. T. Hansen, C. P. Sönksen, *et al.*, "Plectasin is a peptide antibiotic with therapeutic potential from a saprophytic fungus", *Nature*, vol. 437, no. 7061, pp. 975–980, Oct. 2005.

[162] D. Hultmark, A. Engström, H. Bennich, R. KAPUR, and H. G. Boman, "Insect Immunity: Isolation and Structure of Cecropin D and Four Minor Antibacterial Components from Cecropia Pupae", *European journal of biochemistry / FEBS*, vol. 127, no. 1, pp. 207–217, Sep. 1982.

[163] I. Zelezetsky and A. Tossi, "Alpha-helical antimicrobial peptides–using a sequence template to guide structure-activity relationship studies.", *Biochimica et biophysica acta*, vol. 1758, no. 9, pp. 1436–1449, Sep. 2006.

[164] H. M. Chen, W. Wang, D. Smith, and S. C. Chan, "Effects of the anti-bacterial peptide cecropin B and its analogs, cecropins B-1 and B-2, on liposomes, bacteria, and cancer cells", *Biochimica et Biophysica Acta (BBA) - General Subjects*, vol. 1336, no. 2, pp. 171–179, Aug. 1997.

[165] J.-M. Wu, P.-S. Jan, H.-C. Yu, H.-Y. Haung, H.-J. Fang, *et al.*, "Structure and function of a custom anticancer peptide, CB1a", *Peptides*, vol. 30, no. 5, pp. 839–848, May 2009.

[166] B. Bechinger, "Insights into the mechanisms of action of host defence peptides from biophysical and structural investigations", *Journal of Peptide Science*, vol. 17, no. 5, pp. 306–314, Feb. 2011.

[167] M. N. Melo, R. Ferre, and M. A. R. B. Castanho, "Antimicrobial peptides: linking partition, activity and high membrane-bound concentrations", *Nature Reviews Microbiology*, vol. 7, no. 3, pp. 245–250, Mar. 2009.

[168] S. M. Gregory, A. Cavenaugh, V. Journigan, A. Pokorny, and P. F. F. Almeida, "A Quantitative Model for the All-or-None Permeabilization of Phospholipid Vesicles by the Antimicrobial Peptide Cecropin A", *Biophysical Journal*, vol. 94, no. 5, pp. 1667–1680, Mar. 2008.

[169] K. A. Brogden, "Antimicrobial peptides: pore formers or metabolic inhibitors in bacteria?", *Nature Reviews Microbiology*, vol. 3, no. 3, pp. 238–250, Mar. 2005.

[170] W. Wang, D. K. Smith, K. Moulding, and H. M. Chen, "The Dependence of Membrane Permeability by the Antibacterial Peptide Cecropin B and Its Analogs, CB-1 and CB-3, on Liposomes of Different Composition", *The Journal of Biological Chemistry*, vol. 273, no. 42, pp. 27 438–27 448, Oct. 1998.

[171] B. Bechinger and K. Lohner, "Detergent-like actions of linear amphipathic cationic antimicrobial peptides", *BBA - Biomembranes*, vol. 1758, no. 9, pp. 1529–1539, Sep. 2006.

[172] K. He, S. J. Ludtke, W. T. Heller, and H. W. Huang, "Mechanism of alamethicin insertion into lipid bilayers", *Biophysical Journal*, vol. 71, no. 5, pp. 2669–2679, Nov. 1996.

[173] S. S. Efimova, L. V. Schagina, and O. S. Ostroumova, "Channel-forming activity of cecropins in lipid bilayers: effect of agents modifying the membrane dipole potential.", *Langmuir*, vol. 30, no. 26, pp. 7884–7892, Jul. 2014.

[174] L. T. Nguyen, E. F. Haney, and H. J. Vogel, "The expanding scope of antimicrobial peptide structures and their modes of action", *Trends in biotechnology*, vol. 29, no. 9, pp. 464–472, Sep. 2011.

[175] N. K. Brogden and K. A. Brogden, "Will new generations of modified antimicrobial peptides improve their potential as pharmaceuticals?", *International journal of antimicrobial agents*, Jul. 2011.

[176] M.-P. Mingeot-Leclercq, M. Deleu, R. Brasseur, and Y. F. Dufrêne, "Atomic force microscopy of supported lipid bilayers", *Nature Protocols*, vol. 3, no. 10, pp. 1654–1659, Oct. 2008.

[177] E. Sezgin and P. Schwille, "Model membrane platforms to study protein-membrane interactions", *Molecular membrane biology*, vol. 29, no. 5, pp. 144–154, Aug. 2012.

[178] C.-h. Yu and J. T. Groves, "Engineering supported membranes for cell biology", *Medical & Biological Engineering & Computing*, vol. 48, no. 10, pp. 955–963, Jun. 2010.

[179] Y. F. Dufrêne and G. U. Lee, "Advances in the characterization of supported lipid films with the atomic force microscope", *Biochimica et Biophysica Acta (BBA)-Biomembranes*, vol. 1509, no. 1-2, pp. 14–41, Dec. 2000.

[180] P. K. Hansma, J. P. Cleveland, M. Radmacher, D. A. Walters, P. E. Hillner, *et al.*, "Tapping mode atomic force microscopy in liquids", *Applied Physics Letters*, vol. 64, no. 13, p. 1738, 1994.

[181] D. J. Müller, D. Fotiadis, S. Scheuring, S. A. Müller, and A. Engel, "Electrostatically Balanced Subnanometer Imaging of Biological Specimens by Atomic Force Microscope", *Biophysical Journal*, vol. 76, no. 2, pp. 1101–1111, Feb. 1999.

[182] Q. Zhong, D. Inniss, K. Kjoller, and V. B. Elings, "Fractured polymer/silica fiber surface studied by tapping mode atomic force microscopy", *Surface Science Letters*, vol. 290, no. 1-2, pp. L688–L692, Jun. 1993.

[183] T. E. Schäffer, J. P. Cleveland, F. Ohnesorge, D. A. Walters, and P. K. Hansma, "Studies of vibrating atomic force microscope cantilevers in liquid", *Journal of Applied Physics*, vol. 80, no. 7, p. 3622, 1996.

[184] R. Garcia, "Dynamic atomic force microscopy methods", *Surface Science Reports*, vol. 47, no. 6-8, pp. 197–301, Sep. 2002.

[185] H.-J. Butt and M. Jaschke, "Calculation of thermal noise in atomic force microscopy", *Nanotechnology*, vol. 6, no. 1, pp. 1–7, Jan. 1999.

[186] R. Garcia and E. T. Herruzo, "The emergence of multifrequency force microscopy", *Nature Nanotechnology*, vol. 7, no. 4, pp. 217–226, Apr. 2012.

[187] J. Preiner, J. Tang, V. Pastushenko, and P. Hinterdorfer, "Higher Harmonic Atomic Force Microscopy: Imaging of Biological Membranes in Liquid", *Physical Review Letters*, vol. 99, no. 4, p. 046 102, Jul. 2007.

[188] O. Sahin, S. Magonov, C. Su, C. F. Quate, and O. Solgaard, "An atomic force microscope tip designed to measure time-varying nanomechanical forces", *Nature Nanotechnology*, vol. 2, no. 8, pp. 507–514, Jul. 2007.

[189] D. Martinez-Martin, E. T. Herruzo, C. Dietz, J. Gomez-Herrero, and R. Garcia, "Noninvasive Protein Structural Flexibility Mapping by Bimodal Dynamic Force Microscopy", *Physical Review Letters*, vol. 106, no. 19, p. 198 101, May 2011.

[190] S. C. Minne, Y. Hu, S. Hu, B. Pittenger, and C. Su, "NanoScale Quantitative Mechanical Property Mapping Using Peak Force Tapping Atomic Force Microscopy", *Microscopy and Microanalysis*, vol. 16, no. S2, pp. 464–465, Aug. 2010.

[191] C. Su, S. Hu, Y. Hu, N. Erina, and A. Slade, "Quantitative Mechanical Mapping of Biomolecules in Fluid", *MRS Proceedings*, vol. 1261, pages, Feb. 2011.

[192] C. Canale, M. Jacono, A. Diaspro, and S. Dante, "Force spectroscopy as a tool to investigate the properties of supported lipid membranes", *Microscopy Research and Technique*, vol. 73, no. 10, pp. 965–972, Mar. 2010.

[193] H.-J. Butt, B. Cappella, and M. Kappl, "Force measurements with the atomic force microscope: Technique, interpretation and applications", *Surface Science Reports*, vol. 59, no. 1-6, pp. 1–152, Oct. 2005.

[194] D. Alsteens, V. Duprès, S. Yunus, J.-P. Latgé, J. J. Heinisch, *et al.*, "High-Resolution Imaging of Chemical and Biological Sites on Living Cells Using Peak Force Tapping Atomic Force Microscopy", *Langmuir*, vol. 28, no. 49, pp. 16 738–16 744, Dec. 2012.

[195] F. Rico, C. Su, and S. Scheuring, "Mechanical Mapping of Single Membrane Proteins at Submolecular Resolution", *Nano letters*, vol. 11, no. 9, pp. 3983–3986, Sep. 2011.

[196] L. Picas, F. Rico, and S. Scheuring, "Direct Measurement of the Mechanical Properties of Lipid Phases in Supported Bilayers", *Biophysical Journal*, vol. 102, no. 1, pp. L01–L03, Jan. 2012.

[197] H. V. Guzman, A. P. Perrino, and R. Garcia, "Peak Forces in High-Resolution Imaging of Soft Matter in Liquid", *ACS Nano*, vol. 7, no. 4, pp. 3198–3204, Apr. 2013.

[198] T. Fukuma, M. Kimura, K. Kobayashi, K. Matsushige, and H. Yamada, "Development of low noise cantilever deflection sensor for multienvironment frequency-modulation atomic force microscopy", *Review of Scientific Instruments*, vol. 76, no. 5, p. 053 704, 2005.

[199] B. W. Hoogenboom, P. L. T. M. Frederix, J. L. Yang, S. Martin, Y. Pellmont, *et al.*, "A Fabry–Perot interferometer for micrometer-sized cantilevers", *Applied Physics Letters*, vol. 86, no. 7, p. 074 101, 2005.

[200] B. Mokaberi and A. A. G. Requicha, "Compensation of scanner creep and hysteresis for AFM nanomanipulation", *Ieee Transactions on Automation Science and Engineering*, vol. 5, no. 2, pp. 197–206, Apr. 2008.

[201] T. Ando, T. Uchihashi, and N. Kodera, "High-Speed AFM and Applications to Biomolecular Systems", *Annual review of biophysics*, vol. 42, no. 1, pp. 393–414, May 2013.

[202] J. L. Yang, M. Despont, U. Drechsler, B. W. Hoogenboom, P. L. T. M. Frederix, *et al.*, "Miniaturized single-crystal silicon cantilevers for scanning force microscopy", *Applied Physics Letters*, vol. 86, no. 13, p. 134 101, 2005.

[203] M. B. Viani, T. E. Schäffer, A. Chand, M. Rief, H. E. Gaub, *et al.*, "Small cantilevers for force spectroscopy of single molecules", *Journal of Applied Physics*, vol. 86, no. 4, p. 2258, 1999.

[204] M. Leitner, G. E. Fantner, E. J. Fantner, K. Ivanova, T. Ivanov, *et al.*, "Increased imaging speed and force sensitivity for bio-applications with small cantilevers using a conventional AFM setup", *Micron (Oxford, England : 1993)*, vol. 43, no. 12, pp. 1399–1407, Dec. 2012.

[205] M. Zhao, V. Sharma, H. Wei, R. R. Birge, J. A. Stuart, *et al.*, "Ultrasharp and high aspect ratio carbon nanotube atomic force microscopy probes for enhanced surface potential imaging.", *Nanotechnology*, vol. 19, no. 23, p. 235 704, Jun. 2008.

[206] T. Fukuma and M. J. Higgins, *Dynamic-Mode AFM in Liquid*, ser. Biological Applications. Weinheim, Germany: Wiley-VCH Verlag GmbH & Co. KGaA, Apr. 2012.

[207] D. A. Walters, J. P. Cleveland, N. H. Thomson, P. K. Hansma, M. A. Wendman, *et al.*, "Short cantilevers for atomic force microscopy", *Review of Scientific Instruments*, vol. 67, no. 10, p. 3583, 1996.

[208] N. R. Wilson and J. V. Macpherson, "Carbon nanotube tips for atomic force microscopy.", *Nature Nanotechnology*, vol. 4, no. 8, pp. 483–491, Aug. 2009.

[209] T. Ando, T. Uchihashi, N. Kodera, D. Yamamoto, A. Miyagi, *et al.*, "High-speed AFM and nano-visualization of biomolecular processes", *Pflügers Archiv : European journal of physiology*, vol. 456, no. 1, pp. 211–225, Dec. 2007.

[210] T. Ando, T. Uchihashi, and T. Fukuma, "High-speed atomic force microscopy for nano-visualization of dynamic biomolecular processes", *Progress in Surface Science*, vol. 83, no. 7-9, pp. 337–437, Nov. 2008.

[211] T. Ando, N. Kodera, Y. Naito, T. Kinoshita, K. Furuta, *et al.*, "A High-speed Atomic Force Microscope for Studying Biological Macromolecules in Action", *ChemPhysChem*, vol. 4, no. 11, pp. 1196–1202, Nov. 2003.

[212] H. Yamashita, N. Kodera, A. Miyagi, T. Uchihashi, D. Yamamoto, *et al.*, "Tip-sample distance control using photothermal actuation of a small cantilever for high-speed atomic force microscopy", *The Review of scientific instruments*, vol. 78, no. 8, p. 083 702, 2007.

[213] N. R. Wilson and J. V. Macpherson, "Single-walled carbon nanotubes as templates for nanowire conducting probes", *Nano letters*, 2003.

[214] W. Han, S. M. Lindsay, and T. Jing, "A magnetically driven oscillating probe microscope for operation in liquids", *Applied Physics Letters*, vol. 69, no. 26, p. 4111, 1996.

[215] S. Hoof, N. Nand Gosvami, and B. W. Hoogenboom, "Enhanced quality factors and force sensitivity by attaching magnetic beads to cantilevers for atomic force microscopy in liquid", *Journal of Applied Physics*, vol. 112, no. 11, p. 114 324, 2012.

[216] K.-i. Umeda, N. Oyabu, K. Kobayashi, Y. Hirata, K. Matsushige, *et al.*, "High-Resolution Frequency-Modulation Atomic Force Microscopy in Liquids Using Electrostatic Excitation Method", *Applied Physics Express*, vol. 3, no. 6, p. 065 205, Jun. 2010.

[217] H. Asakawa and T. Fukuma, "Spurious-free cantilever excitation in liquid by piezoactuator with flexure drive mechanism", *The Review of scientific instruments*, vol. 80, no. 10, p. 103 703, 2009.

[218] G. C. Ratcliff, D. A. Erie, and R. Superfine, "Photothermal modulation for oscillating mode atomic force microscopy in solution", *Applied Physics Letters*, vol. 72, no. 15, p. 1911, 1998.

[219] D. Ramos, J. Tamayo, J. Mertens, and M. Calleja, "Photothermal excitation of microcantilevers in liquids", *Journal of Applied Physics*, vol. 99, no. 12, p. 124 904, Jun. 2006.

[220] J. R. Barnes, R. J. Stephenson, C. N. Woodburn, S. J. O'Shea, M. E. Welland, *et al.*, "A femtojoule calorimeter using micromechanical sensors", *The Review of scientific instruments*, vol. 65, no. 12, pp. 3793–3798, 1994.

[221] B. R. Ilic, S. Krylov, and H. G. Craighead, "Theoretical and experimental investigation of optically driven nanoelectromechanical oscillators", *Journal of Applied Physics*, vol. 107, no. 3, p. 034 311, Feb. 2010.

[222] S. Nishida, D. Kobayashi, T. Sakurada, T. Nakazawa, Y. Hoshi, *et al.*, "Photothermal excitation and laser Doppler velocimetry of higher cantilever vibration modes for dynamic atomic force microscopy in liquid", *The Review of scientific instruments*, vol. 79, no. 12, p. 123 703, 2008.

[223] T. Fukuma, "Wideband low-noise optical beam deflection sensor with photothermal excitation for liquid-environment atomic force microscopy", *The Review of scientific instruments*, vol. 80, no. 2, p. 023 707, 2009.

[224] D. Kiracofe, K. Kobayashi, A. Labuda, A. Raman, and H. Yamada, "High efficiency laser photothermal excitation of microcantilever vibrations in air and liquids", *The Review of scientific instruments*, vol. 82, no. 1, p. 013 702, 2011.

[225] D. M. Weld and A. Kapitulnik, "Feedback control and characterization of a microcantilever using optical radiation pressure", *Applied Physics Letters*, vol. 89, no. 16, p. 164 102, 2006.

[226] D. J. Müller, H.-J. Sass, S. A. Müller, G. Büldt, and A. Engel, "Surface structures of native bacteriorhodopsin depend on the molecular packing arrangement in the membrane", *Journal of molecular biology*, vol. 285, no. 5, pp. 1903–1909, Feb. 1999.

[227] K. Voitchovsky, S. Antoranz Contera, M. Kamihira, A. Watts, and J. F. Ryan, "Differential Stiffness and Lipid Mobility in the Leaflets of Purple Membranes", *Biophysical Journal*, vol. 90, no. 6, pp. 2075–2085, Mar. 2006.

[228] F. Ostendorf, C. Schmitz, S. Hirth, A. Kühnle, J. J. Kolodziej, *et al.*, "How flat is an air-cleaved mica surface?", *Nanotechnology*, vol. 19, no. 30, p. 305 705, Jun. 2008.

[229] D. Pastré, O. Piétrement, S. Fusil, F. Landousy, J. Jeusset, *et al.*, "Adsorption of DNA to Mica Mediated by Divalent Counterions: A Theoretical and Experimental Study", *Biophysical Journal*, vol. 85, no. 4, pp. 2507–2518, Oct. 2003.

[230] Y. L. Lyubchenko and L. S. Shlyakhtenko, "AFM for analysis of structure and dynamics of DNA and protein–DNA complexes", *Methods*, vol. 47, no. 3, pp. 206–213, Mar. 2009.

[231] M. Bezanilla, S. Manne, D. E. Laney, Y. L. Lyubchenko, and H. G. Hansma, "Adsorption of DNA to Mica, Silylated Mica, and Minerals: Characterization by Atomic Force Microscopy", *Langmuir*, vol. 11, no. 2, pp. 655–659, Feb. 1995.

[232] J. S. Ellis, H. G. Abdelhady, S. Allen, M. C. Davies, C. J. Roberts, *et al.*, "Direct atomic force microscopy observations of monovalent ion induced binding of DNA to mica.", *Journal of microscopy*, vol. 215, no. Pt 3, pp. 297–301, Sep. 2004.

[233] C. Espenel, M.-C. Giocondi, B. Seantier, P. Dosset, P.-E. Milhiet, *et al.*, "Temperature-dependent imaging of living cells by AFM", *Ultramicroscopy*, vol. 108, no. 10, pp. 1174–1180, Sep. 2008.

[234] L. Redondo-Morata, M. I. Giannotti, and F. Sanz, *Stability of Lipid Bilayers as Model Membranes: Atomic Force Microscopy and Spectroscopy Approach*, ser. Biological Applications. Weinheim, Germany: Wiley-VCH Verlag GmbH & Co. KGaA, Apr. 2012.

[235] T. Wieprecht, O. Apostolov, M. Beyermann, and J. Seelig, "Membrane Binding and Pore Formation of the Antibacterial Peptide PGLa: Thermodynamic and Mechanistic Aspects", *Biochemistry*, vol. 39, no. 2, pp. 442–452, Jan. 2000.

[236] P. D. Rakowska, H. Jiang, S. Ray, A. Pyne, B. Lamarre, *et al.*, "Nanoscale imaging reveals laterally expanding antimicrobial pores in lipid bilayers.", *Proceedings of the National Academy of Sciences of the United States of America*, vol. 110, no. 22, pp. 8918–8923, May 2013.

[237] M. G. Ryadnov, A. Bella, S. Timson, and D. N. Woolfson, "Modular Design of Peptide Fibrillar Nano- to Microstructures", *Journal of the American Chemical Society*, vol. 131, no. 37, pp. 13 240–13 241, Sep. 2009.

[238] T. de Paula Rigoletto, C. L. Silva, M. H. A. Santana, R. S. Rosada, and L. G. de la Torre, "Effects of extrusion, lipid concentration and purity on physico-chemical and biological properties of cationic liposomes for gene vaccine applications", *Journal of Microencapsulation*, vol. 29, no. 8, pp. 759–769, Dec. 2012.

[239] S. Garcia-Manyes, G. Oncins, and F. Sanz, "Effect of Temperature on the Nanomechanics of Lipid Bilayers Studied by Force Spectroscopy", *Biophysical Journal*, vol. 89, no. 6, pp. 4261–4274, Dec. 2005.

[240] H. Egawa and K. Furusawa, "Liposome Adhesion on Mica Surface Studied by Atomic Force Microscopy", *Langmuir*, vol. 15, no. 5, pp. 1660–1666, Mar. 1999.

[241] B. P. Gaber and J. P. Sheridan, "Kinetic and thermodynamic studies of the fusion of small unilamellar phospholipid vesicles", *Biochimica et Biophysica Acta (BBA)-Biomembranes*, vol. 685, no. 1, pp. 87–93, Feb. 1982.

[242] P. M. Macdonald and J. Seelig, "Calcium binding to mixed phosphatidylglycerol-phosphatidylcholine bilayers as studied by deuterium nuclear magnetic resonance", *Biochemistry*, vol. 26, no. 5, pp. 1231–1240, Mar. 1987.

[243] L. Ryan, B. Lamarre, T. Diu, J. Ravi, P. J. Judge, *et al.*, "Anti-Antimicrobial Peptides: Folding-Mediated Host Defense Antagonists", *The Journal of Biological Chemistry*, vol. 288, no. 28, pp. 20 162–20 172, Jul. 2013.

[244] B. Lamarre, J. Ravi, and M. G. Ryadnov, "GeT peptides: a single-domain approach to gene delivery", *Chemical Communications*, vol. 47, no. 32, p. 9045, 2011.

[245] B. W. M. Kuipers and H. Gruppen, "Prediction of molar extinction coefficients of proteins and peptides using UV absorption of the constituent amino acids at 214 nm to enable quantitative reverse phase high-performance liquid chromatography-mass spectrometry analysis.", *Journal of agricultural and food chemistry*, vol. 55, no. 14, pp. 5445–5451, Jul. 2007.

[246] R. Thompson, "Imaging and Analysing DNA Structure using Atomic Force Microscopy", Master's thesis, University College London, London.

[247] L. Venema, V. Meunier, P. Lambin, and C. Dekker, "Atomic structure of carbon nanotubes from scanning tunneling microscopy", *Physical Review B*, vol. 61, no. 4, pp. 2991–2996, Jan. 2000.

[248] H. G. Hansma, J. Vesenka, C. Siegerist, G. Kelderman, H. Morrett, *et al.*, "Reproducible Imaging and Dissection of Plasmid DNA Under Liquid with the Atomic Force Microscope", *Science*, vol. 256, no. 5060, pp. 1180–1184, May 1992.

[249] D. Nečas and P. Klapetek, "Gwyddion: an open-source software for SPM data analysis", *Central European Journal of Physics*, vol. 10, no. 1, pp. 181–188, Nov. 2011.

[250] A. D. Bates, A. Noy, M. M. Piperakis, S. A. Harris, and A. Maxwell, "Small DNA circles as probes of DNA topology", *Biochemical Society transactions*, vol. 41, no. 2, pp. 565–570, Apr. 2013.

[251] F. Kouzine, A. Gupta, L. Baranello, D. Wojtowicz, K. Ben-Aissa, *et al.*, "Transcription-dependent dynamic supercoiling is a short-range genomic force", *Nature Structural & Molecular Biology*, vol. 20, no. 3, pp. 396–403, Mar. 2013.

[252] J. M. Fogg, G. L. Randall, B. M. Pettitt, D. W. L. Sumners, S. A. Harris, *et al.*, "Bullied no more: when and how DNA shoves proteins around", *Quarterly Reviews of Biophysics*, vol. 45, no. 03, pp. 257–299, Aug. 2012.

[253] C. A. Laughton and S. A. Harris, "The atomistic simulation of DNA", *Wiley Interdisciplinary Reviews: Computational Molecular Science*, vol. 1, no. 4, pp. 590–600, Jul. 2011.

[254] J. M. Fogg, N. Kolmakova, I. Rees, S. Magonov, H. Hansma, *et al.*, "Exploring writhe in supercoiled minicircle DNA", *Journal of Physics: Condensed Matter*, vol. 18, no. 14, S145–S159, Mar. 2006.

[255] J. E. Deweese, M. A. Osheroff, and N. Osheroff, "DNA topology and topoisomerases", *Biochemistry and Molecular Biology Education*, vol. 37, no. 1, pp. 2–10, Jan. 2009.

[256] D. Demurtas, A. Amzallag, E. J. Rawdon, J. H. Maddocks, J. Dubochet, *et al.*, "Bending modes of DNA directly addressed by cryo-electron microscopy of DNA minicircles", *Nucleic Acids Research*, vol. 37, no. 9, pp. 2882–2893, May 2009.

[257] N. Crampton, M. Yokokawa, D. T. F. Dryden, J. M. Edwardson, D. N. Rao, *et al.*, "Fast-scan atomic force microscopy reveals that the type III restriction enzyme EcoP15I is capable of DNA translocation and looping.", *Proceedings of the National Academy of Sciences*, vol. 104, no. 31, pp. 12 755–12 760, Jul. 2007.

[258] A. Amzallag, C. Vaillant, M. Jacob, M. Unser, J. Bednar, *et al.*, "3D reconstruction and comparison of shapes of DNA minicircles observed by cryo-electron microscopy", *Nucleic Acids Research*, vol. 34, no. 18, e125–e125, Sep. 2006.

[259] M. Zoli, "Twisting and bending stress in DNA minicircles", *Soft Matter*, vol. 10, no. 24, p. 4304, 2014.

[260] J. S. Mitchell, C. A. Laughton, and S. A. Harris, "Atomistic simulations reveal bubbles, kinks and wrinkles in supercoiled DNA.", *Nucleic Acids Research*, vol. 39, no. 9, pp. 3928–3938, May 2011.

[261] M. Maaloum, "A close encounter with DNA", *European biophysics journal : EBJ*, vol. 32, no. 6, pp. 585–587, Oct. 2003.

[262] O. J. Rojas, "Adsorption of polyelectrolytes on mica", *Encyclopedia of Surface and Colloid Science*, 2002.

[263] C. D. Fjell, R. E. W. Hancock, and A. Cherkasov, "AMPer: a database and an automated discovery tool for antimicrobial peptides", *Bioinformatics*, vol. 23, no. 9, pp. 1148–1155, May 2007.

[264] H. Steiner, D. Andreu, and R. B. Merrifield, "Binding and action of cecropin and cecropin analogues: antibacterial peptides from insects.", *Biochimica et biophysica acta*, vol. 939, no. 2, pp. 260–266, Apr. 1988.

[265] K. J. Hallock, D.-K. Lee, and A. Ramamoorthy, "MSI-78, an Analogue of the Magainin Antimicrobial Peptides, Disrupts Lipid Bilayer Structure via Positive Curvature Strain", *Biophysical Journal*, vol. 84, no. 5, pp. 3052–3060, May 2003.

[266] J. Kyte and R. F. Doolittle, "A simple method for displaying the hydropathic character of a protein", *Journal of molecular biology*, vol. 157, no. 1, pp. 105–132, May 1982.

[267] K. S. Akerfeldt, J. D. Lear, Z. R. Wasserman, L. A. Chung, and W. F. DeGrado, "Synthetic peptides as models for ion channel proteins", *Accounts of Chemical Research*, vol. 26, no. 4, pp. 191–197, Apr. 1993.

[268] M. G. Ryadnov, G. V. Mukamolova, A. S. Hawrani, J. Spencer, and R. Platt, "RE coil: an antimicrobial peptide regulator.", *Angewandte Chemie International Edition*, vol. 48, no. 51, pp. 9676–9679, 2009.

[269] W. S. Horne, J. L. Price, and S. H. Gellman, "Interplay among Side Chain Sequence, Backbone Composition, and Residue Rigidification in Polypeptide Folding and Assembly", *Proceedings of the National Academy of Sciences of the United States of America*, vol. 105, no. 27, pp. 9151–9156, Jul. 2008.

[270] P. F. Almeida and A. Pokorny, "Mechanisms of Antimicrobial, Cytolytic, and Cell-Penetrating Peptides: From Kinetics to Thermodynamics", *Biochemistry*, vol. 48, no. 34, pp. 8083–8093, Sep. 2009.

[271] L. Yang, T. M. Weiss, R. I. Lehrer, and H. W. Huang, "Crystallization of Antimicrobial Pores in Membranes: Magainin and Protegrin", *Biophysical Journal*, vol. 79, no. 4, pp. 2002–2009, Oct. 2000.

[272] K. V. R. Reddy, R. D. Yedery, and C. Aranha, "Antimicrobial peptides: premises and promises", *International journal of antimicrobial agents*, vol. 24, no. 6, pp. 536–547, Dec. 2004.

[273] S. A. Beers, A. G. Buckland, R. S. Koduri, W. Cho, M. H. Gelb, *et al.*, "The antibacterial properties of secreted phospholipases A2: a major physiological role for the group IIA enzyme that depends on the very high pI of the enzyme to allow penetration of the bacterial cell wall.", *The Journal of Biological Chemistry*, vol. 277, no. 3, pp. 1788–1793, Jan. 2002.

[274] E. Glukhov, M. Stark, L. L. Burrows, and C. M. Deber, "Basis for selectivity of cationic antimicrobial peptides for bacterial versus mammalian membranes.", *The Journal of Biological Chemistry*, vol. 280, no. 40, pp. 33 960–33 967, Oct. 2005.

[275] P. Wadhwani, R. F. Epand, N. Heidenreich, J. Bürck, A. S. Ulrich, *et al.*, "Membrane-Active Peptides and the Clustering of Anionic Lipids", *Biophysical Journal*, vol. 103, no. 2, pp. 265–274, Jul. 2012.

[276] E. I. Goksu, J. M. Vanegas, C. D. Blanchette, W.-C. Lin, and M. L. Longo, "AFM for structure and dynamics of biomembranes", *Biochimica et Biophysica Acta (BBA)-Biomembranes*, vol. 1788, no. 1, pp. 254–266, Jan. 2009.

[277] E. Lesniewska, P. Emmanuel Milhiet, M.-C. Giocondi, and C. Le Grimellec, "Atomic Force Microscope Imaging of Cells and Membranes", in *Atomic Force Microscopy in Cell Biology*, Elsevier, 2002, pp. 51–65.

[278] S. Garcia-Manyes, L. Redondo-Morata, G. Oncins, and F. Sanz, "Nanomechanics of Lipid Bilayers: Heads or Tails?", *Journal of the American Chemical Society*, vol. 132, no. 37, pp. 12 874–12 886, Sep. 2010.

[279] E. Glukhov, L. L. Burrows, and C. M. Deber, "Membrane interactions of designed cationic antimicrobial peptides: the two thresholds.", *Biopolymers*, vol. 89, no. 5, pp. 360–371, May 2008.

[280] D. Oh, S. Y. Shin, S. Lee, J. H. Kang, S. D. Kim, *et al.*, "Role of the Hinge Region and the Tryptophan Residue in the Synthetic Antimicrobial Peptides, Cecropin A(1-8)-Magainin 2(1-12) and Its Analogues, on Their Antibiotic Activities and Structures", *Biochemistry*, vol. 39, no. 39, pp. 11 855–11 864, Oct. 2000.

[281] D. N. Woolfson, G. J. Bartlett, M. Bruning, and A. R. Thomson, "New currency for old rope: from coiled-coil assemblies to α-helical barrels", *Current Opinion in Structural Biology*, vol. 22, no. 4, pp. 432–441, 2012.

[282] X.-m. Qu, H. Steiner, A. Engström, H. Bennich, and H. G. Boman, "Insect Immunity: Isolation and Structure of Cecropins B and D from Pupae of the Chinese Oak Silk Moth, Antheraea pernyi", *European Journal of Biochemistry*, vol. 127, no. 1, pp. 219–224, Sep. 1982.

[283] H. Hu, C. Wang, X. Guo, W. Li, Y. Wang, *et al.*, "Broad activity against porcine bacterial pathogens displayed by two insect antimicrobial peptides moricin and cecropin B", *Molecules and Cells*, vol. 35, no. 2, pp. 106–114, Feb. 2013.

[284] H. Drew, T. Takano, S. Tanaka, K. Itakura, and R. E. Dickerson, "High-salt d(CpGpCpG), a left-handed Z-DNA double helix", *Nature*, vol. 286, no. 5773, pp. 567–573, Aug. 1980.

[285] F. X. Gallat, N. Matsugaki, N. P. Coussens, K. J. Yagi, M. Boudes, *et al.*, "In vivo crystallography at X-ray free-electron lasers: the next generation of structural biology?", *Philosophical Transactions of the Royal Society B: Biological Sciences*, vol. 369, no. 1647, pp. 20 130 497–20 130 497, Jun. 2014.

[286] S. C. Ha, K. Lowenhaupt, A. Rich, Y.-G. Kim, and K. K. Kim, "Crystal structure of a junction between B-DNA and Z-DNA reveals two extruded bases", *Nature*, vol. 437, no. 7062, pp. 1183–1186, Oct. 2005.

[287] K. Brzezinski, A. Brzuszkiewicz, M. Dauter, M. Kubicki, M. Jaskolski, *et al.*, "High regularity of Z-DNA revealed by ultra high-resolution crystal structure at 0.55 A", *Nucleic Acids Research*, vol. 39, no. 14, pp. 6238–6248, Aug. 2011.

[288] U. Hübner, W. Morgenroth, H. G. Meyer, T. Sulzbach, B. Brendel, *et al.*, "Downwards to metrology in nanoscale: determination of the AFM tip shape with well-known sharp-edged calibration structures", *Applied Physics A: Materials Science & Processing*, vol. 76, no. 6, pp. 913–917, 2003.

[289] K. Hall, T.-H. Lee, A. I. Mechler, M. J. Swann, and M.-I. Aguilar, "Real-time Measurement of Membrane Conformational States Induced by Antimicrobial Peptides: Balance Between Recovery and Lysis", *Scientific Reports*, vol. 4, Jun. 2014.

[290] Y. Shai, "Mode of action of membrane active antimicrobial peptides", *Biopolymers*, vol. 66, no. 4, pp. 236–248, Dec. 2002.

[291] L. T. Nguyen, E. F. Haney, and H. J. Vogel, "The expanding scope of antimicrobial peptide structures and their modes of action", *Trends in biotechnology*, vol. 29, no. 9, pp. 464–472, Sep. 2011.

Appendix A

DNA Protocol

Substrate and Sample Preparation:

Use a large metal puck as your base and glue a teflon layer to the metal puck. A primer such as Bondloc B2030 may need to be applied to the teflon surface in advance to enable glue such as Loctite 406 to glue the teflon to the metal puck. Primer may also need to be applied to the upward-facing side of the teflon in order that a mica disk can then be glued successfully to the teflon. Once dry the teflon can be cut to fit the puck in order not to interfere with its flat placement on the scan tube.

DNA and buffers should be stored in a fridge for continual use, and can be frozen if not needed for a long period of time. The DNA and buffers will need to warm up to room temperature to minimise drift in the MM, and may heat up further once in the microscope.

The DNA used is 3486 bp pMax DNA plasmid obtained from Lonza (Switzerland). The original undiluted concentration is 1.5 μg/μl. A 500x dilution is 3 ng/μl. The final DNA concentation in solution is 0.2 ng/μl.

DNA Adsorption on Mica:

1. Cleave mica substrate
2. Add 25 μl 20 mM $NiCl_2$ solution to the mica substrate
3. Incubate for 2 minutes
4. Add 7 μl 500x diluted DNA solution to the $NiCl_2$
5. Add 25 μl 10 mM HEPES buffer solution
6. Distribute evenly in the meniscus by purging
7. Allow to equilibrate for 30 minutes
8. Mount the sample on the scanner
9. Add 50 μl buffer solution to the cantilever and mount the fluid cell

Appendix B

Lipid Preparation Protocol

This protocol describes the process for creating uniform large lipid bilayers on a mica substrate by forming a negatively charged PC:PG (3:1) lipid suspension. The lipid suspension will be prepared at 4 mg/ml. The buffer used in this instance is 20mM HEPES, 150 mM NaCl.

Forming a Mixed Lipid Solution

1. Remove the lipid powders from the freezer and allow to equilibrate to room temperature before opening

Figure 1: *A digital balance*

Figure 2: *A glass vial with plastic tight fitting cap*

Figure 3: *A vortex for vigorously mixing solutions*

2. Weigh out the desired amount of each dry lipid powder into a teflon capped glass vial (figure 2) using an accurate digital balance (figure 1)

   To form a 3:1 DLPC:DLPG solution at a concentration of 4 mg/ml:

   - 7.5 mg of the zwitterionic lipid (e.g. DLPC)
   - 2.5 mg of the negatively charged lipid (e.g. DLPG)

3. Add the organic solvents to the solution using a glass measuring syringe with a hypodermic needle tip (This is to allow accurate measurement of the heavy and viscous solvents)

   - 600 μl Methanol
   - 300 μl Chloroform

4. Put the lid on the glass vial and shake vigorously to mix - A vortex (see figure 3can be used for this purpose.
   All the powdered lipid must dissolve before the solvent can be evaporated

Drying to Form A Lipid Film

1. Make a small incision in the plastic lid of the glass vial and replace the lid onto the vial
2. Insert the Nitrogen line into the incision
3. Slowly bubble Nitrogen through the solution until the majority of the solvent has evaporated (This may take a few hours)
4. Remove the lid from the vial and leave overnight under a trickling Nitrogen stream in a fume hood to remove any remaining solvent
5. A slightly cloudy thin lipid should form on the base of the vial.
   Ensure all the solvent has evaporated as any solvent will contaminate the experiment

Hydrating to Form a Liposome Suspension

1. Add 1ml DI water or buffer solution to the dried lipid film in the glass vial
2. Tightly affix a new lid (without incision) to the vial and vortex for 2-4 minutes. *If possible affix the vial to the vortex using tape*
3. Place the glass vial in a temperature controlled bath sonicator:
   - Sonication must be performed **above** the transition temperature of both the lipids in solution. See section for a list of transition temperatures.
   - The glass vial must be kept away from the sides of the sonicator using a polystyrene block or wire basket
   - Sonication should be performed for 30-40 minutes
4. Remove the vial from the sonicator - The solution should appear significantly less cloudy than before sonication

   If there is any solvent remaining in the solution this will appear as sediment within the solution. White powder or crystals will be visible and the solution cannot be used for experimentation

Setting up the Extruder

1. The extruder should be set up as in figure 4

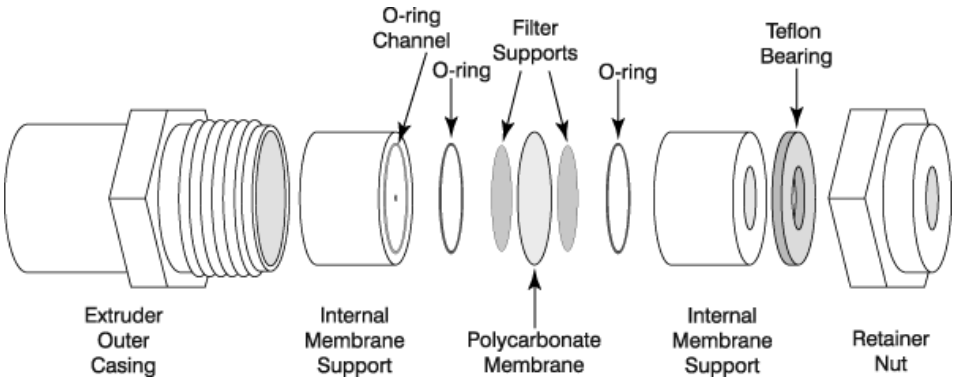

Figure 4: *An expanded view of the extruder*

2. Place the 2 Internal Membrane Supports on a flat surface with the O-rings facing up using the blunt tweezers provided (figure 5)
3. Pre-wet 2 Filter Supports (figure 6) with DI water, or buffer, and place over orifice. The Filter Supports should adhere to the teflon surface inside the O-ring inner diameter.
4. Insert the Internal Membrane Support, with the Filter Support, into the Extruder Outer Casing with the O-ring facing up.
5. Place 1 100 nm Polycarbonate Membrane (figure 7) in the Extruder Outer Casing over the Filter Support and O-ring. **The Polycarbonate Membrane is the thin, shiny disk - do not install one of the blue paper disks which separate the Polycarbonate Membranes**.
6. Pre-wet a second pair of Filter Supports with DI water, or buffer, and place over on the remaining Internal Membrane Support.

7. Carefully place the second Internal Membrane Support into the casing (O-ring facing down) being careful not to twist the Membrane Support when it comes in contact with the Membrane.
8. Place the Teflon bearing into the Retainer Nut.
9. Place the Retainer Nut on the threaded end of the Extruder Outer Casing and tighten.

Tighten the Retainer Nut by hand just until it is finger tight; do not use a wrench.

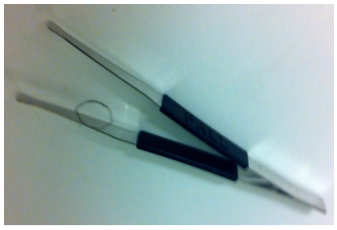

Figure 5: *The blunt tweezers used for manipulating membranes*

Figure 6: *Filter supports for the Avanti extruder*

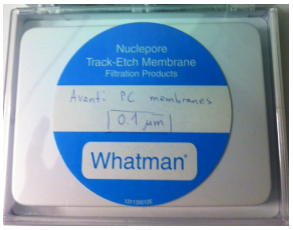

Figure 7: *Membranes for the Avanti extruder*

Extrusion of Vesicles

1. Pre-wet the extruder parts by passing a syringe full of buffer through the extruder, discard the buffer after use
2. Place the extruder heating block onto a hot plate. Insert a thermometer into the well provided in the heating block. Switch the hot plate on, and allow to reach the desired temperature - this will take up to 15 minutes.

   The heating block must be heated to above the transition temperature of the lipids
3. Place the empty gas-tight syringe into one end of the extruder Make sure the empty syringe plunger is set to zero to minimise any air bubbles in the system
4. Place the gas-tight syringe into the other end of the extruder.
5. Before placing the extruder into the heating block:
   - Check the temperature of the heating block, this must be below 80C to avoid damaging the syringes
   - Check that both syringes are fully inserted into the extruder
   - Make note of which syringe is empty and which is full for reference later
6. **The extruder apparatus must be fully assembled before insertion into the heating block to avoid damage**
7. Insert the fully assembled extruder apparatus into the extruder stand with the apex of the hex nut pointing down as in figure 8
8. Use the swing-arm clips to hold the syringes in good thermal contact with the heating block
9. Allow the temperature of the lipid suspension to equilibrate with the temperature of the heating block - this will take 5-10 minutes
10. Gently push the plunger of the filled syringe until the lipid solution is completely transferred to the alternate syringe as in figure 9

Figure 8: *The extruder, fully assembled in the heating block*

Figure 9: *The extruder filled with Multi-Lamellar Vesicles*

11. Gently push the plunger of the alternate syringe to transfer the solution back to the original syringe as in figure 9
12. Repeat previous two steps a minimum of 9 times to total 20 passes through membrane.

    The more the lipid solution is passed though the membrane, the more homogeneous it becomes
13. The final extrusion should be taken from the syringe that was originally empty to reduce the chances of contamination with larger particles or foreign material
14. After the final extrusion, remove the mini-extruder from the heating block
15. Remove the filled syringe from the extruder and inject the lipid solution into a clean sample vial.

    When removing syringes, pull the syringe straight out of the extruder as removing at an angle can cause damage
16. Clean the extruder as detailed in section .

Adsorbing the Lipid Suspension

1. Place 1 μl 1 M $MgCl_2$ solution onto a freshly cleaved mica disk
2. Add 25 μl buffer solution
3. Add 25 μl 5 mg/ml lipid suspension and purge repeatedly to mix the solution on the surface as shown in figure 10
4. Leave to absorb for 30 minutes
5. Wash the surface gently three times with 100 μl buffer solution - discarding the buffer each time
6. Add 100μL buffer solution for AFM for imaging in liquid

Figure 10: *Mixing of the buffer and lipid solutions on a mica disk attached to a metal disk*

Storage of Lipid Suspensions

- Store the vesicle preparation above the transition temperature of the lipid during the experiment
- When not in use, store the vesicle solution at 4^oC.
- Vesicle solutions are not stable in aqueous media for more than 3-4 days when stored at 4^oC
- When using a sample stored at 4^oC follow the steps outlined in section before use
- Do not freeze
- Storage of vesicle solutions at higher temperatures and pH < 5 or > 8 may reduce the lifetime of the vesicle suspension

Using a Lipid Suspension which has been stored at 4^oC

- The suspension must be extruded each morning before use to ensure a regular homogeneous sample is being used
- More complex suspensions or those with a higher transition temperature may require re-sonication each day before. This can be performed in the same way as outlined in section

Cleaning the Extruder After Use

1. Immediately after use, carefully disassemble both syringes.
2. Rinse the syringes with isopropyl alcohol followed by DI water
3. Dry the syringes using a Nitrogen gun
4. If it is necessary to use a sonic cleaner, only clean the needle with the sonic cleaner. Immediately after cleaning in the sonic cleaner, rinse with DI water and dry

Do not allow the syringes to come into contact with any solvents other than DI water or alcohol. Some organic solvents will interact with the glue holding the threaded insert onto the tip of the syringe possibly weakening the bond between the barrel and the insert. The syringes must not be soaked in any solvent for the same reason

Table of Phospholipid Transition Temperatures

Phosphatidylcholine		**Phosphatidylglycerol**		
12:0 PC (DLPC)	-1	12:0 PG (DLPG)	-3	
13:0 PC	14	14:0 PG (DMPG)	23	
14:0 PC (DMPC)	23	16:0 PG (DPPG)	41	
15:0 PC	33	18:0 PG (DSPG)	55	
16:0 PC (DPPC)	41	18:1 PG (DOPG)	-18	
17:0 PC	48	16:0-18:1 PG (POPG)	-2	
18:0 PC (DSPC)	55	**Phosphatidylserine**		
19:0 PC	60	14:0 PS (DMPC)	35	
20:0 PC	66	16:0 PS DPPC)	54	
21:0 PC	72	18:0 PS (DSPC)	68	
22:0 PC	75	18:1 PS (DOPS)	-11	
23:0 PC	79	16:0-18:1 PS (POPS)	14	
24:0 PC	80	**Phosphatic Acid**		
16:1 PC	-36	12:0 PA (DLPA)	31	
18:1c9 PC (DOPC)	-20	14:0 PA (DMPA)	50	
18:1t9 PC	12	16:0 PA (DPPA)	67	
18:1c6 PC	1	18:0 PA (DSPA)	75	
18:2 PC	-53	18:1 PA (DOPA)	-8	
18:3 PC	-60	16:0-18:1 PA (POPA)	28	
20:4 PC	-70			
14:0-16:0 PC	35	**Phosphatigylethanolamine**		
14:0-18:0 PC	40	12:0 PE (DLPE)	29	
16:0-14:0 PC	27	14:0 PE (DMPE)	50	
16:0-18:0 PC	49	16:0 PE (DPPE)	63	118
16:0-18:1 (POPC)	-2	18:0 PE (DSPE	74	100
16:0-22:6 PC	-27	20:0 PE	83	96
18:0-14:0 PC	30	18:1c9 PE (DOPE)	-16	10
18:0-16:0 PC	44	18:1t9 PE	38	64
18:0-18:1 PC	6	18:2 PE	-40	-15
18:1-16:0 PC	-9	18:3 PE		-30
18:1-18:0 PC	9	16:0-18:1 PE (POPE)	25	71

Appendix C

Buffer Protocol

Buffer Preparation:

For 240 mL buffer solution

1. Measure out the dry weights on the balance
2. Add dry weights to 50 ml DI water in a beaker
3. Mix solution thoroughly
4. Add the other 200 ml DI water to the solution and mix
5. Check the pH meter is functioning accurately
   - Check each test solution
     - pH 4
     - pH 7
     - pH 10
   - If the test solutions do not show on the meter correctly - re-calibrate the system
   - After testing - rinse in DI water
6. Check the pH of the buffer solution:
   - If the pH is too low - add alkali (e.g. NaOH) to increase the pH
   - If the pH is too high - add acid (e.g. HCl) to decrease the pH

   Preferable to add acid, as adding alkali adds ions which affect the Debye layer. This effect can be cancelled out by the addition of $CaCl_2$ ions
7. Re-check the solution until it is at the required pH
8. Rinse the pH meter using DI water
9. Store the pH meter by filling the cap with storage solution

40 mM HEPES, 300 mM NaCl Buffer

For 250 mL:

Chemical	Molecular Weight	Molar Concentration (M)	Measured Weight (g)
HEPES	238	0.3	2.38
NaCl	58	0.04	4.35

NaOH Solution

To make 20 ml:
Add 4 pellets NaOH to 20 ml DI water and vortex to dissolve **Must be done in a glass beaker - exothermic reaction**

Appendix D

Apparent Depths of Pores in Model Membranes by AFM

Supported lipid bilayers (SLBs) otherwise known as model membranes are valuable model systems to study the properties of biological membranes and processes. Here negatively charged model membranes are used to mimic bacterial cell membranes to investigate the mechanism of action of antimicrobial peptides prepared as described in chapter 3.

Here the effect of an antimicrobial peptide, designed and synthesised at the National Physical Laboratory by collaborators in the group of Max Ryadnov is examined. The peptide - Amhelit - is a synthetic antimicrobial peptide with sequence KARLAKLRARLYRLKARLARL. This sequence is designed to porate the outer leaflet of a membrane by a number of sequences choices described fully in chapter 6. This mode of action should result in the outer leaflet of the model membrane being removed and a monolayer being exposed.

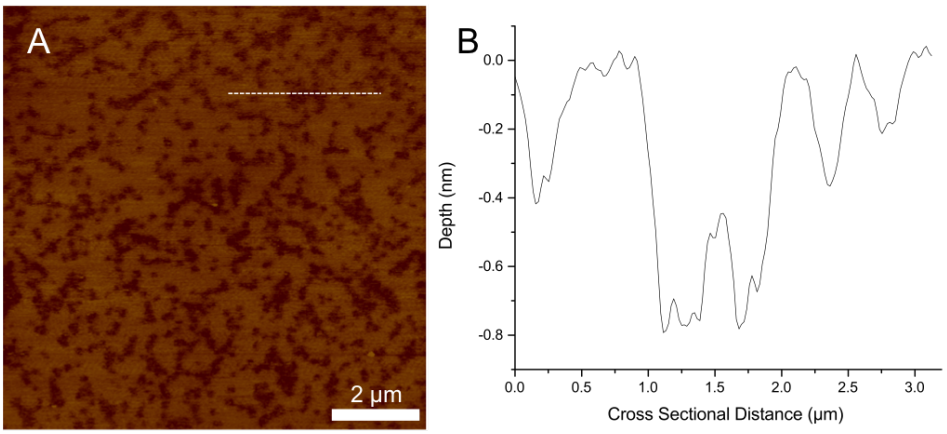

Figure 1: *Poration of a lipid bilayer by Amhelit. A) A model membrane imaged in peak force tapping showing poration of the outer leaflet by Amhelit. B) A line profile taken along the dotted line in A showing the measured depth of poration. Colour Scale: 6 nm. Amhelit concentration: 0.3 µM*

In chapter 6 it was shown that by using minimally invasive imaging techniques developed to image at a low controlled force it is possible to visualise this mechanism of action with the resulting poration measured at a depth of 0.8 nm - significantly less than the depth of the model membrane. An AFM image taken in Peak Force tapping is shown in figure 1, which shows a pore created by Amhelit along with a line profile taken across the pore showing the depth of the poration to be 0.8±0.2 nm.

The model membranes were imaged at a peak force of 60±10 pN and show poration across the model membrane. These pores are uniform in depth at 0.8±0.2 nm. The expected depth of the pore for monolayer poration would be ∼1.6 nm, half of the height of the bilayer. The fact that the pores are not measured by the AFM to the full depth of one monolayer could be attributed to electrostatic interactions between the tip and surface, the presence of peptides on the surface of the exposed monolayer, an effect of the salts used or a combination of a number of factors. However we can be sure that we are not imaging full poration, as this has been shown previously to result in measured pore depths of 2.8 nm in chapter 6.

Prior to this image being taken, a smaller image was taken within the scan area at the same peak force (∼60 pN). This image is shown in figure 2. This image shows much deeper pores formed by Amhelit, measured as 3 nm in depth.

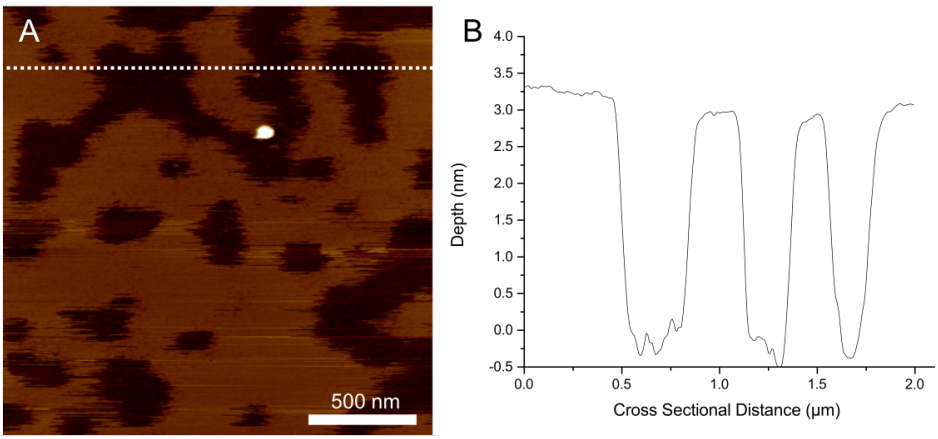

Figure 2: *Poration of a lipid bilayer by Amhelit A) A model membrane imaged in peak force tapping showing poration of the outer leaflet by Amhelit taken prior to 1 at a smaller scan size. B) a Line profile taken along the dotted line marked in A showing the measured depth of the pore. Colour Scale: 10 nm. Amhelit concentration: 0.3 μM*

This shows that imaging at the same set peak force using peak force tapping at smaller scan sizes can result in larger applied forces which disrupt the soft monolayer due to the larger period of time spent by the tip interacting with the same area of the sample at a smaller scan size. Although this effect is expected and intuitive, it causes problems when imaging soft monolayer samples, which are more sensitive to force than a rigid bilayer. The AFM tip pushes through the soft monolayer, which remains adsorbed on the mica and exposed to the buffer solution, once Amhelit has disrupted the top monolayer of the membrane. This could be attributed to the increased interaction of the hydrophobic tails with the AFM tip.

This effect can be seen clearly in figure 3. Whereby image A was taken prior to image B, however A shows a greater depth of poration, visible by the darker colour of the pore even at a larger colour scale. The measured depths of the pores are 0.8 nm for A and 3 nm for B.

Though peak force tapping has been shown to provide excellent force control for high resolution imaging, on many biomolecules, it should be noted that for imaging soft hydrophobic surfaces such as monolayers care should be taken to minimise the applied force in order that surface profiles are correctly measured.

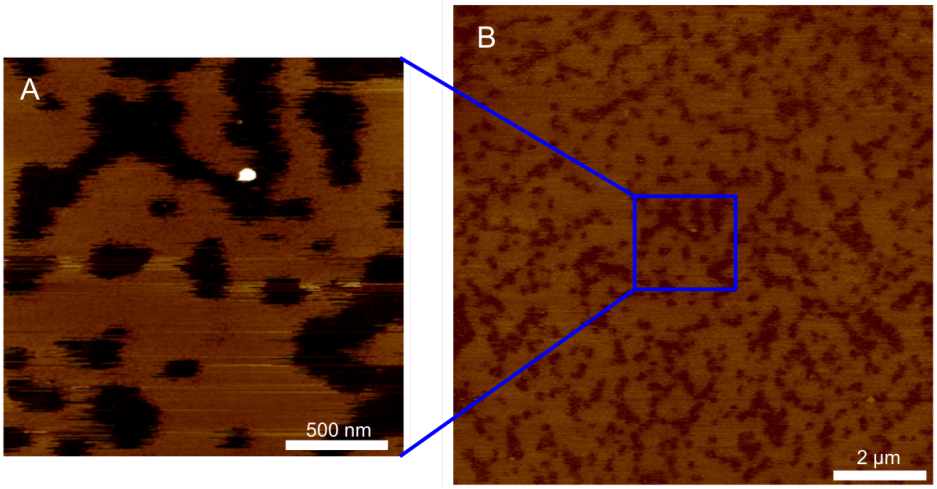

Figure 3: *Images of a model membrane showing the difference in measured depth of poration of a lipid bilayer for the same peak force (∼60 pN at different scan sizes. A) An image showing poration depth of ∼ 3 nm. B) An image taken of the same area at a larger scan size showing a poration depth of ∼0.8 nm. A was taken prior to B. Colour Scale: A) 10 nm B) 6 nm. Amhelit concentration: 0.3 µM*